Fabrication and characterization of superconducting PLD MgB2 thin films

Yue Zhao
University of Wollongong

Fabrication and Characterization of Superconducting PLD MgB_2 Thin Films

A thesis submitted in fulfillment of the
requirements for the award of the degree

Doctor of Philosophy

From

University of Wollongong

By

Yue Zhao, M.E.

Institute of Superconducting & Electronic Materials
Faculty of Engineering

2005

Certification

I , Yue Zhao, declare that this thesis, submitted in fulfillment of the requirements for the award of Doctor of Philosophy, in the Institute for Superconducting & Electronic Materials, Faculty of Engineering, University of Wollongong, is wholly my own work unless other wise referenced or acknowledged. The document has not been submitted for any other academic institution.

Yue Zhao

16 December 2005

Acknowledgement

First of all, I want to thank my supervisors, Prof. Dou and Dr. M. Ionescu, for their instructions and supports through out my PhD study. Dr M. Ionescu also provides major trainings on the operations of PLD deposition system, XRD, and high temperature furnaces.

The Australian Research Council provided the project founding and my APAI scholarship on this work. The University of Wollongong and the Institute for Superconducting & Electronic Material provided financial support to the work.

The magneto-optical imaging in this work was carried out by PhD candidate M. Roussel. The cross-sectional TEM specimen preparation and imaging in Chapter 7 are carried out by Prof. P. Munroe and his colleagues in the Electron Microscopy Unit at UNSW. Here I want to thank their contribution to the thesis work.

Dr. A. V. Pan, Dr. J. Horvat provided major trainning on MPMS and PPMS low temperature physical properties measurement. Dr. D. Wexler provided TEM training. Dr. K. Konstatinov provided SEM training. Dr. Violeta and Dr. P. Whitton provided AFM training. Here I want to thank their warm-hearted helps, lots of time and great patience.

I want to thank Dr Tania's helps for improving my English scientific article writing skill. She has proof read every single piece of my papers that have been published in various journals.

I have had very useful discussions with Dr. E. W. Collings, Dr. X. L. Wang, Dr. D. Q. Shi, Dr. S. H. Zhou, Dr. Saeid, Dr. Sockat, Dr. G. Alvalas and Dr. T Tajima.

Mr. R. Kennel, Mr. N. Mackie, Mr. G. Tillman and Mr. Stuart have offered strong technical support during my PhD research period.

I would like to thank my parents back in China for their persistent support and encouragements to my study.

Finally, I want to thank my wife, Lu Wei, for her dedicated support and complete understanding throughout my PhD study.

Contents

Abstract

The aim of this thesis was to study the thin film of magnesium diboride (MgB_2) superconductor based on PLD synthesis technique. The MgB_2 is a very simple binary compound with a number of surprising properties. The discovery of superconductivity with a critical temperature (T_c) of 39 K in bulk MgB_2 in January 2001 has attracted a huge research interests worldwide in this material. In a hope to substitute MgB_2 superconducting electronics for low temperature superconducting electronics and compete with high temperature superconductors, the preparation techniques of MgB_2 thin films need to be advanced from a material engineering point of view. On the other hand, new studies regarding the different behaviours of MgB_2 thin films and MgB_2 bulks will assist the scientific community to better understand the physics in this superconductor.

We began the study with *in situ* MgB_2 film preparation using normal on-axis geometry. The *in situ* annealing conditions of pulsed laser deposited MgB_2 films were studied. We found that the superconducting properties depend in a crucial way on the annealing conditions: temperature, heating rate and time. We tested the T_c dependence of the *in situ* annealed MgB_2 films by changing various process parameters, including laser energy density, target-substrate distance, background gas, annealing temperatures, heating rates and dwell times. The film processing conditions were optimized and good quality *in situ* films were obtained routinely, with good reproducibility. The hysteresis loops of magnetic moment versus applied field at different temperatures indicate a weak field dependence in high fields. Magneto-optical imaging of the films showed quite homogeneous magnetic flux penetration, indicating structural homogeneity. The films without annealing show no superconductivity.

Another method using *ex situ* annealing has also been tested for a better crystallization of the MgB_2 film, as well as for reference purposes. In the *ex situ* annealing process, we first deposited boron precursor film on a sapphire substrate and then wrapped it in Ta foil and sealed it in a stainless steel tube together with pure Mg pellets, under protective Ar atmosphere. The tube was then annealed in tube furnace and kept at 900ºC for 30 min. With this method, we obtained *ex-situ* MgB_2 films of comparable quality as those reported so far in the literature, and used them as a benchmark to test possible improvements in MgB_2 thin film technology based on PLD.

Significant differences in properties between the *in situ* films and *ex situ* films were found. The *ex situ* annealed MgB_2 film has a $T_{c\ onset}$ of 38.1K, while the *in situ* film has a suppressed $T_{c\ onset}$ of 34.5K. The resistivity at 40K for the *in situ* film is larger than that of the *ex situ* film by a factor of 6. The residual resistivity ratios are 1.1 and 2.1 for the *in situ* and *ex situ* films respectively. The field dependence of the resistivity-temperature curves has been measured. A large slope of the H_{c2}-T curve was obtained for the *in situ* annealed film. The J_c-H curves of the *in situ* film show a much weaker field dependence than those of the *ex situ* film, attributable to stronger flux pinning in the *in situ* film. The microstructural differences between the two types of films are observed by AFM and TEM. The small-grain (<60nm) size and a high oxygen level detected in the *in situ* annealed MgB_2 films may be decisive for the significant improvement of J_c and H_{c2}.

In order to enhance the performance of the MgB_2 films, various amounts of Si up to a level of 18wt% were added into MgB_2 thin films fabricated by pulsed laser deposition. Si was introduced into the PLD MgB_2 films by sequential ablation of a stoichiometric MgB_2 target and a Si target. The T_c's of the Si added MgB_2 thin films

were tested. A J_c enhancement was observed in the Si added MgB_2 films. For the ~3.5wt% Si addition, the best enhancement circumstance, the magnetic critical current density (J_c) of the film at 5K was increased by 50% as compared to the undoped film. The slope of $H_{irr}(T)$ and $H_{c2}(T)$ curves of the 3.5wt% Si added MgB_2 film was slightly higher than that for the undoped film.

For the application in superconducting electronics, the surface smoothness of the MgB_2 thin film is of crucial importance. We pioneered an off-axis deposition geometry in the PLD MgB2 films preparation. Highly smooth and *c*-axis oriented superconducting MgB_2 thin films were successfully achieved with a off-axis geometry. The films were deposited on Al_2O_3-C substrates, aligned perpendicular to a stoichiometric MgB_2 target in a 120 mTorr high purity Ar background gas. An *in situ* annealing was carried out at 650℃ for 1 min in a 760 Torr Ar atmosphere. Despite the short annealing time, an x-ray θ-2θ scan shows fairly good crystallization, according to the clear *c*-axis oriented peaks for the films. Both atomic force microscopy and the x-ray diffraction results indicated that the crystallite size is less than 50nm. The root mean square roughness of our off-axis film was ~4 nm in a 5×5 μm^2 area. The zero resistance T_c value of the best off-axis film reached 32.2 K with a narrow transition width of 0.9 K. The films showed no anisotropy in H_{c2}-T curves when parallel and perpendicular fields were applied relative to the film surface. The slope of H_{c2}-T curves is ~1 T/K, which is still among the highest reported values.

On the basis of successful preparation of smooth off-axis MgB_2 films, we obtained MgB_2/Mg_2Si multilayer structure by sequentially switching a stoichiometric MgB_2 target and a Si target during off-axis pulsed-laser deposition. The transmission electron microscope cross-sectional image of the resulting film exhibits a layered structure with each MgB_2 layer being 40-50 nm thick and the Mg_2Si inter-layers about

5 nm thick. A clear enhanced anisotropy in the irreversibility lines and the vortex activation energy was observed. Pinning and the flux flow activation energy for this type of film was significantly increased in parallel applied fields.

List of Figures

Fig.3-4 The MS spectrum of Ar atmosphere for the chamber at the total pressure of $1x10^{-3}$ Torr. Two argon peaks are present at 40 and 20 amu. The H_2O peak is at 18 amu, and the H_2 peak is at 2 amu.

Fig. 3-5 T_c dependence on in situ annealing temperatures. The T_c was measured by DC susceptibility in ZFC. The thickness of the thicker films is ~1μm; The thickness of the thinner films is ~0.5μm. The heating rate of both groups of films was ~110˚C/min (rapid heating) with a 1 min dwell time, followed by a free cooling at 50°C/min (the power is switched off).

Fig. 3-6 T_c values of MgB_2 films versus in situ annealing ramp time (bottom axis) and heating rate (top axis). The annealing temperature is ~680℃ with 1min dwell time.

Fig. 3-7 The DC susceptibility (ZFC-FC) curves for three different target-substrate distances. Sample #260303 was prepared with 500 mJ/pulse laser energy and 40mm target-substrate distance; the #280503 was prepared with 400 mJ/pulse laser energy and 30mm target-substrate distance; and the #190903 was prepared with 300 mJ/pulse laser energy and 20mm target-substrate distance. All three films have a similar thickness of about 300-400 nm.

Fig. 3-8 SEM images of laser ablated MgB_2 target surface. a) A general look at the ablated ring under 50x magnification. b) Central part of the ablated ring ; c) The margins of the ablated ring . d) Area adjacent to the ablated ring .

Fig.3-9 Area-scan EDS spectrum of the MgB_2 target before and after100 pulses5 J/cm^2 248 nm laser ablation. a) before ablation, b) after ablation, c) on the base of the cones, d) on top of a cone. The inset figures are correlative SEM images of the EDS scanning area.

Fig.3-10 SEM cross-section image of the in situ MgB_2 film.

Fig.3-11 AFM 3D mode image of the MgB_2 film surface. Scale=500x500nm^2

Fig.3-12 TEM bright field image of a planar specimen for the in situ MgB_2 film (a). b) is a SAD pattern from a circular 500 nm area of the film.

Fig.3-13 Magneto-optical image of the in situ MgB_2 film at B_a=8.7mT at 20K after zero field cooling. The film size is 3x3mm^2. The white round spots are defects in the MO indicator. The bright area in the upper middle part of the film is an enhanced flux penetration due to an accidental mechanical scratch on the MgB_2 film.

Fig.3-14 MOI images of in situ annealed film 030703, showing the flux penetration as a function of temperature: (a) 4 K, (b) 7 K, (c) 10K. The applied field is about 10mT for the three sets of observations. The sample is ~3x3 mm2 in dimentions.

Fig.3-15 (a) Hysteresis loops of DC magnetisation for our best on-axis in situ film 190903 at 5K(■), 10K(●), 15K(▲), and 20K(▼) respectively and (b) the calculated J_c of the in situ film from the magnetic hysteresis loops at 5K(■), 10K(●), 15K(▲), and 20K(▼) respectively. (c) detailed magnetization curves at 5 K within the field range of 1000 Oe (0.1 T) with very fine scan of 5 Oe resolution. The inset is a magnification of the curve between 400 Oe and 500 Oe.

Fig.3-16 The resistivity versus temperature curve for a typical on-axis in situ MgB_2 film. The thickness of the film is 450 nm.

Fig.3-17 Field dependence of resistivity-temperature curves. The applied field is (from right to left) 0T, 0.1T, 0.5T, 1T, 2T, 3T, 4T, 5T, 6T, 7T, 8T, and 8.7T respectively.

Fig.3-18 Irreversibility field and upper critical field of the in situ MgB_2 film.

Fig.3-19 Activation energy of the in situ MgB_2 film. The grey lines are U_0 data of bulk-MgB2 cited from ref [1].

Fig.3-20 EDS result of a typical in situ MgB_2 film with 30K magnetic T_c. In order to avoid the interaction with the Al_2O_3 substrate, a low electron beam energy of 5kV was used. The Al Kα signal at 1.5 keV is not noticeable in the spectrum.

Fig.4-1 SEM cross-section images of the two types of films. a: in situ annealed MgB_2 film; b: ex situ annealed MgB_2 film on Al_2O_3-R substrate.

Fig.4-2 AFM 3D images of a) the boron precursor film, the lower plane is the substrate; b) the ex situ annealed MgB_2 film on Al_2O_3-R substrate; c) the ex situ film on Al_2O_3-C substrate; d) the ex situ film on 4H-SiC(0001) substrate.

Fig.4-3 XRD of ex situ annealed films on a) Al_2O_3-R and b) Al_2O_3-C substrates. The MgO signal may come from the oxidization of some excess metal Mg on the film surface.

Fig.4-4 (a): Temperature dependence of resistivity for the two types of MgB_2 films from 5K to 300K in zero field; The inset shows the transition curves between 30K and 40K. (b): The magnetization versus temperature curves. ■: in situ film; ○: ex situ film.

Fig.4-5 Field dependence of ρ(T) curves for a) in situ MgB_2 film and b) ex situ film.

Fig.4-6 Arrhenius plots of the resistance R(H, T) of the a) in situ and b) ex situ films. The applied filed is perpendicular to the film plane.

Fig.4-7 The flux flow activation energy U_0 versus applied field B_a. Two stages of field dependence of U_0 is found in ex situ film.

Fig.4-8 Irreversibility lines and upper critical field versus temperature curves for the in situ and ex situ annealed films. A): Irreversibility lines for the in situ and ex situ films. The data for undoped ex situ MgB_2 film and oxygen alloyed MgB_2 film (Ref. [2]) is displayed in the figure for comparison. B): Upper critical fields versus temperature for the two films. The data for c-axis-oriented MgB_2 films from Ref. [3] are also shown in this figure.

Fig.4-9 Critical current of the two types of MgB_2 films calculated from M-H loops.

Solid symbols: in situ annealed film; lines: ex situ annealed film. The temperature is 5 K, 10 K, 15 K, and 20 K from top to bottom, respectively. The applied field is perpendicular to the film plane.

Fig.4-10 MO images for the in situ film, shown in (a), (b) and the ex situ film, shown in (c), (d) at 4 K. The applied field is (a) 17 mT, 1st set of measurement, (b) 17 mT, 2nd set of measurement, (c) 25.5 mT, 1st set of measurement, and (d) 25.5 mT, 2nd set of measurement.

Fig.4-11 AFM of a) the in situ and b) the ex-situ MgB_2 film on Al_2O_3-Rsubstrate.

Fig.4-12 EDS analysis results for the a) in situ and b) ex situ films. In order to avoid the interaction with the Al_2O_3 substrate, a low electron beam energy of 5kV was used. As a result, no Al signal at about 1.5 KV is detectable. Since the thickness of both films is similar, the difference in oxygen signal intensity can reveal the difference of oxygen level in the two films.

Fig.4-13 AFM 3D image of the ex situ MgB_2 film. The surface topography shows typical randomly oriented grains. The arrow shows a thinner part formed between two grains.

Fig.5-1 AFM deflection image of Si islands on sapphire-R substrate deposited for 50 pulses (10Hz, 5sec). The laser fluence is 300mJ/pulse.

Fig.5-2 EDS Si mapping in the Si doped MgB_2 films. The upper part contains SEM secondary electron images, and the lower part the distribution of Si. a: 3.5% Si addition, b: 11% Si addition. The arrows indicate the Si-rich spots.

Fig.5-3 DC magnetization curves of the films with different Si doping levels. The applied field is 25 Oe for both ZFC and FC measurements.

Fig.5-4 J_c values with different Si doping levels. a: at 5 K, b: at 10 K, c: at 15 K. The applied field B_a is perpendicular to the film plane.

Fig.6-7 $T_{c\ onset}$ versus $T_{substrate}$ curve (left axis) and Magnetization (right axis) versus $T_{substrate}$ at 5K. The T_c and Magnetization values are extracted from ZFC magnetization curves at 5 K in Fig.6-6.

Fig.6-8 AFM deflection image of a 2×2 μm^2 area of the surface of film (d) in Fig.6-4.

Fig.6-9 AFM cross-section profile of the off-axis film #300604V. The vertical distance between the highest and the lowest part indicated by arrows is 22nm.

Fig.6-10 XRD θ-2θ pattern of the off-axis deposited film #300604V with a slow scanning rate of 0.2 degree/min. The vertical lines label the positions for all MgB_2 peaks in powder diffraction database. The unknown peak at 37.56º is also presents in the spectrum of a bare Al_2O_3-C substrate, so we assume it is not from the film.

Fig.6-11 The left figure: Bright field TEM image of a planar specimen a typical off-axis MgB_2 film with a zero-resistivity T_c of 32K. The right figure is a SAD pattern from a Φ500 nm area of the film

Fig.6-12 Resistivity versus temperature for an off-axis film #300604V. The inset is an enlargement of the transition part.

Fig.6-13 The field dependence of resistivity-temperature curves of the off-axis MgB2 film #300604V in a) perpendicular (H//c axis) fields and b) parallel fields (H//a-b plane).

Fig.6-14 The Arrhenius plot of resistance R(T, H) for the off-axis MgB_2 film in a) perpendicular and b) parallel fields.

Fig.6-15 The activation energy U_0 of flux flow versus applied field, B_a for film #300604V.

Fig.7-8 The activation energy, U_0 of flux flow versus applied field, B_a.

List of tables:

List of Publications during PhD study period (from 2002 to 2005)

1. **Y. Zhao**, S. X. Dou M. Ionescu P. Munroe**, "**Significant improvement of activation energy in the MgB_2/Mg_2Si multilayer film", accepted by Appl. Phys. Lett., To be published in Feb. 2006
2. **Y. Zhao**, S. X. Dou M. Ionescu P. Munroe, "Transport properties of multilayered MgB_2/Mg_2Si superconducting thin film" accepted by J. Appl. Phys. To be published in Jun 2006
3. **Y. Zhao**, M. Ionescu, M. Roussel, a. V. Pan, J. Horvat, and S. X. Dou, "Superconducting and microstructural properties of two types of MgB_2 films prepared by pulsed laser deposition, IEEE Transactions on Applied Superconcuctivity" **15,** 3261 (2005).
4. **Y. Zhao**, M. Ionescu, J. Horvat and S. X. Dou, "Off-axis MgB_2 films using an *in situ* annealing pulsed laser deposition method", Supercond. Sci. & Technol. **18**, 395-399 (2005)
5. S. X. Dou, S Soltanian, **Y. Zhao**, E Getin, Z Chen, O. Shcherbakova and J. Horvat "The effect of nanoscale Fe doping on the superconducting properties of MgB_2" Supercond. Sci. Technol. **18**, 710 (2005)
6. M. Roussel, A. V. Pan, A. V. Bobyl, **Y. Zhao**, S. X. Dou, and T. H. Johansen, Magnetic flux penetration in MgB_2 thin films produced by pulsed laser deposition, Supercond. Sci. Technol. **18,** 1391 (2005).
7. **Y. Zhao**, M. Ionescu, J. Horvat and S.X. Dou "Comparative study of *in situ* and *ex situ* MgB_2 films prepared by pulsed laser deposition" Supercond. Science & Technology **17**, S482-S485 (2004)

8. **Y. Zhao**, M. Ionescu, J. Horvat, A.H. Li and S.X. Dou " Si addition in *in situ* annealed MgB_2 thin films by pulsed laser deposition" Superconductor Science & Technology **17** 1247-1252 (2004)

9. M. Ionescu, **Y. Zhao**, M. Roussel, S.X. dou, R. Ramer and M. Tomsic "Flux pinning in MgB_2 thin films grown by pulsed laser deposition" Journal of Optoelectronics and Advanced Materials, **6,** 169-176 (2004)

10. A.V. Pan, **Y. Zhao**, M. Ionescu, S.X. Dou, V.A. Komashko, V.S. Flis, and V.M. Pan, "Thermally activated depinning of individual vortices in $YBa_2Cu_3O_7$ superconducting films", *Physica C*, **407,** 10 (2004)

11. M. Ionescu, A. H. Li, **Y. Zhao**, H. K. Liu, A. Crisan, "Enhancement of critical current density in YBa2Cu3O7-d thin films grown by PLD on YSZ (001) surface modified with Ag nano-dots", J. Phys. D: Applied Physics, **37**, 1824 (2004)

12. **Y. Zhao**, M. Ionescu, A.V. Pan, S.X. Dou and E.W. Collings "*In situ* annealing of superconducting MgB_2 films prepared by pulsed laser deposition" Supercond. Sci. Technol. **16,** 1487-1492 (2003)

Introduction

Magnesium diboride (MgB_2) was found to be a superconductor with a transition temperature, T_c, of 39 K in January 2001 [1]. It has been revealed as a phonon-mediated superconductor with a much higher T_c and a significantly smaller isotope shift than the Bardeen-Cooper-Schrieffer (BCS) theory would predict. Furthermore, MgB_2 is the first example in which the effect of two superconducting gaps is strongly expressed. Its high T_c, high critical current densities and critical fields, large coherence length, simple structure and non-weak-link across the grain boundaries are promising features for both applications to electronic devices and large scale conductors. This warrants the ongoing international effort to investigate this material.

In electronic applications, MgB_2 could play an important role in active and passive high frequency devices. MgB_2's large coherence length and moderately high T_c make it a suitable candidate for uniform and stable Josephson junctions and SQUIDs [2]. Current in-service SQUIDs made from niobium and its alloys must be cooled with liquid helium to about 4K. So researchers are always anxious to find materials that can sustain superconductivity at higher temperatures to ease the extremely high power-consumption on cryocoolers [3]. The T_c of 39 K for MgB_2 enables the realization of electronic circuits based on this material to operate at 20-25 K, achievable by a compact cryocooler, which gives a significant advantage to this material compared to the low-temperature superconductors. MgB_2 also has major advantages over another candidate for Josephson junctions, the high temperature superconductor $YBa_2Cu_3O_{7-x}$ (YBCO), although YBCO has a higher T_c. MgB_2 is chemically more stable over time and a suitable barrier layer is easier to be achieved due to MgB_2's less anisotropy, fewer material complexities, and a longer coherence length than high-T_c cuprates.

Compared to the high-temperature superconductors, MgB_2 is simpler, cheaper and more stable.

The possibility of utilizing MgB_2 in passive high-frequency device applications, e.g. microwave and terahertz (THz) resonators, antennas, filters and RF cavities, is also emerging according to recent studies [4] [5]. For MgB_2, a conservative estimation based on the smaller gap of 2.7 meV gives $R_{s,4K}^{BCS}(10GHz)=1\ \mu\Omega$, which is less than Nb by a factor of 28 [5]. The good H_{c2} behaviour in MgB_2 films [6] could effectively reduce the microwave surface resistance. The low microwave surface resistance has been revealed in both MgB_2 bulk and films [7-9]. The intrinsically low nonlinear response of MgB_2 to microwave could be much easier to achieve than HTS cuprates [4], because MgB_2 will probably benefit from its non-weak-link nature across grain boundaries.

Thin film synthesis is the fundamental step to the realization of electronic devices or MgB_2 coated conductors. The main difficulties for MgB_2 film preparation are Mg's high volatility and extremely high reactivity with oxygen. Various methods have been used for the preparation of MgB_2 films, such as physical vapour deposition (PVD) [10-14], chemical vapour deposition (CVD) [15], and electrochemical plating [16]. Transition temperatures of 39 K or even higher have been achieved in *ex situ* annealed pulsed laser deposition (PLD) films [10] and hybrid physical-CVD (HPCVD) films [15]. A possible problem for application of *ex situ* annealing and HPCVD process in devices processing could be the difficulty in realizing multilayer structures. Although the T_c value still requires improvement, the PLD procedure followed by an *in situ* annealing seems very attractive due to the fact that it requires comparatively simple equipment and is technically capable of implementing multilayer structures for Josephson junctions.

Among those methods, the PLD method is relatively simple and cheap: a target and a substrate inside the vacuum chamber and a laser beam introduced from a window can realize the simplest PLD film forming. On the other hand, the process is influenced by many factors, including the mismatch between the film and substrate lattices, substrate temperature, substrate reactivity, nature of the film material, the deposition geometry, the growth rate and the thickness of the film. My thesis is focused on the PLD fabrication technology of MgB_2 thin films and an understanding of the underlying mechanisms between PLD MgB_2 films synthesis, microstructural properties and their performance.

This thesis is organized as follows: Chapter 1 is a literature review on superconductivity in MgB_2, thin film synthesis methods, and emerging applications for MgB_2 thin films; Chapter 2 introduces the experimental system and characterization techniques employed in this thesis, with the emphasis on the pulsed-laser deposition and annealing technique, AFM and TEM technology, and physical property measurement techniques in PPMS and MPMS systems. A study of on-axis PLD MgB2 thin film processed by in situ annealing was put into Chapter 3. Chapter 4 is a comparative study of *in situ* and *ex situ* MgB_2 films to reveal the correlation between the superconducting performance and the processing conditions of the two types of films. In Chapter 5, a study of property modification by Si addition in on-axis in situ MgB2 films is reported. Chapter 6 reports the study on the significant improvement of the smoothness of the in situ MgB2 films using an off-axis geometry. Root mean square roughness of 4 nm and good T_c of 33 K were achieved in the off-axis films. In Chapter 7, a multilayer MgB2/Mg2Si superconducting film was fabricated with the aid of off-axis deposition method. Significant enhancement of anisotropy in activation energy of thermally assisted flux fluw (TAFF) of the multilayer film was detected.

Finally, Chapter 8 gives the summary and conclutions of this thesis. References follow each chapter.

References

[1] J. Nagamatsu, N. Nakagawa, T. Muranaka, Y. Zenitani, and J. Akimitsu, Nature **410,** 63 (2001).

[2] M. Naito and K. Ueda, MgB_2 thin films for superconducting electronics, Superconductor Science & Technology **17,** R1-R18 (2004).

[3] M. Nisenoff, An assessment of superconducting digital thechnology: the possible impact of the discovery of magnesium diboride, (High Tc Update, 2001) www.iitap.iastate.edu/htcu/nisenoffcomment.html

[4] T. Dahm and D. J. Scalapino, Nonlinear microwave response of MgB_2, Appl. Phys. Lett. **85,** 4436 (2004).

[5] E. W. Collings, M. D. Sumption, and T. Tajima, Magnesium diboride superconducting RF resonant cavities for high energy particle caceleration, Supercond. Sci. Technol. **17,** S595-601 (2004).

[6] A. Gurevich, S. Patnaik, V. Braccini, K. H. Kim, C. Mielke, X. Song, L. D. Cooley, S. D. Bu, D. M. Kim, J. H. Choi, L. J. Belenky, J. Giencke, M. K. Lee, W. Tian, X. Q. Pan, A. Siri, E. E. Hellstrom, C. B. Eom, and D. C. Larbalestier, Very high upper critical fields in MgB_2 produced by selective tuning of impurity scattering, Supercond. Sci. Technol. **17,** 278 (2004).

[7] S. Y. Lee, J. H. Lee, J. Lim, H. N. Lee, S. H. Moom, B. Oh, and M. A. Hein, Effects of Ion Milling on the Microwave Properties of MgB_2 Films, IEEE Transactions on Applied Superconductivity **13,** 3585 (2003).

[8] A. T. Findikoglu, A. Serquis, L. Civale, X. Z. Liao, Y. T. Zhu, M. E. Hawley, F. M. Mueller, V. F. Nesterenko, and Y. Gu, Microwave performance of high-density bulk MgB_2, Appl. Phys. Lett. **83,** 108-110 (2003).

[9] T. Tajima, in *Possibility of MgB_2 Application to Superconducting Cavities*, Paris, France, 2002.

[10] W. N. Kang, H.-J. Kim, E.-M. Choi, C. U. Jung, and S.-I. Lee, Epitaxial MgB_2 Superconducting Thin Films with a Transition Temperature of 39 Kelvin, Science **292,** 1521 (2001).

[11] C. B. Eom, M. K. Lee, J. H. Choi, L. J. Belenky, X. Song, L. D. Cooley, M. T. Naus, S. Patnaik, J. Jiang, M. Rikel, A. Polyanskii, A. Gurevich, X. Y. Cai, S. D. Bu, S. E. Babcock, E. E. Hellstrom, D. C. Larbalestier, N. Rogado, K. A. Regan, M. A. Hayward, T. He, J. S. Slusky, K. Inumaru, M. K. Hass, and R. J. Cava, High Critical current Density and Enhanced Irreversibility Field in Superconducting MgB_2 Thin Films, Nature **411,** 558-560 (2001).

[12] R. Vaglio, M. G. Maglione, and R. D. Capua, High-quality MgB_2 thin films *in situ* grown by dc magnetron sputtering, Supercond. Sci. Technol. **15,** 1236 (2002).

[13] S. D. Bu, D. M. Kim, J. H. Choi, J. Giencke, S. Patnaik, L. Cooley, E. E. Hellstrom, D. C. Larbalestier, and C. B. Eom, Synthesis and Properties of c-axis Oriented Epitaxial MgB_2 Thin Films, Appl. Phys. Lett. **81,** 1851 (2002).

[14] W. Jo, J.-U. Huh, T. Ohnishi, A. F. Marshall, M. R. Beasley, and R. H. Hammond, Appl. Phys. Lett. **80** (2002).

[15] X. H. Zeng, A. V. Pogrebnyakov, A. Kotcharov, J. E. Jones, X. X. Xi, E. M. Lysczek, J. M. Redwing, S. Y. Xu, Q. Li, J. Lettieri, D. G. schlom, W. Tian, X. Q. Pan, and Z. K. Liu, In-situ Epitaxial MgB_2 Thin Films for Superconducting Electronics, Nature Materials **1,** 35 (2002).

[16] A. B. Jadhav and S. H. Pawar, Electrochemical synthesis of superconducting magnesium diboride films: a novel potential technique, Supercond. Sci. Technol. **16,** 752 (2003).

Chapter 1. Literature survey

Magnesium diboride (MgB_2) is a very simple binary compound with, however a number of surprising properties. The discovery of superconductivity with a critical temperature (T_c) of 39 K in MgB_2 in January 2001 [1] has attracted research interests worldwide in this material. The remarkable properties of MgB_2 warrant the on going fundamental study on its superconductivity as well as applied researches.

1.1. Superconductivity in intermediate-temperature superconductor MgB_2

The crystal structure of MgB_2 is hexagonal AlB_2 type. It consists of alternating hexagonal layers of Mg atoms and graphite-like honeycomb layers of B atoms (Fig. 1). The unit cell lattice parameters for MgB_2 are a = 3.086 Å and c = 3.521 Å [2]. MgB_2 is not a new compound, but only after the discovery of its superconductivity in 2001 have scientists put close attention on this compound. Since then there already have been a number of extensive reviews on the superconductivity in MgB_2 that can help us to build up a good understanding of this superconductor [3-6].

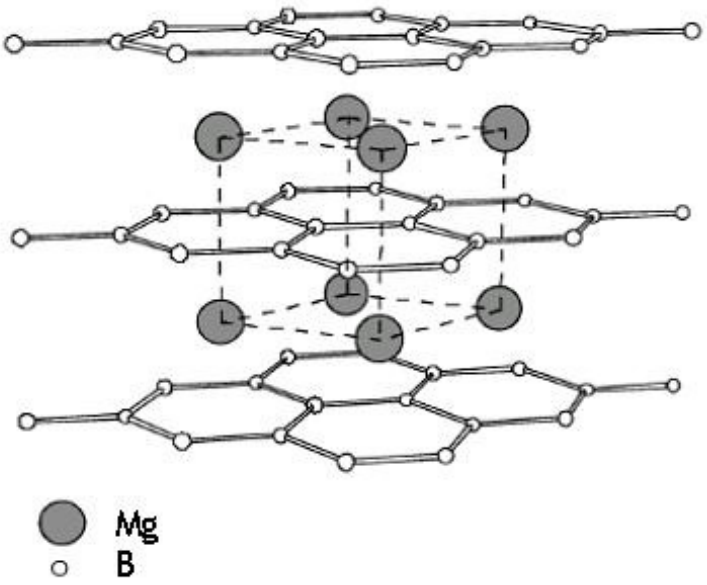

Fig.1-1 MgB_2 crystal structure.

MgB_2 appears to be a conventional, BCS phonon mediated sp superconductor [7] except a much higher T_c than BCS theory would predict from the formula

$$k_B T_c = 1.13\hbar\omega_D exp[-1/VN(E_F)] \qquad (1\text{-}1)$$

where ω_D is the Debye frequency, V the attractive potential between two electrons, $N(E_F)$ the electron density at Fermi surface and $VN(E_F)$ is equivalent to the electron phonon coupling constant λ.

The phonon frequencies ω_D, although very high, are not especially different from other borides and light-element binary compounds that have much lower T_c. Since MgB_2 has no *d* electrons, the electron density of states is low. The extraordinary high T_c for MgB_2 could only be explainable with a strong electron-phonon coupling as expressed through *V*.

The phonon density of states of MgB_2 has been obtained experimentally from the inelastic neutron scattering measurements on polycrystalline samples undertaken by Osborn *et al* [8] and Yildirim *et al* [9]. The two sets of results are in basic agreement, and also confirm the above speculation. The experimental data indicate that the phonon density of states extends as high as 100 meV. There are two bands of phonons: one below 40 meV corresponding primarily to acoustic modes and the other above 50 meV corresponding to optic branches mostly involving the boron motions. The high frequency phonons are also confirmed by specific heat measurements, which provided a Debye temperature for MgB_2 of over 1000 K. The electron–phonon coupling constant λ can be estimated from these data based on the McMillan or Allen-Dynes equation. Using the Allen-Dynes equation with ω_{ln} = 57.9 meV, Osborn *et al* [8] obtained $\lambda \sim 0.9$, indicating an intermediate coupling regime. In their calculation, they

did not assume that a specific phonon mode makes a significant contribution to the superconductivity. The band calculations [10,11], however, predicted that the specific boron in-plane vibration mode (bond-stretching mode) is strongly coupled to electrons (B 2p σ band) near the Fermi level. This is because this phonon mode changes the B orbital overlap, thereby causing strong electron–phonon coupling. This mode has E_{2g} symmetry with an energy of ~ 75 meV. Assuming that this mode dominates electron–phonon coupling in MgB_2 , the λ value can be calculated as 0.9–1.0 by a deformation potential approximation.

Now there has been a consensus over the existence of two gaps in MgB_2 superconductor. The superconducting energy gap (2Δ) of MgB_2 has been measured from various spectroscopic probes (tunnelling [12], far-infrared optics [13], photoemission [14], point contact [15]) as well as from the temperature dependence of physical quantities (specific heat [16], microwave surface resistance [17], penetration depth [18]) at low temperatures. There was a large scattering from 2 to 8meV for Δ in early studies. Later experiments have pointed towards the existence of multiple gaps. One strong evidence for two-gap superconductivity was obtained by specific heat measurements [16]. The specific heat (C) of MgB_2 significantly deviates from the standard one-band BCS behaviour as shown in Fig.1-2. First, there is a significant excess C in the vicinity of $T_c/5$ (~ 8 K). Second, an exponential fit of $C(T)$ in the $T << T_c$ region indicates a small superconducting gap with $2\Delta/k_B T_c$ ~ 1.2. In order to interpret the behaviour of $C(T)$ in MgB_2, Bouquet et al. [16,19] proposed the following semi-quantitative analysis. In their model, $C(T)$ is the sum of the contributions of two

bands of large and small superconducting gaps (Δ_L and Δ_S) with their relative weights x and 1 . x: $C(T) = C_L(T) + C_S(T)$. Then each Ci (T) (i = L or S) can be calculated assuming a BCS temperature dependence for Δi. The calculated C(T) agrees well with the experimentally obtained specific heat over the whole T to T_c range with fitted parameters of $2\Delta_L/k_B T_c \sim 4.0$, $2\Delta_S/k_B T_c \sim 1.2$ and $x \sim 0.55$.

Manzano et al [18] reached a similar conclusion from the temperature dependence of the London penetration depth λ(T). A two-gap analysis for λ(T) gave $2\Delta_L/k_B T_c \sim$ 3.9–4.5, $2\Delta_S/k_B T_c \sim 1.5$, and $x \sim 0.55$, which is in good agreement with the above specific heat results. Some spectroscopic measurements also provided similar results. Tsuda et al. [14] studied the superconducting gap of MgB_2 using high-resolution photoemission spectroscopy. Their spectrum in the superconducting state showed a complex gap structure in contrast to that expected from a simple isotropic gap. This spectrum can be well reproduced using the weighted sum of two Dynes functions with gap values of 5.6 meV ($2\Delta L/k_B T_c \sim 3.6$) and 1.7 meV ($2\Delta_S/k_B T_c \sim 1.1$). The spectroscopy of Cu/ MgB_2 point-contact junctions reported by Szabo et al [15] gave Δ_L = 7 meV and Δ_S = 2.8 meV. Vacuum tunnelling spectroscopy using MgB_2 as an STM tip against an atomically flat 2H-NbSe2 undertaken by Giubileo et al [12] gave Δ_L = 7.8 meV and Δ_S = 3.8 meV.

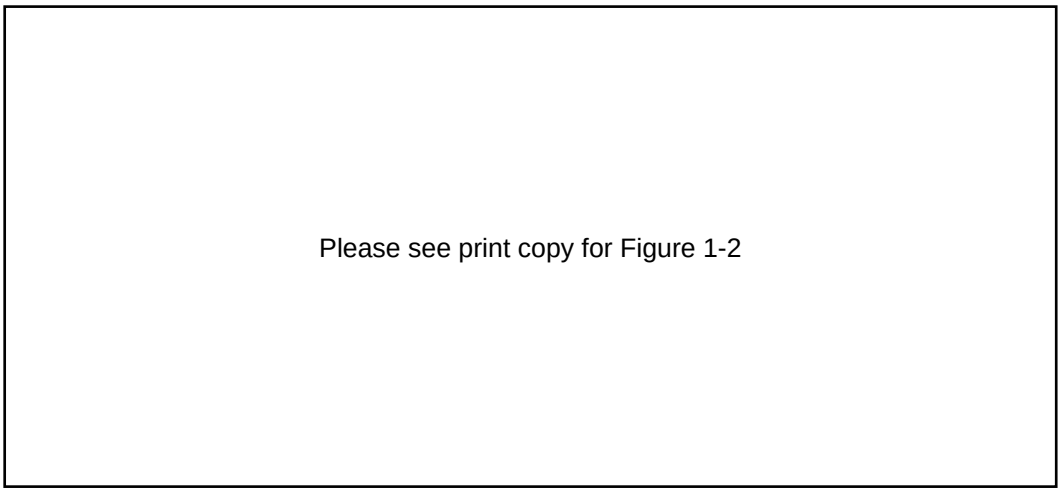

Fig.1-2 Experimental specific heat data (○) as a function of the reduced temperature t (=T/ T_c) from two groups [17, 29]. The data are compared with the BCS-normalized specific heat (thin curve) and also two-gap fits (thick curve). Insets: gaps 2ΔL/kB T_c and 2ΔS/kBT_c versus t (dotted curves) and partial specific heat of both bands (full curves). Figure cited from [19].

The postulation of the two-gap superconductivity of MgB_2 can be justified from the band calculations [20,21]. Band calculations reported by several authors gave essentially identical results.

The σ bands are formed by covalent bonding of the two B sp^2 hybrids, which are directed along a B-B bond. The π-bands are formed by the overlap of B p_z and Mg *s* orbitals. Mg donates its electrons to each of the π bands, i.e. p_z orbitals, of two neighbouring B atoms and therefore Mg is fully ionized. The attractive potential from the Mg^{2+} ions is felt much stronger by a p_z electron than by electrons from the σ bands. This lowers the energy of the π bands resulting in electrons being transferred from σ bands to π bands. This drives the hole doping of the σ bands[11,22]. The shape of

Fermi surfaces of the two bands are shown in fig. 1-3 [23]. The holes at the top of these σ bands manifest two-dimensional properties and are localized in the boron sheets. On the other hand, mostly three-dimensional electrons and holes in the π-bands are delocalized over the whole crystal. Thus, one can say that MgB_2 is held together by strongly covalent bonds within the boron layers and by 'metallic-type' bonds between these sheets. These 2D covalent and 3D metallic type states contribute almost equally to the total density of states (DOS) at the Fermi level [23].

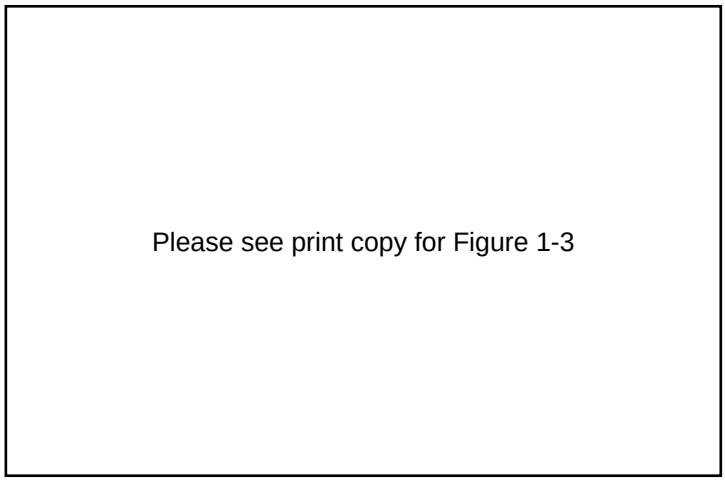

Fig.1-3 Fermi surface of MgB_2 in reciprocal space. The two cylindrical sheets are Fermi surfaces of σ-band. Figure cited from [23]

The fact that MgB_2 is a two-gap superconductor lead to some interesting characteristics that will have important impact in applications. For a two-band superconductor, only an intra-band non-magnetic impurity scattering can decrease the T_c. The special symmetry of electronic state of MgB_2 ensures a low inter-band scattering even in significantly dirty samples. So one can introduce high level of nano-scale defects to enhance pinning and increase the upper critical field H_{c2}, with little sacrifice of the T_c.

1. 2 MgB_2 film synthesis methods

The synthesis of superconducting MgB_2 films has been implemented by a variety of methods. The most common way to develop MgB_2 films is Pulsed Laser Deposition (PLD), which has also been predominately employed in film forming of high temperature superconductor (HTS) and other materials [24-29]. The main advantage of PLD is that it transfers the atoms of target to the substrate without much change of the stoichiometric composition. There is a good review on MgB_2 films by Naito and Ueda in 2004 [3]. The same level of T_c of bulk MgB_2 and J_c as high as $3x10^7$ A/cm^2 at 4.2K in zero-field has been achieved in MgB_2 films. Those exploring works on MgB_2 synthesis has made significant contribution to the application for superconducting electronic devices and superconducting coated conductors using MgB_2, as well as the theoretical study of the nature of MgB_2 superconductivity.

1.2.1 Methods for MgB_2 film Synthesis

If one classifies the preparation methods for MgB_2 films by the steps taken for MgB_2 phase formation, they can be roughly divided into three categories: as-grown film, *in situ* two-step preparation and *ex situ* two-step preparation. We can also classify the methods into physical vapour deposition (PVD), comical vapour deposition (CVD), electrochemical method etc. according to the nature of the film deposition process. Ueda and Naito [3,30] have given extensive reviews of the MgB_2 thin film preparation methods. In the following text, a review of these methods is given in the following sequence: for as-grown film, for *in situ* two-step preparation and for *ex situ* two-step preparation.

1.2.1.1 As-grown methods

The term "as-grown" means that the MgB_2 phase formed during the deposition process, and the resulting film is superconducting without any further heat treatment. For as-grown MgB_2 films, a good T_c was achieved by molecular beam epitaxy (MBE) [31-33]. The condition is as follows: Mg and B metal source, temperature of substrate is 295-320 ℃. The critical temperature T_c is about 34.5-37 K(onset), and a transition width(ΔT_c) of ~0.5℃. The critical current density is $4x10^5$-$4x10^6$ A/cm2 (4.2K, 0T), Residual resistance ratio (RRR) is ~2. For the PLD as-grown film[34], the T_c of the resulting film is 25.0K (onset). Temperature of substrate is 450℃. RRR of the film is ~1.1. Although the target for PLD was Mg-rich, there is still high risk of the deficiency of magnesium in the film under a temperature higher than 300 ℃.

Saito et al found the same behavior in as-grown sputtering prepared films [35]. For sputtering as-grown films, the temperature window of growing is very narrow. At lower of substrate temperature (205 and 220℃), There is excessive Mg in the films and the T_c is very low (7K and 14K at 0T). This may be due to the low temperature formation of the film, which results in a poor crystallization of the MgB_2 film. At higher temperature (252℃), the ratio of Mg to 2B drops to 0.4 and the T_c of the film increases to 27.8 K(0T). The rising temperature of the substrate most probably contributes to a good crystallization of the film. However, a higher temperature contributes to a much higher evaporation rate of magnesium. A further increase in the temperature (268 ℃) results in a semi conducting film, which may be due to the formation of highly Mg-deficient phases and therefore the absence of MgB_2 phase.

The most successful as grown method for MgB_2 film till now (2005) is the hybrid physical-chemical vapor deposition (HPCVD) proposed by Zeng et al [36,37]. In this method, 1000 ppm diborane (B_2H_6) in H_2 ambient gas continuously flows through the

reactor. The temperature of the 4H-SiC (0001) substrate is 730-760 ℃. Mg vapor is generated from Mg slices mounted next to the substrate on a hot plate. A very well in plane aligned epitaxial MgB_2 film is obtain after the reaction. The resultant MgB_2 film has a zero resistance T_c of 39.5K with a narrow transition width of about 0.5K and a very smooth surface of R_{ms} = 3 nm. The J_c is $1.2x10^7$ A/cm^2 at 4.2K in zero field.

It is anticipated that *in situ* MgB_2 films of high crystalline quality and bulk-like T_c may find applications as a new basis for superconducting electronics and may be used for further studies of superconductivity in MgB_2.

1.2.1.2 *In situ* and *ex situ* annealing methods

A post annealing of the film has been found very effective to gain good superconducting properties, especially for MgB_2 films deposited at lower temperature. There are mainly two kinds of post annealing: in-situ annealing and *ex situ* annealing. An *in situ* post annealing is performed directly after the deposition in the same deposition chamber. For an *ex situ* annealing the precursor film needs to be transferred to a sealed chamber or tube which can provide high temperature and high magnesium vapor pressure simultaneously. The vapor of magnesium is usually provided by placing magnesium pellets inside the sealed chamber or tube. A number of groups have achieved bulk-like T_c in MgB_2 films by post annealing. W.N. Kang et al. first achieved the T_c as 39.0K (onset ,0T) by *ex situ* annealing a boron precursor film at 900 ℃ for 30 min [38]. The boron precursor film was deposited on single crystal substrates of $SrTiO_3$ (100) and Al_2O_3-R substrates by PLD method. Then the precursor was placed onto a tantalum tube together with magnesium pellet and sealed in Ar atmosphere. The tubes were heated to 900℃ and kept for 10-30 min. This routine is typical for the post annealing methods, with small differences in the formation of the

precursors, the selection of substrates, temperature and time of annealing, and the tube materials. Eom et al achieved a much enhanced J_c in oxygen doped MgB_2 films by annealing a Mg+B precursor film in a level oxygen-mixed atmosphere [39]. Paranthaman [40], Moon [41], and Zhai et al. [42] employed E-beam evaporation to form B-precursors, Plecenik and Kus et al. [43,44] used thermal co-deposition and formed Mg+B precursors. R. Vaglio et al. [45] used DC magnetron sputtering with MgB_2 and Mg-rich MgB_2 targets. And S.D. Bu et al [46] used RF magnetron sputtering for boron precursor.

It is also worthy to note that some groups have obtained good results with MgB_2 film deposited on flexible substrates. K. Komori et al. obtained good results on hastelloy substrate using PLD method followed by ex-situ annealing [47]. An Yttria stabilized Zirconia (YSZ) buffer layer was first deposited on Hastelloy tape by bias sputtering. The MgB_2 films were then deposited on YSZ buffer layer by PLD. The T_c is 29K (0T) and the H_{c2} (upper critical field) and H_{irr} (irreversibility field) at 4.2 K are 33T and 18T respectively. The tapes show a wonderful small magnetic field dependence of J_c. In zero field, J_c is ~$1.5x10^6 A/cm^2$, and only drops slightly to $1.1x10^5 A/cm^2$ at 10 T. The residual resistance ratio of R290K/R T_c (RRR) is about 0.6~1. Komori proposed that the small value of RRR might be due to the very fine structure (grain size less than 10 nm) in the films as usually seen for *in situ* annealed films. The fine structure and nano-sized MgO inclusion inside the film probably contribute to strong pinning of vortex lattice in the films. Thus low field dependence and high H_{c2} and H_{irr} were achieved.

Kus et al. obtained superconducting MgB_2 films on kapto-E polyamide foils using heat co-deposition with *ex situ* annealing [44]. The Mg–B films were heated to approximately 600℃, but, at the same time, the backside of the structures was attached

to a water-cooled radiator to avoid overheating of the plastic substrate. The resulting MgB_2 films were amorphous with the onset of the superconducting transition at 29 K and a transition width of approximately 3 K. The critical current density was >7x10^5 A/cm2 at 4.2 K, and its temperature dependence indicated a granular film composition with a network of intergranular weak links.

Hur et al. prepared MgB_2 films on boron single crystals by two-step synthesis and observed a T_c enhancement (~41.7K) [48]. A possible explanation for this enhancement is tensile epitaxial strain between the MgB_2 films and the boron substrates, but this is yet to be confirmed. Epitaxial strain at the interface is one method of enhancing the T_c of thin films demonstrated for high – T_c cuprates. These works on cheaper and flexible substrates represent another step towards the application of superconducting MgB_2 to coated conductors.

1.2.1.3 Other MgB_2 film forming methods

Electrochemical method is another viable way to produce MgB_2 film. Abe et al. obtained thick MgB_2 film by electroplating on carbon cathode [49]. Pawar et al. produced a superconducting MgB_2 film by electrochemical synthesis on silver foils[50]. Both aqueous and non aqueous solutions were used during the reaction. The resulting film was then heated at 450℃ for 5 hour. The T_c was 36.4K with a narrow transition width. Electrochemical methods are generally of low cost and the easy to obtain thick films are suitable for coated conductor applications. A main shortage of electrochemical methods is the bad surface quality which hinders potential applications in superconducting electronics

Li et al. have prepared MgB_2 films on stainless steel by a sol-gel method [51]. The magnesium and boron powders were mixed in acetone and deposited onto the substrate.

The samples were sintered at 660-800℃. They obtained a T_c ~37.5K and J_c ~$8x10^4 A/cm^2$ at 5K and 1T. A main problem of the films was a poor adherence to the substrate. This method may provide an economical synthesis route for preparing MgB_2 coated conductors

1.2.2 Microstructures of MgB_2 films from different preparation methods

For PVD methods, the films grown on substrates at room temperature are generally amorphous. The stoichiometry of film is nearly the same as the source (target). In other words, the magnesium doesn't evaporate into the atmosphere. However, these amorphous films obtained at room temperature are not superconducting.

A short-time annealing will crystallize the films rapidly. This process could be achieved ether *in situ* or *ex situ* within a wide range of temperature and time. Usually the *in situ* post annealing was conducted at 550-660℃ for less than 30min.The temperature for crystallization was limited at lower range and the annealing time was controlled and kept very short to minimize the decomposition of magnesium diboride and evaporation of the magnesium. The *ex situ* annealing was achieved at 700-950℃. To keep magnesium within the films, a magnesium pellet must be place inside the annealing tube and sealed together with the films. The magnesium pellet will generate considerably high magnesium vapour which keeps the films within Mg-gas+ MgB_2 phase equilibrium area in the Mg-B phase diagram, studied by Liu et al. [52]. The annealing tube should be made of Ta, Ti, or Nb, which can endure the high temperature and is non reactive with magnesium vapours. When quartz tube is employed, the film and magnesium pellet must be wrapped with Ta or Nb foil to avoid the reaction between quartz and magnesium vapours.

The as-grown MgB_2 films are usually deposited at much lower temperatures, usually 250-330℃. The method could be PLD, MBE or sputtering. The crystallization of this kind of MgB_2 films is poor and the T_c is significantly depressed (30~36K). The T_c increases when increasing the temperature of deposition, however, the films become non-superconducting when the temperature is beyond a certain value. The transformation to semi conductive state with higher substrate temperature was ascribed to the loss of magnesium and lack of MgB_2 phase in the films [35]. The optimal temperature of substrates differs between each method and even between each equipment used. The highest T_c in PLD method was obtained with the substrate temperature of 450℃. The highest T_c in MBE method was obtained on Al_2O_3-R substrate at 320℃. For sputtering, the condition for best J_c value was at ~250℃.

Non-PVD methods can avoid the problem of losing magnesium at high temperature. In HPCVD methods, the substrate temperature could reach as high as 760 ℃. So the superconducting films could grow expitaxially [36,37]. The good crystallization of the films result in a T_c of 39K, equal to that of Bulk MgB_2. The HPVCD method for MgB_2 film contains a minimum amount of oxygen. However, this seems not necessary due to the faster dropping rate of J_c with perpendicular field compared with that of oxygen doped films [39]. In the electroplating method, the formation of the MgB_2 film is performed in the molten electrolyte. The substrate (cathode) was heated to 600℃ in the electrolyte and the plating lasted for 1 hour. The T_c of this film is 36K, quite high among as grown films. The film was not magnesium-deficient, indicating the molten electrolyte is beneficial for preventing the decomposition of MgB_2 phase at high temperature.

Throughout the results of the surveyed literature, it seems that a poor crystallization of the MgB_2 film is associated with a low T_c value, and the orientation of MgB_2-C is beneficial in increasing the T_c. The J_c of MgB_2 film is generally higher than that of bulk MgB_2 and does not differ significantly among the above-mentioned methods. Further more, the J_c is less field dependent in the films than in the bulk MgB_2. This may indicate that the fine structure of thin film provides considerable pinning force on the vertex. The dimension of the films also affects T_c. K. Ueda et al studied the thickness influences on T_c of MgB_2 films [8]. The result was shown in Table 3. It is clear that the thickness of MgB_2 film should be larger than 100nm in order to achieve its highest T_c.

Nearly all the groups doing *ex situ* annealing obtained T_c of 39K and J_c of several million A/cm^2 with the MgB_2 film. For *in situ* annealed MgB_2 films, T_c is only 25~35 K among the best results. However, J_c is 1~10x10^{6}A/cm^2 (7.5~12K, 0T), which is similar with that of the *ex situ* films. As for the as-grown MgB_2 films, PVD method resulted in the same level of T_c and J_c with *in situ* annealing. Encouragingly, the as-grown CVD method achieved T_c of 39K and ever higher J_c than that of the annealed ones.

The *ex situ* annealing method is not suitable for fabricating multi-layer film structures and thus hinders its application to microelectronic devices such as Josephson junctions. However, it could reach higher T_c and better crystallization. So it could be beneficial for the study of MgB_2 coated conductor, microwave generator and fundamental research into superconductivity of MgB_2. The *as grown* and *in situ* annealing methods are suitable for fabricating multi-layer films and the main focus should be raising their T_c and J_c. Electrochemical synthesis and coating-sintering

methods are more economical. They may be suitable routines for fabricating commercial coated superconductors.

1.3 Chemistry and physics of MgB_2 film formation

1.3.1 Formation of MgB_2 phase and its stability

Z.K. Liu et al have carried out a numerical study on the Mg-B binary phase diagram [52]. As shown in Fig. 1-4, at high temperature and low magnesium vapour pressure, the phase composition is gas phase and B. If the vapour pressure is higher than 10^{-6}Torr at ~700℃ or higher than 10 Torr at ~1500℃, the equilibrium phase should be gas and MgB_7. There is a narrow area for the existence of MgB_4 at higher vapour pressure. Further increase of the magnesium vapour pressure leads to MgB_2 phase. Even further increase of the vapour pressure results in solid or liquid magnesium on the film. To fabricate MgB_2 films, the conditions for deposition or annealing must stay within the gas + MgB_2 area of phase equilibrium. So, for the growth temperature of 600℃, a magnesium vapour pressure between 10^{-2} Torr and 1 Torr is necessary. Such high a vapour pressure of magnesium is practically difficult to realize during deposition or *in situ* annealing.

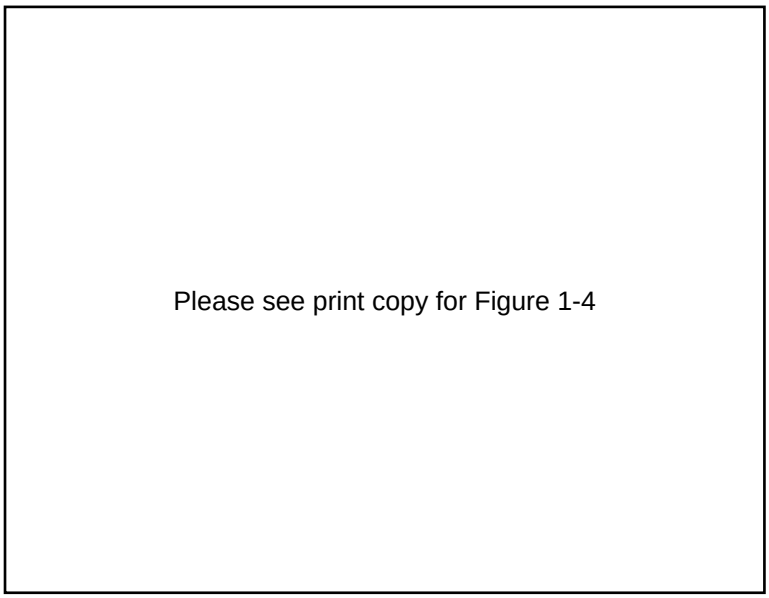

Fig.1-4 Calculated phase diagram of Mg and B. Figure cited from [52].

1.3.2 Crystallization of MgB_2 film

The high volatility of Mg strongly hinders one from achieving well-crystallized MgB_2 films. Magnesium has a strong trend to evaporate at elevated temperatures. In other words, the Mg deposited on a hot substrate has a very low sticking coefficient [33]. Kim et al. have investigated the thermochemistry of MgB_2 thin film synthesis and gave some conclusions in ref [33]. Their main conclusion is that the small Mg sticking coefficient limits the initial growth temperature to less than 300℃ for MgB_2 vacuum deposition methods. On the other hand, the formation of MgB_2 from Mg and boron require a sufficiently high temperature to ensure a high reaction rate. There is a consensus in the literature on MgB_2 film preparation that at temperatures lower than 250 ℃, no MgB_2 can be achieved during the deposition process. According to the theory of structure zone of thin films [53] shown schematically in fig 4, the higher the temperature of substrate, the more crystallization of the film will be obtained. In order

to achieve epitaxial MgB_2 films, the substrate should be kept at temperatures higher than 600℃ (0.3 Tm) as estimated from Fig.1-5.

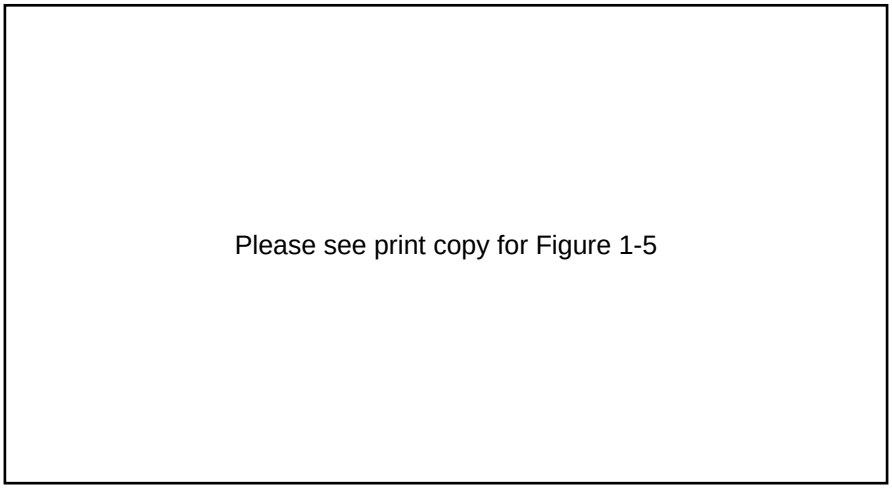

Fig.1-5 Morphology change due to relative temperature of metallic film made by evaporation. Figure cited from [53].

According to the literature, the as-grown and *in situ* annealing MgB_2 does not decompose quickly at temperature up to ~750℃ in an atmosphere of several tens to several hundreds Torr of argon background gas [36,37]. At this temperature, the film could be well crystallized when using suitable substrate. For an *in situ* annealing procedure, the substrate is usually kept at temperatures lower than 250 ℃ during the deposition to keep the Mg/B ratio high in the precursor film. The following quick annealing at high temperatures allows Mg to react with B, and once the MgB_2 phase is formed it will be relatively stable. That could be the reason why *in situ* annealed superconducting films are usually of higher T_c than as grown one. Considering the MgB_2 grain boundary is not necessarily a weak-link [54], the *in situ* annealing procedures are cheaper and easier for the manufacturing of polycrystalline MgB_2 films.

The selection of substrates should consider the reactivity, lattice matching, electric properties, flexibility and cost. Successful substrates for MgB_2 films are single

crystalline Al_2O_3(0001) and $(01\bar{1}2)$, MgO (001), 4H- and 6H-SiC(0001), YSZ, $SrTiO_3$, etc. Concerning the lattice matching and reactivity with MgB_2, SiC(111) have the best lattice match and is the most suitable substrate for epitaxy of MgB_2 film. The surface plane of SiC is hexagonal with lattice parameter a= 3.081 Angstrom. The lattice mismatch with MgB_2 (0001) is 0.16 %. Al_2O_3-C also has a hexagonal surface plane with a lattice parameter a = 4.765Å. From the reports on MgB_2 deposition, MgB_2 lattice is usually rotated 30˚ relative to the Al_2O_3 substrate lattice. I this circumstance, the Al-Al distance in Al_2O_3 (0001) plane along the direction of MgB_2 [001] is 2.751 Å, and the lattice mismatch along that direction is 12%. Other substrates that have been employed include single crystal boron, graphite, stainless steel tape, hastelloy tape, and kapto-E polyamide foil. From the experience of PIT wire works [55-64], Ag, and Cu are reactive with MgB_2 and become brittle. So a buffer layer is needed to prevent the reaction. Fe, Ti, Ta and Nb are less reactive with MgB_2, and they are potential substrates for MgB_2 coated superconductors.

1.4. Potential applications of MgB_2 films

14.1 Electronic devices

In electronic applications, MgB_2 could play an important role in active and passive high frequency devices. Superconductor-insulator-superconductor (SIS) or superconductor-normal metal-superconductor (SNS) Josephson junctions are fundamental elements for a wide range of superconducting electronic devices, including highly magnetic-field sensible superconducting quantum interference devices (SQUIDs), analogue signal and digital signal processing electronics. MgB_2's large coherence length and moderately high T_c make it a suitable candidate for uniform and stable Josephson junctions and SQUIDs [65]. Current in-service SQUIDs made

from niobium and its alloys must be cooled with liquid helium to about 4K. So researchers are always anxious to find materials that can sustain superconductivity at higher temperatures to ease the extremely high power-consumption on cryocoolers [66]. The T_c of 39 K for MgB_2 enables the realization of electronic circuits based on this material to operate at 20-25 K, achievable by a compact cryocooler, which gives a significant advantage to this material compared to the low-temperature superconductors (LTS). MgB_2 also has major advantages over another candidate for Josephson junctions, the high temperature superconductor (HTS) $YBa_2Cu_3O_{7-x}$ (YBCO), although YBCO has a higher T_c. MgB_2 is chemically more stable over time and a suitable barrier layer is easier to be achieved due to MgB_2's less anisotropy, fewer material complexities, and a longer coherence length (ξ= ~5 nm) than the high-T_c cuprates. The low-frequency noise of a proto-type dc SQUIDs made from two SNS MgB_2 junctions early in its development is 2 - 3 orders of magnitude lower than that of the YBCO SQUIDs [67]. Compared to the high-temperature superconductors, MgB_2 is simpler, cheaper and more stable.

The possibility of utilizing MgB_2 in passive high-frequency device applications, e.g. microwave and terahertz (THz) resonators, antennas, filters and RF cavities, is also emerging according to recent studies [68] [69]. One of the most important properties required in high frequency applications is a low microwave surface resistance R_s (or equally, high quality factor $Q = G/R_s$, where G is a geometry factor). The surface resistance is regarded as the sum of a BCS surface resistance, R_s^{BCS}, and residual component, R_{res} [70]. The BCS surface resistance is usually given in a condensed form, $R_s^{BCS}(n\Omega) = (1/T)10^5 f_{GHz}^2 \exp(-\Delta_0 / k_B T)$, where f_{GHz} is the frequency and Δ_0 the gap parameter [69]. For MgB_2, a conservative estimation based

on the smaller gap of 2.7 meV gives $R_{s,4K}^{BCS}(10GHz)$=1 μΩ, which is less than Nb by a factor of 28. R_{res} takes into account the effect of surface imperfections in general (R_{imp}) and trapped magnetic flux (R_{fl}). The magnetically induced residual resistance can be expressed as: $R_{fl}=(H/H_{c2})R_s^{NORM}$, where R_s^{NORM} is normal state surface resistance, H the field for trapped fluxoids, and H_{c2} the upper critical field. The good H_{c2} behaviour in MgB_2 films [71] could effectively reduce the microwave surface resistance. The low microwave surface resistance has been revealed in both MgB_2 bulk and films [72-74]. Another important property of superconducting films for high frequency devices is their nonlinear response, since a large nonlinear response will produce undesirable inter-modulation products, which can mitigate the merits of superconducting devices for telecommunications [68,75-77]. The calculated intrinsic nonlinear response to microwave are at the same level for MgB_2 and YBCO, but the intrinsically low nonlinear response of MgB_2 to microwave could be much easier to achieve than HTS cuprates [68]. A material problem for HTS high-frequency device is the weak-link across grain boundaries, which is closely associated with nonlinear response to microwave, whereas MgB_2 will probably benefit from its non-weak-link nature across grain boundaries. However, the MgB_2 films studied so far have not shown much better nonlinear response property compared to HTS, which demands further optimisation of MgB_2 thin film preparation to eliminate extrinsic sources of nonlinear responses, e.g. possible impurity weak links developed near the film surface [76].

Thin film synthesis is the fundamental step to the realization of electronic devices. The main difficulties for MgB_2 film preparation are Mg's high volatility and extremely high reactivity with oxygen. Various methods have been used for the preparation of MgB_2 films, such as physical vapour deposition (PVD) [32,38,39,45,46], chemical vapour deposition (CVD) [36], and electrochemical plating [50]. Transition

temperatures of 39 K or even higher have been achieved in *ex situ* annealed pulsed laser deposition (PLD) films [38] and hybrid physical-CVD (HPCVD) films [36]. One possible barrier for application of *ex situ* annealing and HPCVD process in devices could be the difficulty in realizing multilayer structures. The *in situ* annealed PLD films generally showed a considerably suppressed T_c of 25~30 K due to oxygen contamination and incomplete crystallization [78-80]. Although the T_c value still requires improvement, the PLD procedure followed by an *in situ* annealing seems very attractive due to the fact that it requires comparatively simple equipment and is technically capable of implementing multi-layer structures for Josephson junctions. Recent studies of the *in situ* annealed PLD MgB_2 films prepared by our group have shown that the T_c onset can be significantly improved to 34.5 K, and that the films show a combination of good superconducting properties [81]. According to a comparative study between different preparing methods, *in situ* prepared film has much higher disorder level, hence, stronger electron scattering [81]. This effectively raises the H_{c2}-T slope and J_c performance [71]. The small-grain feature of an *in situ* MgB_2 film may also lead to a low microwave loss according to better pinning to trapped fluxoids [82].

1.4.1.1 Superconducting Josephson Junctions and SQUIDs

Superconducting Josephson junction technology will have a small but important niche in high-performance digital signal and data processing applications for civilian, commercial, and military terrestrial, as well as space deployment. There has been considerable effort over the past thirty years to develop a viable, reproducible, controllable, and manufacturable Josephson junction technology for use as active elements in digital circuits and systems. MgB_2 has properties that are more amenable to junction technology than do the HTS and LTS materials from technical and

economic viewpoint. Cryogenic refrigeration systems required for operation at temperatures near 25 K are much less complex and less energy-hungry than those operating at temperatures near 4 K, which makes MgB_2 Josephson junction very attractive. The low-frequency noise of proto-type dc SQUIDs is much lower than that of the YBCO SQUIDs early in its development [67].

With superconducting passive microwave devices, the potentially largest market in this segment are filter systems for ground- or satellite based wireless communication systems. Attractive features are an improved coverage in rural areas and better usage of limited transmission bandwidths due to reduced interferences in densely populated areas in cellular phone telecommunication systems. A significant environmental and health benefit will be achieved by realizing such electronic devices.

1.4.1.2 Passive Microwave devices

MgB_2 films will also play an important role in applications of passive microwave devices, such as filters, resonators, and RF cavities. The application of superconducting high-performance filters in base stations for mobile communication will effectively increase sensitivity and selectivity, which makes it a strong candidate in this type of applications. MgB_2 has low surface resistance, intrinsically low nonlinear response and a non-weak-link grain boundary

With superconducting passive microwave devices, the potentially largest market in this segment are filter systems for ground- or satellite based wireless communication systems. Attractive features are an improved coverage in rural areas and better usage of limited transmission bandwidths due to reduced interferences in densely populated areas in cellular phone telecommunication systems. A significant environmental and health benefit will be achieved by realizing such electronic devices.

The technique for MgB_2 film preparation is fundamental and decisive for the device applications, as well as for studies on the physics of the superconductivity in this material. However, present MgB_2 film preparation research has not provided satisfactory material basis for electronic devices to be constructed on. A systematic research on the synthesis of stable and reproducible high quality MgB_2 films and multilayered structure will be the cornerstone for a promising future development of MgB_2 electronic devices.

1.4.2 Coated conductors

In the field of coated conductor applications, HTS has possessed a predominated position. The possibility of working within liquid nitrogen temperature range (~77K) gives HTS coated conductor strong endorsement in the commercial running. However, MgB_2 coated conductor will still gain significant consideration for its own merits.

A major difference from HTS, also known as one of MgB_2's merits, is the non-weak-link across the MgB_2 grain boundary [54]. This makes it possible to develop polycrystalline wires and films to transport electricity. According to recent research results, the grain boundaries of nano-crystalline MgB_2 thin films provide effective pinning to flux and ensure a much improved critical current density (J_c) performance in high fields [83]. The thickness of a grain boundary, ~3nm, is of good match with the coherence length (~5nm) of MgB_2 for vortex pinning. This feature of polycrystalline MgB_2 makes it very attractive to pursue nano-crystalline MgB_2 coated conductor for developing items like compact, lightweight, high power generators, RF source magnets, transformers and motors. Compared to the high-temperature superconductors, MgB_2 is simpler, cheaper and more stable over time.

Thin film preparation is the fundamental step to realize both electronic device and large scale conductors. Among those methods reviewed in this chapter, the PLD method is a simple and cheap method. A target and a substrate inside the vacuum chamber and a laser beam introduced from a window can realize the simplest PLD film forming. On the other hand, the process is influenced by many factors, including the mismatch between the film and substrate lattices, substrate temperature, substrate reactivity, nature of the film material, the deposition geometry, the growth rate and the thickness of the film. My thesis is focused on the PLD fabrication technology of MgB_2 thin films, an understanding of the underlying mechanisms between PLD MgB_2 films synthesis and their performance in J_c and H_{c2}, and the mechanism of properties enhancement by addition of inclusions and addition process with which the dopants and inclusions are introduced.

References of Chapter 1:

[1] J. Nagamatsu, N. Nakagawa, T. Muranaka, Y. Zenitani, and J. Akimitsu, Nature **410,** 63 (2001).

[2] J. D. Jorgensen, D. G. Hinks, and S. Short, Lattice properties of MgB_2 versus temperature and pressure, Phys. Rev. B **63,** 224522 (2001).

[3] M. Naito and K. Ueda, MgB_2 thin films for superconducting electronics, Supercond. Sci. & Technol. **17,** R1-R18 (2004).

[4] D. Mijatovic, MgB_2 thin films and Josephson Devices, PhD Thesis, University of Twente, 2004.

[5] P. C. Canfield, S. L. Budko, and D. K. Finnemore, An Overview of the Basic Physical Properties of MgB_2, Physica C **385,** 1-7 (2002).

[6] *Superconducting magnesium diboride*; *Vol.*, edited by A. Narlikar (Nova Science, New York, 2002).

[7] S. L. Bud'ko, Lapertot, C. Petrovic, C. E. Cunningham, N. Anderson, and P. C. Canfield, Boron Isotope Effect in Superconducting MgB_2, Phys. Rev. Lett. **86,** 1877-1880 (2001).

[8] R. Osborn, E. A. Geremychkin, A. I. Kolesnikov, and D. G. Hinks, Phonon Density of States in MgB_2, Phys. Rev. Lett. **87,** 017005-1--4 (2001).

[9] T. Yildirim, O. Gulseren, J. W. Lynn, C. M. Brown, T. J. Udovic, Q. Huang, N. Rogado, K. A. Regan, M. A. Hayward, J. S. Slusky, T. He, M. K. Haas, P. Khalifah, K. Inumaru, and R. J. Cava, Giant Anharmonicity and Nonlinear Electron- Phonon Coupling in MgB_2: A Combined First-Principles Calculation and Neutron Scattering Study, Phys. Rev. Lett. **87,** 037001-1--4 (2001).

[10] J. Kortus, I. I. mazin, K. D. Belashenko, V. P. Antropov, and L. L. Boyer, Superconductivity of Metallic Boron in MgB_2, Phys. Rev. Lett. **86,** 4656 (2001).

[11] J. M. An and W. E. Pickett, Superconductivity of MgB_2: Covalent Bonds Driven Metallic, Phys. Rev. Lett. **86,** 4366 (2001).

[12] F. Giubileo and e. al, Phys. Rev. Lett. **87,** 177008 (2001).

[13] R. A. Kaindl, M. A. Carnahan, J. Orenstein, and D. S. Chemla, Far-Infrared Optical Conductivity Gap in Superconducting MgB_2 Films, Phys. Rev. Lett. **88,** 027003 (2002).

[14] S. Tsuda, T. Yokoya, T. Kiss, Y. Takano, K. Togano, H. Kito, H. Ihara, and S. Shin, Phys. Rev. Lett. **87,** 177006 (2001).

[15] P. Szabo, P. Samuely, J. Kacmarcik, T. Klein, J. Marcus, D. Fruchart, S. Miraglia, C. Marcenat, and A. G. Jansen, Phys. Rev. Lett. **87,** 137005 (2001).

[16] F. Bouquet, R. A. Fisher, N. E. Phillips, D. G. Hinks, and J. D. Jorgensen, Specific Heat of Mg11B2: Evidence for a Second Energy Gap, Phys. Rev. Lett. **87,** 47001 (2001).

[17] B. B. Jin, N. Klein, W. N. Kang, H.-J. Kim, E.-M. Choi, S.-I. Lee, T. Dahm, and K. Maki, Energy gap, penetration depth, and surface resistance of MgB_2 thin films determined by microwave resonator measurements, Phys. Rev. B **66,** 104521 (2002).

[18] F. Manzano, A. Carrington, N. E. Hussey, S. Lee, A. Yamamoto, and S. Tajima, Phys. Rev. Lett. **88,** 47002 (2002).

[19] F. Bouquet, Y. Wang, R. A. Fisher, D. G. Hinks, J. D. Jorgensen, A. Junod, and N. E. Phillips, Phenomenological two-gap model for the specific heat of, Europhys. Lett. **56,** 856-862 (2001).

[20] A. Y. Liu, I. I. Mazin, and J. Kortus, Beyond Eliashberg superconductivity in MgB_2: anharmonicity, two-phonon scattering, and multiple gaps, Phys. Rev. Lett. **87,** 087005 (2001).

[21] H. J. Choi, M. L. Cohen, and S. G. Louie, Anisotropic Eliashberg theory of MgB_2: Tc, isotope effects, superconducting energy gaps, quasiparticles, and specific heat, Physica C **385,** 66 (2003).

[22] I. I. Mazin, O. K. Andersen, O. Jepsen, O. V. Delgov, J. Kortus, A. A. Golubov, A. B. Kuzmenko, and D. v. d. Marel, Two-gap Superconductivity in MgB_2: Clean or Dirty?, Phys. Rev. Lett. **89,** 107002 (2002).

[23] I. I. Mazin and V. P. Antropov, Electronic Structure, Electron-phonon Coupling, and Multiband Effects in MgB_2, Physica C **385,** 49 (2003).

[24] H. M. Christen, Pulsed laser deposition of $YBa_2Cu_3O_{7-\delta}$ for coated conductor applications: current status and cost issues, cond-mat/0110357 (2001).

[25] Q. X. Jia, S. R. Foltyn, P. N. Arendt, and J. F. Smith, High-temperature Superconducting Thick Films With Enhanced Supercurrent Carrying Capability, Appl. Phys. Lett. **80,** 1601 (2002).

[26] O. C. Mantel, H. S. J. van der Zant, A. J. Sternfort, and C. Dekker, Thin Films of the Charge-density-wave Oxide $Rb_{0.30}MoO_3$ by Pulsed-laser Deposition, Phys. Rev. B **55,** 4817-4824 (1997).

[27] G. M. Daly, D. B. Chrisey, J. M. Pond, M. S. Osofsky, M. Miller, P. Lubitz, J. S. Horwitz, R. C. Y. Auyeung, and R. J. Soulen, in *Pulsed Laser Deposition of High Temperature Superconducting and Metalic Thin Films For Novel Three Terminal Device applictions*, 1997, p. 226-237.

[28] J. T. Dickinson, D. R. Ermer, and S. C. Langford, Appl. Surf. Sci. **127-129,** 7-20 (1998).

[29] *Pulsed Laser Deposition of Thin films*; *Vol.*, edited by D. B. Chrisey and G. K. Hubler (Wiley, New York, 1994).

[30] K. Ueda and M. Naito, Growth of Superconducting MgB_2 Thin Films, Cond-mat/0203181 (2002).

[31] K. Ueda and M. Nato, As-grown superconducting MgB_2 thin films prepared by molecular beam epitaxy, Appl. Phys. Lett. **79,** 2046 (2001).

[32] W. Jo, J.-U. Huh, T. Ohnishi, A. F. Marshall, M. R. Beasley, and R. H. Hammond, Appl. Phys. Lett. **80** (2002).

[33] J. Kim, R. K. Singh, J. M. Rowell, N. Newman, L. Gu, and D. J. Smith, Thermochemical analysis of MgB_2 synthesis by molecular-beam epitaxy, Journal of Crystal Growth **270,** 107-112 (2004).

[34] G. Grassano, W. Ramadan, V. Ferrando, E. Bellingeri, D. Marre, C. Ferdeghini, G. Grasso, M. Putti, and A. S. Siri, In-situ Magnesium Diboride Superconducting Thin Films Grown by Pulsed Laser Deposition, Cond-mat/0103572 (2001).

[35] A. Saito, A. Kawakami, H. Shimakage, and Z. Wang, As-grown Deposition of Superconducting MgB_2 Thin Films by Multiple-target Sputtering System, Jpn. J. Appl. Phys. **41,** L127-129 (2002).

[36] X. H. Zeng, A. V. Pogrebnyakov, A. Kotcharov, J. E. Jones, X. X. Xi, E. M. Lysczek, J. M. Redwing, S. Y. Xu, Q. Li, J. Lettieri, D. G. schlom, W. Tian, X. Q. Pan, and Z. K. Liu, In-situ Epitaxial MgB_2 Thin Films for Superconducting Electronics, Nature Materials **1,** 35 (2002).

[37] X. H. Zeng, A. V. Pogrebnyakov, M. H. Zhu, J. E. Jones, X. X. Xi, S. Y. Yu, E. Wertz, Q. Li, J. M. Redwing, J. Lettiery, V. Vaithyanathan, D. G. Schlom, Z. K. Liu, O. Trithaveesak, and J. Schubert, Superconducting MgB_2 thin films on silicon carbide substrates by hybrid physical-chemical capor depostion, Appl. Phys. Lett. **82,** 2097-2099 (2003).

[38] W. N. Kang, H.-J. Kim, E.-M. Choi, C. U. Jung, and S.-I. Lee, Epitaxial MgB_2 Superconducting Thin Films with a Transition Temperature of 39 Kelvin, Science **292,** 1521 (2001).

[39] C. B. Eom, M. K. Lee, J. H. Choi, L. J. Belenky, X. Song, L. D. Cooley, M. T. Naus, S. Patnaik, J. Jiang, M. Rikel, A. Polyanskii, A. Gurevich, X. Y. Cai, S. D. Bu, S. E. Babcock, E. E. Hellstrom, D. C. Larbalestier, N. Rogado, K. A. Regan, M. A. Hayward, T. He, J. S. Slusky, K. Inumaru, M. K. Hass, and R. J. Cava, High Critical current Density and Enhanced Irreversibility Field in Superconducting MgB_2 Thin Films, Nature **411,** 558-560 (2001).

[40] M. Parathaman, C. Cantoni, H. Y. Zhai, H. M. Chriten, T. Aytug, S. Sathyamurthy, E. D. Specht, J. R. Thompson, D. H. Lowndes, H. R. Kerchner, and D. K. Christen, Appl. Phys. Lett. **78,** 3669 (2001).

[41] S. H. Moon, J. H. Yun, H. N. Lee, J. I. Kye, H. G. Kim, W. Chung, and B. Oh, High critical current densities in superconducting MgB_2 thin films, Appl. Phys. Lett. **79,** 2429 (2001).

[42] H. Y. Zhai, H. M. Christen, L. Zhang, M. Parathaman, C. Cantoni, B. C. Sales, P. H. Fleming, D. K. Christen, and D. H. Lowndes, J. Mater. Res. **16,** 2759 (2001).

[43] A. Plecenik, L. Satrapinsky, P. Kus, S. Gazi, S. Benacka, I. Varra, and I. Kostic, MgB_2 superconductor thim films on Si and Al2O3 substrates, Physica C **363,** 224 (2001).

[44] P. Kus, A. Plecenik, L. Satrapinsky, Y. Xu, and R. Sobolewski, Superconducting properties of MgB_2 thin films prepared on flexible plastic substrates, Appl. Phys. Lett. **81,** 2199 (2002).

[45] R. Vaglio, M. G. Maglione, and R. D. Capua, High-quality MgB_2 thin films *in situ* grown by dc magnetron sputtering, Supercond. Sci. Technol. **15,** 1236 (2002).

[46] S. D. Bu, D. M. Kim, J. H. Choi, J. Giencke, S. Patnaik, L. Cooley, E. E. Hellstrom, D. C. Larbalestier, and C. B. Eom, Synthesis and Properties of c-axis Oriented Epitaxial MgB_2 Thin Films, Appl. Phys. Lett. **81,** 1851 (2002).

[47] K. Komori, K. Kawagishi, Y. Takano, S. Arisawa, H. Kumakura, and M. Fukutomi, A New Approach for the Fabrication of MgB_2 Superconducting Tape with Large In-field Transport Jc, Appl. Phys. Lett. **81,** 1047 (2002).

[48] N. Hur, P. A. Sharma, S. Guha, M. Z. Cieplak, D. J. Werder, Y. Horibe, C. H. Chen, and S.-W. Cheong, High-quality MgB_2 films on boron crystals with onset Tc of 41.7 K, Appl. Phys. Lett. **79,** 4180-2 (2001).

[49] H. Abe, K. Yoshii, K. Nishida, M. Imai, and H. Kitazawa, Superconducting Properties of Electroplated MgB_2 Films, MRS 2003 Fall Meeting Proceedings**,** EE7.6 (2003).

[50] A. B. Jadhav and S. H. Pawar, Electrochemical synthesis of superconducting magnesium diboride films: a novel potential technique, Supercond. Sci. Technol. **16,** 752 (2003).

[51] A. Li, X. L. Wang, M. Ionescu, S. Soltanian, J. Horvat, T. Silver, H. K. Liu, and S. X. Dou, Fast formation and superconductivity of MgB_2 thick films grown on stainless steel substrate, Physica C **361,** 73-78 (2001).

[52] Z.-K. Liu and D. G. Schlom, Thermodynamics of the Mg-B System: Implications for the Deposition of MgB_2 Thin Films, Appl. Phys. Lett. **78,** 3678-3680 (2001).

[53] W. Z. Yu, *Theory of fabrication, techniques , and application of thin films* (Metallurgy industry press, Beijing, 1998).

[54] D. C. Larbalestier, L. D. Cooley, M. O. Rikel, and e. al, Strongly linked current flow in polycrydtalline forms of the superconductor MgB_2, Nature **410,** 186 (2001).

[55] A. V. P. Sihai Zhou, Huakun Liu, Joseph Horvat, and Shixue Dou, Effect of Various Mechanical Deformation Processes on Critical Current Density and Microstructure in MgB_2 Tapes and Wires, Supercond. Sci. Technol. **15,** 1490-1493 (2002).

[56] A. V. P. Sihai Zhou, Huakun Liu, Shixue Dou, Single- and Multi-filamentary Fe-sheathed MgB_2 Wires, Physica C **382,** 349-354 (2002).

[57] B. A. Glowacki, M. Majoros, M. Vickers, J. E. Evetts, Y. Shi, and I. McDougall, Superconductivity of powder-in tube MgB_2 wires, Supercond. Sci. Technol. **14,** 193-199 (2001).

[58] S. Soltanian, X. L. Wang, I. Kusevic, E. Babic, A. H. Li, M. J. Qin, J. Horvat, H. K. Liu, E. W. Collings, E. Lee, M. D. Sumption, and S. X. Dou, High-transport critical current density above 30 K in pure Fe-clad MgB_2 tape, Physica C **361,** 84-90 (2001).

[59] M. D. Sumption, M. Bhatia, M. Rindfleisch, M. Tomsic, and E. W. Collings, Transport and magnetic J(c) of MgB_2 strands and small helical coils, Applied Physics Letters **86** (2005).

[60] M. Bhatia, M. D. Sumption, M. Tomsic, and E. W. Collings, Influence of heat-treatment schedules on magnetic critical current density and phase formation in bulk superconducting MgB_2, Physica C-Superconductivity and Its Applications **415,** 158-162 (2004).

[61] E. W. Collings, E. Lee, M. D. Sumption, M. Tomsic, X. L. Wang, S. Soltanian, and S. X. Dou, Continuous- and batch-processed MgB_2/Fe strands - transport and magnetic properties, Physica C-Superconductivity and Its Applications **386,** 555-559 (2003).

[62] E. W. Collings, E. Lee, M. D. Sumption, and M. Tomsic, Transport and magnetic properties of continuously processed MgB_2, Rare Metal Materials and Engineering **31,** 406-409 (2002).

[63] M. D. Sumption, E. W. Collings, E. Lee, X. L. Wang, S. Soltanian, and S. X. Dou, Reduction and elimination of external-field AC loss in MgB_2/Fe wire by in situ magnetic shielding, Physica C-Superconductivity and Its Applications **378,** 894-898 (2002).

[64] S. Soltanian, X. L. Wang, A. H. Li, E. W. Collings, M. D. Sumption, E. Lee, H. K. Liu, and S. X. Dou, Fabrication and critical current density in 16-filament stainless steel/Fe/ MgB_2 square wire, Solid State Communications **124,** 59-62 (2002).

[65] M. Naito and K. Ueda, MgB_2 thin films for superconducting electronics, Superconductor Science & Technology **17,** R1-R18 (2004).

[66] M. Nisenoff, An assessment of superconducting digital thechnology: the possible impact of the discovery of magnesium diboride, (High Tc Update, 2001) www.iitap.iastate.edu/htcu/nisenoffcomment.html

[67] Y. Zhang, D. Kinion, J. Chen, J. Clarke, D. G. Hinks, and G. W. Crabtree, Appl. Phys. Lett. **79,** 3995 (2001).

[68] T. Dahm and D. J. Scalapino, Nonlinear microwave response of MgB_2, Appl. Phys. Lett. **85,** 4436 (2004).

[69] E. W. Collings, M. D. Sumption, and T. Tajima, Magnesium diboride suoerconducting RF resonant cavities for high energy particle caceleration, Supercond. Sci. Technol. **17,** S595-601 (2004).

[70] J. H. Hinken:, *Superconductor electronics* (Springer, New York, 1989).

[71] A. Gurevich, S. Patnaik, V. Braccini, K. H. Kim, C. Mielke, X. Song, L. D. Cooley, S. D. Bu, D. M. Kim, J. H. Choi, L. J. Belenky, J. Giencke, M. K. Lee, W.

Tian, X. Q. Pan, A. Siri, E. E. Hellstrom, C. B. Eom, and D. C. Larbalestier, Very high upper critical fields in MgB_2 produced by selective tuning of impurity scattering, Supercond. Sci. Technol. **17,** 278 (2004).

[72] S. Y. Lee, J. H. Lee, J. Lim, H. N. Lee, S. H. Moom, B. Oh, and M. A. Hein, Effects of Ion Milling on the Microwave Properties of MgB_2 Films, IEEE Transactions on Applied Superconductivity **13,** 3585 (2003).

[73] A. T. Findikoglu, A. Serquis, L. Civale, X. Z. Liao, Y. T. Zhu, M. E. Hawley, F. M. Mueller, V. F. Nesterenko, and Y. Gu, Microwave performance of high-density bulk MgB_2, Appl. Phys. Lett. **83,** 108-110 (2003).

[74] T. Tajima, in *Possibility of MgB_2 Application to Superconducting Cavities*, Paris, France, 2002.

[75] A. V. Velichko, M. J. Lancaster, and A. Porch, Nonlinear microwave properties of high Tc thin films, Supercond. Sci. Technol. **18,** R24-49 (2005).

[76] A. J. Purnell, L. F. Cohen, H. Y. Zhai, H. M. Christen, M. P. Paranthaman, D. H. Lowndess, L. Hao, and J. C. Gallop, Nonlinear microwave response of an MgB_2 thin film, Supercond. Sci. Technol. **17,** 681.

[77] J. Booth, K. T. Leong, S. Y. Lee, J. H. Lee, B. Oh, H. N. Lee, and S. H. Moon, Nonlinear microwave response of MgB_2 thin films, Supercond. Sci. Technol. **16,** 1518-1522 (2003).

[78] D. H. A. Blank, H. Hilgenkamp, A. Brinkman, D. Mijatovic, G. Rijinders, and H. Rogalla, Superconducting Mg-B Films by Pulsed-laser Depostion in an in situ Two-step Process Using Multicomponent Targets, Appl. Phys. Lett. **79,** 394-396 (2001).

[79] H. Y. Zhai, H. M. Christen, L. Zhang, C. Cantoni, M. Parathaman, B. C. Sales, D. K. Christen, and D. H. Lowndes, Superconducting magnesium diboride films on Si

with Tc0~24 K grown via vacuum annealing from stoichiometric precursors, Appl. Phys. Lett. **79,** 2603 (2001).

[80] A. Berenov, Z. Lockman, X. Qi, Y. Bugoslavsky, L. F. Cohen, M.-H. Jo, N. A. Stelmashenko, V. N. Tsaneva, M. Kambara, N. H. Babu, D. A. Cardwell, M. G. Blamire, and J. L. MacManus-Driscoll, Growth of strongly biaxially aligned MgB_2 thin films on sapphire by postannealing of amorphous precursors, Appl. Phys. Lett. **79,** 4001-3 (2001).

[81] Y. Zhao, M. Ionescu, J. Hovard, and S. X. Dou, Comparative study of in situ and ex situ MgB_2 films prepared by pulsed laser deposition, Supercond. Sci. Technol. **17,** S482-485 (2004).

[82] N. Hakim, C. Kusko, and S. Sridhar, The Superconducting Gap of in-situ MgB_2 Thin Films by Microwave Surface Impedance Measurements, Appl. Phys. Lett. **81,** 3603 (2002).

[83] Y. Bugoslavsky, L. F. Cohen, G. K. Perkins, M. Polichetti, T. J. Tate, R.Gwilliam, and A. D. Caplin, Enhancement of the high-field critical current density of superconducting MgB_2 by proton irradiation, Nature **411,** 561 (2001).

Chapter 2. Experimental Methods

2.1 MgB_2 thin film preparation

2.1.1 Pulsed laser deposition (PLD) system for MgB_2 thin film

PLD is a versatile technique for preparing a wide range of thin films and multilayer structures [1]. The fundamental process of PLD is that the energy of focused laser beam transfers to the atoms of the target material, and forms a locally restricted ultra high-pressure gas of the target material. The high-pressure gas then develops into a shock wave, and interacts with the background gas to form a plasma plume of the species. The PLD method is quite simple regarding the requirements for equipment. A target and a substrate inside the vacuum chamber and a laser beam introduced from a window can realize the simplest PLD setup for film deposition. However, the interactions between laser beam and target, the interactions between the ablated species and background gas inside the plume and the behavior of atoms arriving and leaving the substrate surface involve complicated processes and some are still debated [2].

A number of unique features of the PLD technique makes it advantageous over conventional thin-film deposition techniques like sputtering, Molecular-Beam Epitaxy (MBE) and CVD.

One of its great advantages, and certainly one of the reasons for its ready acceptance among material scientists, is the attractive start-up cost of PLD research. The cost advantage is especially striking when one considers that PLD systems can produce films with quality comparable to molecular beam epitaxy (MBE) systems that cost 10 times as much or more [1].

Another advantage of PLD, in terms of both case of use and cost, resides in the fact that the energy source that creates the plume of species, the laser, is independent from the deposition system. Thus, complex multilayer films are straightforward to produce within a single system by moving various targets into and out of the beam of focal point. And by using mirrors to change the beam path, several deposition systems can be clustered around a single laser to create an entire deposition laboratory.

During the plume expansion after the laser hits the target, internal thermal and ionization energies are converted into kinetic energies of the ablated particles. The mass and pressure of the ambient gas determine the interaction with the ablated species, i.e., attenuation of the kinetic energy occurs during expansion caused by multiple collisions. This results in a wide range of kinetic energies of the ablated species - from high energy (typically up to 100 eV) in vacuum to low energies (typically 0.1 eV) in sufficiently large ambient pressure [3]. This feature of PLD can be used to modify the film growth since a change in the kinetic energies of the ablated species influences the kinetic energy of the particles arriving at the substrate.

Moreover, comparing with other methods the relatively easy removal of species from stoichiometric targets enables the fabrication of complex multi-component films. This is especially beneficial for MgB_2 because Mg and B have very different vapor pressures and usually require co-deposition from separate Mg and Boron sources in other deposition methods.

The PLD technique allows a stoichiometric transfer of the target material to the substrate. However, in the case of deposition of a very volatile element a target with an additional amount of the volatile element is needed to compensate for the excessive loss of the high-volatility element. The very high Mg vapor pressure determines a high

volatility of Mg. Measures to compensate for Mg loss, -either to deposit a Mg cap layer on the film surface or to employ a Mg-rich target, is needed.

The PLD setup in ISEM

The PLD deposition system used in this work was build by ISEM staff.

Figure2-1 schematically shows the PLD system used in this work. The targets are installed on a 6-pole carousel and the substrate is mounted on a disk substrate holder on top of the resistive heating wire, in a 52L spherical high vacuum chamber. The K-type thermocouple is placed in the middle of the substrate holder and closely attached to the hot plate. When calibrating the surface temperature at the sample, another thermocouple is attached to the substrate holder surface with silver paste. Before the deposition, the vacuum is usually better than $8x10^{-8}$ Torr after more than 16Hr baking at 200˚C under vacuum. Argon (purity 99.995%) was used as background gas. The background gas pressure (~120mTorr) during the deposition is controlled both up-stream and down-stream, with a pin valve on the Ar delivery and with the throttling of the gate valve on the pumping port, respectively. In this way, a robust control of pressure inside the deposition chamber can be achieved within a wide range.

There are two shields between the target and the substrate. One is a fixed shield with a 30 mm diameter opening. This shield is protecting the other targets on the carousel from contaminations during the ablation of the active target. The other shield is working as a shutter and is situated in front of the substrate. Its role is to protect the substrate or the sample by blocking the plume when necessary (target cleaning or target changing during deposition).

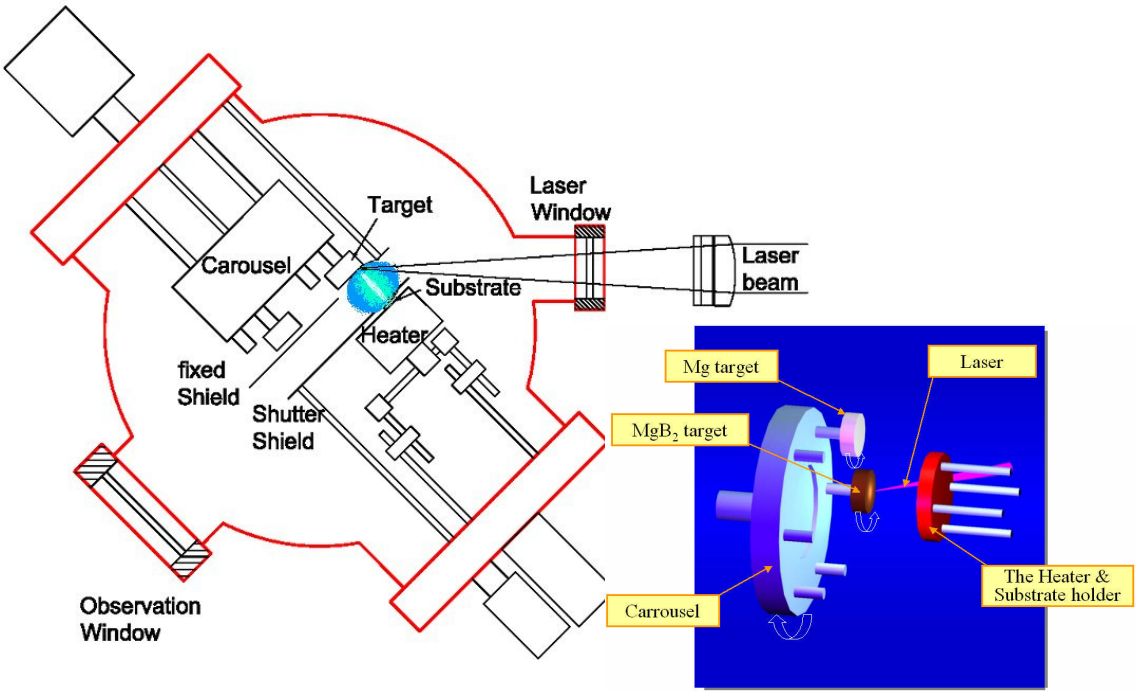

Fig.2-1 The schematics of the PLD setup used for this work. The right figure is a 3-D illustration of the on-axis deposition geometry for MgB_2 in situ annealed film. The target-substrate distance is adjustable by changing the height of the heater supporting frame before mounting the part to the chamber.

The light source used for these deposition experiments was a KrF excimer laser (Lambda Physik Compex 301, wavelength λ = 248 nm) with a pulse duration of about 25 ns (FWHM) and a pulse repetition rate of up to 10 Hz, delivering a maximum energy of 1,100 mJ/pluse. The laser beam was focused by two perpendicularly assembled cylindrical lenses, with the focal length of 700, situated outside the chamber. The focused laser beam was 45°from the target normal, and the plume was generally perpendicular to the target surface. The total energy loss at the lens and the window is less than 10%, so in the following text we still use the nominal energy detected when the laser beam is coming out from the Laser generator as laser energy.

The substrates used in this work were mainly Al_2O_3 R- and C-cut, and single-side polished to average roughness R_a < 1 nm. The selection of Al_2O_3 substrate was because of their good stability with MgB_2 at elevated temperatures up to 950℃ [4,5]. The substrate size was 3 x 3 mm^2 and 5x2.5 mm^2 mostly cut from 2 inch x 0.4 mm Al_2O_3 wafers using a diamond cutter.

A commercial stoichiometric MgB_2 target (84% density, SCI Engineered Materials) was used for the *in situ* film deposition. Figure 2-2 shows the XRD pattern of the polycrystalline MgB2 target. Trace amount of MgO and MgB_4 phase is detectable. A Mg target (99.9% purity, Goodfellow Inc.) was used for a Mg cap layer deposition. For the Si addition purpose, a single crystal Si target with better than 99.9% purity was used. A commercial boron target (40% density, 99.9% purity, Good fellow Inc.) was employed for the *ex situ* boron precursor film deposition.

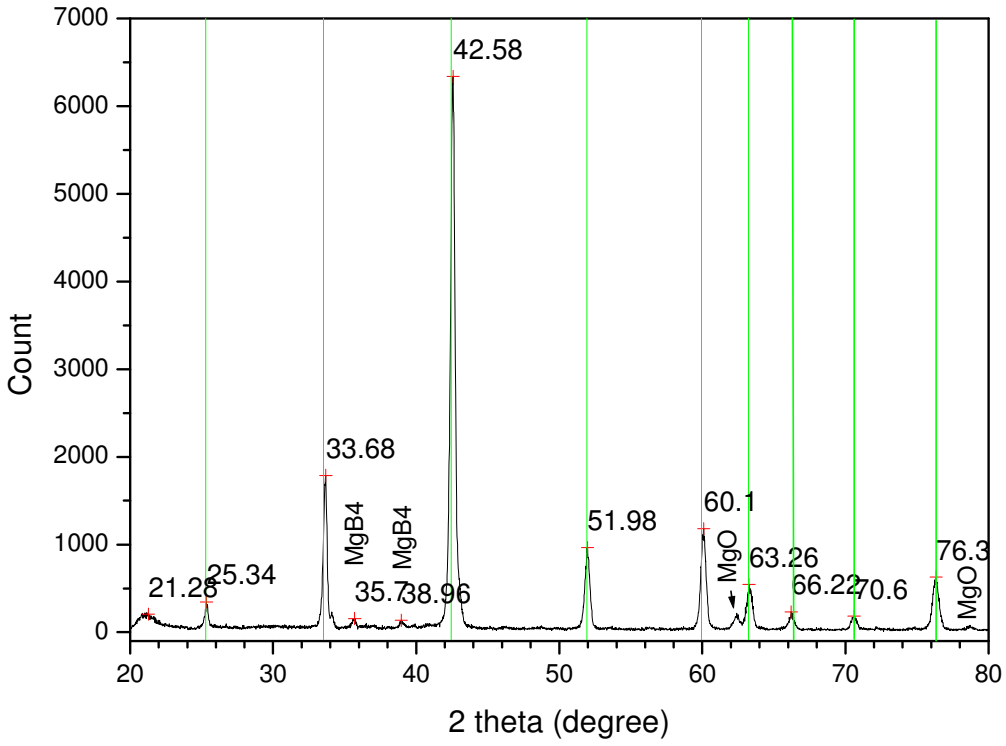

Fig.2-2 XRD spectrum of the stoichiometric MgB_2 target. The vertical lines indicate the peak positions for MgB_2.

2.1.2 The *in situ* annealing procedure

For the *in situ* annealing procedure, the precursor film was deposited by ablation of the stoichiometric MgB_2 target. After the deposition of Mg + B precursor film, a Mg cap layer was deposited on top of the precursor by ablating a pure Mg target. The *in situ* annealing process was conducted in a 760Torr argon atmosphere. The heater was heated to 450-800˚C and maintained at that temperature for 1~10min. Different types of heating procedure were used, a rapid one to heat the sample at a rate of about 110˚C/min (t_{ramp}=4min), and a slower one to heat the sample more slowly at various rates from 25˚C/min to 63˚C/min (t_{ramp}=7-17min). We also used a range of annealing dwell times, from 1min to 5 min. It was found difficult to keep the annealing temperature stable within the first 1min of the annealing time due to an overshoot, and we considered the peak temperature as the annealing temperature. After the dwell, the power of the heater was switched off, allowing the sample to cool freely with a cooling rate of about 50°C/min.

2.1.3 The *ex situ* annealing procedure

For the *ex situ* annealing procedure, a boron precursor film was deposited from a boron target (~40% density) in a 10^{-7}-10^{-6} Torr vacuum. The substrate was also kept at 250˚C during the deposition. The precursor film was then wrapped in Ta foil and sealed in a stainless steel tube in an Ar atmosphere, together with Mg pellets. The tube was gradually pushed into a 900˚C tube furnace and kept for 30min. The accuracy of the temperature control was ± 1˚C, and the temperature of the annealing furnace has been calibrated using a calibrated thermocouple. The time of putting the sealed tube to the annealing position and drawing the sealed tube from annealing zone to room temperature area were both controlled to be 5 min.

To ensure a non-oxidizing atmosphere inside the stainless steel tube after sealing it, a homemade purging apparatus was constructed as shown in Fig.2-3. The end of the stainless steel tube has been sealed by hot impact-forging. The wrapped boron film was loaded into the tube close to the end of the stainless tube together with Mg pellets. Then the tube was connected to the purging system, and purged with argon 3 times and then filled with argon to 1 atm. Finally the tube was locally heated to white-hot color by a gas torch and sealed by hammering. The sealed part of the tube is then cut off, and the ~80mm long sealed tube with the sample inside is ready for *ex situ* annealing.

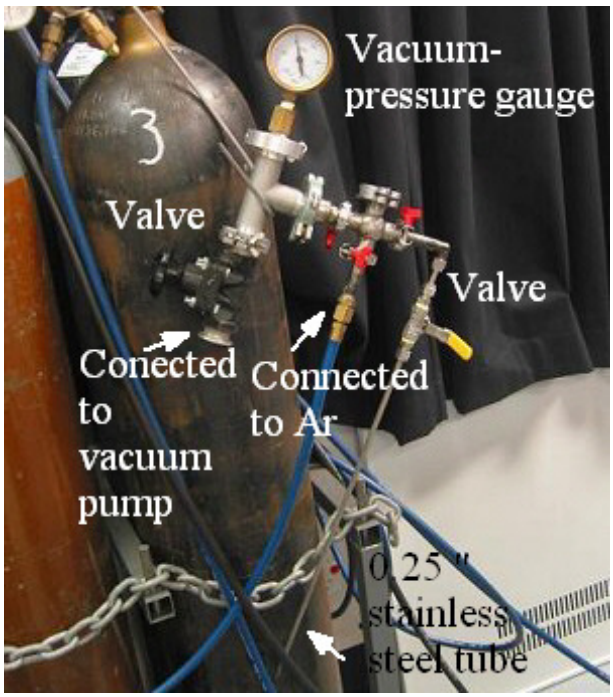

Fig.2-3 The homemade seal-in-argon apparatus for the ex situ annealing of MgB_2 film.

2.2 Microstructure characterization

2.2.1 Scanning Electron Microscopy (SEM) observation

The SEM used in this work was Leica-Cambridge S440 field emission SEM equipped with the Oxford EDS system. The filament of SEM was LaB_6 type (occasionally tungsten type filaments were used). The EDS of our SEM has 4 X-ray

energy analyzers with detectable energy up to 20 keV and energy resolution up to 0.05 keV. Another SEM system equipped with EDS (JOEL JSM-6460A) with similar standard was employed in the characterization of laser ablated surfaces of the MgB_2 target.

In the observation of MgB_2 films on insulator substrates, the main problem could be the accumulation of charge on the surface of the film, due to the poor conductance of electrons through the substrate. The charge could result in an excessive brightness in the secondary electron image, a continuous image drifting, and a blur image under high magnification. So in order to get crisp secondary electron images, several measures had to been taken during the SEM investigation carried out in this work.

(1) The MgB_2 film surface was electrically connected to the SEM aluminum specimen stage by a conductive tape or silver paste. This was proven to be an effective way to reduce the surface charge accumulation.

(2) The probe current (spot size) should be significantly reduced. Generally, the probe current should be set to its default value for conductive specimen. However, For MgB_2 films on sapphire substrates, there is usually a charging up with the default probe current which result in a blurred image. This is especially severe when observing the cracked cross-section of the film. A significantly reduced probe current usually eliminates the charging. For our Leica-Cambridge S440 SEM, we decreased the probe current from 600 pA to 50-100 pA, in order to obtain sharp SEM images.

(3) The extra high tension (EHT) should be slightly decreased. In SEM, the EHT must be high enough to provide a good image but low enough to prevent specimen charging. The default EHT is 20 kV for the Leica-Cambridge SEM, but we usually use relatively lower EHT (10-20 kV) for MgB_2 films in secondary electron imaging.

A problem one could face in EDS is that the electron-specimen interaction zone could be larger than the film thickness. Typically, with a standard 20 kV acceleration voltage, the interaction zone could be as deep as 5 μm from the surface, so the signal from the substrate is mixed into that from the MgB_2 film. With a reduced acceleration voltage, the interaction zone is also reduced. However, the reduced electron energy could also fail to induce characteristic X-rays, so special attention should be paid to checking if the acceleration energy is higher than the X-ray excitation energy for major peaks for all the elements in an EDS spectrum. With an acceleration voltage of 7 kV, the electron-specimen interaction zone is smaller than approximately 350nm for MgB_2 and the signal from the substrate underneath an MgB_2 film thicker than 350nm is totally suppressed form the EDS of our MgB_2 films.

2.2.2 Transmission Electron Microscopy (TEM) detection

Transmission Electron Microscopy is a technique used for analyzing the morphology, crystallographic structure, and even composition of a specimen. TEM provides a much higher spatial resolution than SEM, and can facilitate the analysis of features at atomic scale (in the range of a few nanometers) using electron beam energies in the range of 60 to 350 keV.

Two TEMs were used in this work. One (JEOL, JEM 2010), shown in Fig.2-4 is located at the University of Wollongong (UoW). The maximum beam energy of this instrument is 200 keV, corresponding to an electron wave length λ_e of 0.0025 nm. The best point to point resolution is 0.19nm. This TEM is equipped with EDS, which can detect light elements down to boron. Another TEM used in this work (Philips CM200) is located in the University of New South Wales (UNSW), and is also employing a beam energy of 200keV.

Fig.2-4 (left) JEOL JEM 2010 TEM at UoW; (right) Philips CM200 TEM at UNSW.

Unlike the SEM which relies on dislodged or reflected electrons from the specimen to form an image, the TEM collects the electrons that are transmitted through the specimen. A TEM uses an electron gun to produce the primary beam of electrons that will be focused by lenses and apertures into a very thin, coherent beam. This beam is then controlled to strike the specimen. A portion of this beam gets transmitted through the specimen, is collected, and processed to form the image.

For crystalline materials, the specimen diffracts the incident electron beam, producing local diffraction intensity variations that can be translated to form an image. For amorphous materials, contrast is achieved by variations in electron scattering as the electrons traverse the chemical and physical differences within the specimen.

The greatest consideration when performing TEM analysis is sample preparation. The quality of sample preparation contributes greatly to whether the

micrograph will be good or not, so analysts are required to exercise the necessary diligence in preparing the sample for TEM analysis.

For the planar observation, the specimen is prepared by a standard disk drilling - substrate dimpling and ion beam polishing preparation procedure, as shown in Fig.2-5. The Al_2O_3 substrate is extremely brittle and it was found that whenever it was ground to thinner than 200 μm it would break into pieces. So we used the dimpler to thin the disk from the backside of the substrate without any pre-thinning. The 3mm disk was very brittle after the ion milling, and was carefully bonded to a 3 mm copper grid with a long hole using Gatan G1 resin to prevent any breaking.

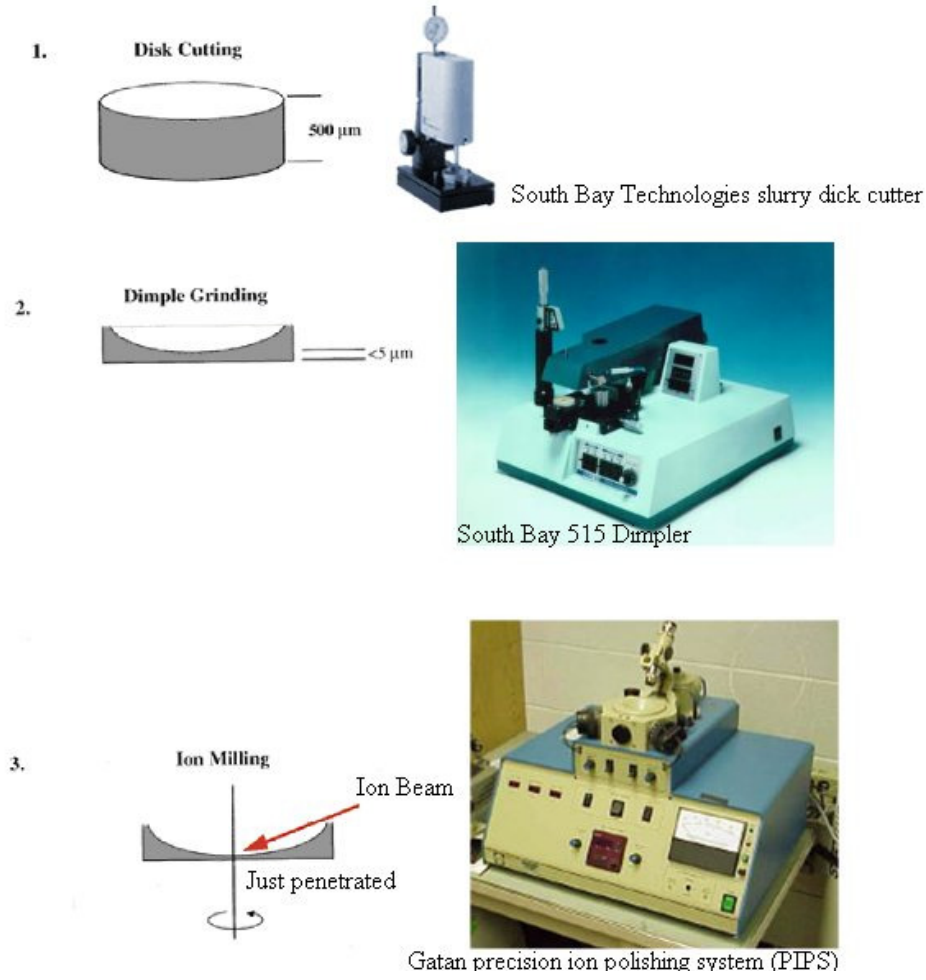

Fig.2-5 The steps for planar TEM specimen preparation in this work.

For the cross-sectional observation of our MgB_2 films, the TEM specimen was prepared by the Electron Microscopy Unit at UNSW using a focused ion beam (FIB) technique, as shown in Fig.2-6. The FEI xP200 focused ion beam miller uses a fine, energetic beam of gallium ions that scan over the surface of the specimen. At high beam currents the gallium beam rapidly sputters away the specimen surface that allows subsurface cross-sections to be prepared. If the beam current is reduced, the secondary electrons or secondary ions emitted from the specimen surface can be detected and used to form high-resolution images.

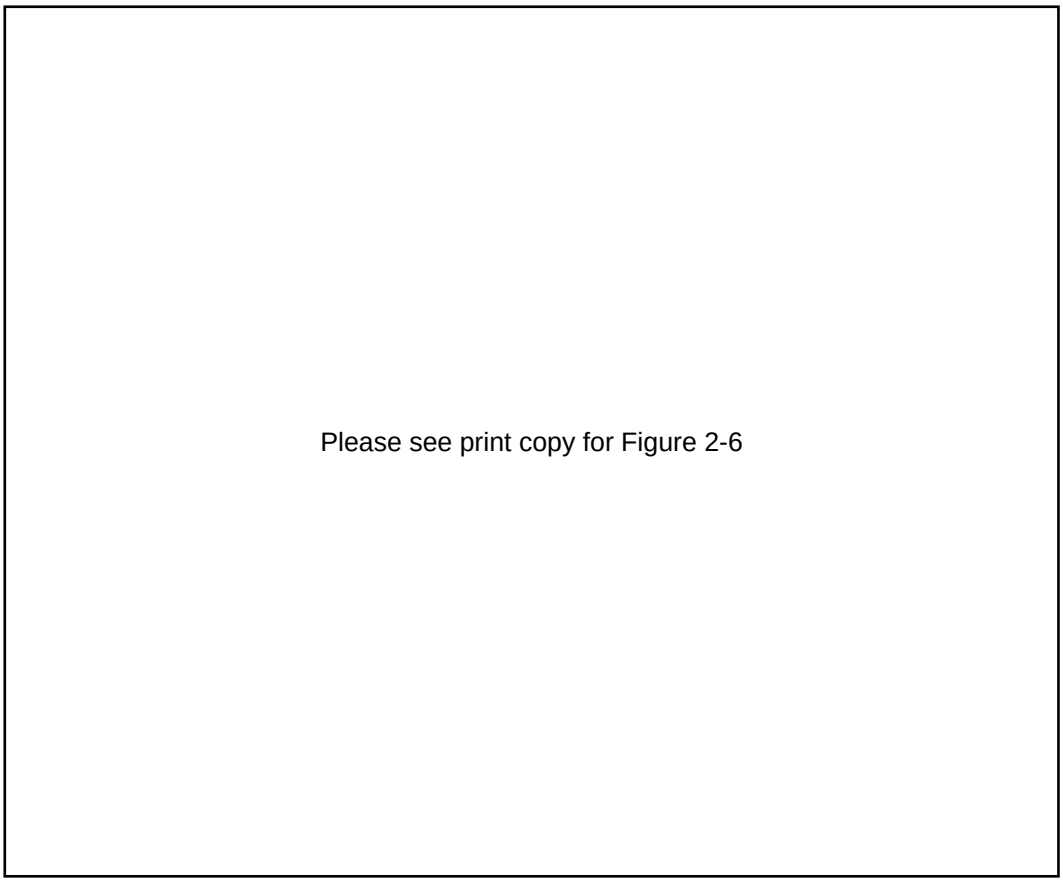

Fig. 2-6: The FIB system (FEI xP200) at UNSW and an illustration of the steps used for FIB preparation of a cross-sectional TEM specimen. a) Sample definition and

rough milling, b) Fine milling and final polish, c) Cut, d) Lift out. Photos (a,b,c,d) are reprinted from P. Gnauck "Application of the CrossBeam® Technology to TEM sample preparation and Nanolithography" [6].

2.2.3 X-ray diffraction (XRD) analysis

XRD is the most convenient non-destructive tool to analyze structural properties of a wide range of matter ranging from fluids, to powders, to perfect crystals. For research, basic material supplying, production and engineering, XRD is an indispensable method for materials characterization and quality control. The thin film crystallography system used in this work was a MAC-Science (Model M03XHF22), equipped with θ-2θ, glancing angle, ω-scan function and high temperature options. The equipment employs a copper target (λ=1.5418 Å) for X-ray generation.

The MgB_2 films prepared in this work were usually textured, however, the average crystal size was small, of the order of 300nm, and therefore the diffracted signal from such a poorly crystallized film is weak. This makes it very difficult to detect diffraction peaks in θ-2θ scan for MgB_2 films. We find several measures are of crucial importance to obtain good XRD results:

- The surface of the films must be well aligned in the diffraction plane of the X-ray apparatus. The standard method for specimen alignment was to place the substrate onto a blob of bluetag and carefully press the surface of the film with a flat-surface object such as a piece of glass. The diffraction signal from the Al_2O_3 substrate was used as a guide for alignment, and it should exceed 10^5 counts for a good alignment. Otherwise, the specimen should be realigned. When the alignment is not satisfactory, the background signal from the

substrate could be too high, which makes the weak signal from the MgB_2 film hard to detect.

- The scanning should be carried out using a large number of angular steps and a slow scanning rate in order to reliably reveal the peaks from the MgB_2 film. Also, since the signal from MgB_2 is very weak, it is important to distinguish a spike from the real signal. A long collection time at each angle will reduce the possibility of an arbitrarily high intensity. We use a scan rate of 0.2 degree / min for the θ-2θ scan of MgB_2 films.

2.2.4 Atomic force microscopy (AFM)

Atomic force microscopy (AFM) is a method for measuring surface topography on a scale from angstroms to 100 micrometer. The technique involves imaging a sample through the use of a probe, or tip, microfabricated from Si or Si_3N_4 with a radius of 20 nm. The tip is held several nanometers above the surface using a feedback mechanism that measures surface–tip interactions on the scale of nano Newtons. AFM uses a laser beam deflection system, introduced by Meyer and Amer [7,8], where a laser beam is reflected from the back of the reflective AFM cantilever and onto a position-sensitive detector as shown in Fig.2-7. In addition to basic AFM, the instrument is capable of producing images in a number of other modes, including tapping, magnetic force, electrical force, and pulsed force.

.

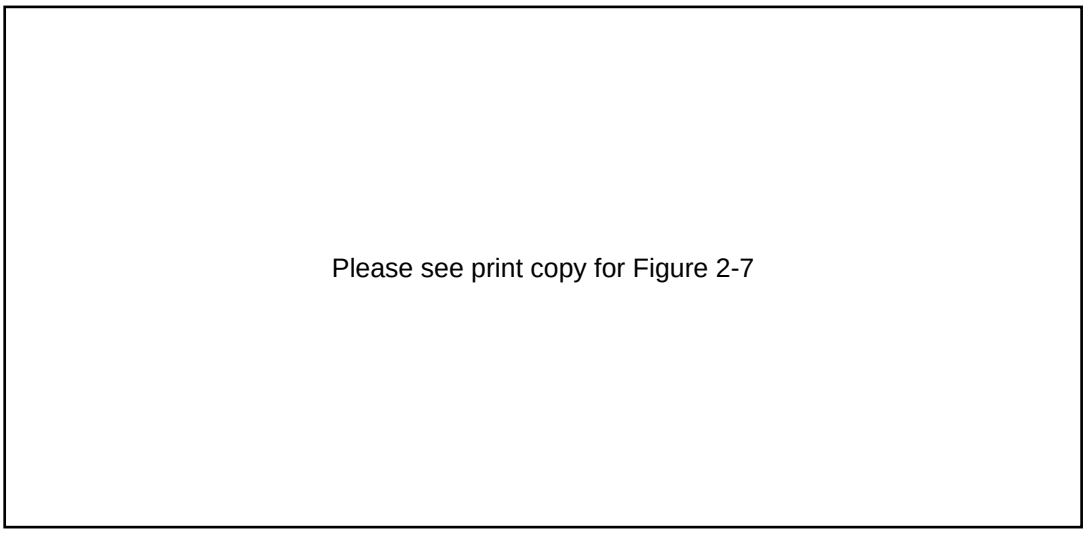

Fig.2-7 Concept of AFM and the optical lever: (left) Beam deflection system, using a laser and photodector to measure the beam position; (right) The SEM of a standard tip (SEM image cited from [9]).

AFM operates by measuring attractive or repulsive forces between a tip and the sample [10]. Laser beam deflection offers a convenient and sensitive method of measuring cantilever deflection. AFMs can generally measure the vertical deflection of the cantilever with picometer resolution. To achieve this, most AFMs today use the optical lever, a device that achieves resolution comparable to an interferometer while remaining inexpensive and easy to use[9]. The optical lever (fig 2-6) operates by reflecting a laser beam off the cantilever. Angular deflection of the cantilever causes a twofold larger angular deflection of the laser beam. The reflected laser beam strikes a position-sensitive photo detector consisting of two side-by-side photodiodes. The difference between the two photodiode signals indicates the position of the laser spot on the detector and thus the angular deflection of the cantilever. In "contact" mode, the instrument lightly touches a tip at the end of a leaf spring or "cantilever" to the sample. As a raster-scan drags the tip over the sample (for some types of AMF it is the sample that is scanning), the vertical deflection of the cantilever is monitored. A motor driving

the Z-axis running of the scanner will react to the change of the deflection to make the force of the tip touching the sample approximately constant. The Z-running is recorded as the height signal [9].

The AFM System used in this work was "Dimension 3100" from Digital Instruments, as shown in Fig.2-8. Only contact mode was used for the AFM inspection of the surface topography and the thickness measurement of the MgB_2 films. The tips and cantilevers are standard Si_3N_4 type with a tip-end radius of 20 nm.

Fig.2-8: The Dimension 3100 AFM (Digital Instruments) at UoW

2.3 Magnetic and transport properties measurements

2.3.1 The PPMS and the MPMS systems

In the study of physical properties of the MgB_2 films we have taken advantages of two highly sensitive magnetometers: the Physical Property Measurement System (PPMS) 9T and the Magnetic Property Measurement System (MPMS) XL5T from Quantum Design, (as shown in Fig.2-9).

Fig. 2-9 PPMS (left) and MPMS (right) from Quantum Design

The Quantum Design PPMS represents a unique concept in laboratory equipment: an open architecture, variable temperature-field system, designed to perform a variety of automated measurements. Sample environment controls include fields up to ± 9 Tesla and temperature range of 4.2 - 400 K. Its advanced expandable design combines many features in one instrument to make the PPMS one of the most versatile instruments of its kind.

PPMS Features:

- Dc and ac susceptibility measurements in fields up to ± 9.0 Tesla.
- Four independent channels for performing standard 4-probe dc resistivity measurements. The maximum current is 0.5A (this is limited by the size of the current leads).
- Sealed sample chamber with 2.6 cm diameter sample access and the 12 electrical leads, capable to carry out 4-probe transport measurement on 3 samples simultaneously.
- Temperature Sweep Mode

The Magnetic Property Measurement System (MPMS) sample magnetometer has become the industry standard for performance and reliability since its introduction in 1983 by Quantum Design. Utilizing Superconducting Quantum Interference Device

(SQUID) technology, combined with patented enhancements, the MPMS-XL5T sample magnetometer achieves superior measurement sensitivity, dynamic range, and reproducibility otherwise unattainable. The modular MPMS design integrates a SQUID detection system, a precision temperature control unit residing in the bore of a high-field superconducting magnet, and a sophisticated computer operating system. Hysteresis magnetization loops in field up to 5 T, Zero fled Cooling (ZFC) and Field Cooling (FC) DC magnetization measurement for T_c detection purpose were carried out on the MPMS.

Parameters for the MPMS at ISEM:

Maximum Sample Size: 9 mm

Field Uniformity: 0.01% over 4 cm

Temperature Range: 1.9-400 K (800 K with optional oven)

Magnetic field: up to ± 5.0 Tesla

Sensitivity for magnetic moment measurement: 10^{-7} emu

2.3.2: Four-probe transport measurement

The 4-probe transport measurement was conducted using the PPMS system. The brass sample stage has a diameter of 1 inch. We glued a piece of very thin cigarette paper (could be any other paper that is thin, tough, and easily penetrated by G-vanish) on top of the brass surface with G-vanish to create an insulating barrier between the sample and the holder. The 5x2mm substrate with the MgB_2 film was then attached to the paper by G-vanish, which is an excellent electric insulator with good thermal conductivity and good adherence and strength at low temperatures. The procedure was designed to reduce the opportunity for a short circuit when attaching the four probes to the film, while ensuring a good thermal sink for the superconducting film to reduce the

local heating. For the case when the field was applied parallel to the film surface, a copper cube was first glued onto the brass top surface of the stage. Then the paper and the film were attached onto the vertical side of the copper cube, as shown in Fig.2-10. The four probes were attached to the film surface by silver paint (PELCO® Conductive Silver 187) with extreme care on the shape of the connecting spot. The contact resistance between the probe and the film surface was usually kept <10 Ω.

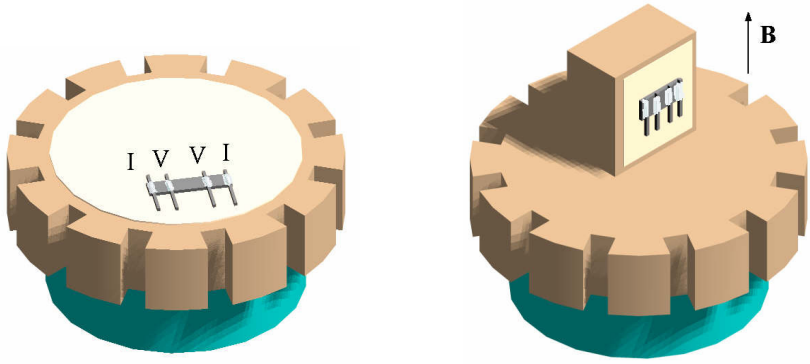

Fig.2-10: Illustrations for four-probe setup for transport measurement in PPMS. The points labeled "I" were current contacts, and the points labeled "V" were voltage contacts. (Left) Magnetic field is perpendicular to the film surface circumstance. (Right) Magnetic field is parallel to the film surface. In both cases the testing current flowing in the MgB_2 film is perpendicular to the applied field.

2.3.3 Magneto-optical imaging (MOI)

During all phases of investigation of magnetic and current-carrying properties of superconductors it has been considered desirable to apply a method for the visualization and measurement of the spatial distribution of the magnetic flux density. In particular, to achieve a profound microscopic understanding of global properties of superconductors such as magnetization, magnetic susceptibility and critical transport currents it is necessary to use a local probe [11].

The physical idea behind the magneto-optical imaging technique is the Faraday effect [12,13], i.e. the rotation of the light polarization vector induced by magnetic field, as schematically shown in Fig.2-11. The magneto-optical Faraday effect provides a method which allows one to combine relatively high spatial resolution and magnetic sensitivity with short measurement times and large imaging areas. Due to the progress in magneto-optical measurement techniques as well as the progressive requirements of the research into high-temperature superconductors (HTS), this method has become used to a greater and greater extent during the last ten years. Since, up to now, no significant magneto-optical Faraday effect has been observed in superconductors, one has to rely on well-suited magneto-optical layers (MOLs) as magnetic field sensing elements. Today, the most popular indicator is the ferri-magnetic Bi:YIG film with in-plane spontaneous magnetization. Application of a perpendicular magnetic field creates an out-of-plane component of the magnetization responsible for the Faraday rotation.

The Magneto-optical set-up

As shown in the right image of Fig.2-11, the MOL indicator is placed in the light beam path between a polarizer and an analyser positioned at 90 degrees of each other. If a magnetic field is present and is perpendicular to the film, the magnetization of the Bi:YIG will be tilted out of the plane. The perpendicular component of the magnetization will cause a Faraday rotation of the light. The rotation angle will be small where the magnetic field is small, and large in regions of high fields. After leaving the analyser the light will therefore have an intensity distribution that reflects the magnitude of the field in the plane of the indicator film.

We employed MOI technique to investigate the local homogeneity of the superconducting phase and the flux penetration behaviour of different MgB_2 films

using a home-made MOI system, set-up at ISEM (fig.2-10). The MOI set-up was constructed by Dr A. V. Pan and PhD student M. Roussel of ISEM, UoW. The system can reach a temperature down to 4K and a external field of 50mT. The best imaging resolution is about 5 μm on the specimen. Some MO imaging on the *in situ* film #030703 and the *ex situ* film #120803E was conducted at the University of Oslo using a similar MOI equipment by Roussel. In both systems, the temperature is continuously adjustable between 4.2 K and 300K.

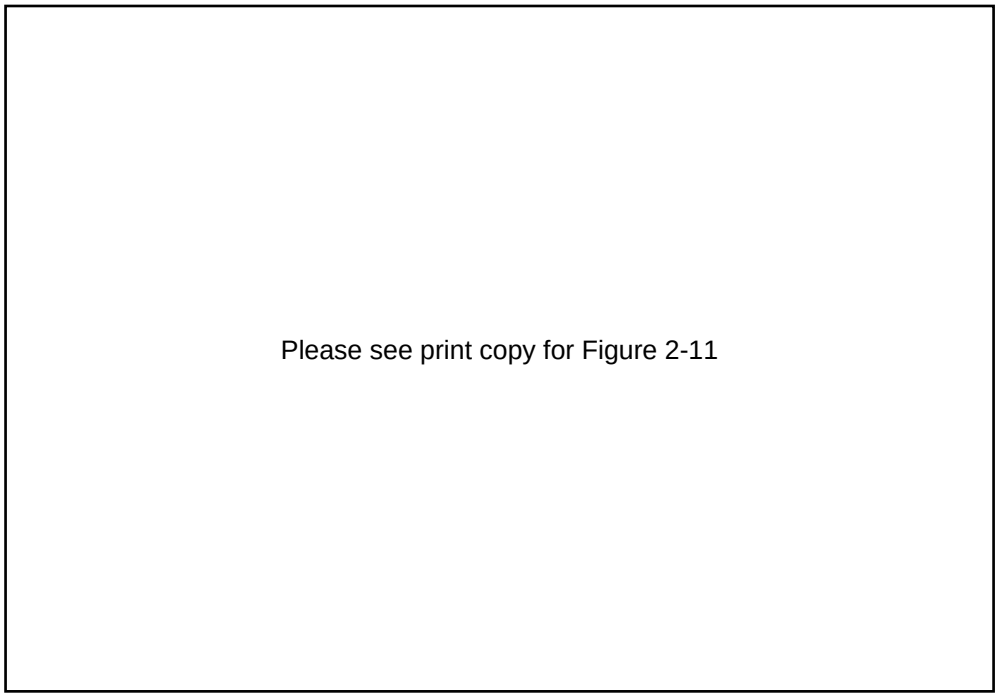

Fig. 2-11: (left) An illustration of Faraday effect and (right) a typical MOI set up. Figures cited from the web site of the MO unit at the University of Oslo [14]

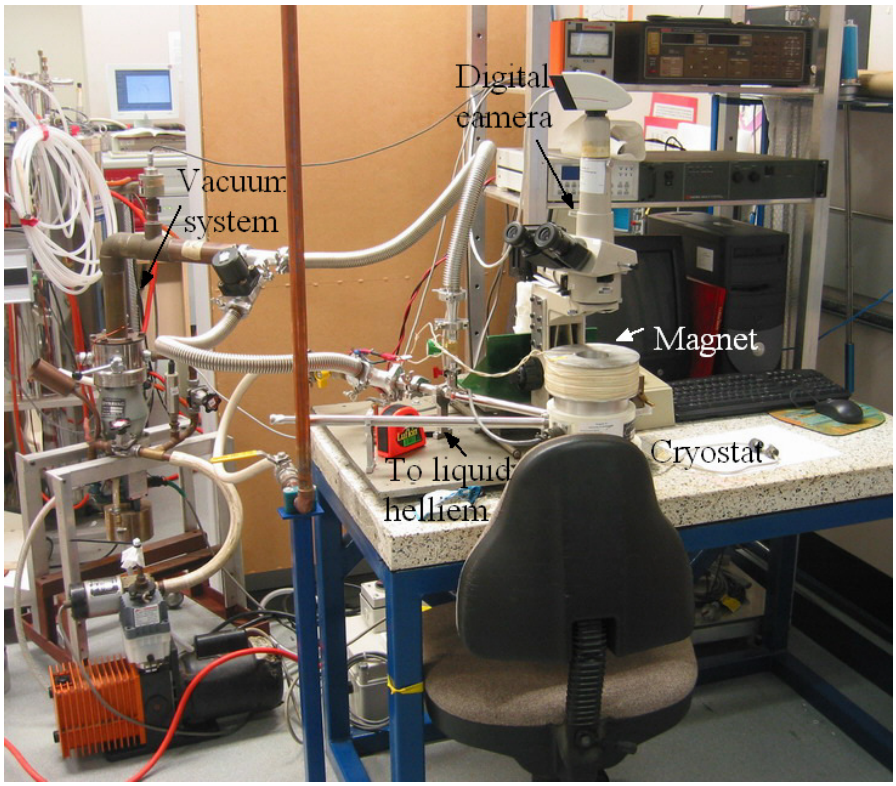

Fig.2-12 The MOI system in ISEM.

References

[1] D. B. Chrisey and G. K. Hubler, *Pulsed Laser Deposition of Thin films* (Wiley, New York, 1994).

[2] J. McKinnon, Pulsed laser deposition of superconducting films, PhD Thesis, University of Wollongong, 2003.

[3] D. B. Geohegan, in *Pulsed laser deposition of thin films*, edited by D. B. Chrisey and G. K. Hubler (Wiley, New York, 1994).

[4] W. N. Kang, H. J. Kim, E. M. Choi, C. U. Jung, and S. I. Lee, MgB_2 Superconducting Thin Films with a Transition Temperature of 39 Kelvin, Science **292,** 1521 (2001).

[5] T. He, J. M. Rowell, and R. J. Cava, Appl. Phys. Lett. **80,** 291 (2002).

[6] P. Gnauck, Application of the CrossBeam Technology to TEM sample preparation and Nanolithography.

[7] G. Meyer and N. M. Amer, Novel optical approach to atomic force microscopy, Appl. Phys. Lett. **53,** 1045-1047 (1988).

[8] G. Meyer and N. M. Amer, Simultaneous measurement of lateral and normal forces with an optical-beam-deflection atomic force microscope, Appl. Phys. Lett. **57,** 2089-2091 (1990).

[9] D. Baselt, The tip-sample interaction in atomic force microscopy and its implications for biological applications, PhD Thesis, California Institute of Technology, 1993.

[10] G. Binnig, C. F. Quate, and C. Gerber, Atomic force microscope, Phys. Rev. Lett. **56,** 930-933 (1986).

[11] C. Jooss, J. Albrecht, H. Kuhn, S. Leonhardt, and H. Kronmuller, Magneto-optical studies of current distributions in high-Tc superconductors, Rep. Prog. Phys. **65,** 651-788 (2002).

[12] W. DeSorbo, Study of the Intermediate State in Superconductors using Cerium Phosphate Glass, Phys. Rev. Lett. **4,** 406-408 (1960).

[13] P. B. Alers, Structure of the Intermediate State in Superconducting Lead, Phys. Rev. **105,** 104-108 (1957).

[14] http://www.fys.uio.no/super/mo/#mo.

Chapter 3 PLD MgB_2 thin films using *in situ* annealing

Due to the difficulties in fabricating MgB_2 films, there is yet not a unanimous method to produce superconducting films for the superconducting electronics and large-scale applications. Obstacles in the formation of MgB_2 films come mainly from two factors: the high volatility of magnesium (vapour pressure ~$1x10^{-6}$ Torr at 250℃ and 8.3Torr at 727℃) and its high reactivity with oxygen. Generally, as reviewed in chapter 1, MgB_2 film preparation methods are classified into three types, as grown, *in situ* annealing and *ex situ* annealing. To date, good T_c (close to the bulk value) has been achieved by *ex situ* annealing [1,2]. The main shortcoming of the *ex situ* annealing method is the difficulty in realizing multi-layer structures, which are essential for making junctions or other superconducting electronic devices. The as-grown method is capable of producing multi-layer structures. As grown MgB_2 films with a good T_c of 37K have been obtained by molecular beam epitaxy (MBE) [3,4]. Some other methods, such as PLD [5] and magnetic sputtering [6], can also achieve as grown superconducting MgB_2 films, but the T_c properties are not as good as the MBE-fabricated films. *In situ* high temperature annealing carried out immediately after the deposition has proven to be effective to obtain high T_c [7]. The advantage of the *in situ* annealing method is that it can achieve multi-layer structures and high T_c in the films simultaneously. Zeng et al. [8] have obtained epitaxial MgB_2 films by a new method, hybrid physical-chemical vapour deposition (HPCVD). The T_c value of their films reached the same level as bulk MgB_2. This is a significant improvement of the preparation of MgB_2 films. Further work on optimisation of this as grown method may lead to applications in superconducting electronic devices manufactured from this material.

As shown in the literatures on *in situ* annealing of MgB_2 films, the annealing parameters are hard to select. The magnesium vapour pressure inside the deposition chamber cannot be made high enough to prevent the evaporation of magnesium. So, in order to keep stoichiometry in the MgB_2 film, the annealing temperature should be low and the duration should be short. On the other hand, a reasonably high annealing temperature and long dwell time is necessary for MgB_2 phase formation and crystallization in the films. Since the process behind the formation of the superconducting phase in the MgB_2 film is still under debate, it is very interesting to study how the *in situ* annealing conditions influence the microstructure and superconducting properties of MgB_2 films.

In this chapter, we applied different temperatures, heat treatment durations and heating rates on the *in situ* annealing of PLD MgB_2 films. Optimal annealing conditions were obtained according to the T_c measured in the prepared films. The annealing process is discussed with the help of the T_c curves, XRD results, atomic force microscopy, magneto-optical imaging, and magnetization hysteretic curves.

3.1 The function of the argon background gas

The background gas we used is 120 mTorr ultrahigh purity argon, following the reported background gas used in MgB_2 thin film preparations [8,9]. For a significantly higher argon pressure, 400 mTorr, no MgB_2 film can be deposited on the substrate under laser energy densities up to 5 J/cm^2. In vacuum (no back ground gas) of $5x10^{-6}$ Torr, a film is again hardly detectable on the substrate after deposition. The plume in 120 mTorr Ar atmosphere from a stoichiometric MgB_2 target is shown in Fig. 3-1. With a better base vacuum below $9x10^{-8}$ Torr, the plume is bluish, whilst for a worse base vacuum of $7x10^{-7}$ Torr, the plume is greenish.

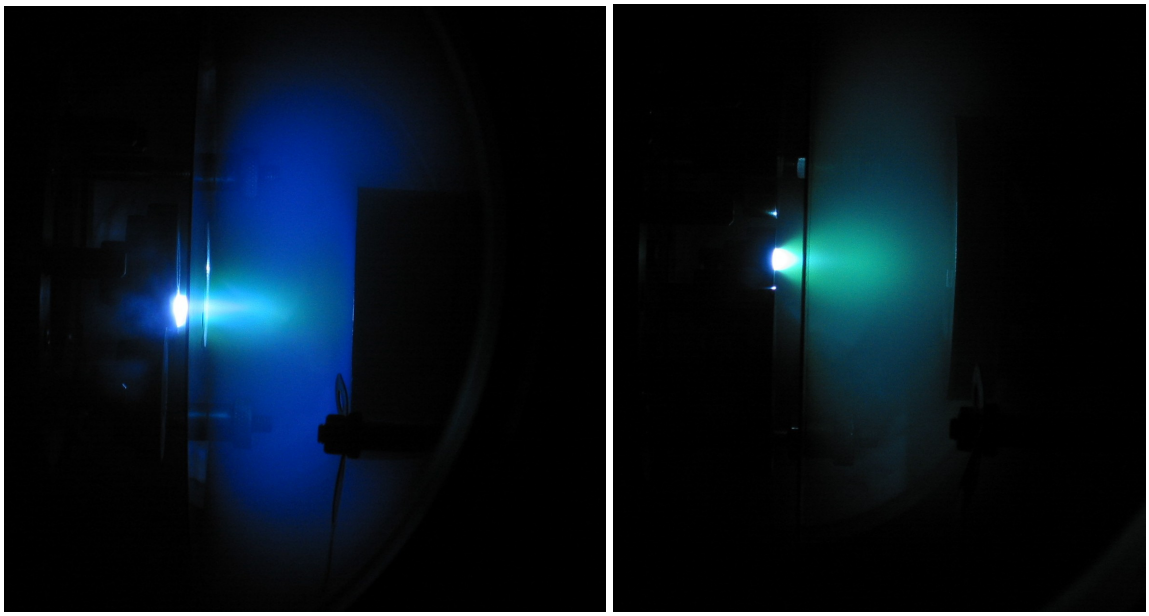

Fig. 3-1 The plumes from a stoichiometric MgB_2 target in a 120 mTorr argon background gas. On the left the base vacuum was $9x10^{-8}$ Torr, and on the right $7x10^{-7}$ Tor. The laser energy was 350 mJ/pulse.

Fig. 3-2 shows the laser plumes with different Ar deposition pressures. As can be seen clearly, the outskirt of the plume becomes bright bluish from pale greenish with the increasing argon pressure from $1x10^{-6}$ Torr to 290 mTorr. The length of the plume becomes larger up to the deposition pressure of 200mTorr and then it decrease with the further increase of Ar pressure. Figure 3-3 shows a laser plume at the optimum deposition pressure of 120 mTorr, using a laser fluence of 350 mJ/pulse, and a Target-substrate distance of 23 mm.

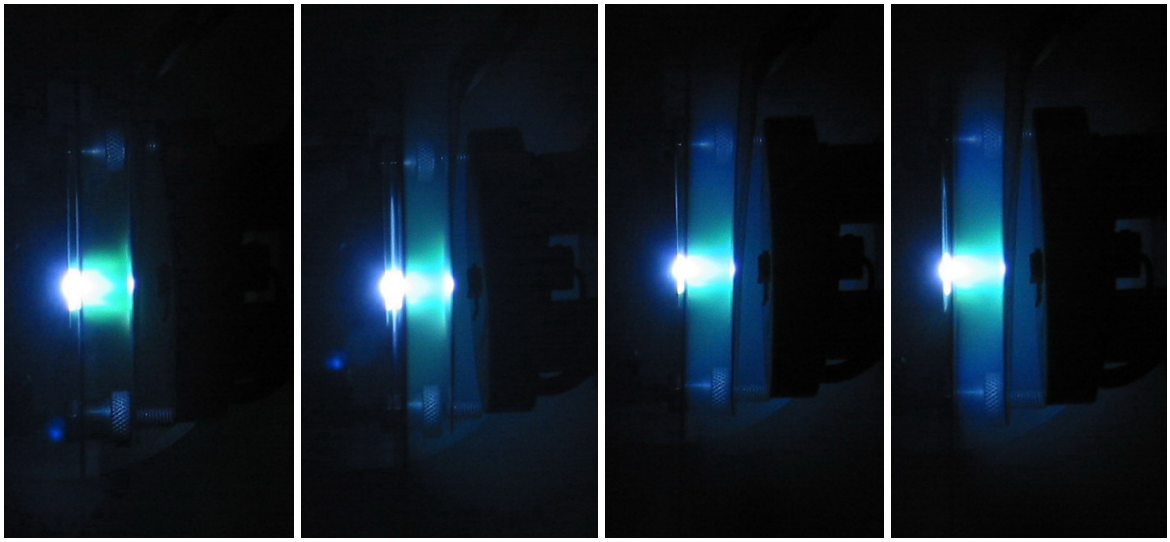

a b c d

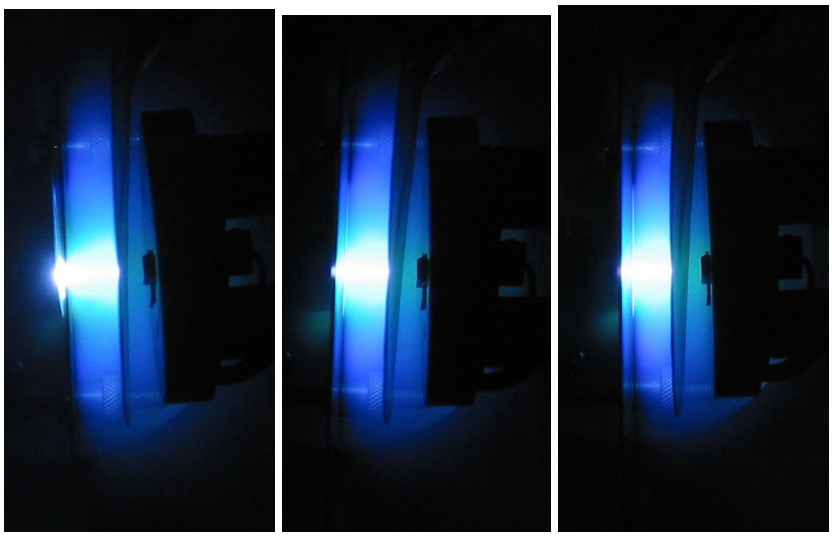

e f g

Fig.3-2 Laser plumes at different Ar pressures. a) 1x10^{-6}Torr; b) 80mTorr; c) 100mTorr; d) 120mTorr; e) 200mTorr; f) 260mTorr; g) 290 mTorr. The laser fluence was 350mJ/Pulse.

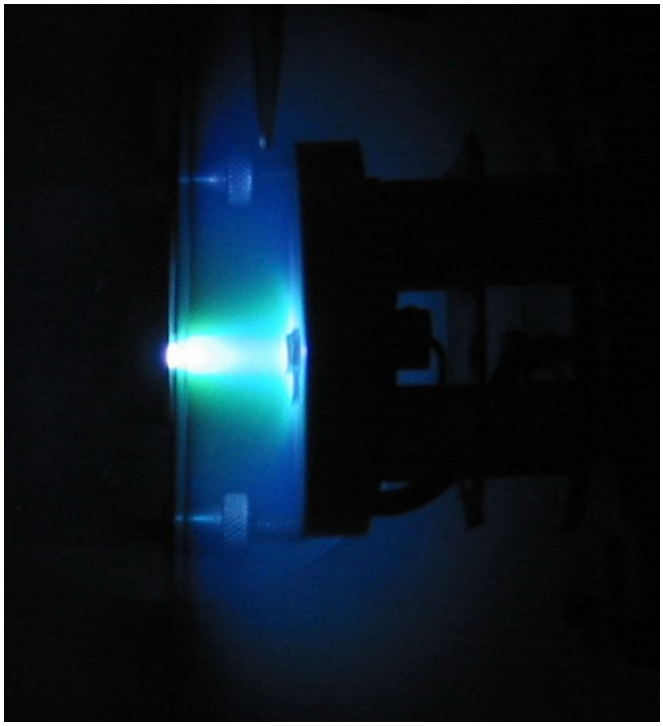

Fig.3-3 The laser plume of MgB_2 on-axis deposition. The argon pressure was 120mTor, the laser fluence was 350mJ and the target-substrate distance was 23mm.

The background gas is of great importance for the dynamics of the ablated species during the laser deposition and the evaporation of Mg during the annealing process. The interactions between the background gas and the ablated species for PLD have been intensively studied for the deposition of a number of materials [10-12]. Since the excitation state and the kinetic energy of an impinging atom strongly influence the process of thin films formation, the mechanisms that we have observed can be important for the control of MgB_2 film growth. In fact, energetic particles can cause re-sputtering of the film, largely influencing the growing film stoichiometry, especially for the most volatile elements, like Mg in MgB_2. Thus, while the slowing down effect of the ambient gas contributes to reduce the release of Mg from the deposit, the arrival of a larger extent of excited/ionised species on the growing films could enhance surface atomic mobility and favour films growth at lower substrate temperatures, due

to an increase of the thermal energy released in the impact region. Moreover, due to the distance-released pressure threshold nature of the shock wave effect, this behaviour will occur at larger distances from target for lower Ar buffer gas pressure, as a function of the target-to-substrate distance, which optimises the amount of plume atoms arriving on the substrate with a higher degree of internal excitation energy and a lower kinetic energy[10].

Since a minimum number of collisions must occur between the ejected species and the ambient gas atoms for a shock wave to develop [13], and considering that the particles mean-free-path is inversely proportional to the ambient gas pressure, an approximately inverse proportionality is expected for the distance-related pressure threshold for shock wave formation. This observation is in accordance with the experimental findings [6], where deposition of as-grown MgB_2 superconducting films was successfully obtained only by increasing the Ar gas pressure to a few tens of mTorr with a target-substrate distance of ~15mm. Moreover, in such experimental condition a blue plume was formed in agreement with Amoruso's results that the onset of shock waves lead to the experimentally observed change of the plume visible emission from green to blue[10].

When the chamber is well sealed and pumped for a long time at the baking temperature of 95°C, the main impurity in the argon filled atmosphere is water vapour and hydrogen. Fig. 3-4 shows the spectrum from a residual gas analyser mass spectrometer, at the pressure of $1x10^{-3}$ Torr argon filled atmosphere of our 52L spherical deposition chamber. The ion current for H_2O is about two orders smaller than the Ar ion current. Due to the present of water vapour in the atmosphere, a considerable amount of MgO phase is detected in the annealed MgB_2 film. As a

evidence, we found oxygen peaks in the EDS spectra of the final films and MgO diffraction rings in the TEM SAED pattern.

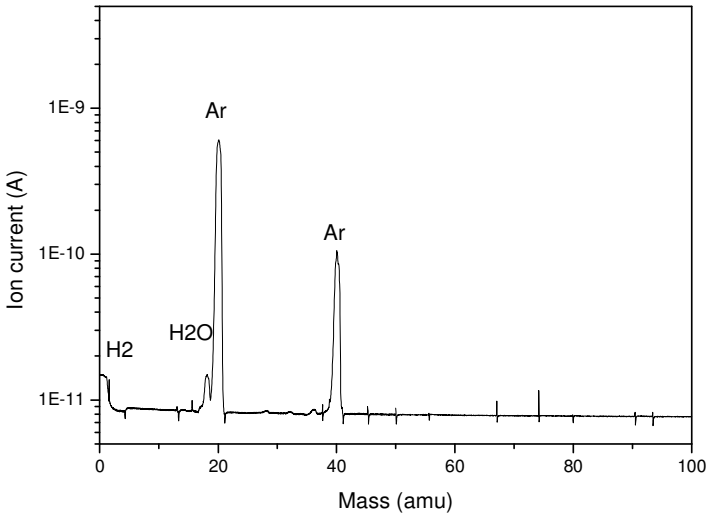

Fig.3-4 The MS spectrum of Ar atmosphere for the chamber at the total pressure of $1x10^{-3}$ Torr. Two argon peaks are present at 40 and 20 amu. The H_2O peak is at 18 amu, and the H_2 peak is at 2 amu.

We noticed that the pressure of the argon atmosphere during annealing could also be crucial to the superconducting properties of the MgB_2 films. A 760 Torr background gas pressure is necessary to obtain superconducting films, and the films annealed with at a lower Ar pressure of ~120mTorr were non-superconducting. This may be explained by the strong scattering effect of the high background gas pressure, which is beneficial to keep a high local Mg vapour pressure near the surface of the MgB_2 film, preventing the decomposition.

3.2 The influence of annealing temperature and heating rate on the T_c

Magnetic T_c measurements show that there is a quite narrow temperature window for *in situ* annealing of MgB_2 films (Fig. 3-5). The films shown in Fig. 3-5 were rapidly heated (110℃/min) during annealing. The thicker films (~1μm) have higher T_c than the thinner films (~0.5μm), which we believe is due to the fact that the surface Mg loss

is less severe in the thicker film than that in the thinner film. The $T_{c\ onset}$ increased when the annealing temperature rose from ~640℃ to ~700℃, whereas the films became non-superconducting if annealing temperature was raised further. The highest $T_{c\ onset}$ for the thicker films is 29.6K (annealed at 720℃, 1min), and the highest $T_{c\ onset}$ for the thinner film is 27K (annealed at 690℃, 1min). We also noticed that the $T_{c\ offset}$ (the temperature at which the transition is finished) is high with the annealing temperature of 670°C, which means the superconducting phase is more homogeneous at that annealing temperature.

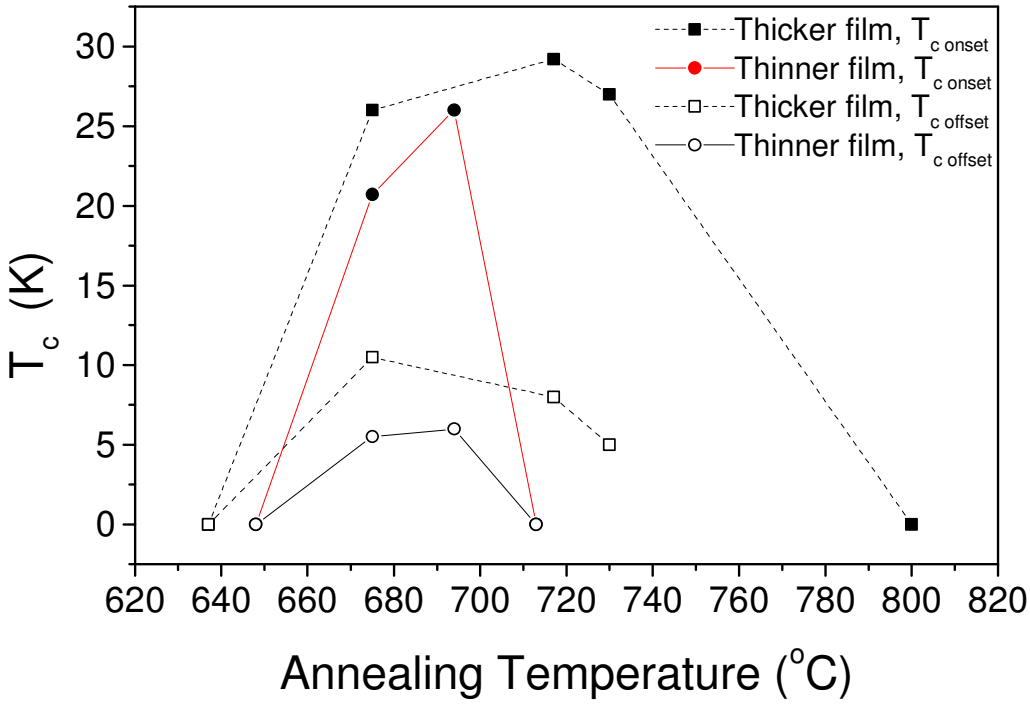

Fig. 3-5. T_c dependence on in situ annealing temperatures. The T_c was measured by DC susceptibility in ZFC. The thickness of the thicker films is ~1μm; The thickness of the thinner films is ~0.5μm. The heating rate of both groups of films was ~110℃/min (rapid heating) with a 1 min dwell time, followed by a free cooling at 50℃/min (the power is switched off).

We examined the influence of the heating rate on T_c of the thinner films at an annealing temperature between 680~690℃. As shown in Fig. 3-6, the $T_{c\ onset}$ of the film with slow heating (63℃/min) is 17K, lower than that of the rapid-heated (110℃/min) one. At a heating rate of 38℃/min, the $T_{c\text{-}onset}$ increases to 27K, and the $T_{c\ offset}$ increases to 8K. By further decreasing the heating rate to 25℃/min, the T_c of the produced film drops to 20K. A relatively slow heating rate of about 38℃/min seems to be beneficial to obtain high $T_{c\ onset}$ and a narrower transition width. A difficulty of T_c comparison between rapid heated annealing and slow heated annealing is that the temperature lag between the thermocouple and the sample may change with different heating rate. The temperature calibration reveals that the position for the controlling thermocouple is changing its temperature more slowly than the sample position. At very high heating rates, the sample temperature could be about 20℃ higher than the detected value from the thermocouple, whereas the difference is much smaller (<5℃) at lower heating rates such as 38℃/min. So the reason for a lower $T_{c\ onset}$ between the heating rates of 110℃/min and 63℃/min may be that the rapidly heated film actually withstood a higher peak temperature. The short ramp time is not favourable for the phase forming of MgB_2. However, if the heating rate is too slow, the evaporation of Mg at high temperatures could take away too much Mg and result in Mg deficiency.

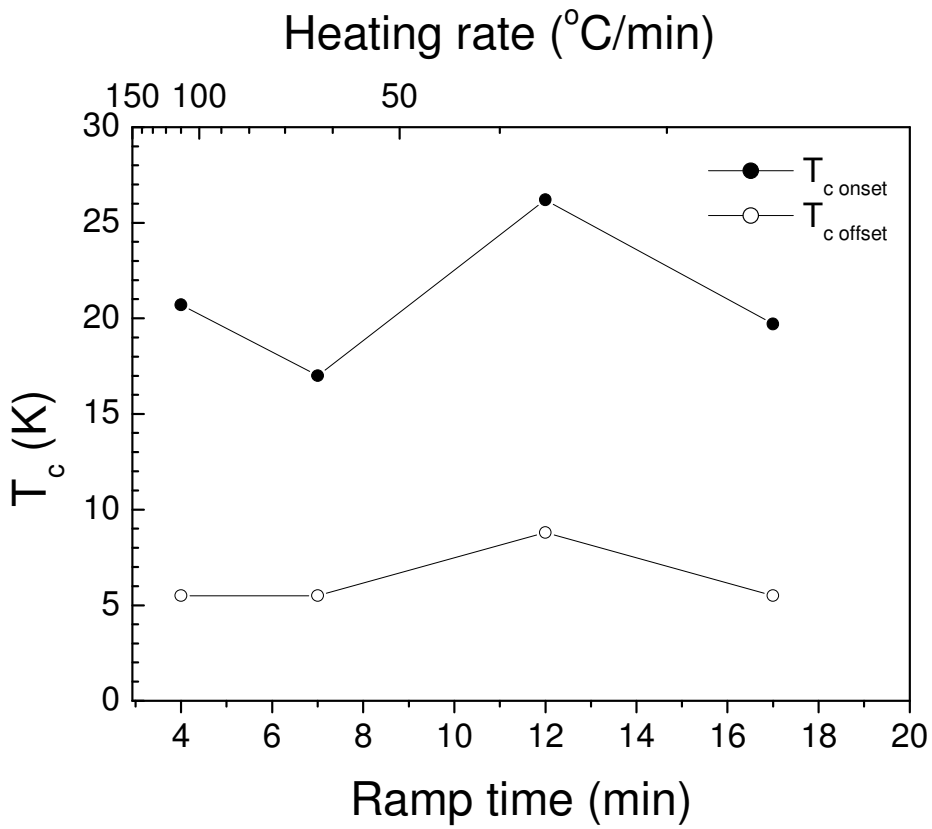

Fig. 3-6 T_c values of MgB_2 films versus in situ annealing ramp time (bottom axis) and heating rate (top axis). The annealing temperature is ~680 ℃ with 1min dwell time.

A longer annealing time, 10 min at 640℃ and 800℃ with rapid heating, was also attempted. However, the films were not superconducting. A probable reason could be that the magnesium cap layer was not enough to compensate the Mg loss. The 3 min magnesium deposition provides a cap layer of 800nm thickness. We also carried out 15min depositions to deposit thicker cap layers, but still could not get a superconducting film by 10 min annealing, which indicates Mg evaporation at temperatures above 640°C is too rapid for a long-period MgB_2 phase formation.

Based on the results described above, we consider that the optimal *in situ* annealing conditions for ~0.5μm film from stoichiometric MgB_2 target are to heat the

films at a rate of ~38℃/min to 680~690°C and hold the temperature for 1min, followed by free cooling down to room temperature at about 50°C/min.

3.3 The laser energy and the target and substrate distance

With the optimised annealing conditions for deposition pressure and annealing temperature discussed in last section, we have studied the influence of the laser energy and the target-substrate distance. Ideally, the energy of the species arriving at the surface of the substrate should be such as to favour their retention on the substrate, plus some extra spare energy to allow for diffusion on the surface of the substrate and the growing film. As the kinetic energy of the ejected species is a function of the laser beam energy, the proper adjustment of it is crucial for the film growth. The guiding rule-of-thumb for adjusting the laser beam energy was to increase it until the length of the visible plume was matching the target-substrate distance. This principle is an effective and simple way to make sure that the ejected species have suitable low kinetic energies and high level of excitation to favour a better crystallization of the growing film.

Figure 3-7 shows the T_c of the three samples listed in Table 3-1 by DC susceptibility in ZFC mode. It is clear that with a shorter target-substrate distance, the superconducting transition is sharper, which may indicate a better MgB_2 phase homogeneity in the short target-substrate distance case. A comparison of different laser energy flow and substrate-target distance is listed in Table 3-1.

The possible mechanisms that lead to a slightly higher critical temperature and a narrower transition zone in films of shorter target-substrate distances could be the fact that a shorter target-substrate distance means less collision between the ejected species and the background gas atoms. We speculate that during the collisions, two kinds of effects may take place. One is the excitation and ionization of the ejected species and

another is the inclusion of impurity atoms from the background atmosphere into the plume.

Table 3-1 T_c values of MgB_2 films versus laser energy and target-substrate distance, D_{T-S}.

Laser energy	500 mJ/pulse	420 mJ/pulse	300 mJ/pulse
D_{T-S}	40 mm	30 mm	20 mm
$T_{c\ onset}$	28 K	29 K	30 K
ΔT_c	~17K	~10 K	~5 K

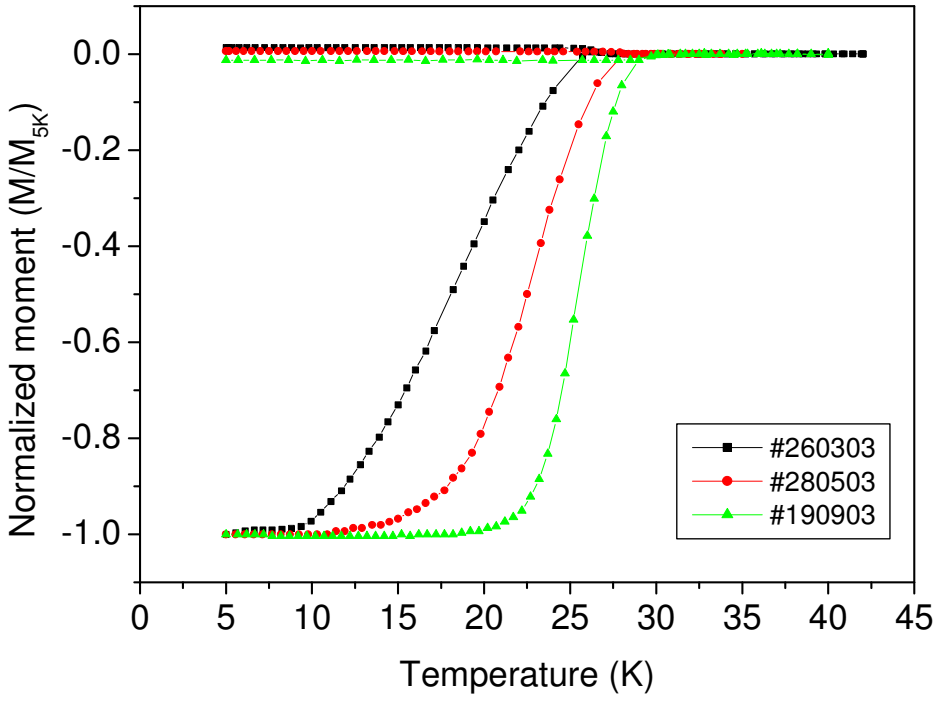

Fig. 3-7 The DC susceptibility (ZFC-FC) curves for three different target-substrate distances. Sample #260303 was prepared with 500 mJ/pulse laser energy and 40mm target-substrate distance; the #280503 was prepared with 400 mJ/pulse laser energy and 30mm target-substrate distance; and the #190903 was prepared with 300 mJ/pulse laser energy and 20mm target-substrate distance. All three films have a similar thickness of about 300-400 nm.

According to Amoruso et al. [10], just a few millimetres away from the target surface, a shock wave could be generated after the ablation of MgB_2 in around 150mTorr argon ambient gas. After the shock wave is formed, the population of ionized species decrease with the distance [13]. We assume that a large population of excited species arriving the substrate surface will favour the bonding between boron and magnesium atoms, which is important for the phase formation and crystallization of MgB_2 in the following *in situ* annealing process.

The inclusion of impurity atoms from the background atmosphere into the plume could be a function of the length of the plume. The longer the plume, the greater the interface between the plume and the background gas present in the deposition chamber, which could favour an increase probability for impurity atoms to be included into the plume. Once included into the plume, the impurity atoms like oxygen or carbon will be carried onto the surface of the growing film. As the result, the target-substrate distance could be a critical factor for the level of impurity present in the forming MgB_2 film. It has been revealed that carbon can take the boron place in MgB_2 lattice[14,15], and aluminium can substitute for a large proportion of magnesium[16]. Although the experimental results for oxygen in MgB_2 lattice is rarely seen, it is possible that some level of oxygen could exist in MgB_2 phase in our *in situ* annealed films, due to the non-equilibrium nature of the fast annealing process. The impurities in the MgB_2 phase could lead to the decrease of T_c, as well as to the broadening of the superconducting transition.

3.4 The change of target surface morphology after laser ablation

During the ablation process, the interaction between the laser beam and the target results in structural modifications of the target. We observed a cone structure on the stoichiometric MgB_2 target surface after laser ablation. Initially, the surface of the

targets used in this work, were polished by 200 mesh sand paper before each deposition. During the deposition, the surface is gradually degraded and develops cones. Fig. 3-8 shows the surface of MgB_2 target after a 400mJ/pulse (5 J/cm^2) ablation at 10Hz for 5min. A ring of about 15 mm diameter is clearly visible on the MgB_2 target. In our case, the laser spot on the target was 7.5mm x 1.5 mm, and elliptical in shape. Within the ablated ring, each individual spot received about 100 laser pulses at 5J/cm^2. The middle of the ablated area contains big cones of about 50 μm, and small cones of about 20 μm in diameter near the edge. The cone structure is finer and more homogeneous on the margins of the ablated area. The shape of each cone is nearly cylindrical and has a sphere at the top, indicating melting during the ablation.

A similar cone structure has been observed in many other laser ablated materials, including YBCO superconductors [17]. The reason of the cone structure is yet not very clear. In many cases it was argued that the creation of the cones is linked to the preferential ablation due to impurities, or in other cases, due to the phenomena of laser induced surface structure observed in the case of ablating single crystal targets [17] .

The presence of cone structure raises a few problems for the PLD fabrication of MgB_2 films. One is the change of deposition rate. Since the deposition rate decreases after a cone structure is developed, the control of film thickness become complex. Another effect is the possible difference in target surface. The easy-to-be-vaporised component will be deficient at the surface layer, e.g. in YBCO the target is usually yttrium-rich. An MgB_2 target is easy to decompose preferentially during heating and form Mg vapors, with boron remaining behind.

Conceptional, stoichiometric ablation of complex targets is the essence of the PLD. However, when the amount of heat left in the target after each laser shot can build up,

and may lead to the target decomposition. If this is also the case when a MgB_2 target is ablated by laser, then we should anticipate a gradually decreased Mg content with the growth of the film. Figure 3-9 shows the EDS analysis results of the MgB_2 target before and after 248 nm laser ablation. After ablation, Mg content is decreased on target surface. The sphere on top of the cone structure suffered dramatic Mg lost, which is in consistence with its appearance that indicates a melting during the ablation.

To reduce the Mg deficiency at the top of a PLD MgB_2 film, it is beneficial to slightly displace the MgB_2 target during the deposition to keep M-B ratio constant in the resultant film. A Mg cap layer would also help to compensate the Mg deficiency in the film.

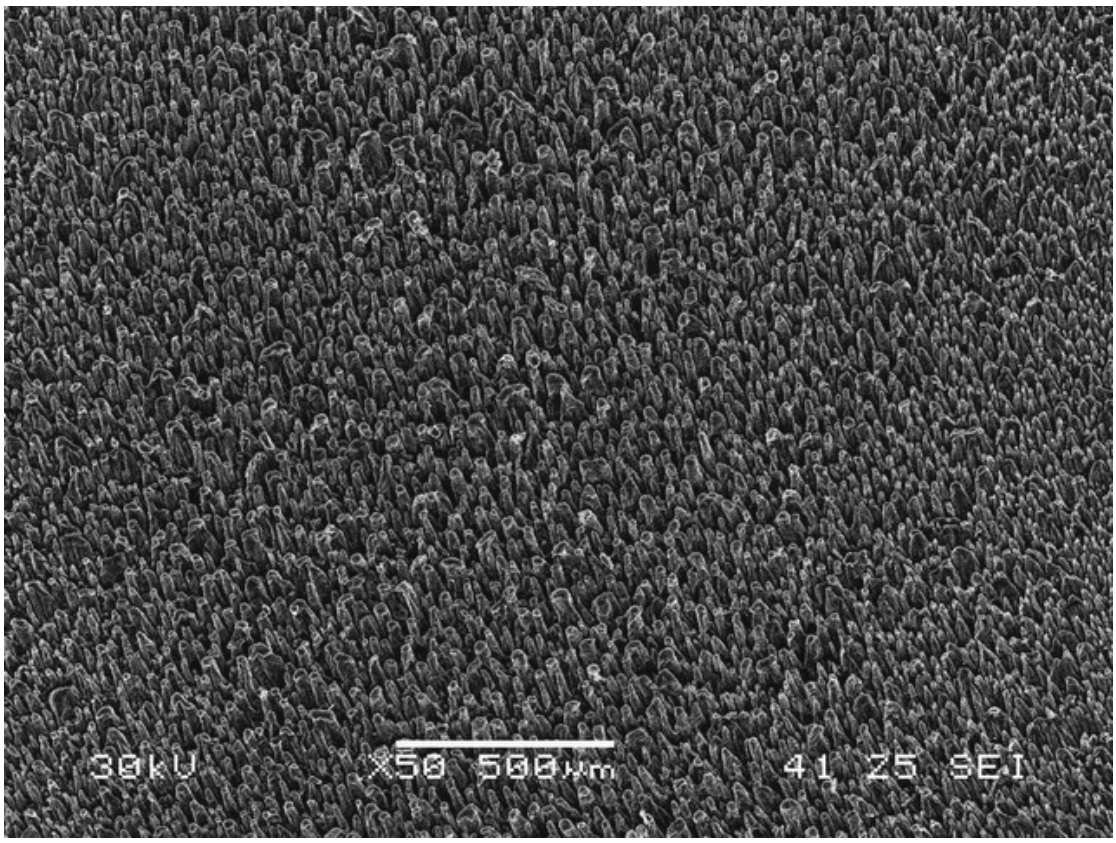

a

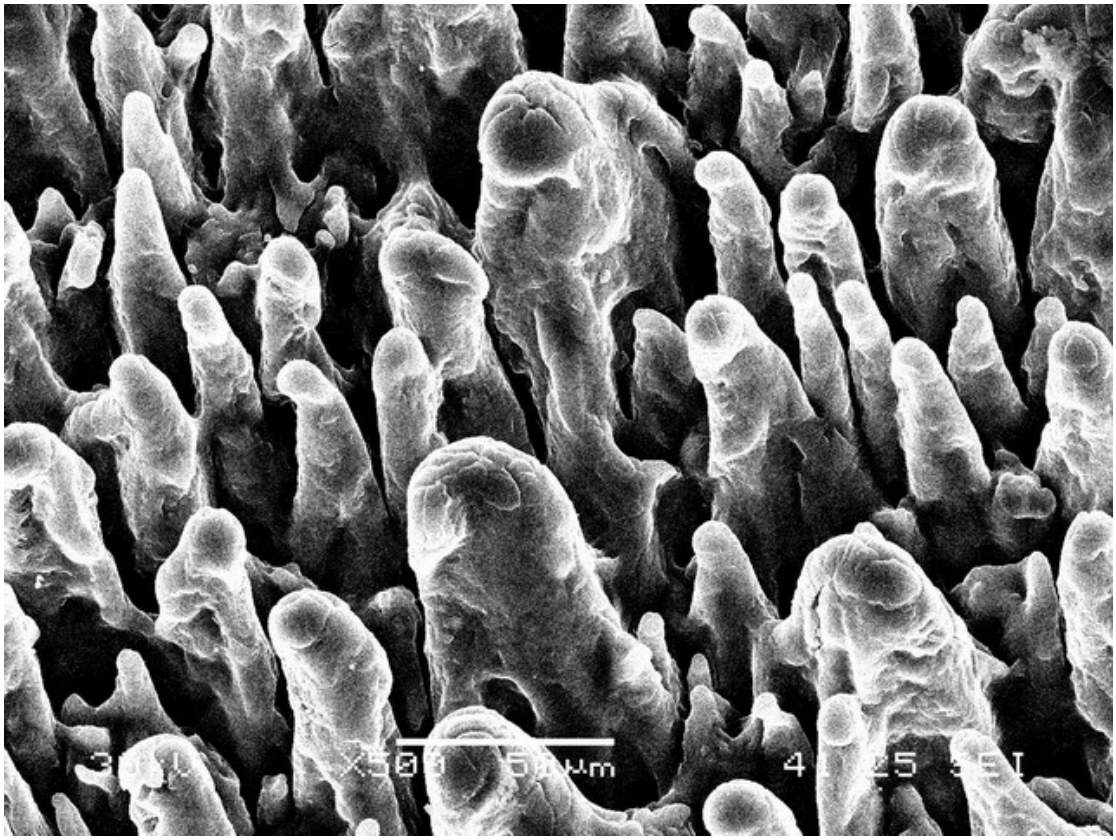

b

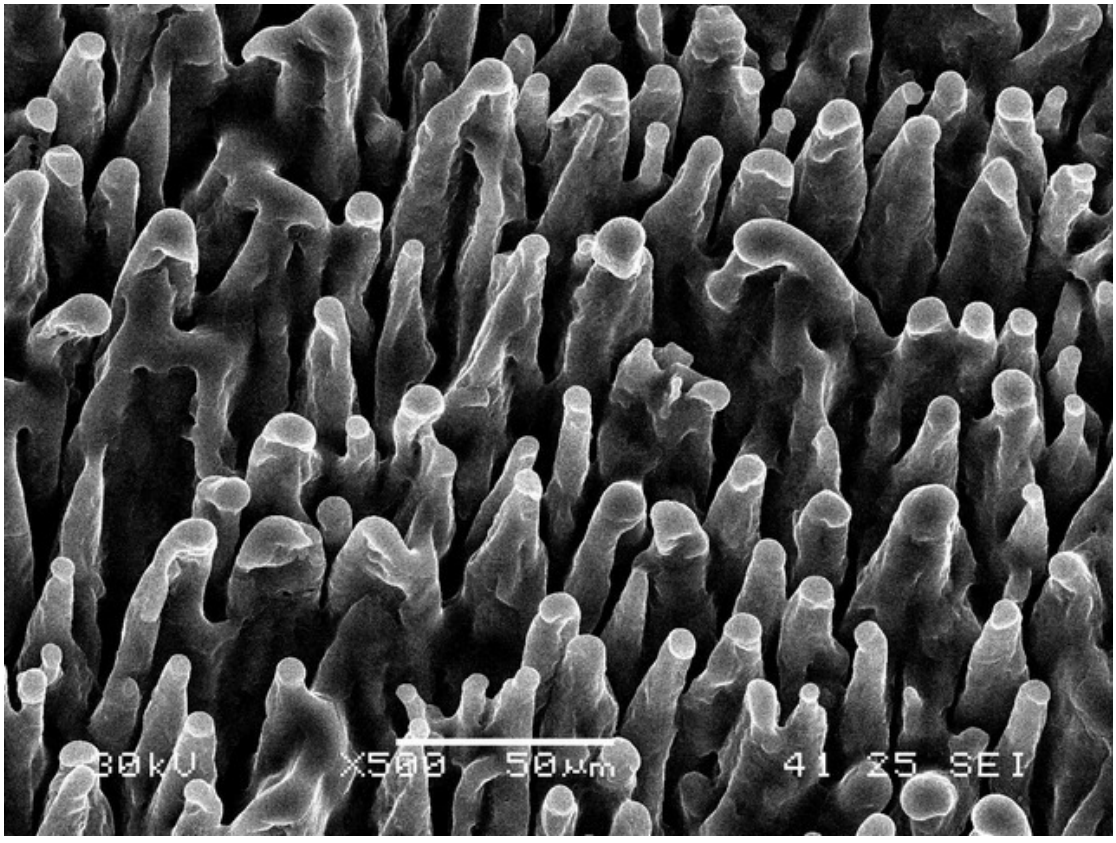

c

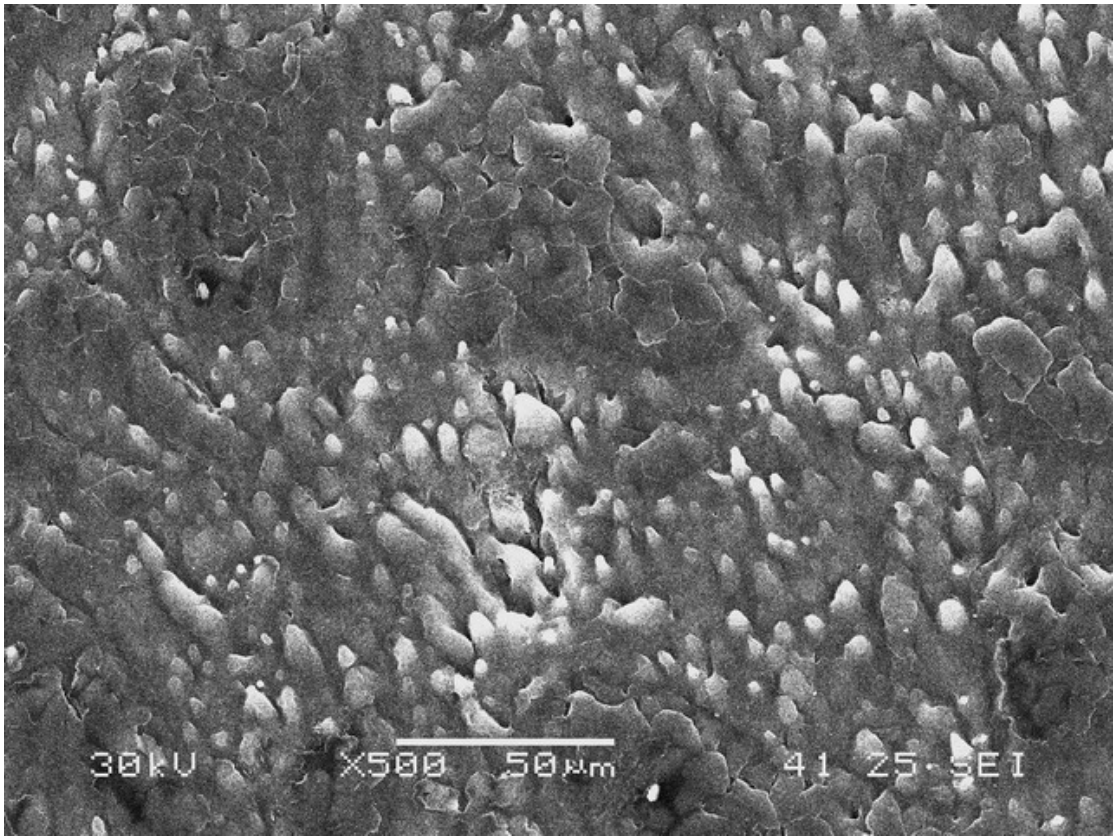

d

Fig. 3-8 SEM images of laser ablated MgB_2 target surface. a) A general look at the ablated ring under 50× magnification. b) Central part of the ablated ring ; c) The margins of the ablated ring . d) Area adjacent to the ablated ring . The magnification of images b, c and d is 500×.

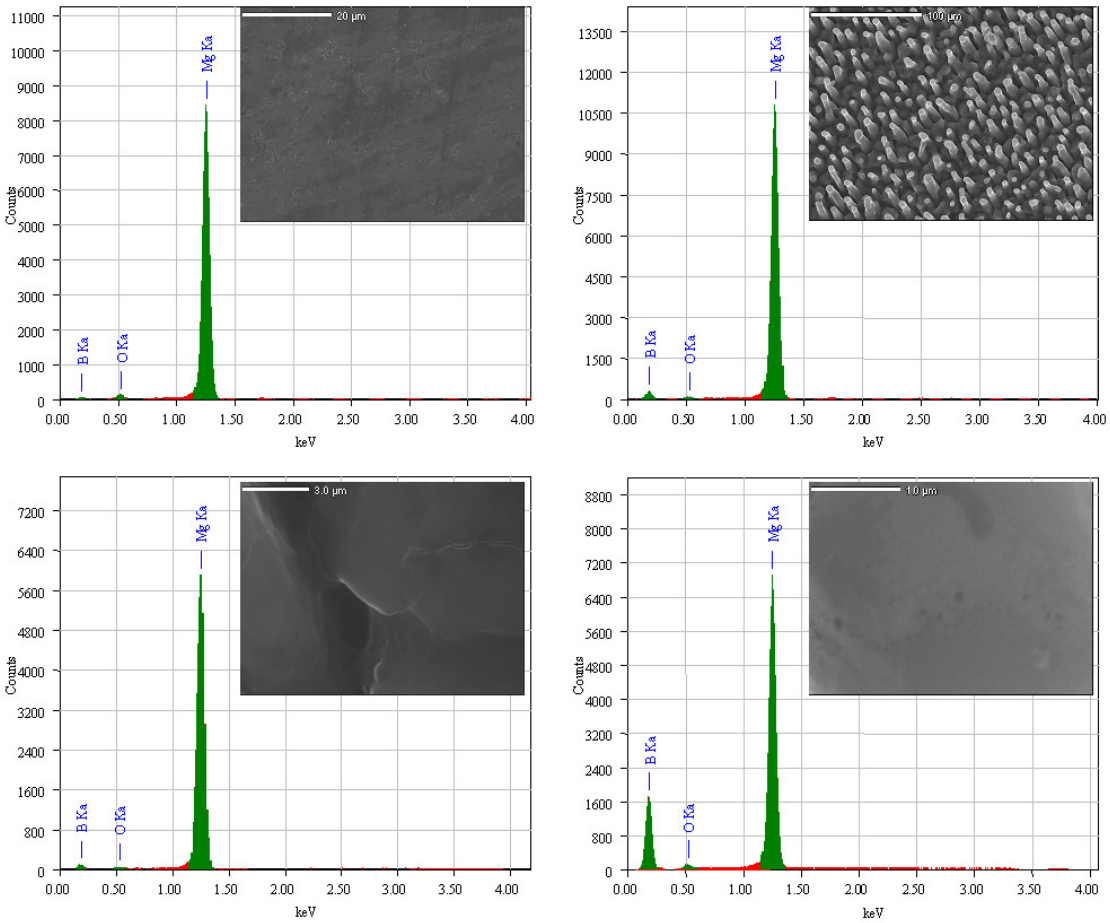

Fig.3-9 Area-scan EDS spectrum of the MgB_2 target before and after100 pulses, 5 J/cm^2, 248 nm laser ablation. a) before ablation, b) after ablation, c) on the base of the cones, d) on top of a cone. The inset figures are correlative SEM images of the EDS scanning area.

3.5 Microstructure of the *in situ* MgB_2 films

The surface topography of the films was observed by SEM and AFM. Fig.3-10 is the SEM cross-sectional image of a typical *in situ* annealed PLD MgB_2 film. It is obvious that the surface is very rough with densely packed droplets sized up to 1 µm. Other than this, the film matrix looks dense and homogeneous. The scan in Fig.3-11 shows more details of the film surface in 500x500 nm^2 range. Contrary to the *ex situ* annealed MgB_2 films [18], the surface topography does not show any crystallite with

regular facets. For purposes of application to electronic devices, a significant improvement of surface smoothness is very necessary.

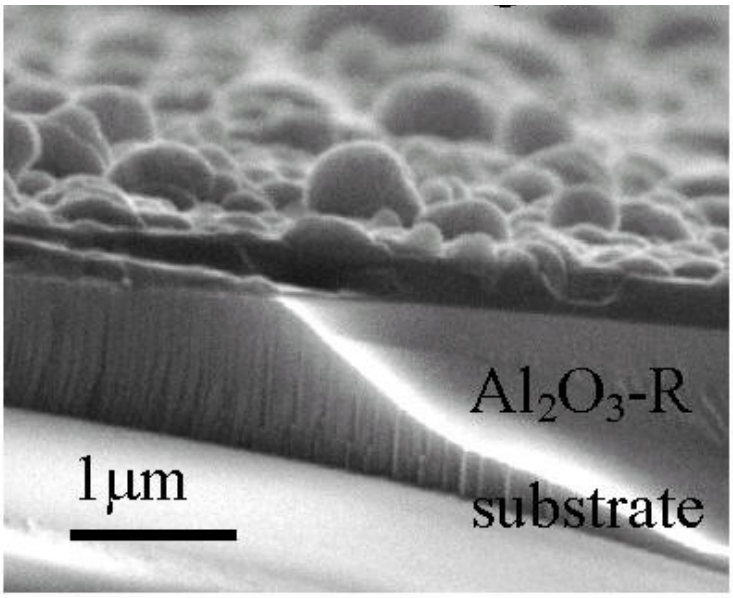

Fig.3-10 SEM cross-section image of the in situ MgB_2 film.

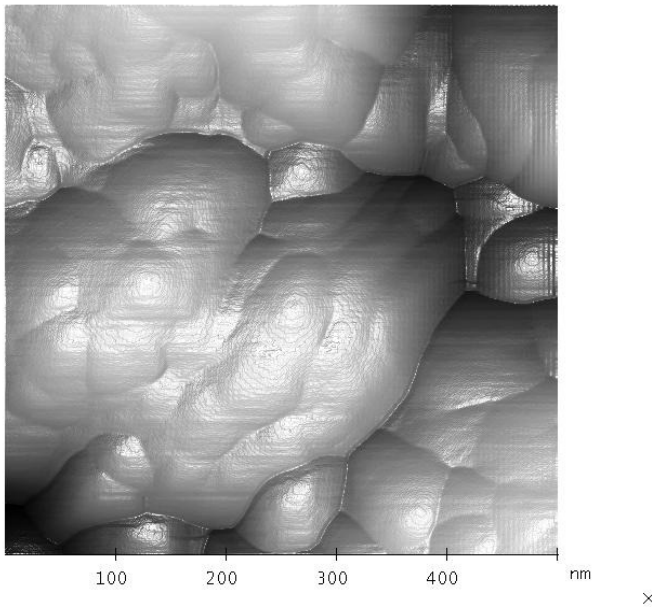

Fig.3-11 AFM 3D mode image of the MgB_2 film surface. Scale=500x500nm^2

Fig. 3-12 shows TEM and SAED pattern for the *in situ* MgB_2 film. A small-grain feature is clearly revealed by both the bright field (BF) image and the SAED ring patterns. The grain size is about 20-30nm judging from the BF image. Strong diffraction signal from MgO also appear in the SAED image, indicating a significant

amount of MgO phase exists in the film.

Considerable oxygen may be brought into the precursor due to magnesium's high reactivity with oxygen [1,19]. Upon a closer look at the SAED pattern in Fig.3-12, we find that the rings from MgO are constructed with distinguishable diffraction spots, while the rings from MgB_2 are more continuous. This indicates a generally larger grain size of MgO than that for MgB_2. These large MgO grains (>20nm), therefore, can barely contribute to the pinning enhancement in our *in situ* film due to their unfavorable size.

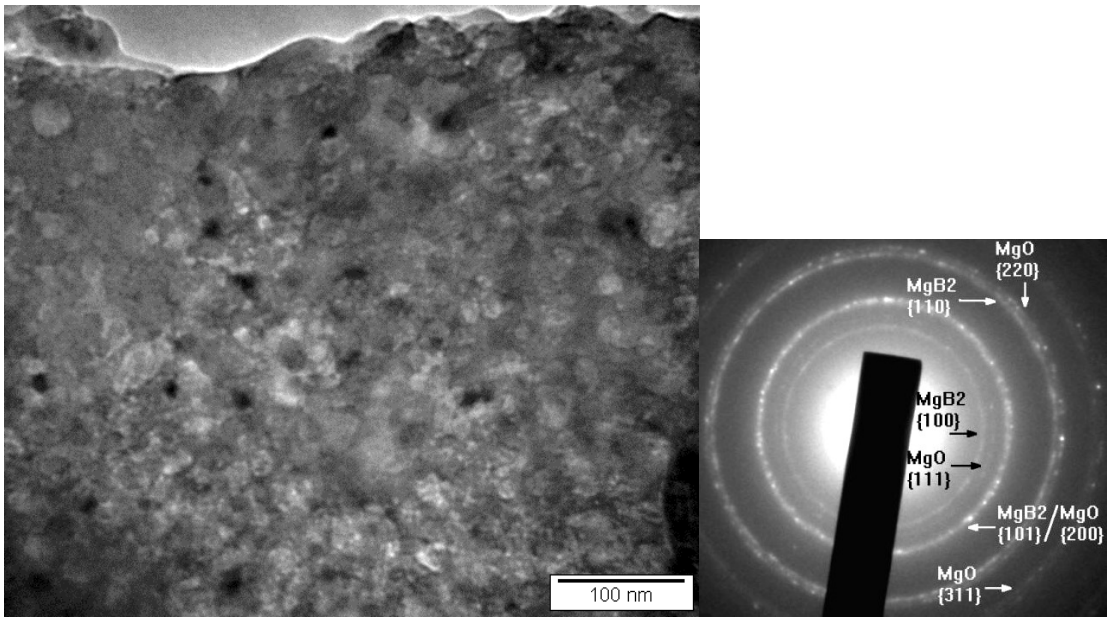

a b

Fig. 3-12 TEM bright field image of a planar specimen for the in situ MgB_2 film (a). b) is a SAD pattern from a circular 500 nm area of the film.

The XRD patterns of all the *in situ* annealed films did not show obvious peaks other than those from the Al_2O_3-R substrate. This indicates that the *in situ* annealed MgB_2 have poor crystallinity. Furthermore, the lack of crystalline orientation in the thin film may also contribute the absence of any MgB_2 peaks [20].

3.6 The Jc and flux penetration behaviour of the on-axis MgB_2 films

Figure. 3-13 shows the magneto-optical image of film #280503 at 20 K and 8.7 mT. The brighter the area is, the stronger is the flux density. The regular rooftop pattern of the magnetic flux distribution at 20 K revealed the homogeneity of current flow all over the film.

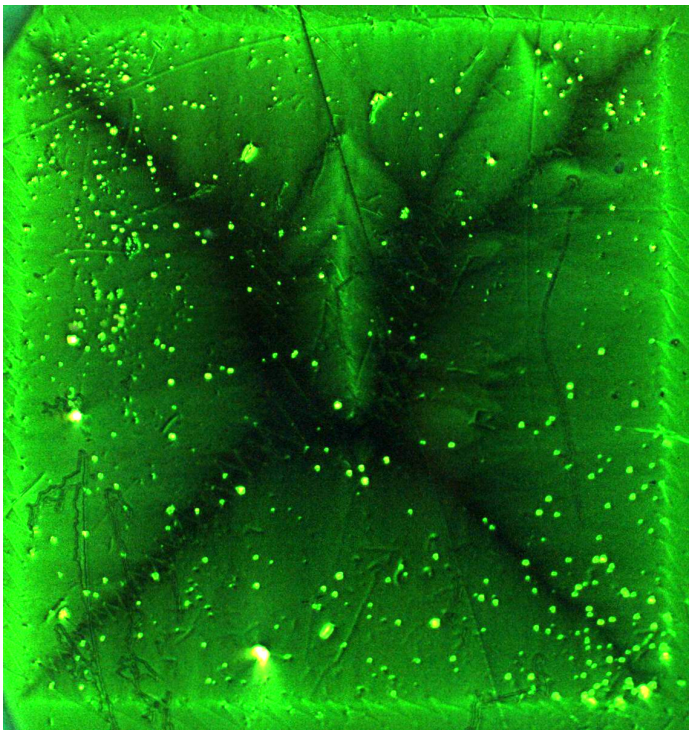

Fig.3-13. Magneto-optical image of the in situ MgB_2 film at B_a=8.7mT at 20K after zero field cooling. The film size is 3x3mm^2. The white round spots are defects in the MO indicator. The bright area in the upper middle part of the film is an enhanced flux penetration due to an accidental mechanical scratch on the MgB_2 film.

The flux penetration of the *in situ* MgB_2 film is governed by both external parameters such as temperature and applied field, as well as by the internal parameters such as grain size, defects, etc. For temperatures under about 10 K, abrupt avalanches can be observed in the film, as shown in Fig. 3-14. When the temperature was increased, we can notice a gradual flux penetration near the edge of the sample. When the temperature is higher than 7K, the gradual flux penetration becomes predominant. At low temperatures, the paths of each avalanche are totally non-reproducible for

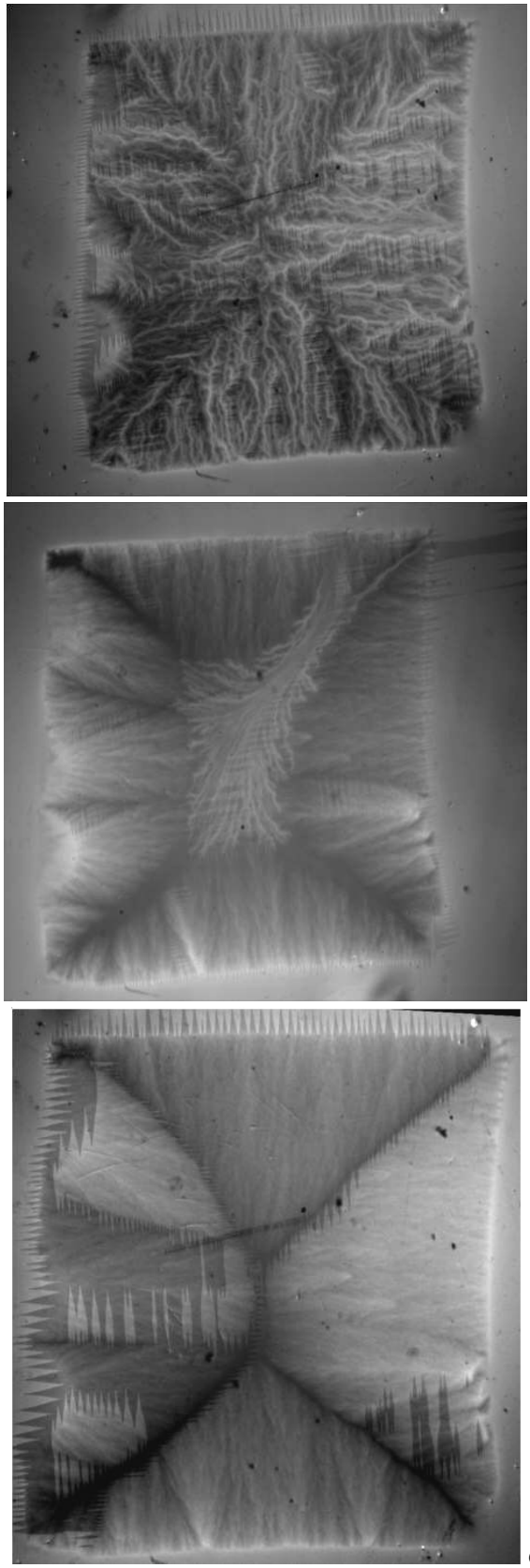

Fig. 3-14 MOI images of in situ annealed film 030703, showing the flux penetration as a function of temperature: (a) 4 K, (b) 7 K, (c) 10K. The applied field is about 10mT for the three sets of observations. The sample is ~3x3 mm^2 in dimentions.

different sets of measurements taken on the same sample. This behaviour is in accordance with some of the early reports on MOI of the MgB_2 thin films. However, Ye et al. [21] found that an ultra-pure MgB_2 film prepared by HPCVP does not show abrupt flux avalanche at temperatures down to 4.2K. As argued by Ye et al [21], the very low level of defects and clean grain boundaries could lead to a very low flux flow resistivity

$$\rho_f = \rho_n \mu_0 H_{c2}/B_a \quad (3\text{-}1)$$

which prevents the rapid development of flux avalanches. We attribute the flux jump in our film to the high level of defects and very fine grain-size. These characters will be revealed in the following microstructural study and could be the reason of very strong pinning found in our MgB_2 films.

The DC magnetization hysteresis loops of MgB2 film (#190903) is shown in fig. 3-15 (a) for different temperatures. The applied magnetic field was perpendicular to the film surface. Considering that in low fields the magnetic flux penetration in the film takes place homogeneously, as shown in magneto optical images in Fig 3-14, the standard expression of Bean model could be valid to obtain the critical current. J_c values were calculated from the ΔM-B_a curve using the simple expression [22],

$$J_c = 20\Delta M/[a(1-a/3b)]. \quad (3\text{-}2)$$

where a=0.5cm and b=0.25 cm are the length and width of the rectangular film, $\Delta M = \Delta m/V$ is the magnetization difference, Δm (emu) is the magnetic moment difference in the hysteretic loop, and $V=(0.5\text{x}0.25\text{cm}^2\text{x}(6\text{x}10^{-5}\text{cm})$ is the volume of the film. Although the model neglects the J_c difference within the sample, the result could provide an approximate J_c value of the thin film [1]. The J_c values are shown in Fig. 3-15 (b). At 5K, J_c value shows a weak field dependence and remain about $1\text{x}10^6$ A/cm^2 at 5 T. The J_c at 10 K and 15 K has a high value at zero field, but drops sharply with

the increase in the applied field. However, at $B_a \geqslant 0.2$ T, the J_c decreases much more slowly, indicating strong pinning at high fields.

The hysteresis loop at 5K exhibits a strong fluctuation region for fields lower than 0.2 T, while the loops at 10K, 15K and 20 K do not show such instability. These fluctuations have been linked to the abrupt flux penetration into the sample, which is called flux jump. Unlike the big flux jump in bulk MgB_2 superconductors, the flux jump in MgB_2 thin films is small and extremely frequent, as illustrated in figure 3-11 (c). Each individual flux jump could occur with only 15 Oe field change. This observation is in agreement with Zhao et al's report on small and dense flux jumps in MgB_2 films [23].

According to Zhao et al, the flux jump can be triggered when the gradient of magnetic flux profile inside the sample exceeds some critical value. After a very short time (usually in the order of ms [24]) the magnetic profile drops to a new configuration with a lower gradient, then the flux only creeps slowly until the gradient of magnetic flux profile induced by varying the external field exceeds the critical value again. In each jump many vortices are involved in the thermo-magnetic avalanche, which normally expands to a large part of the sample volume. In thin films, however, the situation is completely different: many small local avalanches occur (as shown in Fig 3-15(c)). Although the H-T region for flux jumps appear unchanged in different rounds of measurements for MgB_2 thin films under identical conditions, the specific positions and the magnitude of the small flux jumps are however completely unreproducible . All these cannot be explained by the adiabatic theory.

The different avalanches observed in bulk samples and thin films may be induced by the different structural details and thermal diffusibility within the sample [25]. For example, in bulk samples, there are many large grain boundaries, which act as strong

pinning centres. The gradient of the flux profile near these boundaries can be broken at a certain limit. Once a blast occurs in a bulk sample, the thermal energy induced by the drastic flux motion cannot easily diffuse out and be carried away within the local environment. Therefore this self-heating will lead to the increase of the region in which the vortex instability occurs leading to a large jump on the magnetization in a bulk superconductor [24]. One can also understand from this picture that the number of flux jumps cannot be large in bulk samples. In thin films the situation can be very different. On one hand the microstructural results (in section 3.5) indicate a high density of small defects formed during the preparation process of the thin films leading to much stronger critical current densities. Therefore there are many places for the avalanche to nucleate. On the other hand thermal diffusion is much easier in thin film samples due to their very small thickness and large surface area. Subsequently, in thin films each avalanche is small in magnitude but the number of avalanches can be very large. This picture may give an explanation to many small vortex avalanches observed in Nb-film [26] and the YBCO film [27]. The very fine disorder structure and the relatively better thermal diffusion in thin films are two key factors to be considered here as well.

The boundary point for small flux jump is defined as the clear kink point shown in the hysteresis loop. Above this field no flux jumps could be observed above the noise background of the instrument. This is very helpful to illustrate the field and temperature region in which the application of the MgB_2 film can be hampered by thermal instability.

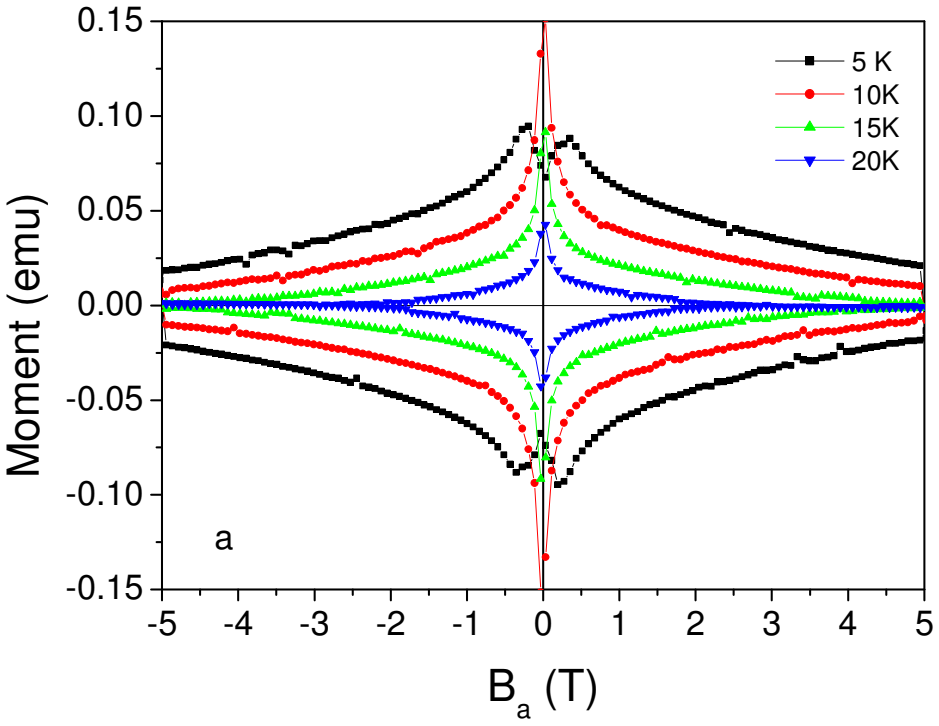
0.15
0.10
0.05
0.00
-0.05
-0.10
-0.15
Moment (emu)
5 K
10K
15K
20K
a
-5
-4
-3
-2
-1
0
1
2
3
4
5
B_a (T)

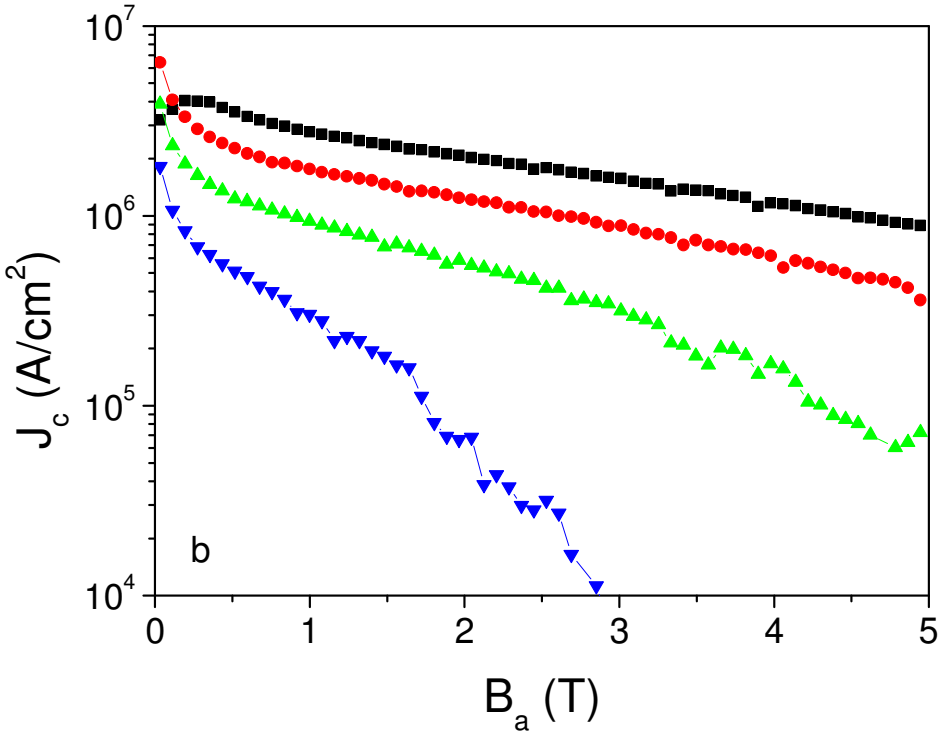
10^7
10^6
10^5
10^4
J_c (A/cm^2)
b
0
1
2
3
4
5
B_a (T)

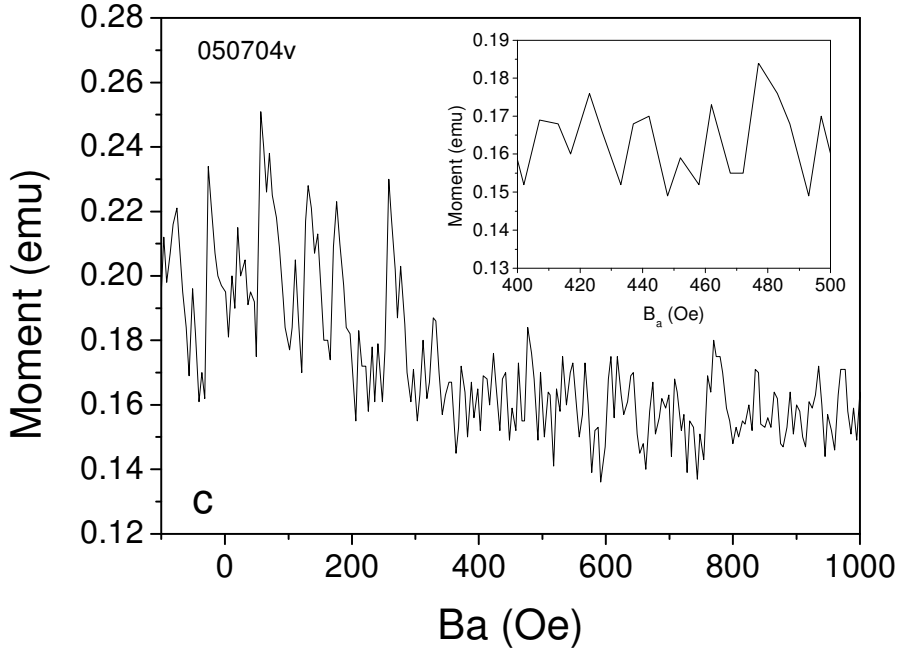

Fig. 3-15 (a) Hysteresis loops of DC magnetisation for our best on-axis in situ film 190903 at 5K(■), 10K(●), 15K(▲), and 20K(▼) respectively and (b) the calculated J_c of the in situ film from the magnetic hysteresis loops at 5K(■), 10K(●), 15K(▲), and 20K(▼) respectively. (c) detailed magnetization curves at 5 K within the field range of 1000 Oe (0.1 T) with very fine scan of 5 Oe resolution. The inset is a magnification of the curve between 400 Oe and 500 Oe.

From Fig. 3-15 we can see that the J_c performance of the *in situ* MgB_2 film remains reasonably good at temperatures up to 15K. The good performance in fields could render in situ MgB_2 films as a possible candidate in high field applications, e.g. magnetic resonance imaging (MRI), compact magnets, compact generators. However, the J_c drops too quickly with field at 20 K. 20 K is the temperature that new compact cryocoolor can be used and is usually considered a threshold for economic operation of superconductors. Since pinning force is significantly reduced at temperatures near T_c,

future efforts in raising the T_c of this type of in situ MgB2 films to 39K could improve the Jc performance at 20 K and open a gate for many commercial applications.

3.7 Transport measurement results

3.7.1 Resistivity dependence on temperature

The temperature dependence of resistivity of *in situ* MgB_2 film (#190903) is shown in figure 3-16. The transport T_c is 32 K, 2 K higher than the magnetically detected T_c shown in Fig. 3-7. The residual resistance ratio (RRR) is about 1.1 and the resistivity difference between 300K and 40K ($\Delta\rho_{40K\text{-}300K}$) is 19μΩcm for the *in situ* MgB_2 film. The residual resistivity at 40 K is about 100 μΩcm. This value is much higher than the reported resistivity value of around 1 μΩcm for single crystals [28].

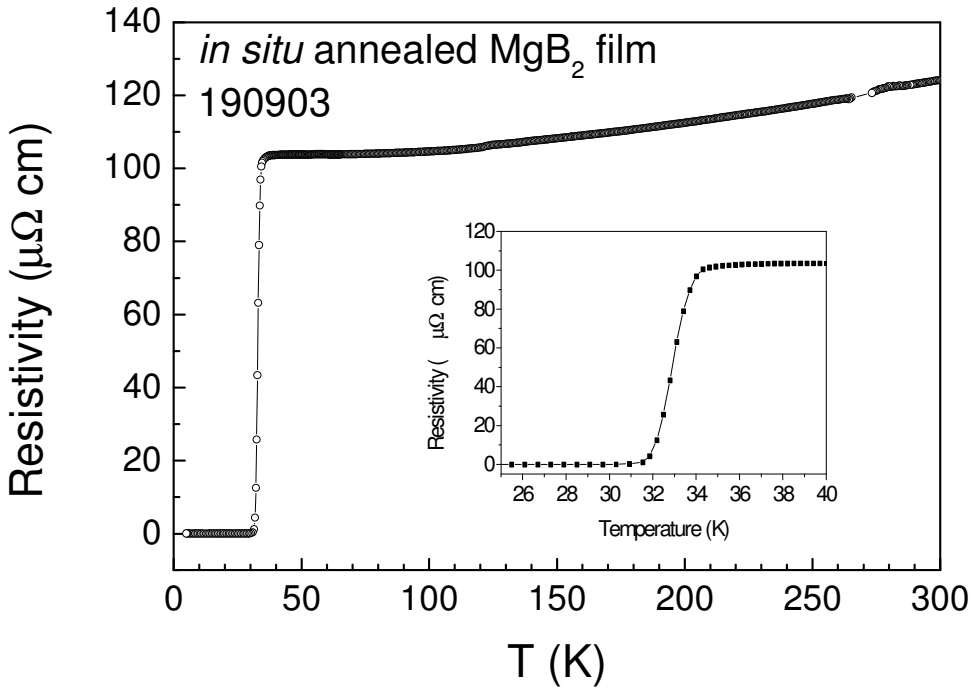

Fig.3-16 The resistivity versus temperature curve for a typical on-axis in situ MgB_2 film. The thickness of the film is 450 nm.

The resistivity is influenced by two categories of effects, the intergrain effects and the intragrain effects. The intergrain effects mainly include MgO or BO_x present along the grain boundaries, the porosity, Mg deficiency phases, e.g. MgB_4, and metallic Mg

in the MgB_2 sample. The TEM image of our MgB_2 film shows no pores. Significant MgO diffraction signals are present in the SAED pattern, as shown in Fig. 3-12(b). The MgO phases with considerable size could significantly reduce the effective current carrying area. Since MgB_4 or MgB_7 diffraction signals are not recognizable in the SAED image, we assume that Mg deficiency phase is not a main current blocking factor.

Rowell has made an in-depth review on the high resistivity among MgB_2 thin films [29,30]. It turns out that a comparison of resistivity data for a wide variety of samples, from single crystals to films, wires and polycrystalline bulk, is surprisingly informative. The majority of MgB_2 samples exhibit resistivity that is much higher than the low values that are seen in a relatively small number of single crystals, bulk samples and films. In many cases, the resistivity is increased over the single crystal values by orders of magnitude. Even at these high values, there is often still a metallic temperature dependence of the resistivity, and surprisingly, T_c is often at or near the bulk value of 39 K. The resistivity increase has been ascribed to a reduction in the effective current-carrying cross-sectional area of the sample. If this loss of cross-sectional area is the dominant factor contributing to the increase in resistivity of MgB_2 samples, then the critical current density must be decreased by the same loss in the effective area.

For intragrain effects, the fine grain structure, the possible intragrain MgB_xO_y precipitates and substitutional dopant atoms could contribute to the shortening of the electron mean free path (mfp) in MgB_2. Eltsev *et al* have reported that the in-plane mfp in MgB_2 is 24 nm at 40 K, and thus is about 4.5 nm at 300 K [28]. So a grain size that is smaller than 24 nm should increase the electron scattering and lead to a higher resistivity value. The grain size of our *in situ* MgB_2 film is generally 10-50 nm judging

from the TEM and AFM images. If any defect is present in the grains, the mfp would be shorter than 24 nm.

In the case that the reduction of effective current carrying area is the only effect that influence the resistivity, there will be a scaling up of the resistivity curves, i.e. the shape of the resistivity curve is exactly the same with that of the MgB_2 single crystal, only the resistivity value is multiplied by a factor that is reverse of the of the current carrying area reduction ratio. For single crystal MgB_2, the $\Delta\rho_{300\text{-}40K}$ is 4 μΩcm [28], while for our *in situ* MgB_2 film the $\Delta\rho_{300\text{-}40K}$ is 19 μΩcm. This probably indicates that the effective current carrying area is reduced by about 5-fold. The residual resistivity of single crystal MgB_2 film is 1 μΩcm, and the residual resistivity of our MgB_2 film should be 5 μΩcm without considering the intragrain effects. The experimental residual resistivity value of 100 μΩcm indicates that the intra grain scattering could be the dominating effect that increase the resistivity values of the MgB_2 film.

3.7.2 Irreversibility field, upper critical field, and flux flow activation energy

The field dependence of resistivity-temperature curves reveals a number of physical properties of superconductors. The resistivity curves of the *in situ* annealed MgB_2 film in perpendicular fields (H⊥film plane) of up to 8.7 Tesla is shown in fig. 3-17. One clear feature of the film is that it does not show any magnetic resistivity in high fields. Another feature is that the width of the flux flow regime in the curve is not changing much with the applied field, which indicates well-maintained flux pinning in high fields.

The irreversibility field and upper critical field are extracted from the ρ-T curves at 10% and 90% ρ_{Tc}. The irreversibility line and upper critical fields are plotted in Fig.3-18. A high H_{c2}-T slope of the H_{c2} curve, of about 1.0 T/K, is revealed. The high H_{c2} slope indicates strong scattering in the *in situ* MgB_2 film, which is in accordance with

fine grain structure shown in TEM study and possibly a high level of defects suggested by the high residual resistivity. For dirty MgB_2 samples, there is no significant H_{c2} saturation at low temperatures and the experimental H_{c2}-T curves are approximately linear [31,32]. Based on this observation, we extrapolate that $H_{c2}(0) \approx$ 36 T at 0 K, using a linear equation,

$$H_{c2}(0)=H'_{c2}T_c \quad (3\text{-}3)$$

where $H'_{c2}=|dH_{c2}/dT|$ near T_c. An estimation of the electron mean-free path l using the equations for superconductors in GL theory,

$$H_{c2}(T) = \Phi_0/(2\pi\xi^2) \quad (3\text{-}4)$$

and

$$\xi(T) = 0.855(\xi_0 l)^{1/2}/[1-T/T_c]^{1/2} \text{ (in the dirty limit)} \quad (3\text{-}5)$$

where Φ_0 is the flux quantum and ξ_0 taken as the single crystal coherence length of ~6.0 nm [28], gives $l \approx 2.3$ nm and $\xi \approx 3.1$ nm at zero temperature.

Although the activation energy of the thermally assisted flux flow (TAFF) for MgB_2 is significantly higher than that of HTS, TAFF is still detectable through the resistivity-temperature curves for different applied fields [33]. The activation energy U_0 of our MgB_2 and multilayer films is estimated by Arrhenius law [33-35],

$$\rho = \rho_0 \exp(-U_0 / k_B T) \quad (3\text{-}6)$$

where ρ_0 is a field-independent pre-exponential factor, and k_B is the Boltzmann's constant. Fig 3-19 shows the activation energy of flux creep versus applied field, B_a. The U_0 behaviour can be fit into the power law $U_0 \sim B^{-n}$. The blue line is a duplication of U_0 data from a bulk MgB_2 sample in ref [33]. It is clear that U_0 for our MgB_2 film drops much slower than MgB_2 bulk in high fields, which again indicates well-maintained pinning in high fields.

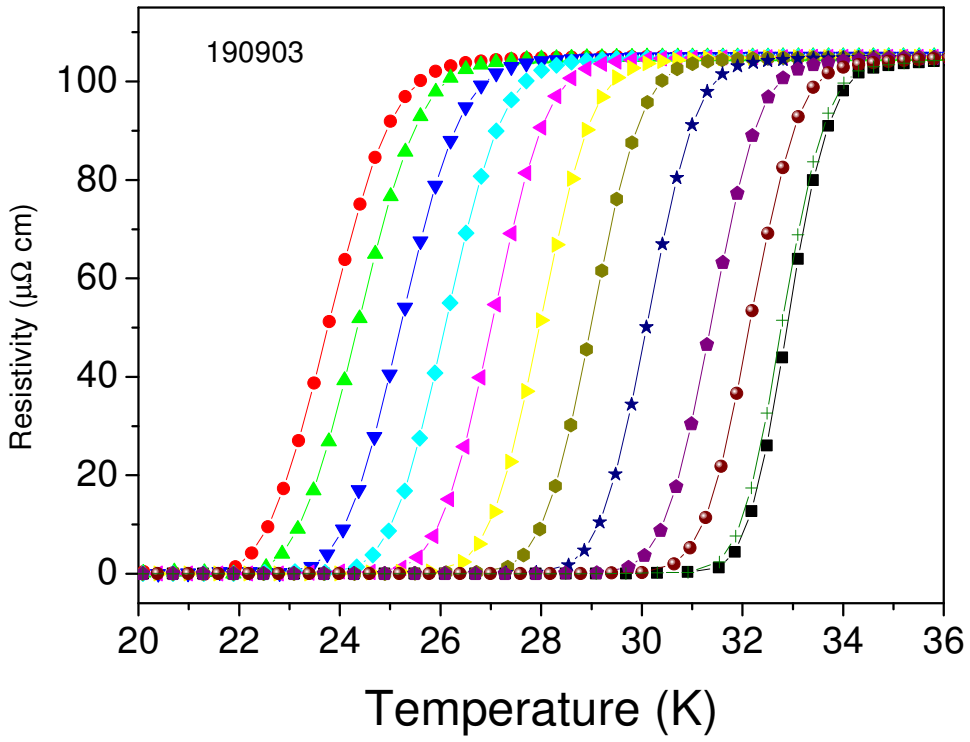

Fig. 3-17 Field dependence of resistivity-temperature curves. The applied field is (from right to left) 0T, 0.1T, 0.5T, 1T, 2T, 3T, 4T, 5T, 6T, 7T, 8T, and 8.7T respectively.

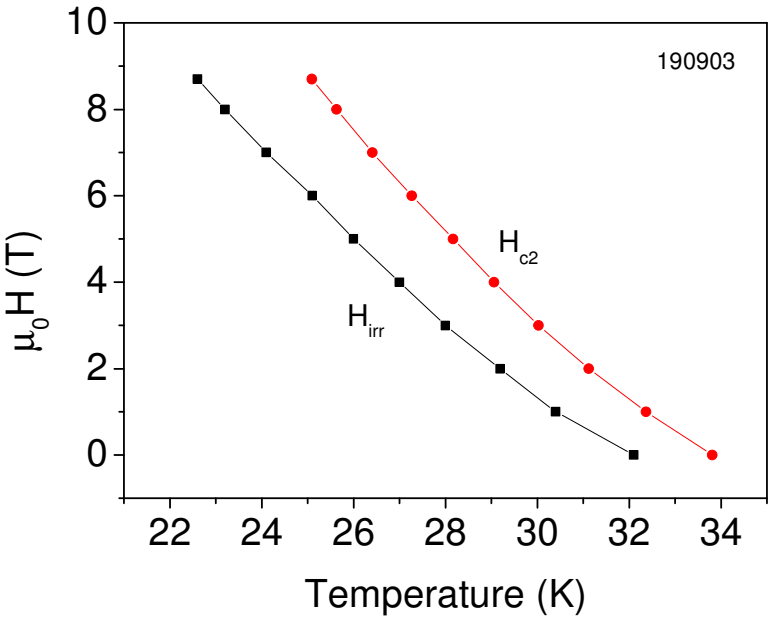

Fig. 3-18 Irreversibility field and upper critical field of the in situ MgB_2 film.

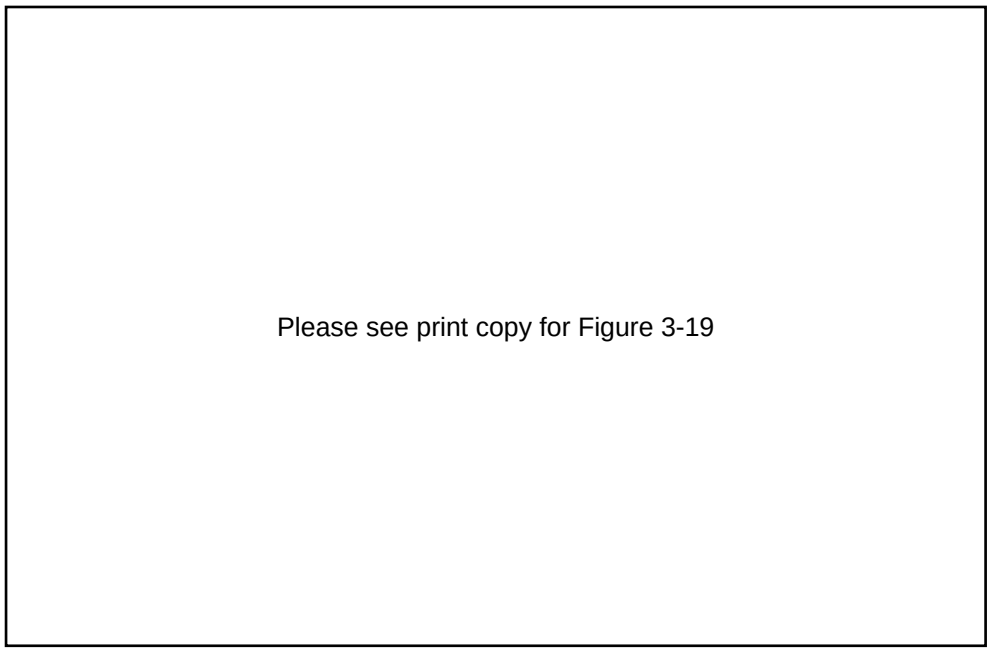

Fig. 3-19 Activation energy of the in situ MgB_2 film. The grey lines are U_0 data of bulk-MgB2 cited from ref [33].

3.8 Discussion on the reduction of T_c in the *in situ* MgB_2 films

Although the reason for the lower than the bulk $T_{c\ onset}$ and wide transition width of the films remains an open question, it seems that the T_c decrease is related to the annealing conditions. A common view on the decrease of T_c in MgB_2 films is that the magnesium is easily lost during deposition and *in situ* annealing. This could result in the formation of MgB_4, MgB_6, MgB_7, or MgB_{12} in the film [36]. Hinks et. al. have demonstrated that MgB_2 is a line compound in the phase diagram instead of a solid solution [37]. As the result, the formation of $Mg_{1-x}B_2$ is unlikely to be an explanation for the decrease in T_c. According to Saito and co-workers, Mg-deficient MgB_2 films do not present a T_c lower than that of the stoichiometric ones [5]. The result is consistent with Hinks' work, which also shows that the T_c value does not change significantly in

Mg-deficient MgB_2 bulks [37]. However, if too much magnesium in the films is lost during deposition and annealing, it is hard to form the MgB_2 phase in the first place, and the film will become non-superconducting. That is probably why we obtain non-superconducting films at higher annealing temperature or longer annealing times. Poor crystallization may also affect the T_c value of the MgB_2 film [5]. The mechanism nay be the lattice distortion due to a high level of disorder or amorphous structure in the films. The relatively low temperature and short annealing time of *in situ* annealing seem likely to result in poor crystallization of MgB_2 films and make the films with suppressed T_c or even non superconducting.

Impurities, like oxygen and carbon (from pump oil) in the MgB_2 lattice or MgO phase precipitated from the matrix, may also contribute to the decrease of the T_c value [1]. In the EDS spectrum of the as grown MgB_2 film show a significant oxygen peak as well as a small carbon peak, as shown in Fig. 3-19. Idrobo et al. [38] have observed $Mg_2B_3O_x$ phases in bulk MgB2 samples and predicted lower T_c values of 18.3 K and 1.6 K for Mg_2B_3O and $Mg_2B_3O_2$, respectively. Their calculation results can explain well the T_c suppression and transition broadening in oxygen-rich MgB_2 films.

The as-grown films in our experiments are not superconducting, but after a short post-deposition annealing at 640~730℃, the films became superconducting. This indicates that the formation of MgB_2 and some degree of crystallization occurs during the *in situ* annealing process.

Considering the extremely high temperature in the PLD plume, most of the species arriving at the substrate should be atoms or ions of magnesium and boron or B-rich compounds such as MgB_4 or MgB_7 instead of MgB_2 molecules. Due to the relatively low substrate temperature and high deposition rate, the mobility and diffusion of magnesium and boron atoms should be quite low, and the reaction forming MgB_2 can

be suppressed, as well as the crystallization. That is probably why no superconductivity was observed in the as grown films in our experiments.

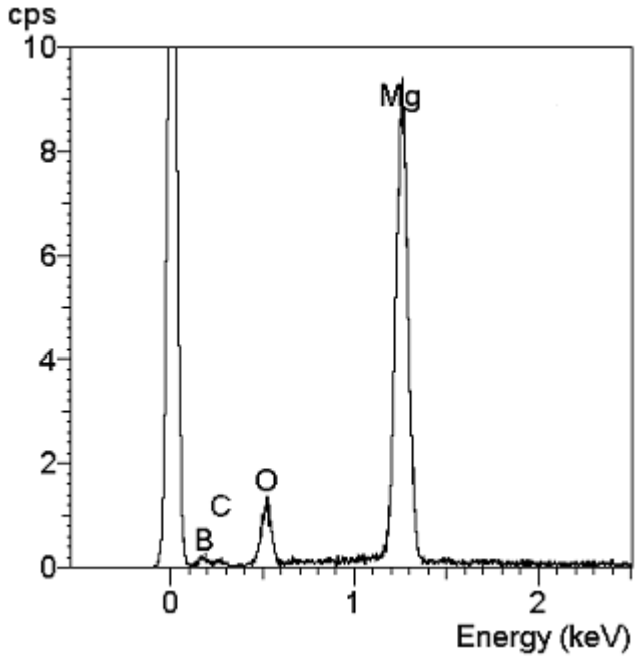

Fig. 3-20 EDS result of antypical in situ MgB_2 film with 30K magnetic T_c. In order to avoid the interaction with the Al_2O_3 substrate, a low electron beam energy of 5kV was used. The Al Kα signal at 1.5 keV is not noticeable in the spectrum.

When the annealing begins, the competition of two processes is supposed to be triggered. One process is the evaporation of magnesium in the film. The other process is the formation of MgB_2 phase. This competition is crucial for the selection of *in situ* annealing conditions. By keeping the magnesium in the films during annealing, the formation of MgB_2 phase is favoured. From the T_c change versus heating rate in Fig. 2, it appears that MgB_2 phase is better formed by keeping the MgB_2 film at a lower temperature for a longer time before heating it to a higher temperature.

To analyse the MgB_2 phase evolution in the film during annealing, it is necessary to refer to the MgB_2 phase diagram. The phase diagram of the magnesium-boron system has been studied by Liu et al using thermodynamic calculations [39]. Their

results showed that the magnesium vapour pressure determines the equilibrium solid phase in the Mg-B binary system. At ~700℃ the MgB_2 phase can remain at a magnesium vapour pressure higher than $1x10^{-2}$ Torr. If the magnesium vapour pressure is lower than this value, the equilibrium solid phase would change to MgB_4 or other compounds with a low magnesium content. This critical vapour pressure is, however, too high to be achieved inside a PLD chamber, even during the pulse of the plume. So, there is always a risk of losing too much magnesium during the *in situ* annealing process at ~700℃.

The magnesium cap layer can provide Mg vapour for a limited period at high temperature. According to observations, a 800nm-thick magnesium layer disappeared within <1 min when heated above 500℃. The free magnesium in the film, which has not reacted with boron, would also be evaporated at the annealing temperature of about 700℃. After the sources of magnesium are exhausted, the MgB_2 phase formed in the film begins to decompose. In our experiment, the films annealed at 800℃ were not superconducting, indicating that the MgB_2 phase decomposed significantly within 1 min at that temperature, even for the films with a thick magnesium cap layer. The exhausting of magnesium cap layer and decomposition of MgB_2 may also explain the T_c drop at very slow heating rate during annealing.

At low annealing temperatures, the problem is likely to be the poor Mg-B reactivity and poor crystallization of the film. The diffusion coefficients of Mg and B atoms are comparatively low at lower temperatures. According to our experiments, annealing at 650°C for 1min is not enough to form the MgB_2 phase. However, some groups obtained superconducting films by *in situ* annealing at 600℃ for just a few minutes or even seconds [9]. Probably the differences in microstructure and density of the precursor films resulted in the different annealing behaviour.

Another characteristic of the *in situ* MgB_2 films is their weak field dependence of J_c together with high H_{c2} values in low temperature as already illustrated in this chapter. We believe this is again linked with the high level of defects in the film. This issue will be discussed in greater detail in the next chapter, a comparative study of *In situ* and *ex situ* annealed MgB_2 films.

3.9 Summary

We examined the process parameters of *in situ* annealed PLD MgB_2 thin film, which includes depositing Mg+B precursor film at low substrate temperature and then heating the film to an elevated annealing temperature to form the MgB_2 phase. We found the T_c of the *in situ* PLD MgB_2 films is very dependent on the annealing parameters. With a stoichiometric MgB_2 target, the optimal *in situ* annealing temperature appears to be 670-690°C with a very short dwell of 1 min. A base vacuum of $9x10^{-8}$ Torr level is necessary for good T_c. The target surface after laser ablation has cone structure, which is attributable to the droplets splashed on the films surface resulting a very rough surface topography. The T_c is not significantly influenced by the substrate to target distance within the range of 30-50mm. Due to the short annealing time, the film has small grain size and high disorder level. This has been characterized by AFM and TEM, and indicated by the resistivity-temperature curves and the weak field dependence on the applied field. Under the optimal annealing conditions, the MgB_2 film has a zero resistivity T_c of 32K. At 5 K, the J_c from magnetization hysteresis loops is at the order of $1x10^6$ A/cm^2 in fields as high as 5T.

References

[1] C. B. Eom, M. K. Lee, J. H. Choi, L. J. Belenky, X. Song, L. D. Cooley, M. T. Naus, S. Patnaik, J. Jiang, M. Rikel, A. Polyanskii, A. Gurevich, X. Y. Cai, S. D. Bu, S. E. Babcock, E. E. Hellstrom, D. C. Larbalestier, N. Rogado, K. A. Regan, M. A. Hayward, T. He, J. S. Slusky, K. Inumaru, M. K. Hass, and R. J. Cava, High Critical current Density and Enhanced Irreversibility Field in Superconducting MgB_2 Thin Films, Nature **411,** 558-560 (2001).

[2] W. N. Kang, H.-J. Kim, E.-M. Choi, C. U. Jung, and S.-I. Lee, Epitaxial MgB_2 Superconducting Thin Films with a Transition Temperature of 39 Kelvin, Science **292,** 1521 (2001).

[3] J. Kim, R. K. Singh, J. M. Rowell, N. Newman, L. Gu, and D. J. Smith, Thermochemical analysis of MgB_2 synthesis by molecular-beam epitaxy, Journal of Crystal Growth **270,** 107-112 (2004).

[4] K. Ueda and M. Naito, In-situ Growth of Superconducting MgB_2 Thin Films by Molecular Beam Epitaxy, Cond-mat/0210259 (2002).

[5] A. Saito, A. Kawakami, H. Shimakage, and Z. Wang, As-grown Deposition of Superconducting MgB_2 Thin Films by Multiple-target Sputtering System, Jpn. J. Appl. Phys. **41,** L127-129 (2002).

[6] G. Grassano, W. Ramadan, V. Ferrando, E. Bellingeri, D. Marré, C. Ferdeghini, G. Grasso, M. Putti, P. Manfrinetti, A. Palenzona, and A. Chincarini, As-grown magnesium diboride superconducting thin films deposited by pulsed laser deposition, Supercond. Sci. Technol. 1**4,** 762-764 (2001).

[7] H. M. Christen, H. Y. Zhai, C. Cantoni, M. Paranthaman, B. C. Sales, C. Rouleau, D. P. Norton, D. K. Christen, and D. H. Lowndes, Superconducting Magnesium

Diboride Films with Tc=24K Growth by Pulse Laser Deposition with in-situ Anneal, Physica C 3**53,** 157 (2001).

[8] X. H. Zeng, A. Sukiasyan, X. X. Xi, Y. F. Hu, E. Wertz, W. Tian, S. S. H, X. Q. Pan, J. Lettieri, D. G. Schlom, C. O. Brubaker, Z. K. Liu, and Q. li, Superconducting Properties of Nanocrystalline MgB_2 Thin Films Made by an in-situ Annealing Process, Appl. Phys. Lett. 7**9,** 1840-1842 (2001).

[9] A. Brinkman, d. Mijatovic, G. Rijnders, V. Leca, H. J. H. Smilde, I. Oomen, A. A. Glibov, F. Roesthuis, S. Harkema, H. Hilgenkamp, D. H. A. Blank, and H. Rogalla, Superconducting thin films of MgB_2 on Si by pulsed laser deposition, Physica C 3**53,** 1 (2001).

[10] S. Amoruso, M. Armenante, R. Bruzzese, N. Spinelli, R. Velotta, M. Vitiello, and X. Wang, Pressure effects during excimer laser ablation of magnesium diboride targets, Applied Surface Science 2**08-209,** 39-44 (2003).

[11] G. Reisse and S. Weissmantel, Pulsed laser deposition of hexagonal and cubic boron nitride films, Applied Physics A 6**9,** 749 (1999).

[12] V. N. Tsaneva, N. A. Stelmashenko, I. N. Martev, Z. H. Barber, and M. G. Blamire, Characterisation of the optical emission of the plasma plume during pulsed laser deposition of superconducting MgB_2 thin films, Vacuum 6**9,** 267-271 (2002).

[13] D. B. Geohegan, chapter 5 in P*ulsed laser deposition of thin films,* edited by D. B. Chrisey and G. K. Hubler (Wiley, New York, 1994).

[14] V. Braccini, A. Gurevich, J. E. Goecke, M. V. Jewell, C. B. Eom, D. C. Larbalestier, A. Pogrebnyakov, Y. Cui, B. T. Liu, Y. F. Hu, H. M. Redwing, Q. Li, X. X. Xi, P. K. Singh, T. Gandikota, J. Kim, B. Wilkens, N. Newman, J. Rowell, B. Moeckly, B. Ferrando, C. Tarantini, M. Marre, M. Putti, V. Ferdeghini, T. Vaglio,

and E. Haanappel, High-field superconductivity in alloyed MgB_2 thin films, Phys. Rev. B 7**1,** 012504 (2005).

[15] S. M. Kazakov, R. Puzniak, K. Rogacki, A. V. Mironov, N. D. Zhigadlo, J. Jun, C. Soltmann, B. Batlogg, and J. Karpinski, Carbon substitution in MgB_2 single crystals: Structural and superconducting properties, (2005).

[16] M. J. Qin, S. Keshavarzi, S. Soltanian, X. L. Wang, H. K. Liu, and S. X. Dou, Sample-size dependence of the magnetic critical current density in MgB_2 superconductors, Physical Review B 6**9** (2004).

[17] S. R. Foltyn, chapter 4 in P*ulsed laser deposition of thin films,* edited by D. B. Chrisey and G. K. Hubler (Wiley, New York, 1994).

[18] W. N. Kang, H. J. Kim, E. M. Choi, C. U. Jung, and S. I. Lee, MgB_2 Superconducting Thin Films with a Transition Temperature of 39 Kelvin, Science 2**92,** 1521 (2001).

[19] Y. Zhao, M. Ionescu, J. Hovard, and S. X. Dou, Comparative study of in situ and ex situ MgB_2 films prepared by pulsed laser deposition, Supercond. Sci. Technol. 1**7,** S482-485 (2004).

[20] A. Berenov, Z. Lockman, X. Qi, Y. Bugoslavsky, L. F. Cohen, M.-H. Jo, N. A. Stelmashenko, V. N. Tsaneva, M. Kambara, N. H. Babu, D. A. Cardwell, M. G. Blamire, and J. L. MacManus-Driscoll, Growth of strongly biaxially aligned MgB_2 thin films on sapphire by postannealing of amorphous precursors, Appl. Phys. Lett. 7**9,** 4001-3 (2001).

[21] Z. X. Ye, Q. Li, Y. F. Hu, A. V. Pogrebnyakov, Y. Cui, X. X. Xi, J. M. Redwing, and Q. Li, Magneto-Optical Imaging Studies of Flux ropagation in Ultra-Pure and Carbon-Doped MgB_2 Thin Films, IEEE Transactions on Applied Superconcuctivity 1**5,** 3273 (2005).

[22] E. M. Gyorgy, R. B. v. Dover, K. A. Jackson, L. F. Schneemeyer, and J. V. Waszczak, Anisotropic critical currents in $Ba_2YCu_3O_7$ analyzed using an extended Bean model, Appl. Phys. Lett. 5**5,** 283 (1989).

[23] Z. W. Zhao, H. H. Wen, S. L. Li, Y. M. Ni, H. P. Yang, W. N. Kang, H. J. Kim, e. M. Choi, and S. I. Lee, Smearing of Suoerconduvting critical current density by dense and small flux jumps in MgB_2 thin films, Phys. Rev. B 6**5,** 064512 (2001).

[24] M. R. Wertheimer and J. l. G. Gilchrist, J. Phys. Chem. Solids. 2**8,** 2509 (1967).

[25] S. L. Wipf, Phys. Rev. 1**61,** 404 (1967).

[26] C. A. Duran, P. L. Gammel, R. E. Miller, and D. J. Bishop, Phys. Rev. B 5**2,** 75 (1995).

[27] P. Leiderer, J. Boneberg, P. Brll, V. Bujok, and S. Herminghaus, Phys. Rev. Lett 7**1,** 2646 (1993).

[28] Y. Eltsev, S. Lee, K. Nakao, N. Chikumoto, S. Tajima, N. Koshizuka, and M. Murakami, Phys. Rev. B 6**5,** R140501 (2002).

[29] J. M. Rowell, The widely variable resistivity of MgB_2 samples, Supercond. Sci. Technol. 1**6,** R17-R27 (2003).

[30] J. M. Rowell, S. Y. Xu, X. H. Zeng, A. V. Pogrebnyakov, Q. Li, X. X. Xi, J. M. Redwing, W. Tian, and X. Pan, Critical current density and resistivity of MgB_2 films, Appl. Phys. Lett. 8**3,** 102 (2003).

[31] S. L. Bud'ko, C. Petrovic, G. Lapertot, C. E. Cunningham, P. C. Canfield, M.-H. Jung, and A. H. Lacerda, Phys. Rev. B 6**3,** 220503(R) (2001).

[32] A. Gurevich, S. Patnaik, V. Braccini, K. H. Kim, C. Mielke, X. Song, L. D. Cooley, S. D. Bu, D. M. Kim, J. H. Choi, L. J. Belenky, J. Giencke, M. K. Lee, W. Tian, X. Q. Pan, A. Siri, E. E. Hellstrom, C. B. Eom, and D. C. Larbalestier, Very

high upper critical fields in MgB_2 produced by selective tuning of impurity scattering, Supercond. Sci. Technol. 1**7,** 278 (2004).

[33] A. Sidorenko, V. Zdravkov, V. Ryazanov, S. Horn, S. Klimm, R. Tidecks, A. Wixforth, Th. Koch, and T. Schimmel, Thermally Assisted Flux Flow in MgB_2 : Strong Magnetic Field Dependence of the Activation Energy, cond-mat/0406062 (2004).

[34] T. T. M. Palstra, B. Batlogg, R. B. v. Dover, L. F. Schneemeyer, and J. V. Waszczak, Critical currents and thermally activated flux motion in high-temperature superconductors, Appl. Phys. Lett. 5**4,** 763 (1989).

[35] T. T. M. Palstra, B. Batlogg, R. B. v. Dover, L. F. Schneemeyer, and J. V. Waszczak, Dissipative flux motion in high-temperature superconductors, Phys. Rev. B. 4**1,** 6621 (1990).

[36] D. H. A. Blank, H. Hilgenkamp, A. Brinkman, D. Mijatovic, G. Rijinders, and H. Rogalla, Superconducting Mg-B Films by Pulsed-laser Depostion in an in situ Two-step Process Using Multicomponent Targets, Appl. Phys. Lett. 7**9,** 394-396 (2001).

[37] D. G. Hinks, J. D. Jorgensen, H. Zheng, and S. Short, Synthesis and Stoichimetry of MgB_2, Physica C 3**82,** 166-176 (2002).

[38] J. C. Idrobo, S. Ogut, T. Yildirim, R. F. Klie, and N. D. Browning, Electronic and superconducting properties of oxygen-ordered MgB_2 compounds of the form $Mg_2B_3O_x$, Phys. Rev. B. 7**0,** 172503 (2004).

[39] Z.-J. Liu, S. H. Zhou, X. X. Xi, and Z.-K. Liu, Thermodynamic reactivity of the magnesium vapor with substrate materials during MgB_2 deposition, Physica C 3**97,** 87-94 (2003).

Chapter 4. Comparative study on *in situ* and *ex situ* annealed MgB_2 thin films

In this chapter we first report the synthesis of *ex situ* MgB_2 films prepared by pulsed laser deposition. The differences in both microstructure and superconductivity between the *in situ* and *ex situ* annealed MgB_2 films are then determined and discussed. This comparative study is aimed to understand the very different behaviors between films undergone different fabrication processes and the correlative underlying mechanism with the aid of microstructural analysis. This knowledge could also be instructional for optimization of the MgB_2 film synthesis methods.

4.1 Experimental

For the *ex situ* annealed MgB_2 film, a boron precursor film was deposited from a boron target in a 10^{-7}-10^{-6} Torr vacuum. Commercial 2–inch boron target (99.9% pure, ~40% density Goodfellow Inc.) fabricated by hot pressing was used. The target was freshly prepared and is believed to have very low oxygen contamination.

The substrate was kept at 250℃ during the deposition. The precursor film was then wrapped in a Ta foil and sealed in a stainless steel tube in an Ar atmosphere, together with Mg pellets. The tube was put into a 900℃ furnace and kept for 30min. It takes 5min to gradually transfer the sample in and out of the high temperature zone. The *ex situ* annealing conditions follow Kang et al.'s optimized procedure [1], with which the resultant film is reported to have good c-axis texture on Al_2O_3-C substrate. There types of substrates, Al_2O_3-R $(01\bar{1}2)$, Al_2O_3-C (0001) and 4H-SiC (0001) were

used. For 4H-SiC (0001), the surface plane is hexagonal, with a=3.073 Å, which matches very well with the MgB2 (0001) plane with a=3.086 Å.

The preparation of the *in situ* annealed film is described in Chapter 3, using the optimized conditions. The precursor film was deposited on Al_2O_3-C substrates from a stoichiometric MgB_2 target (84% density). The pulsed laser (248nm, 300mJ/pulse) was focused to an elliptical spot with dimensions of 7mm x 1.5mm on the target. The deposition time for MgB_2 is 5min with a laser repetition of 10Hz. During the deposition, the substrate was kept at 250℃ and in Ar at 120mTorr. A ~800nm thick Mg cap layer was then deposited onto the precursor film. The film was heated *in situ* to 685 ℃ in 12 min and kept at this temperature for 1min in a 1atm Ar atmosphere. We prepared each type of MgB_2 film several times under the same conditions, and good reproducibility in T_c was found in both types of films.

The transport measurements were carried out on a PPMS-9T magnetometer system, using the standard 4-probe method described in Chapter 2. The zero-field-cooled magnetization-temperature curves and magnetization hysteresis loops of the films were measured on an MPMS-5T magnetometer. In each measurement the applied field was perpendicular to the film plane. Critical current density J_c was calculated from the height of magnetization loops, $\Delta M(emu/cm^3)$, using the standard equation (3-2) based on the Bean model. Due to the similarity in dimensions of our films (0.55cm x 0.25cm x 350nm), the obtained J_c can be used for comparative purposes. The irreversibility field (H_{irr}) and H_{c2} at each temperature were selected as

the point of 10% and 90% of the normal state resistivity at 40 K in the resistivity-T curves, respectively.

4.2 Microstructural difference between the *ex situ* and *in situ* MgB_2 films

The surface topography and the thickness of the films were determined by both atomic force microscopy and scanning electron microscopy. The cross-sectional SEM images of the two films are shown in Fig 4-1. We took 350nm as the thickness of the *in situ* annealed film in the calculations of J_c and resistivity, but this value is actually a lower estimate of the effective thickness of the *in situ* film due to the existence of big particulates on the film (Fig. 4-1a). The thickness of the *ex situ* annealed film is also about 350nm, which is more accurate because of the comparatively smooth surface of the film (Fig. 4-1b).

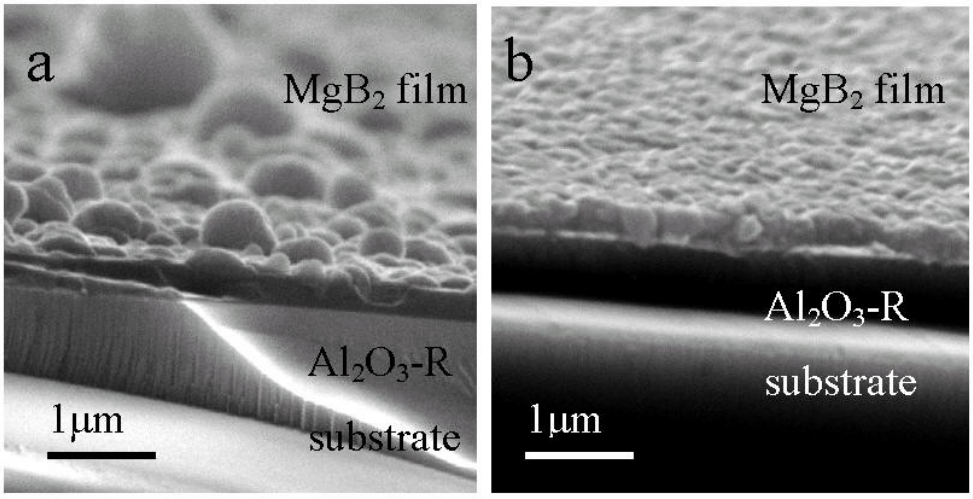

Fig. 4-1 SEM cross-section images of the two types of films. a: in situ annealed MgB_2 film; b: ex situ annealed MgB_2 film on Al_2O_3-R substrate.

The surface topography of the *ex situ* films are shown in Fig. 4-2. The boron precursor films are very smooth on each kind of substrate, as shown in Fig. 4-2 (a).

Considering the low deposition temperature and rapid growth rate, the observed smooth surface indicates amorphous film growth. The *ex situ* annealed film shows typical crystallized surface on the three types of substrates, as shown in fig. 4-2 b) c) and d). The average thickness of the *ex situ* annealed film is increased by a factor of about 1.8-2.0 compared with the boron precursor, and this is in accordance with the volume change of a complete 2B+Mg (vapor)→ MgB_2 reaction.

The *ex situ* film on Al_2O_3-R substrate shows random grain orientation in Fig. 4-2 (b). The individual blocks, which are probably crystallites, are about 400 nm in size. This grain size is consistent with the SEM cross-section observation in Fig. 4- 1(b). The *ex situ* film on Al_2O_3-C substrate shows similar grain size for that on Al_2O_3-R, with less sticking-out grains. The *ex situ* film on SiC showed some exceptionally large grains of about 1μm.

Fig. 4-3 shows the XRD patterns for the two types of *ex situ* films. Upon an inspection of the two patterns, the *ex situ* film on Al_2O_3-C shows a c-axis preferred grain orientation, while the *ex situ* film on Al_2O_3-R does not show meaningful peaks. The hexagonal lattice structure of Al_2O_3-C surface plane has a better lattice match with MgB_2 (0001) plane than the rectangular lattice of Al_2O_3-R surface plane. It is reasonable to assume that the *ex situ* film on Al_2O_3-C has better crystallization and stronger C-axis orientation due to a better lattice match.

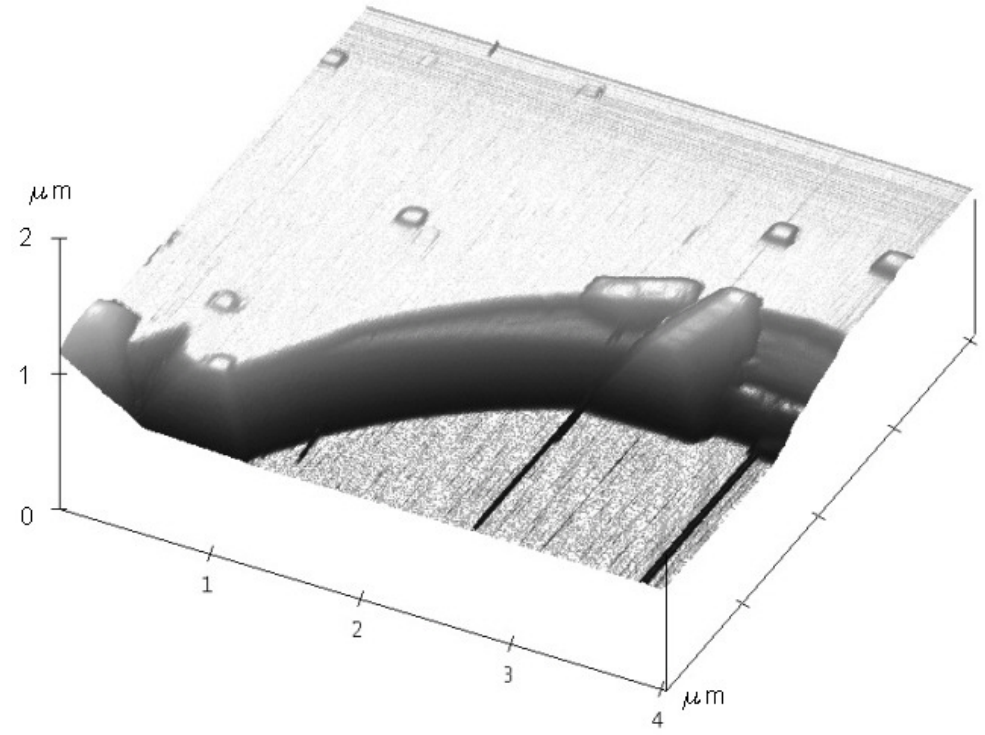

a

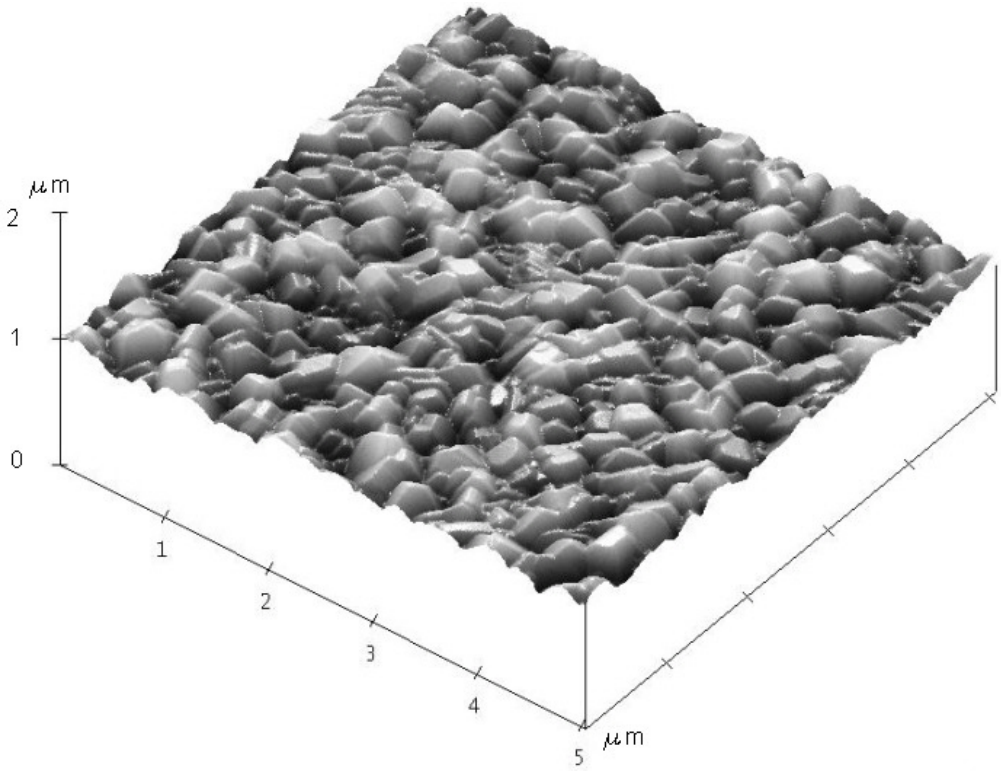

b

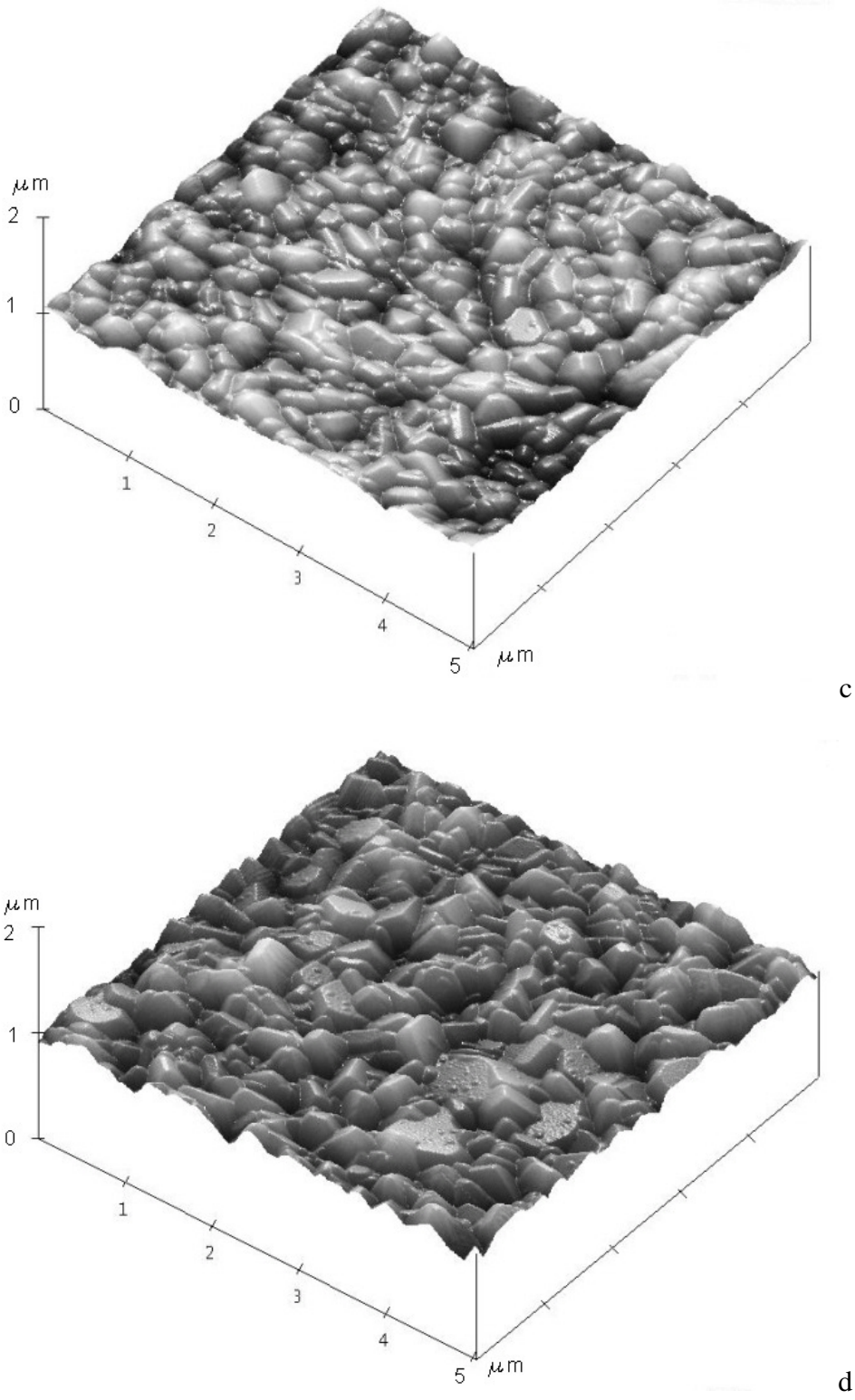

Fig. 4-2 AFM 3D images of a) the boron precursor film, the lower plane is the substrate; b) the ex situ annealed MgB_2 film on Al_2O_3-R substrate; c) the ex situ film on Al_2O_3-C substrate; d) the ex situ film on 4H-SiC(0001) substrate.

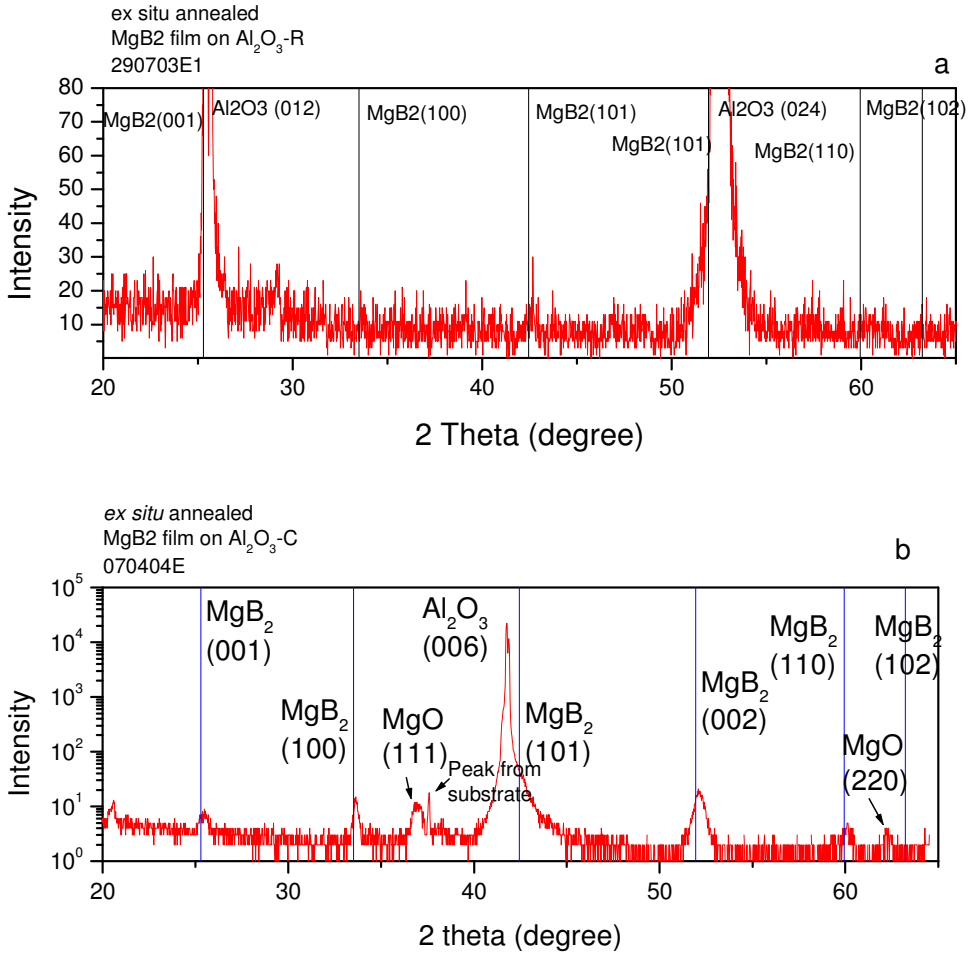

Fig. 4-3 XRD of ex situ annealed films on a) Al_2O_3-R and b) Al_2O_3-C substrates. The MgO signal may come from the oxidization of some excess metal Mg on the film surface.

Considering the *in situ* MgB2 films is not oriented, further transport and magnetic measurements for comparison purposes were carried out only on the *ex situ* films on Al_2O_3-R substrate in the comparative study with *in situ* films.

4.3 Superconducting transition of the two types of films

4.3.1 Superconducting transition temperatures and residual resistivity

Fig. 4-4 (a) shows the resistivity-temperature curves of the two films. The $T_{c\ onset}$ is 38.1K with a widths ΔT=1 K for the *ex situ* film #120803E. The best *in situ* annealed film in Chapter 3 has a $T_{c\ onset}$ of 34K and ΔT=2 K. The *ex situ* annealed film has a higher T_c and a narrower transition width in the ρ-T curves. However, we notice that the bulk diamagnetism transition in the M-T curve for the *in situ* film (ΔT=5 K) (Fig 4-4 b), is actually sharper than for the *ex situ* annealed film (ΔT=9 K), which indicates a more homogeneous superconducting phase in the *in situ* film, as shown in fig.4-4 (b). Also shown in Fig.4-4 (a), the resistivity value of the *in situ* annealed film is quite high, ~120 μΩ·cm at 300 K, whereas the value for the *ex situ* film is as low as 36 μΩ·cm. The values of the resistivity difference, $\Delta\rho_{300\text{-}40K}$, are both 19 μΩ·cm for the two films. Since the transport property for an MgB_2 sample is probably governed by both intra-grain scattering and inter-grain connectivity [2,3], it is difficult to distinguish these two aspects of the influences only from the ρ-T curves. From a comparison of the ρ-T curves of our *ex situ* annealed film and a clean MgB_2 single crystal [4], the $\Delta\rho_{300\text{-}40K}$ of our film is about five times the value for the single crystals. If we attribute the increase of $\Delta\rho_{300\text{-}40K}$ to a reduction of effective current carrying area by five fold, the "real" residual resistivity of our *ex situ* film should be 3.4 μΩ·cm, not too far from the residual resistivity value of about 1 μΩ·cm for single crystals [4], which indicates that the *ex situ* film is fairly clean inside the MgB_2 grains.

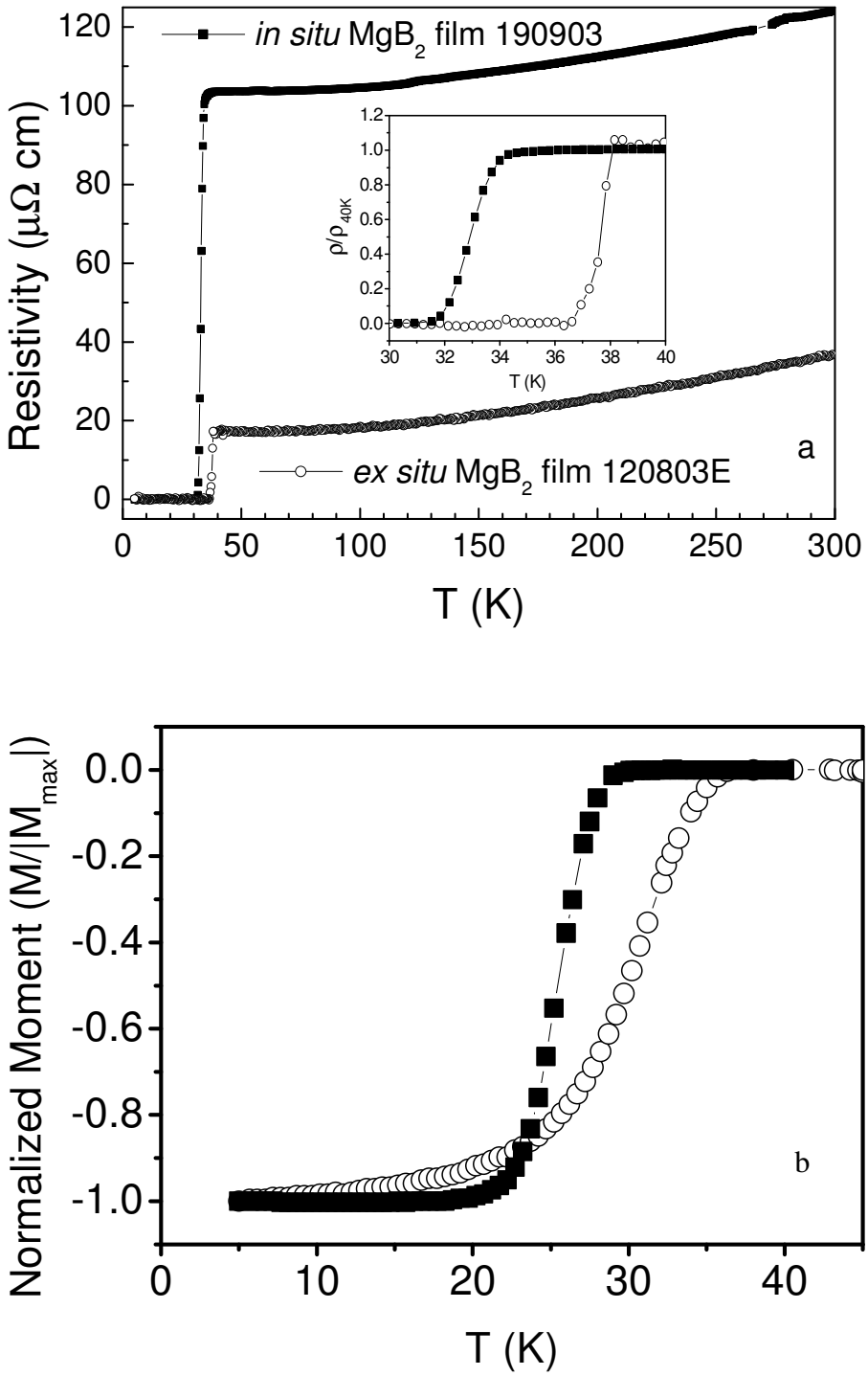

Fig. 4-4 (a): Temperature dependence of resistivity for the two types of MgB_2 films from 5K to 300K in zero field; The inset shows the transition curves between 30K and 40K. (b): The magnetization versus temperature curves. ■: in situ film; ○: ex situ film.

4.3.2 Field dependence of ρ(T) curves for the two types of MgB_2 films

Figure 4-5 shows the ρ(T) curves of the two types of films in perpendicular fields (B) up to 8.7 T. From this figure, it is clear that the T_c of the *in situ* film (Fig 4-5 a) decreases much slower with field that that for the *ex situ* film (Fig 4-5 b). The *in situ* film is superconducting at about 22K in 8.7T field. In contrast, the T_c for *ex situ* film in 8.7 T field has decreased to ~10 K.

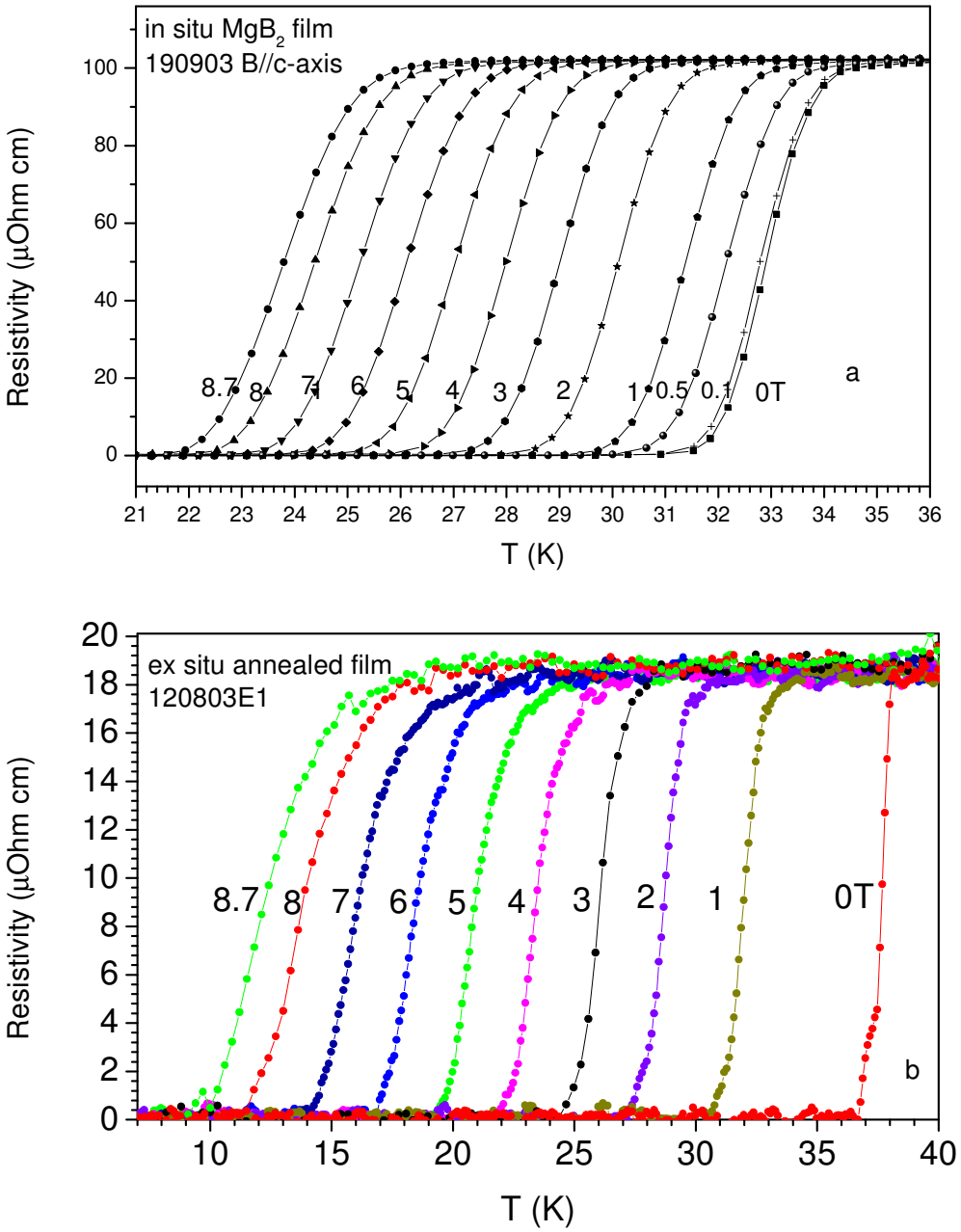

Fig.4-5 Field dependence of ρ(T) curves for a) in situ MgB_2 film and b) ex situ film.

The activation energies U_0 of the types of MgB_2 films have been estimated from an Arrhenius law [5-7] using equation (3-6). The Arrhenius plots of resistance R(T, H) for the two types of films in perpendicular fields are shown in Fig. 4-6. In both *in situ* (Fig. 4-6 a) and *ex situ* films (Fig. 4-6 b), there is clearly a linear part in each ln(R)-1/T curve which represents the TAFF regime in the films. Figure 4-7 shows the activation energy of flux flow versus applied field, B_a. U_0 is related to magnetic field by $U_0 \sim B^{-n}$, in accordance with literature on MgB_2 and other superconductors [6,8-10]. For the *in situ* film, the value of exponent n is 0.18±0.02. Two stages of field dependence of U_0 were found in the *ex situ* film. In fields up to 5 T the n value is 0.49±0.01, and in fields between 5T and 8.8 T the n value is 3.7±0.3. U_0 drops sharply in fields higher than 5 T for the *ex situ* film, indicating a rapid weakening of effective pinning in the *ex situ* film. The crossover of two stage of linear field dependence is similar with what has been observed in perpendicular fields for high temperature superconductors [6], which indicates a transition from 3D to 2D vortices pinning mechanism. However, the mechanism of the crossover in our *ex situ* film is not clear. We presume this could relate to the elimination of active pinning centers at grain boundary or impurity sites in high fields. By contrast, the $\ln(U_0)$-ln(B) curve of our *in situ* film is approximately straight in fields up to 9T and with a very small slope of n=0.2. This indicates a much stronger pinning in our *in situ* film which does not degrade in high fields, comparing with the reports on activation energy of MgB_2 bulk and thin films[10,11].

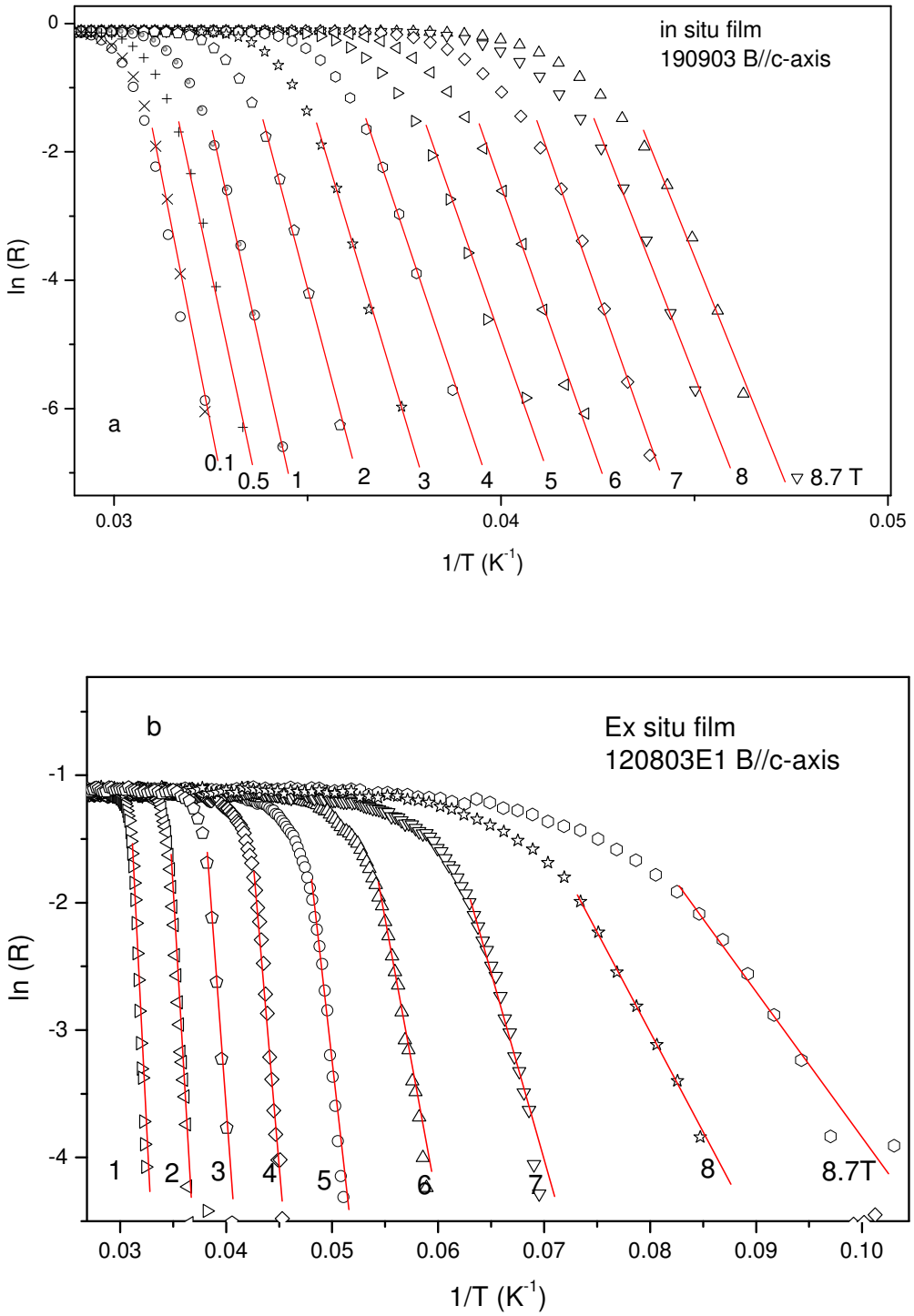

Fig.4-6 Arrhenius plots of the resistance R(H, T) of the a) in situ and b) ex situ films.

The applied filed is perpendicular to the film plane.

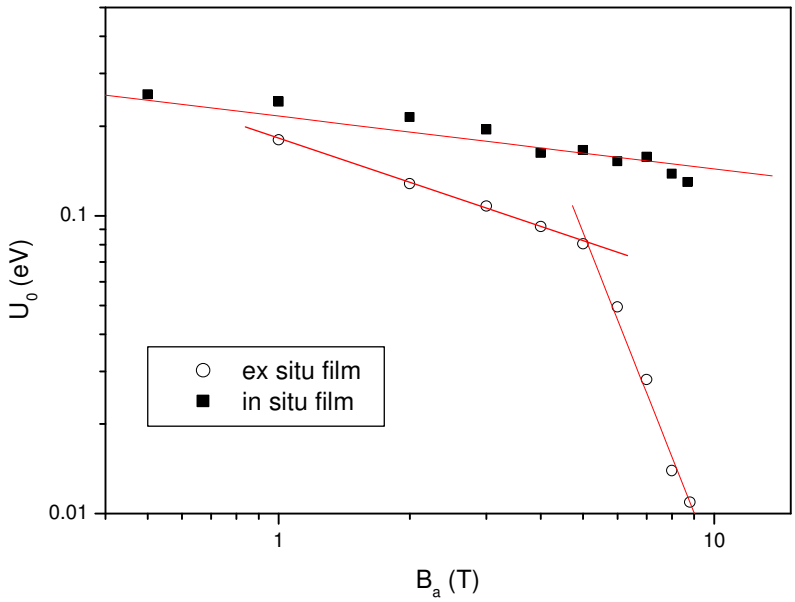

Fig.4-7 The flux flow activation energy U_0 versus applied field B_a. Two stages of field dependence of U_0 is found in ex situ film.

Fig. 4-8 shows the temperature dependence of H_{irr} and H_{c2} for the MgB_2 films. The applied field is perpendicular to the film plane. The data for MgB_2 films from the literature [12,13] is shown for comparison. The slope of the H_{irr} (H_{c2})-T curve (Fig. 4-8 a) for the *in situ* annealed film is significantly higher than for the *ex situ* film. The H_{irr} values and the slope of H_{irr} -T curve of our *in situ* annealed film are higher than the oxygen alloyed *ex situ* film reported by Eom et al [12], which indicates a further enhancement of pinning force in our *in situ* annealed film. Figure 4-8b shows a comparison of H_{c2} between the *in situ* and *ex situ* films. It is in agreement with the viewpoint of Gurevich et al. that MgB_2 samples with higher resistivity have larger H_{c2}-T slope [13]. Since both films do not present a grain orientation according to XRD and AFM observation, the comparison of H_{c2} between the two films can be reliable in revealing the difference in scattering level. The slope of H_{c2}-T for our *in situ* film is about 1.1T/K in the temperature range from 25K to 30K. Employing a simple linear

extrapolation in equation (3-3), the H_{c2} value at 0T was estimated to be as high as 36T. This value is significantly higher than the values of $H_{c2//}(0)$=21 T and $H_{c2\perp}(0)$=7.3 T for the clean MgB_2 single crystals [4], indicating a very strong scattering in our *in situ* film. The *ex situ* film shows a low H_{c2} slope of 0.46 T/K attributable to a weak intra-grain scattering, which implies that the impurity precipitates and other disorders inside the *ex situ* film are at a low level.

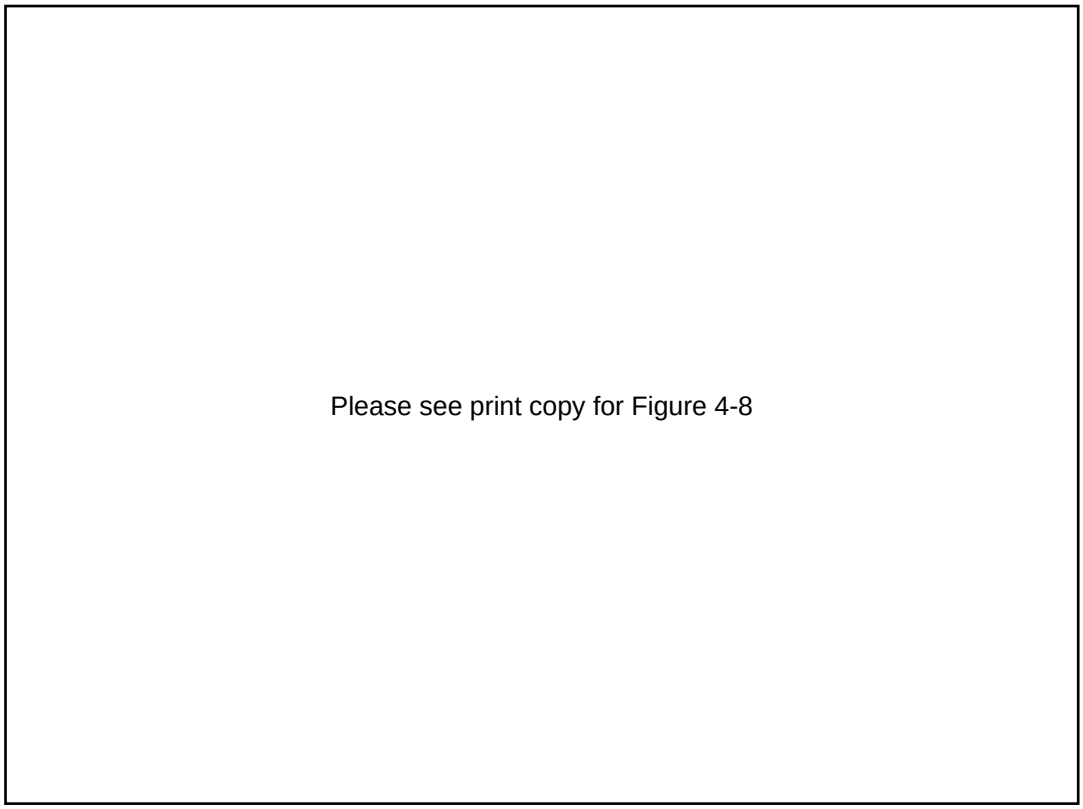

Fig.4-8. Irreversibility lines and upper critical field versus temperature curves for the in situ and ex situ annealed films. A): Irreversibility lines for the in situ and ex situ films. The data for undoped ex situ MgB_2 film and oxygen alloyed MgB_2 film (Ref. [12]) is displayed in the figure for comparison. B): Upper critical fields versus temperature for the two films. The data for c-axis-oriented MgB_2 films from Ref. [13] are also shown in this figure.

4.4 Superconducting behaviors in magnetic fields for the *in situ* and *ex situ* films

4.4.1 Dependence of critical current density on the applied field and temperature

The field dependence of J_c of the two films is shown in Fig. 4-9. The J_c value of the *ex situ* film is higher than the *in situ* film in zero field, but decreases sharply with the increasing applied fields. The *in situ* annealed MgB_2 film shows a weak field dependence of J_c, suggesting good pinning in high fields. The J_c of the *in situ* film at 5 K and 5 T remains about 10^6 A/cm^2, whereas the J_c for the *ex situ* film drops to less than 10^4 A/cm^2 in the same field and temperature. The J_c behavior of the *ex situ* annealed MgB_2 film is very similar to that of clean MgB_2 bulks, which also indicates a lack of flux pinning in high fields.

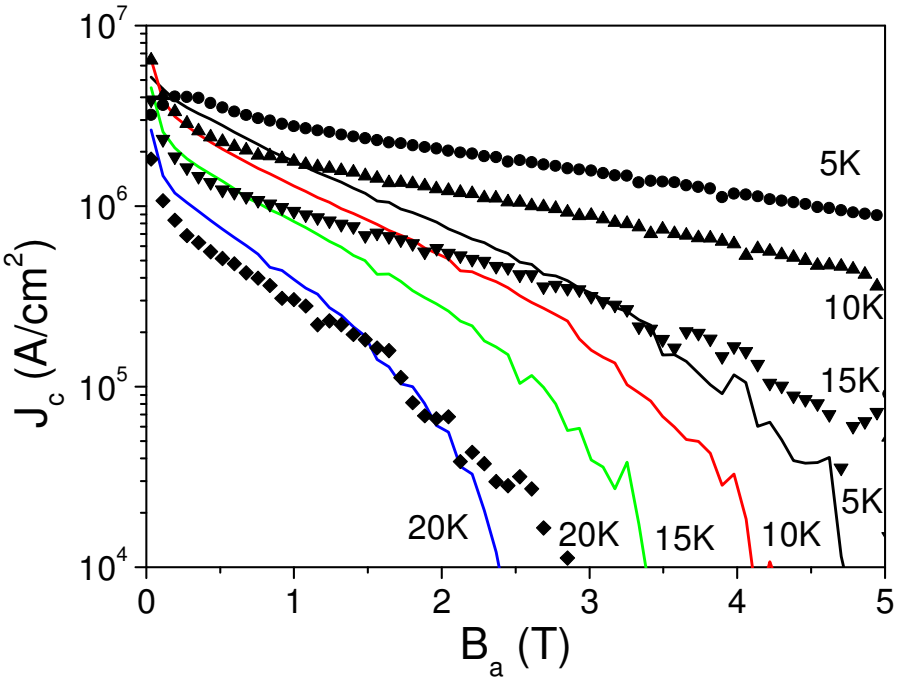

Fig.4-9 Critical current of the two types of MgB_2 films calculated from M-H loops. Solid symbols: in situ annealed film; lines: ex situ annealed film. The temperature is 5K, 10K, 15K, and 20K from top to bottom, respectively. The applied field is perpendicular to the film plane.

4.4.2 Flux penetration behavior detected by magneto-optical imaging

The magneto optic (MO) imaging was carried out at the University of Oslo, employing a bismuth substituted yttrium iron garnet indicator film. The indicator film was placed directly on top of the MgB_2 film. The magnetic field B_a was applied perpendicularly to the film surface. All images were taken at a constant temperature after samples have been zero-field cooled.

The MO images in Fig. 4-10 show some interesting differences in the flux penetration behavior. The images correspond to a map of the out-of-plane component of the local magnetic field. The brighter the area, the stronger is the magnetic flux. At 4K, the magnetic flux penetrates both films by abrupt avalanches. The *in situ* film shows a parallel penetration pattern from each edge of the sample, while the *ex situ* film shows a dendritic penetration. Upon inspection of Fig. 4-10, we found that the penetration paths in the *in situ* film are not reproducible in different sets of measurements. In contrast, the dendrites for the *ex situ* film are nearly identical for different set of measurements, although the development rate of each path may vary. The non-reproducible flux avalanche at low temperature for the *in situ* film is characteristic of MgB_2 films, corresponding to thermo-magnetic instability [14]. The fact that, at the same applied field, flux penetrates the *in situ* film much further than the *ex situ* film implies an easier local heat-up for the *in situ* film, which could be attributable to a small thermal conductivity of the *in situ* film. The penetration behavior of the *ex situ* film resembles that observed in superconductors with microscopic defects, indicating defect-controlled flux jumps in the *ex situ* film. An

explanation for the interesting differences found in MO observation may link the microstructural characteristics of the films to their superconducting properties.

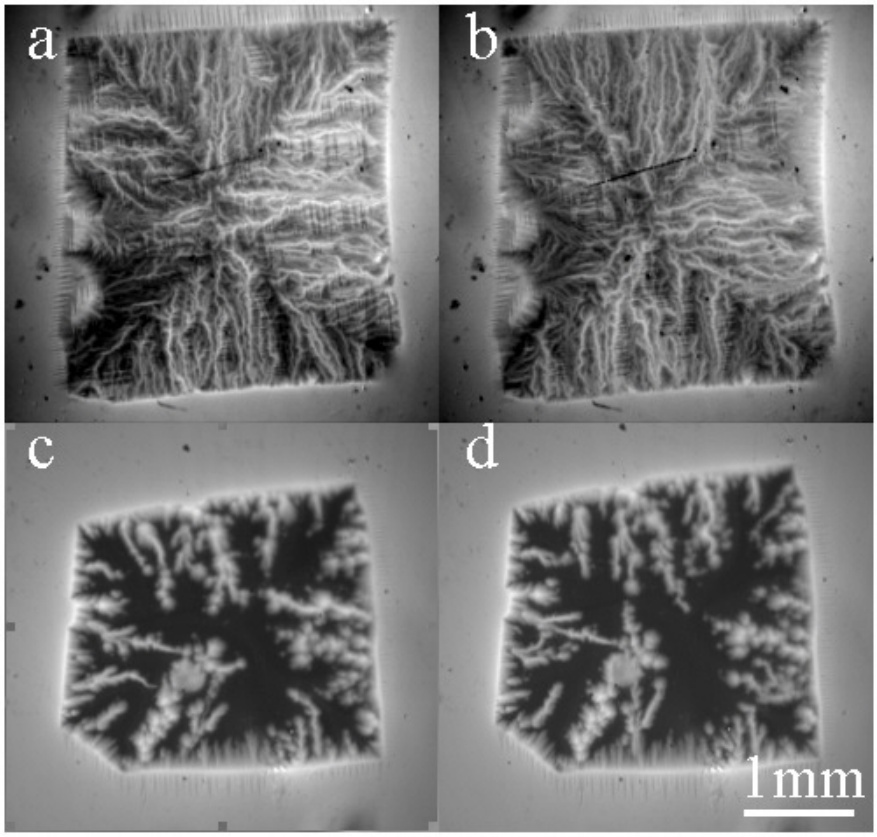

Fig. 4-10. MO images for the in situ film, shown in (a), (b) and the ex situ film, shown in (c), (d) at 4K. The applied field is (a) 17 mT, 1st set of measurement, (b) 17 mT, 2nd set of measurement, (c) 25.5 mT, 1st set of measurement, and (d) 25.5mT, 2nd set of measurement.

4.5 Discussions on the differences of H_{c2}, J_c and magnetic behavior between the two types of film

The AFM scan of the *in situ* annealed film, shown in Fig. 4-11, reveals much smaller rounded cells of 30-100 nm in diameter. Considering the lack of crystalline surface characteristics for the cells, it is possible that inside these cells are even smaller

grains. The very-fine-grain structure of the *in situ* annealed film probably results from the low annealing temperature and short annealing time. The clear microstructural differences between the two films may be decisive for the significant difference between the field dependence of their J_c. In the *in situ* films, the small grains with large amount of grain boundaries, usually about 3 nm wide, are of desirable dimensions for efficient pinning [15]. Whereas in the *ex situ* film, the grain boundary pinning is less pronounced for the relatively larger grains, which is attributed to a higher annealing temperature and longer annealing time.

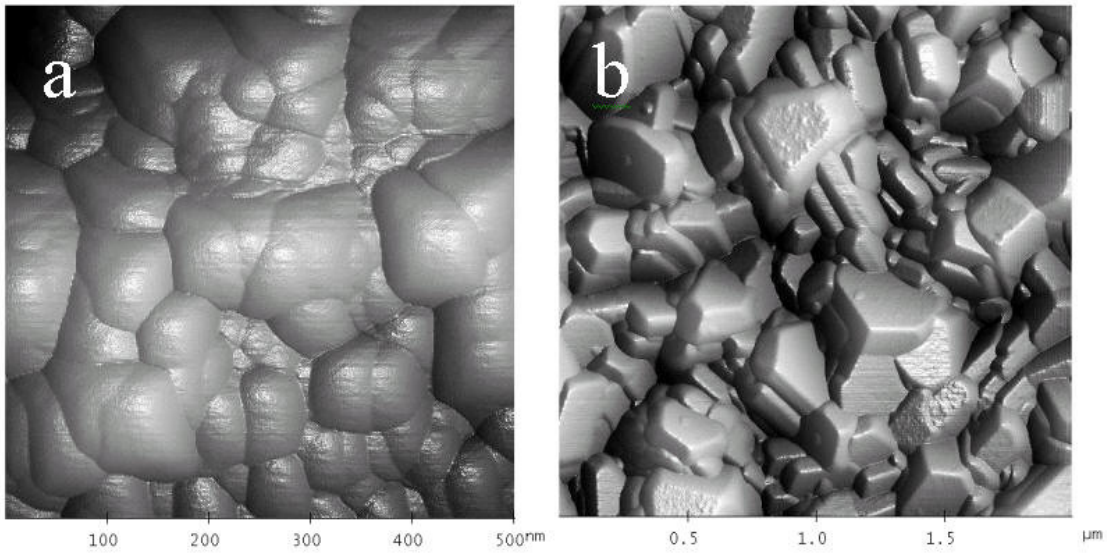

Fig. 4-11 AFM of a) the in situ and b) the ex-situ MgB_2 film on Al_2O_3-Rsubstrate.

With the *in situ* preparation, the precursor film is deposited from a stoichiometric MgB_2 target. Thus the Mg and B atoms or clusters are finely mixed together in the precursor. The fine mixture, in turn, favours rapid MgB_2 phase formation. During the short annealing process, namely a 12min ramping up process and a 1 min dwell at 685 ℃, a superconducting MgB_2 phase was formed, but a long-range diffusion is unlikely. Large amounts of disorders are probably still in their initial positions, which should be

finely dispersed in the film, leading to enhanced intra-grain scattering and flux pinning, as well as an increased residual resistivity and a small thermal conductivity. The observed nano-grain structure is usually found in this type of film [16,17]. As suggested by Bugoslavsky *et al*., the finely distributed grain boundaries could also serve as effective pinning centers [18].

Impurities may also play an important role in the increase in H_{c2} and the enhancement of flux pinning in the *in situ* film. As shown in the EDS result (Fig. 4-12), the oxygen level in the *in situ* annealed film is obviously higher than in the *ex situ* annealed film. Due to the high reactivity of Mg with oxygen, a significant amount of oxygen may be introduced into the *in situ* film during the MgB_2 deposition process. In the *ex situ* procedure, the deposition of boron precursor is much less sensitive to oxygen and the existence of oxygen is more likely to be in MgO phase along the grain-boundaries and on the film surface. As discussed in the literature [12,13], the oxygen in MgB_2 bulk and thin film could substitute for boron or exist as MgO precipitates. In both circumstance the intra-band scattering is enhanced, and effectively increases the slope of the H_{c2}-T curve for the MgB_2 thin film [13]. Despite the high oxygen level, the T_c of our *in situ* film was not dramatically suppressed. This is consistent with the theoretical prediction by Mazin and Antropov that the inter-band scattering rate between σ and π band would be small and the T_c is less influenced by intra-band scattering in MgB_2 [2,19]. Although the SAED signal reveals that the grain size of MgO is generally larger than 20 nm in our *in situ* film, a proportion of nano-sized MgO particles, which are usually observed in oxygen-rich MgB_2 films [12], could

provide effective pinning centers and contributes to fine-grain structure, thus leading to a further enhancement of critical current density in high fields.

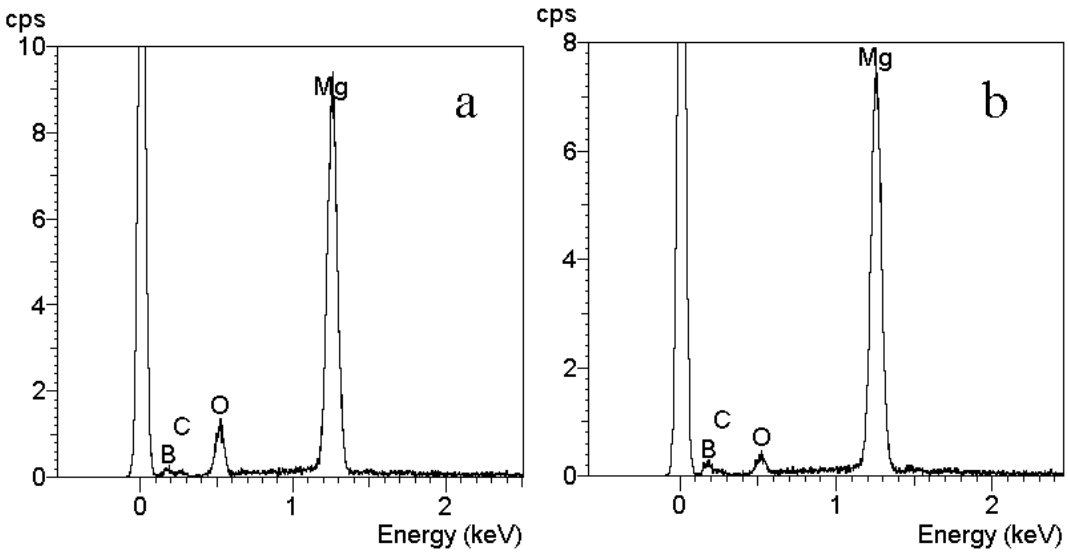

Fig. 4-12 EDS analysis results for the a) in situ and b) ex situ films. In order to avoid the interaction with the Al_2O_3 substrate, a low electron beam energy of 5kV was used. As a result, no Al signal at about 1.5KV is detectable. Since the thickness of both films is similar, the difference in oxygen signal intensity can reveal the difference of oxygen level in the two films.

Since the *ex situ* film has undergone a much higher annealing temperature and longer annealing time, it is reasonable to see a stronger crystallization after the annealing. During the grain coarsening process, the movement of the grain boundaries probably expels the disorders such as vacancies, dislocations, impurity atoms or precipitates, from the matrix to the grain boundaries. Intra-grain scattering usually increases the slope of H_{c2} (T) and provides flux pinning, while makes little suppression of the T_c. Thus the relatively clean MgB_2 grains in our *ex situ* film might lead to the

poor J_c and H_{c2} performance. Klie *et al.* have observed the presence of BO_x-MgO_y-BO_z secondary phase along grain-boundaries in MgB_2 bulk samples [20,21]. In some peculiar positions, such as where three big MgB_2 grains meet together, the impurities are particularly likely to concentrate, and microscopic pores could also develop at the triple junctions and act as a source of cracks. Such positions are usually the thinnest part of the film as can be seen from the AFM image in Fig. 4-13. These thinner, non-superconducting, or lower T_c parts [21] in the film may act as a preferred path for the flux penetration shown in Fig. 4-10 (c) and (d).

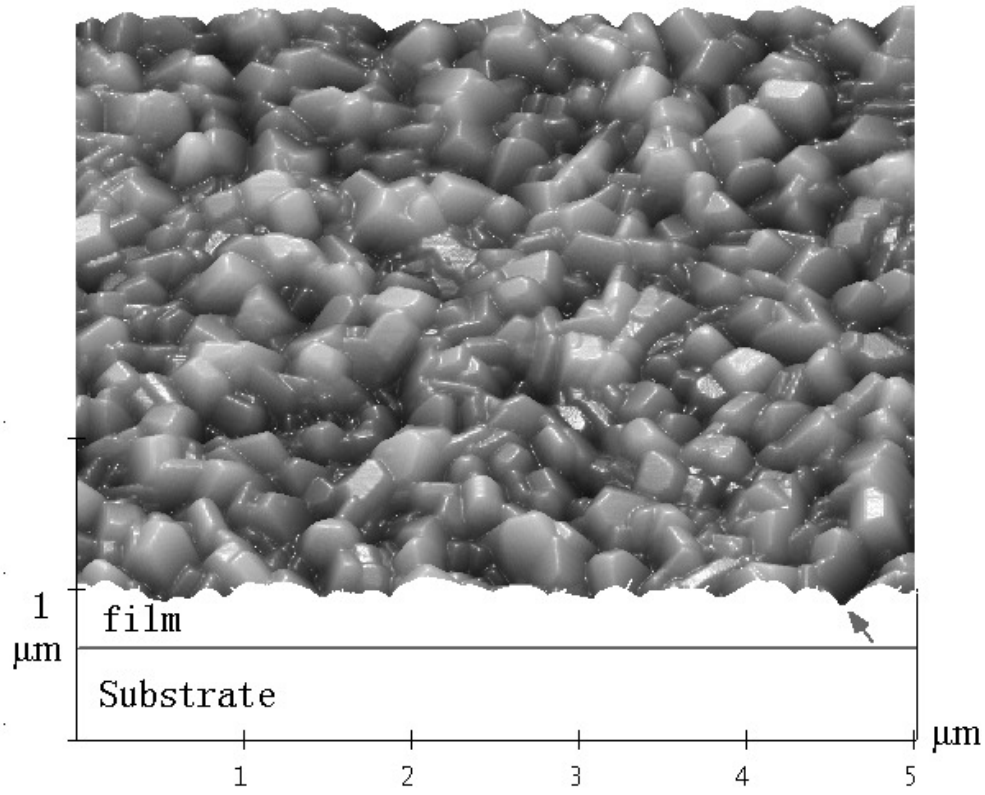

Fig.4-13. AFM 3D image of the ex situ MgB_2 film. The surface topography shows typical randomly oriented grains. The arrow shows a thinner part formed between two grains.

4.6 Summary of Chapter 4

Significant difference of flux pinning as well as the slope of H_{c2}-T curve was detected between the *ex situ* and *in situ* annealed MgB_2 films in this comparative study. The small-grain and high-level-disorder feature of the *in situ* annealed film, which is attributable to the low annealing temperature and short annealing time, may mainly contribute to the significant improvement of flux pinning in the *in situ* MgB_2 film. In contrast, our *ex situ* film is constructed of comparatively larger and probably cleaner grains with weak links between the grains, as a result of the annealing process which is in the grain-growing region. As a consequence, defect-controlled flux jump was observed by MO imaging in our *ex situ* annealed MgB_2 film. Therefore, a low temperature quick MgB_2 phase formation could be beneficial for maintaining disorder in the film, and thus of importance for high performance MgB_2 film preparation.

The comparatively high oxygen content in the in situ films is revealed by EDS. A proportion of Oxygen may exist in the in situ film as nano-sized MgO particles, which could provide effective pinning centers and contributes to fine-grain structure, thus leading to a further enhancement of critical current density in high fields.

References:

[1] W. N. Kang, E.-M. Choi, H.-J. Kim, H.-J. Kim, and S.-I. Lee, Growth of superconducting MgB2 thin films via post annealing techniques, Physica C: Superconductivity **385,** 24-30 (2003).

[2] I. I. Mazin, O. K. Andersen, O. Jepsen, O. V. Delgov, J. Kortus, A. A. Golubov, A. B. Kuzmenko, and D. v. d. Marel, Two-gap Superconductivity in MgB_2: Clean or Dirty?, Phys. Rev. Lett. **89,** 107002 (2002).

[3] J. M. Rowell, The widely variable resistivity of MgB2 samples, Supercond. Sci. Technol. **16,** R17-R27 (2003).

[4] Y. Eltsev, S. Lee, K. Nakao, N. Chikumoto, S. Tajima, N. Koshizuka, and M. Murakami, Phys. Rev. B **65,** R140501 (2002).

[5] T. T. M. Palstra, B. Batlogg, R. B. v. Dover, L. F. Schneemeyer, and J. V. Waszczak, Critical currents and thermally activated flux motion in high-temperature superconductors, Appl. Phys. Lett. **54,** 763 (1989).

[6] T. T. M. Palstra, B. Batlogg, R. B. v. Dover, L. F. Schneemeyer, and J. V. Waszczak, Dissipative flux motion in high-temperature superconductors, Phys. Rev. B. **41,** 6621 (1990).

[7] A. Sidorenko, V. Zdravkov, V. Ryazanov, S. Horn, S. Klimm, R. Tidecks, A. Wixforth, Th. Koch, and T. Schimmel, Thermally Assisted Flux Flow in MgB2 : Strong Magnetic Field Dependence of the Activation Energy, cond-mat/0406062 (2004).

[8] T. Yang, Z. H. Wang, H. Zhang, Y. Nie, J. Fang, H. Luo, X. FWu, and S. Y. Ding, In-plane and out-of-plane magnetoresistivity in a MTG Er-doped YBCO crystal, Supercond. Sci. Technol. **15,** 586-591 (2002).

[9] N. Y. Fogel, V. G. Cherkasova, O. A. Koretzkaya, and A. S. Sidorenko, Thermally assisted flux flow and melting transition for Mo/Si multilayers, Phys. Rev. B. **55,** 85-88 (1997).

[10] S. Y. Xu, Q. Li, E. Wertz, Y. F. Hu, A. V. Pogrebnyakov, X. H. Zeng, X. X. Xi, and J. M. Redwing, High critical current density and vortex pinning of epitaxial MgB2 thin films, Physical Review B **68** (2003).

[11] M. J. Qin, S. Keshavarzi, S. Soltanian, X. L. Wang, H. K. Liu, and S. X. Dou, Sample-size dependence of the magnetic critical current density in MgB2 superconductors, Physical Review B **69** (2004).

[12] C. B. Eom, M. K. Lee, J. H. Choi, L. J. Belenky, X. Song, L. D. Cooley, M. T. Naus, S. Patnaik, J. Jiang, M. Rikel, A. Polyanskii, A. Gurevich, X. Y. Cai, S. D. Bu, S. E. Babcock, E. E. Hellstrom, D. C. Larbalestier, N. Rogado, K. A. Regan, M. A. Hayward, T. He, J. S. Slusky, K. Inumaru, M. K. Hass, and R. J. Cava, High Critical current Density and Enhanced Irreversibility Field in Superconducting MgB_2 Thin Films, Nature **411,** 558-560 (2001).

[13] A. Gurevich, S. Patnaik, V. Braccini, K. H. Kim, C. Mielke, X. Song, L. D. Cooley, S. D. Bu, D. M. Kim, J. H. Choi, L. J. Belenky, J. Giencke, M. K. Lee, W. Tian, X. Q. Pan, A. Siri, E. E. Hellstrom, C. B. Eom, and D. C. Larbalestier, Very

high upper critical fields in MgB2 produced by selective tuning of impurity scattering, Supercond. Sci. Technol. **17,** 278 (2004).

[14] T. H. Johansen, M. Baziljevich, D. V. Shantsev, P. E. Goa, Y. M. Galperin, W. N. Kang, H. J. Kim, E. M. Choi, M. S. Kim, and S. I. Lee, Complex Flux Dynamics in MgB_2 Films, Nature.

[15] Y. Bugoslavsky, L. Cowey, T. J. Tate, G. K. Perkins, J. Moore, Z. Lockman, A. Berenov, J. LMacManus-Driscoll, A. D. Caplin, L. F. Cohen, H. Y. Zhai, H. M. Christen, M. P. Paranthaman, D. H. Lowndes, M. H. Jo, and M. G. Blamire, Effective vortex pinning in MgB_2 thin films, Supercond. Sci. Technol. **15,** 1392-1397 (2002).

[16] D. H. A. Blank, H. Hilgenkamp, A. Brinkman, D. Mijatovic, G. Rijinders, and H. Rogalla, Superconducting Mg-B Films by Pulsed-laser Depostion in an in situ Two-step Process Using Multicomponent Targets, Appl. Phys. Lett. **79,** 394-396 (2001).

[17] W. Jo, J.-U. Huh, T. Ohnishi, A. F. Marshall, M. R. Beasley, and R. H. Hammond, Appl. Phys. Lett. **80** (2002).

[18] Y. Bugoslavsky, L. Cowey, T. J. Tate, G. K. Perkins, J. Moore, Z. Lockman, A. Berenov, J. L. MacManus-Driscoll, A. D. Caplin, L. F. Cohen, H. Y. Zhai, H. M. Christen, M. P. Paranthaman, D. H. Lowndes, M. H. Jo, and M. G. Blamire, Effective vortex pinning in MgB_2 thin films, Supercond. Sci. Technol. **15,** 1392-1397 (2002).

[19] I. I. Mazin and V. P. Antropov, Electronic Structure, Electron-phonon Coupling, and Multiband Effects in MgB_2, Physica C **385,** 49 (2003).

[20] R. F. Klie, J. C. Idrobo, N. D. Browning, K. A. Regan, N. S. Rogado, and R. J. Cava, Direct observation of nanometer-scale Mg- and B-oxide phases at grain boundaries in MgB_2, Appl. Phys. Lett. **79,** 1837-1839 (2001).

[21] J. C. Idrobo, S. Ogut, T. Yildirim, R. F. Klie, and N. D. Browning, Electronic and superconducting properties of oxygen-ordered MgB_2 compounds of the form $Mg_2B_3O_x$, Phys. Rev. B. **70,** 172503 (2004).

Chapter 5. Modification of MgB_2 thin film properties by Si addition

5.1 Introduction

In order to improve the performance of MgB_2 superconductor, enhancement of the pinning force in this material is very necessary. To this end, doping in MgB_2 bulk and tape has been carried out, using various elements or compounds. It has been shown that among the Li [1,2], C [3-7], Al [8,9], Si [2,3,10], Ti [11], SiC[12], SiO[4], B_4C [13], Y_2O_3 [14], and $ZrSi_2$ [15] doping materials reported for MgB_2 bulk and tapes , Si appears competitive with respect to the improvement in the pinning force as well as in maintaining the transition temperature [2,3,10]. The dopants work mainly in two ways: one is to substitute Mg or B atoms in the MgB_2 lattice with the dopant atoms, causing intra-grain scattering and an increase in the upper critical field (H_{c2}). For this kind of doping, two most intensively investigated dopants are C and Al; another way is to introduce dispersive inclusions, preferably nanometer-sized, to provide more pinning centers in the MgB_2 superconductor. According to the two-band phonon-mediated superconductivity revealed in MgB_2 [16-19], the orthogonality of the electron orbitals in the two bands of MgB_2 suppresses interband scattering [17], but only the interband scattering has a pair-breaking effect in the two-band superconductor. This is perhaps why the second type of dopant, which causes little interband scattering, does not significantly suppress the T_c in doped MgB_2.

Si easily reacts with a Mg + B mixture and forms Mg_2Si at a rather low temperature (600℃) [20]. It has been shown that after Si doping, the Mg_2Si phase formed inside the MgB_2 matrix is finely dispersed, and thus could function as a source of pinning centers without much suppression of the T_c [10]. On the other hand, it remains an open question if Si can substitute for Mg or B atoms in the MgB_2 lattice. A

recently reported research has shown that it is unlikely that Si enters the MgB_2 grains to any noticeable extent [21]. Thus it seems invalid to assume an intra-grain scattering caused by Si substitution. However, one can still anticipate Si-induced changes in the intra-grain properties that occur in some other ways, for example, by grain refining in MgB_2 due to Si-rich inclusions along the grain boundaries, which could also have an influence on the intra-grain scattering.

In general, the J_c of MgB_2 film is one order of magnitude or more higher than the J_c of the bulk material. The improvement of J_c in thin film was usually attributed to the much higher effective current-carrying area than in the bulk [22]. Another major characteristic for the MgB_2 films is the high oxygen level, which can also be regarded as oxygen doping [23]. Highly dispersed fine particles of MgO have been reported to form inside the films [23,24]. Klie et al. observed polycrystalline bulk MgB_2 with a scanning transmission electron microscope (STEM) and found several types of oxygen-enriched precipitates, namely BO_x (width<4nm) and BO_x-MgO_y-BO_z (width~10-15nm) along the grain boundaries [25], and coherent ordered oxide MgBO-nMgB_2-MgBO (20-100nm) inside the grains [26]. In films, the amount of precipitates could be very high. These precipitates are of favorable sizes to act as pinning centers, which improves the critical current density in the MgB_2 samples. Moreover, *in situ* annealed MgB_2 films have small grain sizes [27-29], which were assumed to be a consequence of the short annealing time in their fabrication. Since the grain boundaries are not weak links for MgB_2, this may lead to an increase in flux pinning due to the presence of a high volume of grain boundaries. By introducing Si into *in situ* annealed MgB_2 films, there could be some combined doping effects as a result of the coexistence of Si and oxygen. It is then interesting to see if controlled Si addition

could provide further pinning centers based on the strong pining that already exists and improve the superconducting properties in the *in situ* MgB_2 films.

In this chapter we show that a small amount of Si addition in MgB_2 film enhances the pinning force in the *in situ* films, and improves the J_c values at low temperatures while giving no significant further decrease of the T_c.

5.2 Si addition in the MgB2 films using PLD deposition

The Si addition is carried out based on the on-axis deposition conditions optimized in Chapter 3. The laser energy was 300mJ/pulse, resulting in a fluence of ~3.6 J/cm^2 on the target, and the pulse repetition during the deposition was 10Hz. A sapphire-R substrate with dimensions of about 5.5x2.5x0.5 mm^3 was attached to a resistive heater with silver paste. During the deposition, the substrate temperature was kept at 250℃.

To accomplish the doping, a target-switching method was employed. In this method, three targets were mounted onto a carousel. These targets were a stoichiometric MgB_2 target (84% density), a Si single crystal target, and a pure Mg target, respectively. The Si addition was achieved by sequentially ablating the MgB_2 and the Si target 10 times during the deposition. In each round, the Si target was ablated for various times from 1sec to 27sec, according to the different doping levels that we wished to achieve, and the MgB_2 target was ablated for 26-30sec to give the final films a similar thickness. For the undoped sample the deposition time was 5 min. Finally, a ~800nm cap layer of pure Mg was deposited onto the film surface to prevent Mg loss during the annealing process.

The entire deposition process was carried out in a high-purity Ar background gas at 120 mTorr, and only after a base vacuum better than 1x10^{-7} Torr was achieved inside the deposition chamber. After the deposition process, the pressure of the high

purity Ar was increased to 760 Torr, and then the sample was heated from 250℃ to 680℃ in 12 min and maintained at that temperature for 1 min. At the end of the holding time, the power was switched off, and the sample was free cooled down to room temperature at a cooling rate of about 50 ℃/min, following the detailed conditions given in Chapter 3.

For the preparation of the series of Si added MgB_2 film including the referential undoped MgB_2 film, the Laser energy during the deposition was set at 300 mJ/pulse, However, due to the aging of the KrF gas in the laser system, the actual laser energy drifted to a lower energy of about 250 mJ/pulse judging from the length of the plume, even though the shown laser energy is still 300mJ/pulse on the control panel indicator. The drifted laser energy resulted in a slower growth of the MgB_2 film and raised the chance of bringing more impurities from the background gas into the film. Though we have refilled the KrF gas every two months and kept adjusting the operating voltage according to the detected laser energy output, this aging effect is still not neglectable. This can probably explain why the T_c and J_c performance of the reference film is slightly lower than our best *in situ* MgB2 film #190903 studied in Chapter 3 & 4.

The thickness of the *in situ* annealed films is approximately 350nm according to cross-section observation by SEM. The nominal Si content added into MgB_2 films was controlled by the Si deposition time. The Si growth rate of ~0.2 nm/sec at 10Hz was calibrated on a bare substrate using the same deposition conditions as during the doping of the MgB_2 films. The Si content in the films was checked by energy dispersive x-ray spectroscopy.

5.3 Si content and distribution in the Si-added MgB_2 films

The Si content in the MgB_2 films was checked by EDS. Since boron is not quantitatively detectable in EDS, the Si content was calculated from the Si/Mg ratio, assuming two circumstances: a) only MgB_2 and Si phases were present; and b) only MgB_2 and Mg_2Si phases were present in the *in situ* annealed films. The discrepancy in the Si content between the nominal and the detected value is large due to the probable existence of other phases, such as MgB_4, MgO or excess Mg in the *in situ* annealed films. However, the XRD results of the films cannot show any such impurity peaks or even MgB_2 peaks, which may be caused by the small-grain size or the incomplete crystallization of the *in situ* annealed films. The nominal Si content and the detected Si content in the MgB_2 films together with magnetic $T_{c\ onset}$ and transport $T_{c\ onset}$ values are listed in Table 5-1. In the following text, we refer to the nominal Si content only.

Table 5-1. Si content and corresponding T_c in the in situ annealed MgB_2 films produced by PLD.

Sample No.	0	1	2	3	4	5	6
Nominal Si content (wt%)	0	1.5	3.5	5	7	11	18
Measured Si content (wt%) -assuming MgB_2 +Si	_	0.6	1.6	2.0	5.9	8.6	11.4
Measured Si content (wt%) -assuming MgB_2+Mg_2Si	_	0.6	1.7	2.1	6.2	10.0	13.9
Magnetic $T_{c\ onset}$ (K)	27	27	26	26	24	25	23
Transport $T_{c\ onset}$ (K) - of 90% ρ_{40K}	32.2	30.4	30.4	28.7	28.8	28.8	24.3

For different Si addition levels, the Si deposited on each layer is a few angstroms thick for several seconds of deposition time. This short deposition time usually gives separated islands instead of a continuous film. As shown in the AFM image (Fig.5-1), flat islands of about 100nm diameter are presented on the surface of a polished Al_2O_3-R substrate after a 5sec 10Hz Si deposition. In our Si added MgB_2 films, a similar Si

added layer was inserted after approximately each 35nm of MgB_2 film, along the normal axis of the 350nm-thick film. Based on this fine distribution of Si, we assume that Si is spatially homogenous inside the resulting MgB_2 films, and a substantial reaction between the dispersed Si and the matrix may take place after the *in situ* annealing.

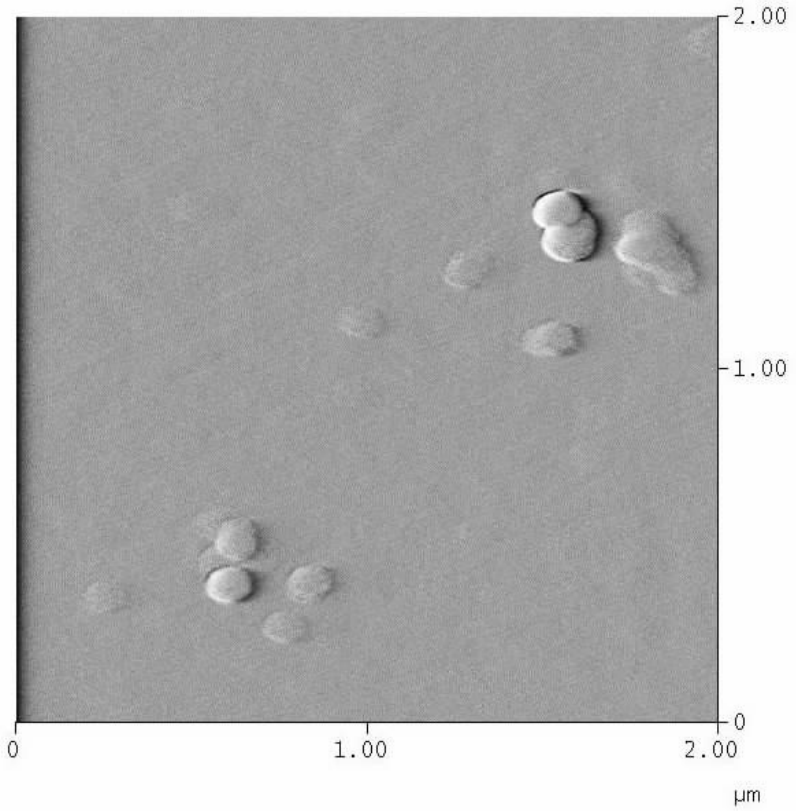

Fig. 5-1. AFM deflection image of Si islands on sapphire-R substrate deposited for 50 pulses (10Hz, 5sec). The laser fluence is 300mJ/pulse.

Figure. 5-2 shows a mapping of the Si distribution by EDS in the 3.5% and 11% Si added films. The surface of the Si added MgB_2 films is similar to the SEM image of the undoped film, which has a large number of particulates on its surface. The particulates were most probably splashed from the MgB_2 target onto the film during the MgB_2 deposition process. The Si distribution appears to be more homogeneous in the 3.5% Si film than in the 11% Si film. Some Si concentrations in the 11% Si doped

film represent Si droplets, and could be attributed to the splashing effect too. Between the droplets, the distribution of Si appears to be homogenous. In the process of assessing the Si content of the films by EDS, only the areas between the droplets were considered for analysis.

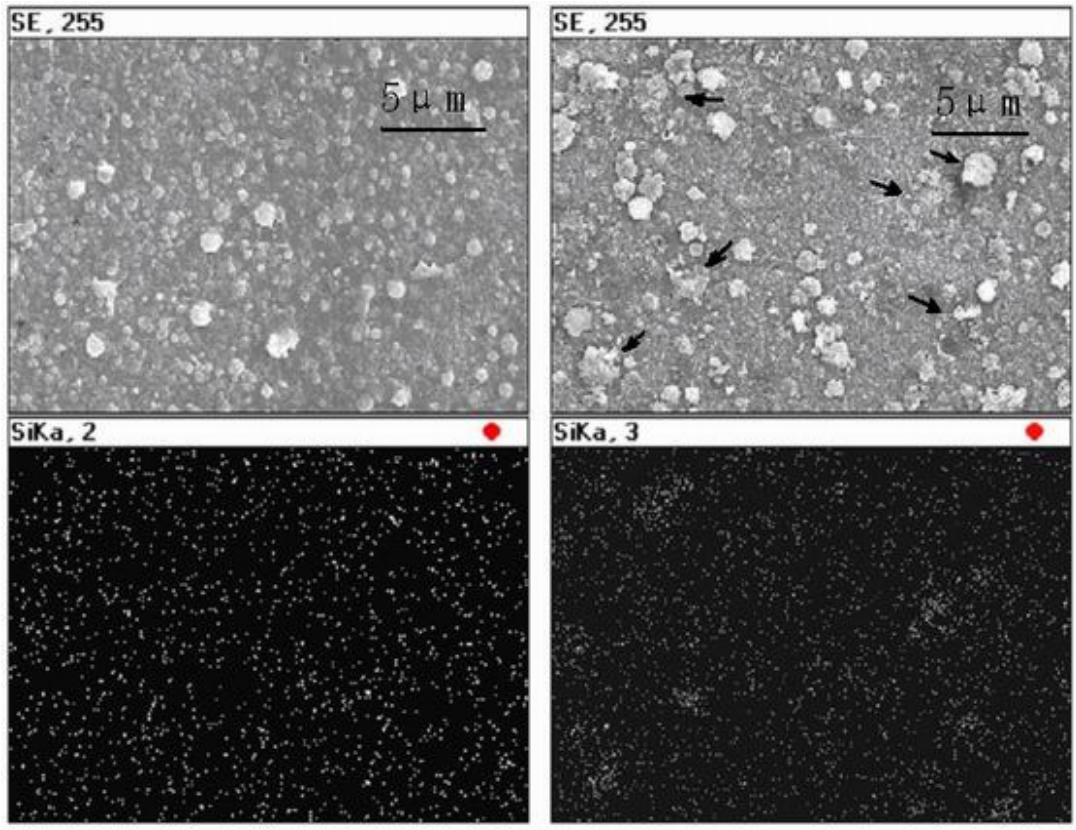

a b

Fig. 5-2. EDS Si mapping in the Si doped MgB_2 films. The upper part contains SEM secondary electron images, and the lower part the distribution of Si. a: 3.5% Si addition, b: 11% Si addition. The arrows indicate the Si-rich spots.

5.4 T_c and J_c dependence on the Si addition level

The zero field cooled and field cooled DC magnetization curves for the films with different Si content are shown in Fig.5-3. The undoped MgB_2 film has a suppressed $T_{c\ onset}$ of 27K, and shows a very wide transition width ΔT, revealing an inhomogeneous superconducting transition. This could be a consequence of high level disorders in the

film, which are probably caused by the oxygen contamination introduced during the deposition and an insufficient crystallization due to the short annealing time. From Fig.5-3 we find that the transition width is slightly narrowed with moderate Si doping. This seems in agreement with the fact that Si is helpful for MgB_2 phase formation [21]. However, further work is still necessary to clarify this point. The $T_{c\ onset}$ of 1.5% Si MgB_2 film is same as that of the undoped film. The $T_{c\ onset}$ values remain around 25K up to a doping level of 11% Si. A further increase in the Si doping level to 18% results in a significant suppression of T_c to 23K. The same trend of T_c change was also revealed in the resistivity measurements listed in Table 5-1. The magnetic T_c is lower than the transport T_c of the same set of samples. The difference may come from the fact that the resistivity measurement could be more influenced than the magnetization by surface effects. The small change in $T_{c\ onset}$ with the Si addition level indicates that Si does not go into the MgB_2 lattice, which agrees with the observed absence of Si in MgB_2 grains in the bulk Mg-B-Si system [21].

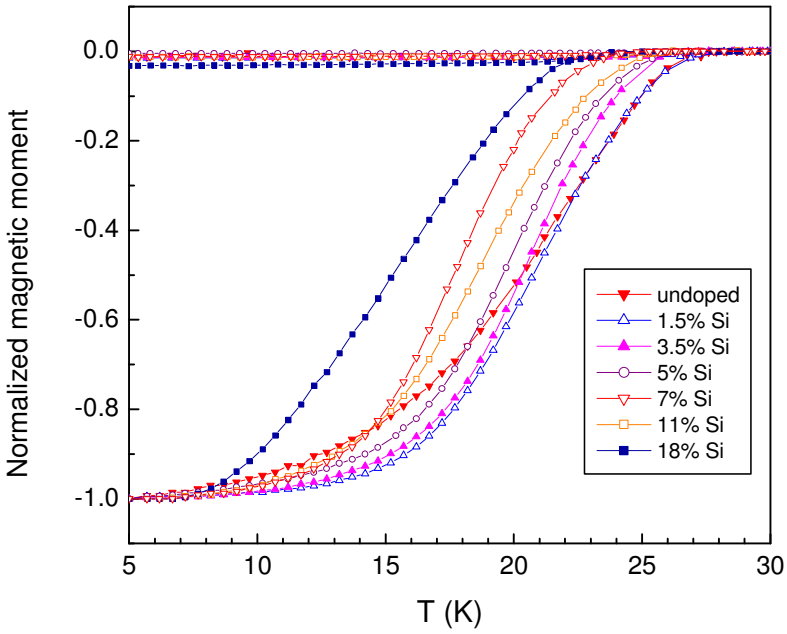

Fig. 5-3 DC magnetization curves of the films with different Si doping levels. The applied field is 25Oe for both ZFC and FC measurements.

The magnetic J_c was calculated from the magnetization loops based on the Bean model. Since the magneto-optical image of the *in situ* annealed films shows homogeneous flux penetration all over this type of MgB_2 film, the equation is valid for calculating the J_c values of the films. All the samples have a similar shape and dimensions (~0.55cm x 0.25cm x 350nm), so the results could be reliable in revealing the comparative changes of J_c with different Si addition levels.

The change in J_c with Si addition is shown in Fig.5-4. At 5K, the J_c values for both the 1.5% and 3.5% Si films are increased compared with the undoped film. The 3.5% Si film has the highest J_c, about 1.3x 10^6 A/cm^2 in a 1.5T field and 4x10^5 A/cm^2 in a 5T field, which is generally about fifty percent higher than the J_c value for the undoped MgB_2 film. In low fields at 5K, the J_c curves show flux jump indicating magneto-thermal instability in the films. At 10K, the improvement in J_c is much smaller than at 5K, especially in the high field regime. The change in J_c for samples with up to 5% Si addition becomes unnoticeable at 15K. The J_c is significantly suppressed by 7%, 11% and 18% Si addition at all the measurement temperatures (5K, 10K and 15K). The highest J_c in 5K and 10K is achieved by 3.5% Si addition using the current method. It is not quite clear whether the good homogeneity of the Si distribution in the 3.5wt% Si film is playing an important role in the J_c improvement. Therefore, the possibility of obtaining optimal J_c improvement with a higher doping level should not be ruled out.

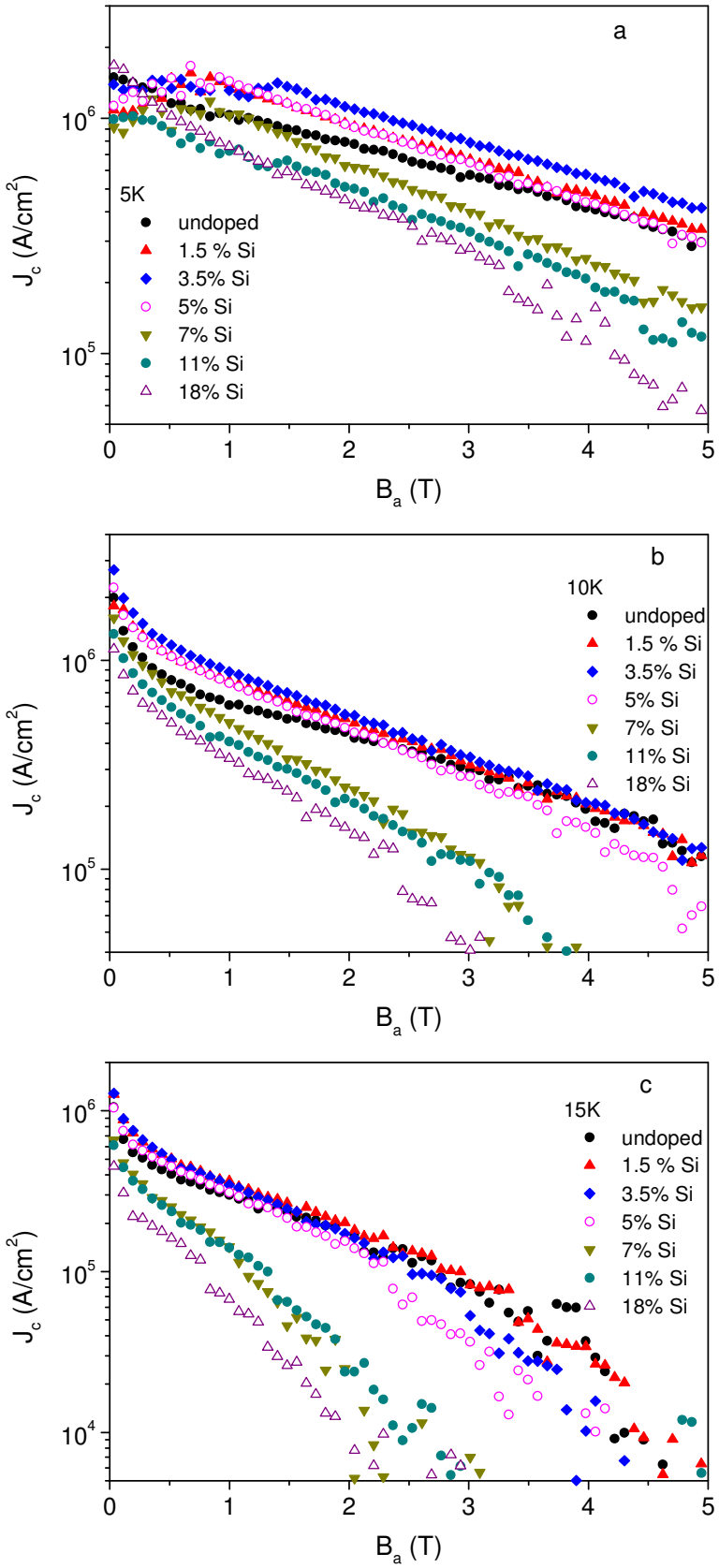

Fig. 5-4. J_c values with different Si doping levels. a: at 5K, b: at 10K, c: at 15K. The applied field B_a is perpendicular to the film plane.

5.5 Irreversibility field, upper critical fields and residual resistivity in the Si-added films

Figure 5-5 shows the irreversibility lines and upper critical fields of the 3.5% Si doped and undoped MgB_2 films. It can be seen that the H_{irr} for the Si doped films is higher than that for the undoped sample when the temperature is lower than 24K, which is evidence for a pinning enhancement in the 3.5% Si added films. We can also see a similar trend in the H_{c2} curves of the films. The increase in the slope of the $H_{c2}(T)$ curve for the 3.5% Si doped film and the similarity in T_c values between the 3.5% Si film and the undoped film indicate some degree of enhancement of the intra-band scattering, assuming the film is still in the two-gap superconductor regime. Given that Si does not go into the MgB_2 lattice [21], the scattering may come from some other imperfections in the Mg or B plane, such as Mg vacancies, introduced due to the Si addition in the samples.

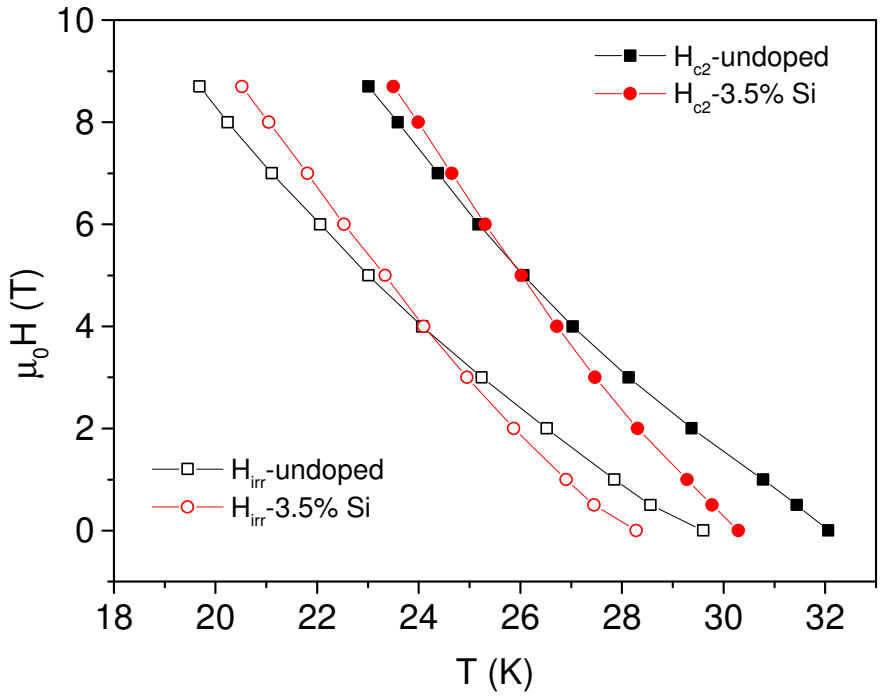

Fig. 5-5. Irreversibility lines and upper critical fields of the 3.5% Si doped and undoped MgB_2 films.

Figure 5-6 shows the temperature dependence of the resistivity of three films (undoped, 3.5% Si, and 5% Si) in applied fields from 0 to 8.7 T. The error in the resistivity values is about 15%, due to the uncertainties in measuring the film dimensions. An up-shift of the T_c's in high fields is clearly seen in the 3.5% Si film, whereas the whole set of T_c curves slides down to lower temperatures in the 5% Si film. According to the resistivity results, up to 18% Si addition, ρ_{40K} increases with the increasing Si addition level. The residual resistivity ratio ($RRR_{300\text{-}40K}$) remains approximately at the same level, varying randomly from 1.05 to 1.2 for all the samples. The values of ρ_{300K} (150~700μΩ cm) of our Si doped films are in the intermediate resistivity regime for MgB_2 [30], indicating a high disorder level inside the MgB_2 grains.

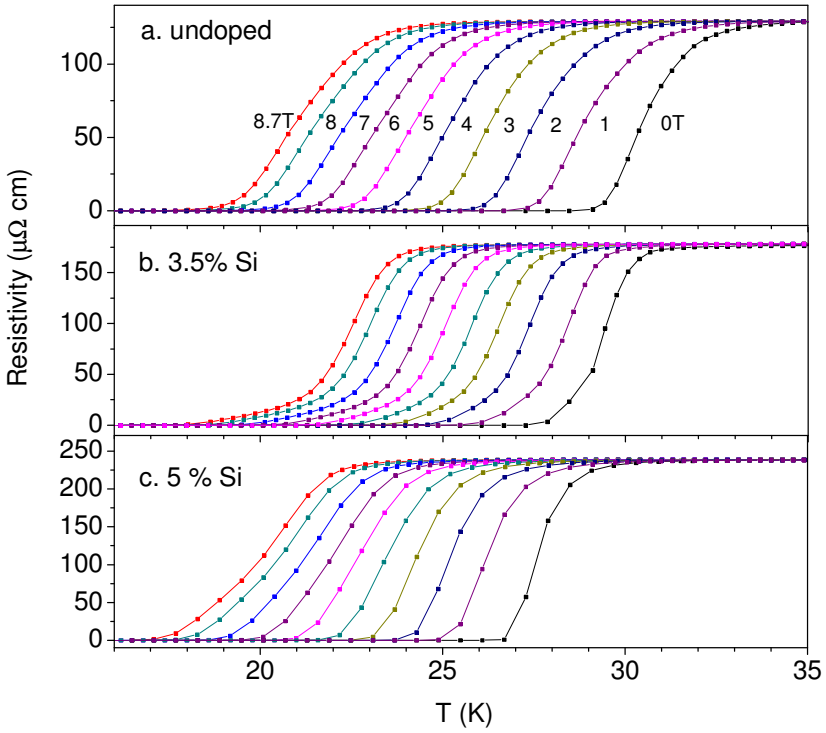

Fig. 5-6. The resistivity versus temperature curves in fields from 0T to 8.7T. a: undoped film; b: 3.5wt% Si film; c: 5wt% Si film.

5.6 Discussion on the correlation between the performance enhancement and the Si addition level

Compared with MgB_2 bulk, MgB_2 thin film is usually of higher density and has better connections between the grains. For bulk doping, an increase in J_c could be partially attributed to the improvement in density and in the connections between the MgB_2 grains. Therefore, a high doping level of about 10% is essential [15]. However, the density of films is unlikely to be improved by these low level Si additions.

One could detect an unambiguous enhancement in pinning if there is an increase in J_c values after doping the films. With Si addition in MgB_2 film, the effective current carrying area probably decreases due to the introduction of more volume of non-superconducting phase. The consequent weak links could lead to the deterioration in J_c and the increase in resistivity that is seen in our Si added MgB_2 films. We plot the curves of J_c and resistivity versus Si addition levels in Fig. 5-7. Since the magnetic J_c at 0T and 5K is difficult to measure owing to the flux jumps shown in Fig. 5-4(a), we pick J_c values from the points at 1.5T at 5K. The overall trend for ρ_{40K} is to increase with the Si addition level. The inversely proportional relation between the J_c and resistivity of the samples with high Si content could be attributed to a reduction in the effective current carrying area with increasing the amount of Si, according to Rowell's study on the J_c-resistivity correlation [30]. For the samples with lower Si levels, there is a maximum value of J_c with 3.5% Si addition, which may be explained as the result of a competition between the pinning enhancement and the weakening of inter-grain links. Therefore, the enhancement of pinning and improvement of J_c can only be achieved with small Si addition levels.

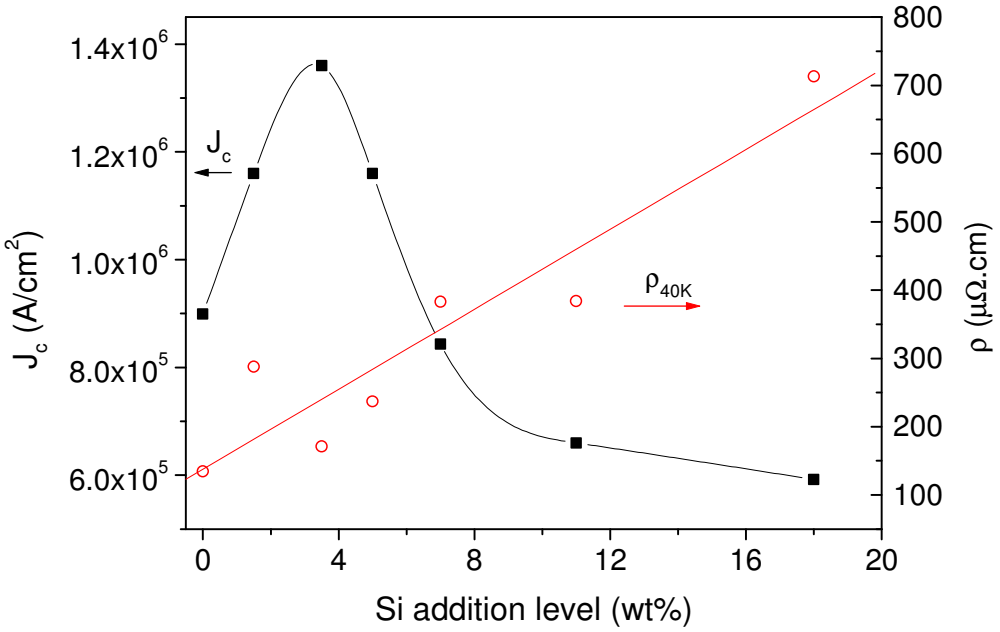

Fig. 5-7. The J_c and ρ_{40K} versus Si addition level in the doped films. The solid squares represent the magnetic J_c at 5K and 1.5T. The open circles represent residual resistivity ρ_{40K}.

5.7 Conclusions

We studied a series of Si addition levels into the *in situ* annealed MgB_2 film by a target-switching method. The Si dopant is highly dispersed inside the resulting films. A clear improvement in J_c by low level Si doping in MgB_2 *in situ* films was achieved without a significant decrease of the T_c. The highest improvement in J_c was obtained for 3.5wt% Si addition using this method. The slope of the $H_{c2}(T)$ curve for 3.5% Si added film is higher than that of the undoped film, indicating an increase in intra-grain scattering.

References:

[1] Y. G. Zhao, X. P. Zhang, P. T. Qiao, H. T. Zhang, S. L. Jia, B. S. Cao, M. H. Zhu, Z. H. Han, X. L. Wang, and B. L. Gu, Effect of Li Doping on Structure and Superconducting Transition Temperature of $Mg_{1-x}Li_xB_2$, Physica C **361,** 91 (2001).

[2] M. R. Cimberle, M. Novak, P. manfrinetti, and A. Palenzona, Magnetic characterization of sintered MgB_2 samples: effect of the substitution or doping with Li, Al and Si, Supercond. Sci. Tech. **15,** 34 (2002).

[3] S. H. Zhou, A. V. Pan, M. J. Qin, X. L. Wang, H. K. Liu, and S. X. Dou, Effects of Si and C Doping on the Superconducting Properties of MgB_2, Advances in Cryogenic Engineering: Transactions of the International Cryogenic Materials Conference **711,** 554-560 (2004).

[4] A. Matsumoto, H. Kumakura, H. Kitaguchi, and H. Hatakeyama, Effect of SiO2 and SiC doping on the powder-in-tube processed MgB_2 tapes, Supercond. Sci. Technol. **16,** 926 (2003).

[5] A. V. Pogrebnyakov, J. M. Redwing, J. E. Giencke, C. B. Eom, V. Vaithyanathan, D. G. Schlom, A. Soukiassian, S. B. Mi, C. L. Jia, J. Chen, Y. F. Hu, Y. Cui, Q. Li, and X. X. Xi, Carbon-doped MgB_2 thin films by hybrid physical-chemical vapor deposition, IEEE Trans. on Appl. Superconductivity **15,** 3321 (2005).

[6] A. V. Pogrebnyakov, X. X. Xi, J. M. Redwing, V. Vaithyanathan, D. G. Schlom, A. Soukiassian, S. B. Mi, C. L. Jia, C. B. Eom, J. Chen, Y. F. Hu, Y. Cui, and Q. Li, Properties of MgB_2 thin films with carbon doping, Appl. Phys. Lett. **85,** 2017-2019 (2004).

[7] V. Braccini, A. Gurevich, J. E. Goecke, M. V. Jewell, C. B. Eom, D. C. Larbalestier, A. Pogrebnyakov, Y. Cui, B. T. Liu, Y. F. Hu, H. M. Redwing, Q. Li, X. X. Xi, P. K. Singh, T. Gandikota, J. Kim, B. Wilkens, N. Newman, J. Rowell, B. Moeckly, B. Ferrando, C. Tarantini, M. Marre, M. Putti, V. Ferdeghini, T. Vaglio, and E. Haanappel, High-field superconductivity in alloyed MgB_2 thin films, Phys. Rev. B **71,** 012504 (2005).

[8] M. Putti, C. Ferdeghini, M. Monni, I. Pallecchi, C. Tarantini, P. Manfrinetti, A. Palenzona, D. Daghero, R. S. Gonnelli, and V. A. Stepanov, Critical field of Al-doped MgB_2 samples: Correlation with the suppression of the σ-band gap, Phys. Rev. B. **71,** 144505 (2005).

[9] M. Putti, M. Affronte, P. Manfrinetti, and A. Palenzona, Effects of Al doping on the normal and superconducting properties of MgB_2: A specific heat study, Phys. Rev. B **68,** 094514 (2003).

[10] X. L. Wang, S. H. Zhou, M. J. Qin, P. R. Munroe, S. Soltanian, H. K. Liu, and S. X. Dou, Significant enhancement of flux pinning in MgB_2 superconductor through nano-Si addition, Physica C **385,** 461-465 (2003).

[11] B. Q. Fu, Y. Feng, G. Yan, Y. Zhao, A. K. Pradhan, C. H. Cheng, P. Ji, X. H. Liu, C. F. Liu, L. Zhou, and K. F. Yau, High critical current density in Ti-doped MgB_2/ Ta/Cu tape by powder-in-tube process, J. Appl. Phys. **92,** 7341-7344 (2002).

[12] S. X. Dou, S. Soltanian, J. Horvat, X. L. Wang, P. Munroe, S. H. Zhou, M. Ionescu, H. K. Liu, and M. Tomsic, Enhancement of the Critical Current Density and Flux Pinning of MgB_2 Superconductor by Nanoparticle SiC Doping, Appl. Phys. Lett. **81,** 3419 (2002).

[13] A. Yamamoto, J.-i. Shimoyama, S. Ueda, I. Iwayama, S. Horii, and K. Kishio, Effects of B4C doping on critical current properties of MgB_2 superconductor, Supercond. Sci. Technol. **18,** 1323-1328 (2005).

[14] J. Wang, Y. Bugoslavsky, A. Berenov, L. Cowey, A. D. Caplin, L. F. Cohen, J. L. MacManus-Driscoll, L. D. Cooley, X. Song, and D. C. Larbalestier, High critical current density and improved irreversibility field in bulk MgB_2 made by a scaleable, nanoparticle addition route, Appl. Phys. Lett. **81,** 2026-2028 (2002).

[15] Y. Ma, H. Kumakura, A. Matsumoto, H. Hatakeyama, and K. Togano, Improvement of critical current density in Fe-sheathed MgB_2 tapes by ZrSi2, ZrB2 and WSi2 doping, Supercond. Sci. Technol. **16,** 852-856 (2003).

[16] A. Y. Liu, I. I. Mazin, and J. Kortus, Beyond Eliashberg superconductivity in MgB_2: anharmonicity, two-phonon scattering, and multiple gaps, Phys. Rev. Lett. **87,** 087005 (2001).

[17] I. I. Mazin, O. K. Andersen, O. Jepsen, O. V. Delgov, J. Kortus, A. A. Golubov, A. B. Kuzmenko, and D. v. d. Marel, Two-gap Superconductivity in MgB_2: Clean or Dirty?, Phys. Rev. Lett. **89,** 107002 (2002).

[18] I. I. Mazin and V. P. Antropov, Electronic Structure, Electron-phonon Coupling, and Multiband Effects in MgB_2, Physica C **385,** 49 (2003).

[19] H. J. Choi, M. L. Cohen, and S. G. Louie, Anisotropic Eliashberg theory of MgB_2: Tc, isotope effects, superconducting energy gaps, quasiparticles, and specific heat, Physica C **385,** 66 (2003).

[20] T. He, J. M. Rowell, and R. J. Cava, Appl. Phys. Lett. **80,** 291 (2002).

[21] L. D. Cooley, K. Kang, R. Klie, Q. Li, A. Moodenbaugh, and R. Sabatini, Formation of MgB_2 at low temprtatures by reaction of Mg with B6Si, Supercond. Sci. Technol. **17,** 942 (2004).

[22] J. M. Rowell, S. Y. Xu, X. H. Zeng, A. V. Pogrebnyakov, Q. Li, X. X. Xi, J. M. Redwing, W. Tian, and X. Pan, Critical current density and resistivity of MgB_2 films, Appl. Phys. Lett. **83,** 102 (2003).

[23] C. B. Eom, M. K. Lee, J. H. Choi, L. J. Belenky, X. Song, L. D. Cooley, M. T. Naus, S. Patnaik, J. Jiang, M. Rikel, A. Polyanskii, A. Gurevich, X. Y. Cai, S. D. Bu, S. E. Babcock, E. E. Hellstrom, D. C. Larbalestier, N. Rogado, K. A. Regan, M. A. Hayward, T. He, J. S. Slusky, K. Inumaru, M. K. Hass, and R. J. Cava, High Critical current Density and Enhanced Irreversibility Field in Superconducting MgB_2 Thin Films, Nature **411,** 558-560 (2001).

[24] A. Gurevich, S. Patnaik, V. Braccini, K. H. Kim, C. Mielke, X. Song, L. D. Cooley, S. D. Bu, D. M. Kim, J. H. Choi, L. J. Belenky, J. Giencke, M. K. Lee, W. Tian, X. Q. Pan, A. Siri, E. E. Hellstrom, C. B. Eom, and D. C. Larbalestier, Very high upper critical fields in MgB_2 produced by selective tuning of impurity scattering, Supercond. Sci. Technol. **17,** 278 (2004).

[25] R. F. Klie, J. C. Idrobo, N. D. Browning, K. A. Regan, N. S. Rogado, and R. J. Cava, Direct observation of nanometer-scale Mg- and B-oxide phases at grain boundaries in MgB_2, Appl. Phys. Lett. **79,** 1837-1839 (2001).

[26] R. F. Klie, J. C. Idrobo, N. D. Brtowning, A. Serquis, Z. Y. T, X. Z. Liao, and F. M. Mueller, Observation of coherent oxide precipitates in polycrystallline MgB_2, Appl.Phys. Lett. **80,** 3970 (2002).

[27] X. H. Zeng, A. Sukiasyan, X. X. Xi, Y. F. Hu, E. Wertz, W. Tian, S. S. H, X. Q. Pan, J. Lettieri, D. G. Schlom, C. O. Brubaker, Z. K. Liu, and Q. li, Superconducting Properties of Nanocrystalline MgB_2 Thin Films Made by an in-situ Annealing Process, Appl. Phys. Lett. **79,** 1840-1842 (2001).

[28] Y. Zhao, M. Ionescu, A. V. Pan, and S. X. Dou, In situ annealing of superconducting MgB_2 films prepared by pulsed laser deposition, Supercond. Sci. Technol. **16,** 1487 (2003).

[29] H. Y. Zhai, H. M. Christen, L. Zhang, C. Cantoni, M. Parathaman, B. C. Sales, D. K. Christen, and D. H. Lowndes, Superconducting magnesium diboride films on Si

with Tc0~24 K grown via vacuum annealing from stoichiometric precursors, Appl. Phys. Lett. **79,** 2603 (2001).

[30] J. M. Rowell, The widely variable resistivity of MgB_2 samples, Supercond. Sci. Technol. **16,** R17-R27 (2003).

Chapter 6. Off-axis MgB_2 films using an *in situ* annealing pulsed laser deposition method

Since the discovery of superconductivity in MgB_2 2001, a variety of methods have been used for the preparation of MgB_2 films, such as physical vapor deposition (PVD) [1-5], chemical vapor deposition (CVD) [6], and electrochemical plating [7]. T_c's of 39 K or even higher have been achieved in *ex situ* annealed PLD films [1] and Hybrid Physical-CVD (HPCVD) films [6]. The *in situ* annealed PLD films generally showed a considerably suppressed T_c of ~25 K due to oxygen contamination and incomplete crystallization [8-11]. Although the T_c value still requires improvement, the PLD procedure with an *in situ* annealing seems very attractive due to the fact that it requires comparatively simple equipment and is technically capable of preparing multi-layer films. In Chapter 3 we have shown that the T_c of the *in situ* annealed PLD MgB_2 films can be significantly improved to 34 K, and the films show a combination of good superconducting properties [12].

However, the *in situ* annealed MgB_2 films prepared by PLD generally have many sub-micron and micron-sized particulates on their surfaces published in the literature and our own work [10-12]. The bad surface quality of this type of films hinders its applications in superconducting junctions or any other electronic devices. The presence of particulates on PLD films results from the splashing effect, which brings the melted droplets or detached fragments of the target to the films surface. This is also a common problem of PLD films of a number of materials. Several methods have been developed to prevent particulates on PLD thin films [13,14]. Probably the most accepted solution is to apply an off-axis geometry, which places the substrate perpendicular or even at 180° relative to the target [15,16]. The off-axis method has been proved effective and is easily adapted to PLD optical and electronic thin films,

including HTS thin films, [14-18]. However, we are not aware of any report on off-axis deposition of superconducting MgB_2 films.

In this chapter, we report on the growth of smooth MgB_2 thin films with PLD using the off-axis geometry.

6.1 Fundamentals of off-axis deposition

Due to considerations on deposition rate, the substrates are usually placed parallel with and facing the target in a PLD deposition process. This geometry is usually called on-axis geometry. The off-axis deposition geometry was first introduced in sputtering deposition to reduce the big particles sputtered from the target. In a off-axis geometry, the substrate is usually placed at an angle of 90-180º to the target. The basic mechanism for off-axis deposition is the scattering of light species by the background gas. These light species travel in a randomized path due to interaction between the plume and the background gas, whereas the trajectory of big fragments and droplets are not changed by background gas and pass by the film surface (see Fig 6-1: the substrate is perpendicular to the target surface, and Fig 6-2: the substrate is 180° to the target surface). As a result, the surface roughness of the off-axis deposition film is dramatically improved [16].

There are some issues during the off-axis deposition that may prevent the successful deposition of MgB_2 thin films: 1) the deposition rate is significantly decreased by the off-axis geometry. In the deposition process of materials active elements, the slow growth rate could also increase the level of impurities such as oxygen, which will get a higher chance to react with or be adsorbed by the fresh film surface. 2) in a off-axis geometry, both the thickness and homogeneity could be adversely affected. Due to deference in the distance from the target between

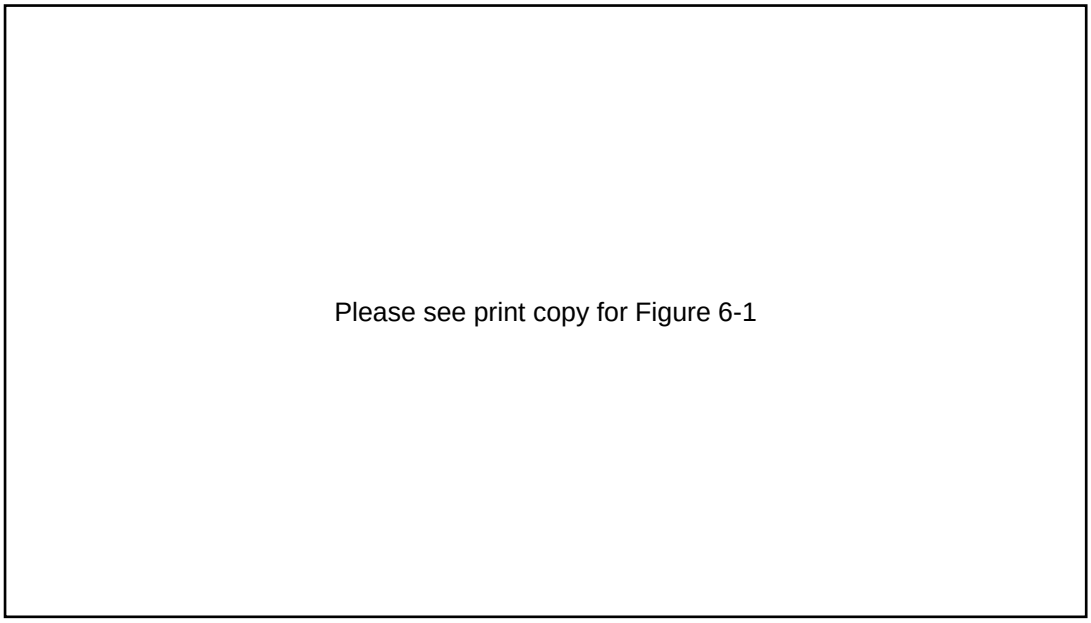

Fig.6-1 Illustration of on axis deposition and off-axis deposition. Figure cited from ref [19]

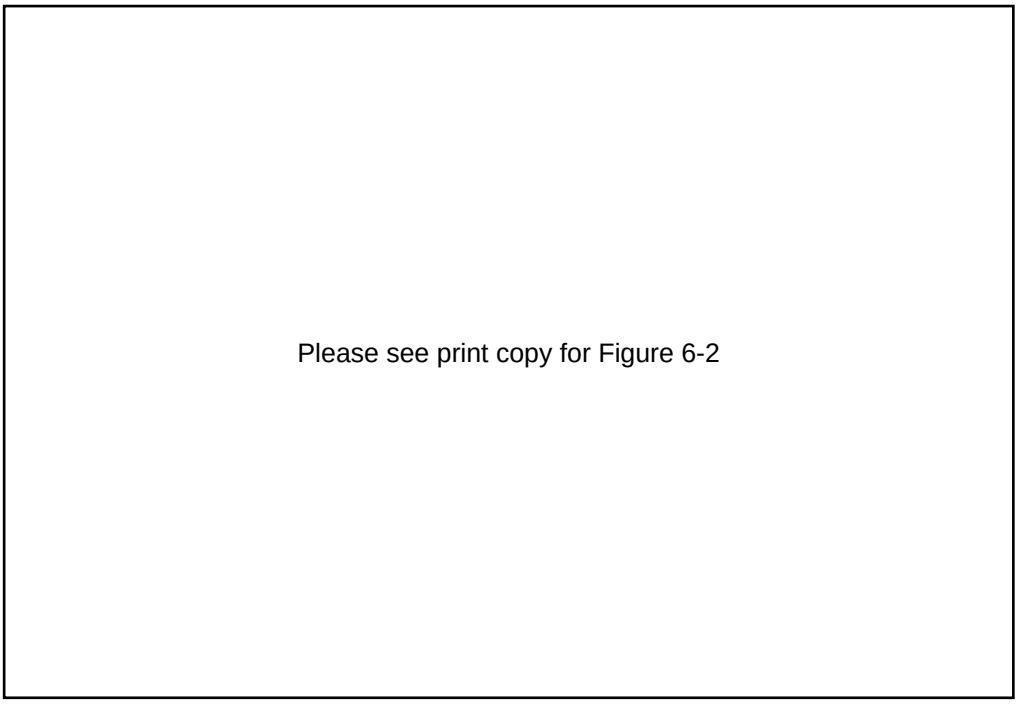

Fig.6-2 Kennedy 's design of the off-axis deposition of smooth YBCO film. Figure cited from [16].

different parts of the substrate, the deposition rate could be very different in different parts of the substrate. Atoms with different masses will be scattered by the background gas atoms differently. As the result, the population of light atoms scattered along an off-axis direction will be larger on those parts of the substrate that are closer to the target, while the heavy atoms or clusters could concentrate in those parts which are further away from the target.

The first issue is inevitable. To reduce the impurity contamination, one can improve the base vacuum to reduce the impurity level in the background gas. The second issue could be solved by rotating the substrate in-plane, and thus increase the film homogeneity. So far, no report on off-axis PLD deposition of MgB_2 films has been reported except the present work.

6.2 Experimental details of the off-axis PLD deposition in this work

The PLD process is carried out in the same system as the on-axis deposition process that was described in Chapter 3. The stoichiometric MgB_2 target (84% density) and a magnesium target were set on a carousel in the chamber. Sapphire-C cut substrates with dimensions of about 6×2 mm^2 were used. For normal on-axis deposition, the substrate was mounted onto the resistive heater facing the target, using silver paste. In off-axis geometry, the substrate was parallel to the normal axis of the target surface and aligned to the center of the laser spot. The distance between the target and the substrate was about 25 mm for the off-axis deposition. A piece of metal screen was also attached to the heater just in front of the substrate to construct a shaded off-axis geometry [15], as shown in Fig.6-3.

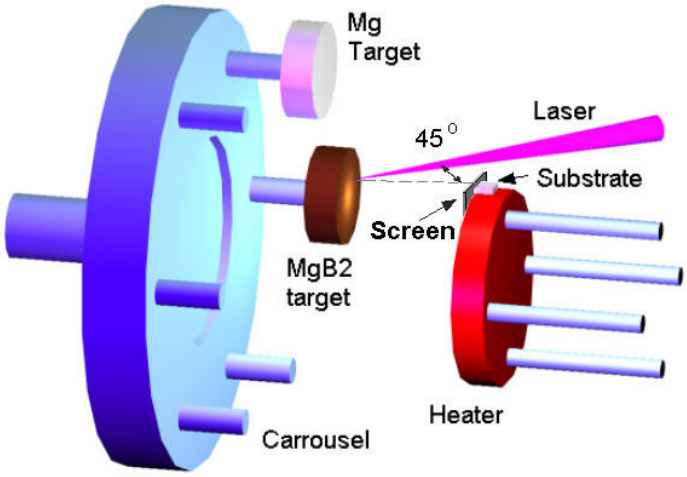

Fig. 6-3. Schematic Illustration of the off-axis deposition geometry for MgB_2 thin film deposition.

The laser ablation process is exactly the same as our normal on-axis deposition described in Chapter 3. The laser beam was focused to an elliptical spot of ~7×1.5 mm^2 on the stoichiometric MgB_2 target with a density of 84%. The chamber was first evacuated to a base vacuum of ~8×10^{-8} Torr and then filled with high purity argon to 120 mTorr as the background gas. During the deposition, the heater was kept at 250℃. At the end of the deposition, the Mg target was switched to the depositing position to provide a protective Mg cap-layer. This Mg layer was controlled to be ~800nm thick. Then the Ar pressure was increased to 760 Torr before the *in situ* annealing. The films were heated to 635-660℃ in 12 min and kept at that temperature for 1min. The power supply to the heater was then switched off, and the sample was cooled together with the heater at a cooling rate of approximately 50℃/min. Before the deposition, the temperature difference between the film position and the control thermocouple was calibrated. The annealed off-axis films have a thickness of 400-600nm, as detected by atomic force microscopy.

The surface of the *in situ* annealed films was examined by scanning electron microscopy, and the surface topography was further studied by AFM. We measured the temperature dependence of the resistivity in applied magnetic fields on a PPMS-9T magnetometer using a standard four-probe method and a dc current density of 10 A/cm^2. In both H//*ab*-plane and H⊥*ab*-plane cases, the testing current was perpendicular to the applied field. The hysteresis loops were measured on an MPMS-5T SQUID magnetometer with the applied field perpendicular to the film surface.

6.3 Optimization of the off-axis preparation parameters

To improve the surface quality of the off-axis films while maintaining a good Tc and a reasonable deposition rate, we tested a few off-axis deposition conditions. We also have examined the influence of substrate temperature during the deposition on the Tc of the resultant off-axis films.

6.3.1 The influence of laser energy and growth rate on the surface morphology of off-axis MgB_2 film.

We compare the surface of the off-axis films under different deposition conditions and an on-axis film in Fig.6-4. For the on-axis deposited MgB_2 film, the film surface is covered with densely packed particulates, generally about one-micron in diameter. This kind of rough surface is quite common in the reported *in situ* annealed MgB_2 films [10,11]. The off-axis deposited films generally do not contain many micron-sized particulates. However the surface roughness is not always low in off-axis deposited MgB_2 films. As shown in Fig.6-4(b), under a comparatively high laser energy flux (500 mJ/pulse) and laser repetition frequency (10 Hz), the film surface looks loose and rough although few big particulates were found. At a lower laser energy flux (300 mJ/pulse) or smaller frequency (5 Hz), the films (films c and d respectively) are

smoother. The long bumps observed on the surface of film (c) in Fig. 6-4 are droplets splashed from the MgB_2 target that landed on the inclined surface of the film, due to slight exposure of the substrate surface to the laser spot. With a shading screen in place, these long-shape features were effectively prevented, as shown in Fig.6-4(d). The number of micron-sized particulates on film (d) determined from SEM surface images is less than 1/100μm^2, which meets the general surface requirement for electronic films. In the remaining part of this chapter, we only refer to the best off-axis films prepared under the same conditions as our off-axis film (d).

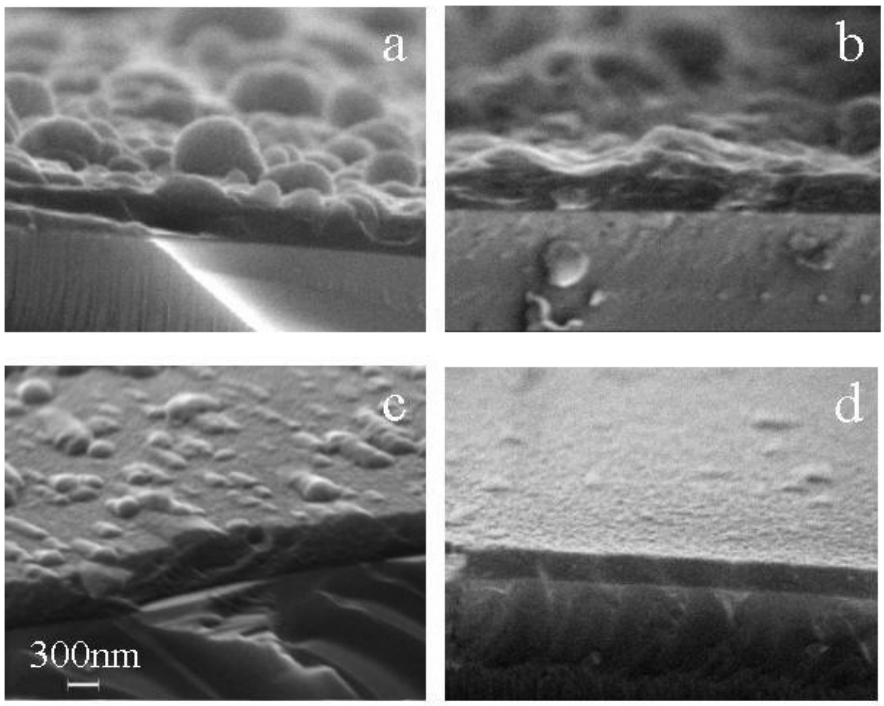

Fig.6-4. SEM cross-sectional images of four films on Al_2O_3 –C substrates using different deposition conditions, namely (a): on-axis deposition, laser energy flux = 300 mJ/pulse, laser repetition frequency = 10 Hz, growth rate=12 Å/sec; (b) off-axis, E=500mJ/pulse, F=10Hz, 16Å/sec; (c) off-axis, E=300mJ/pulse, F=10Hz, 4 Å/sec; and (d) shaded off-axis, E=500mJ/pulse, F=5Hz, 2 Å/sec. The scale is the same for all four images.

6.3.2 The influence of annealing conditions and substrate temperature on the T_c of the off-axis films

We first re examine the optimal annealing temperature of the off-axis MgB2 films. A much lower annealing temperature is found to be suitable for the off-axis films. As shown in Fig.6-5, with the annealing temperature of 650ºC, the film has magnetic $T_{c\ onset}$ of 29K and a transition width of about 9K. The $T_{c\ onset}$ slightly increases to 30K with a higher annealing Temperature of 660ºC, but the transition is much wider. For a lower annealing temperature of 635ºC, both the $T_{c\ onset}$ and the transition are worsened.

According to the off-axis geometry, the Mg:B ratio in the off-axis precursor film may differ from the on-axis precursor films.

The annealing temperature of 650ºC with 1min dwell time is selected as an optimal annealing temperature.We attribute this lower annealing temperature of off-axis films to the better phase formation during the relatively long deposition time. The Mg:B ratio in the off-axis precursor film is probably lower than that in the on-axis films due to the very different deposition geometry. This will cause to Mg deficiency during the annealing at 660 ºC, which can explain the broadening of the transition.

For off-axis deposition, the deposition rate is much lower than on-axis deposition. The substrate temperature during off-axis deposition process becomes more important due to a longer deposition time. Ueda et al. reported that in MBE a substrate temperature of 300K can lead to as grown superconducting MgB_2 film with a Tc of 34-36K [20,21]. So it is interesting to test if the T_c performance of our off-axis film can be improved by optimizing the substrate temperature.

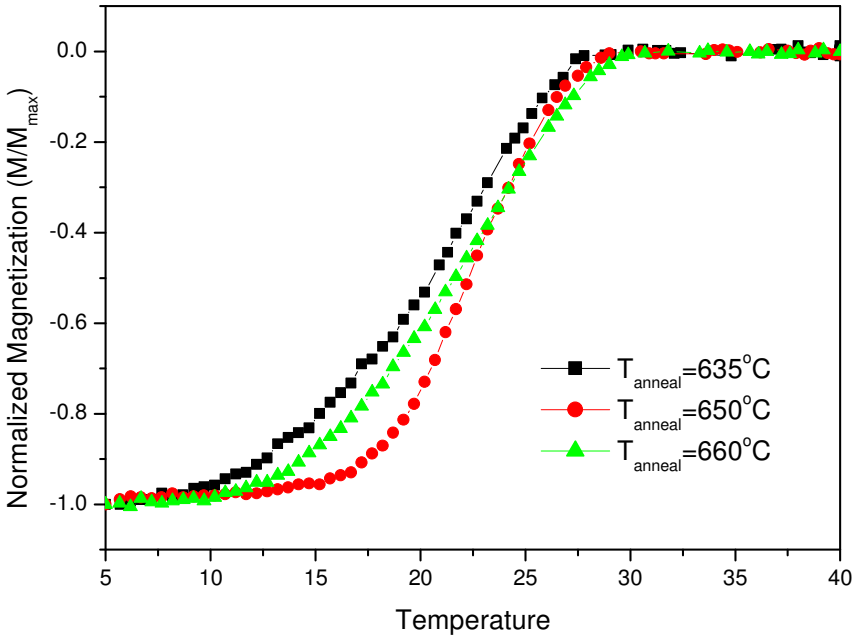

Fig. 6-5 The ZFC magnetization curves for the off-axis MgB_2 films prepared with different annealing temperatures. The substrate temperature during deposition is 250ºC for all the samples. The ramp time from 250ºC to the annealing temperature is 12 min and the dwell time is 1min.

Figure 6-6 shows the ZFC magnetization curves of off-axis films deposited at different substrate temperatures. The T_c increased with increasing the substrate temperature before reaching 250°C. Above 250°C, the films abruptly lost superconductivity when the substrate temperature increased from 270°C to 275°C, as can be seen in Fig 6-7. The highest T_c has been achieved in sample #300604V with substrate temperature of 250°C. Most of the following characterizations were carried out on this sample.

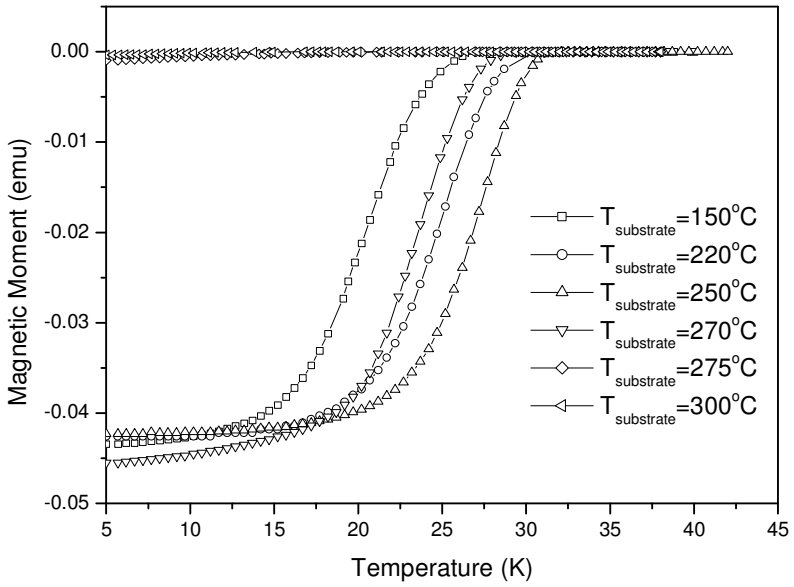

Fig.6-6 ZFC magnetization curves of off-axis MgB_2 films deposited at different substrate temperatures. The in situ annealing temperature is 650 ºC with 1 min dwelling time.

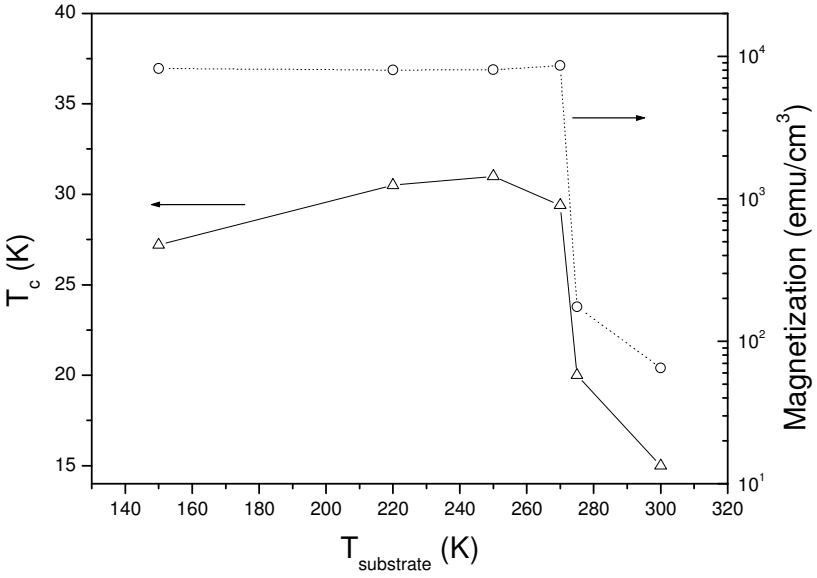

Fig.6-7 $T_{c\ onset}$ versus $T_{substrate}$ curve (left axis) and magnetization (right axis) versus $T_{substrate}$ at 5K. The T_c and magnetization values are extracted from ZFC magnetization curves at 5 K in Fig.6-6.

We explain the dramatic loss of superconductivity in MgB_2 film at 275°C as a result of significant Mg evaporation at 275°C. Because our MgB_2 target is stoichiometric, the Mg evaporation at 275°C is severe enough to alter the Mg:B ratio on the surface of the substrate, and destroy the superconductivity in the film. Ueda's MBE method can maintain superconductivity in their *in situ* MgB_2 films with a higher substrate temperature of 300°C. This is probably because the Mg:B vapor generating ratio is 10:1, much higher than in our case [21].

On the other hand, it is reasonable to see an increase of T_c with increasing substrate temperature up to 270°C, due to the fact that surface mobility, diffusion and the activity of Mg and B are all increased with a higher substrate temperature. This should favor the MgB_2 phase formation and crystallization during the subsequent *in situ* annealing and finally resulting in a better MgB_2 film.

6.4 Microstructural properties of our off-axis films.

6.4.1 Atomic Force Microscopy results on surface topography of the off-axis films.

The smooth surface of the off-axis film in Figure 6-4(d) is revealed in more detail by AFM, as shown in Fig.6-8. The surface of the film is homogeneously constructed of round islands with diameters of about 50 nm. The nano-crystalline structure accompanied by a considerable volume of grain boundaries provides enhanced pinning to flux vortices [22], therefore the J_c properties of the MgB_2 film might be improved. The average height of these round islands is 5-10 nm (see Fig.6-9) resulting in a root mean square roughness (R_q) of 4 nm in a 5×5 μm scan area. The roughness of the film is comparable with the best MgB_2 films prepared by MBE [23] and HPCVD [6], which generally have R_q values of 2-4nm.

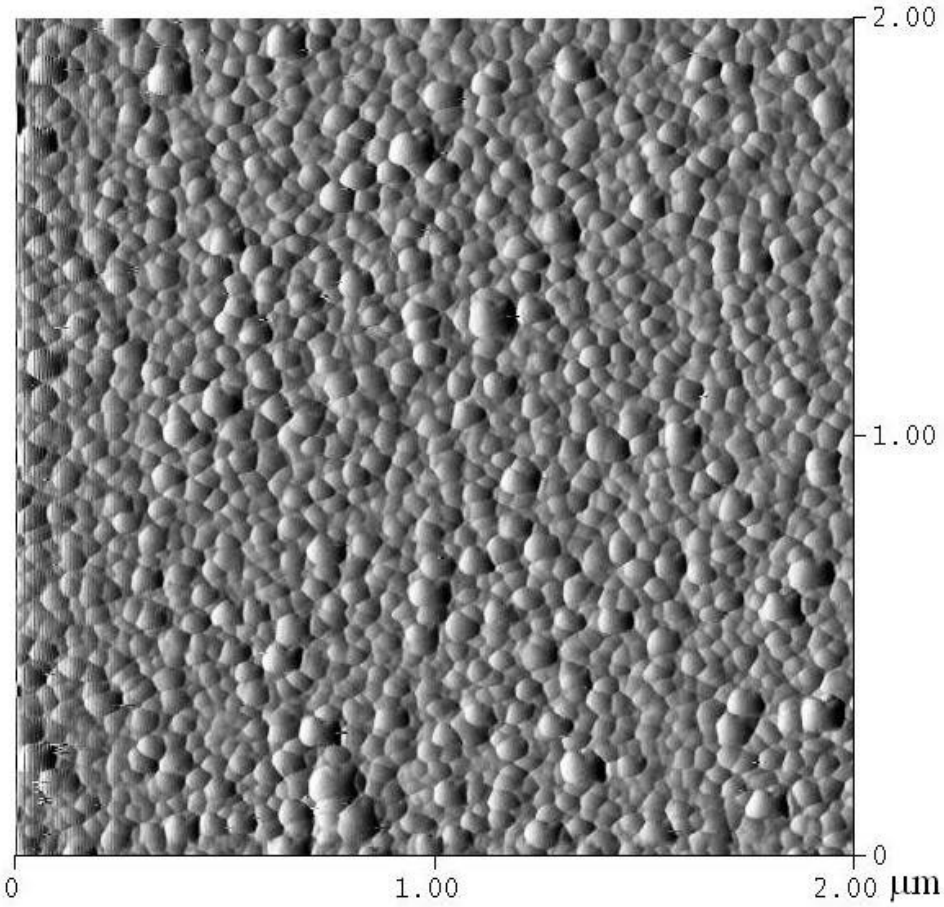

Fig.6-8. AFM deflection image of a 2×2 μm^2 area of the surface of film (d) in Fig.6-4.

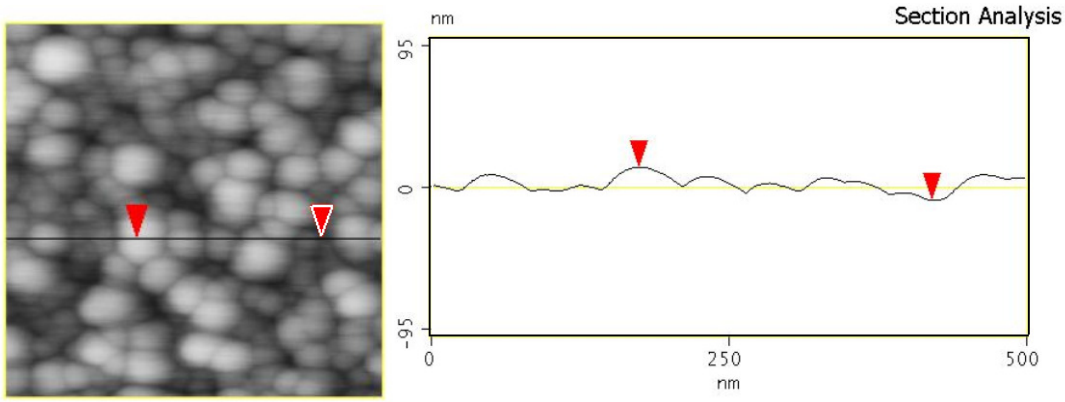

Fig.6-9. AFM cross-section profile of the off-axis film #300604V. The vertical distance between the highest and the lowest part indicated by arrows is 22nm.

6.4.2 The texture of the off-axis MgB_2 film

The x-ray θ-2θ pattern of an off-axis film is shown in Fig.6-10. Two peaks from MgB_2 (001) and (002), and a faint peak of Mg are visible, indicating that the grains in the film are *c*–axis oriented and that the film contains a small amount of free magnesium. It is evident that the very quick annealing process of only one minute at 650℃ has triggered a reasonably good crystallization in the slowly deposited off-axis MgB_2 film. The full width at half maximum (FWHM) of MgB_2 (002) peak is broadened from 0.33° (the value of the target) to 0.68°. The broadening of the peaks is probably due to the small-grain feature and high level of disorder, which is also indicated by AFM and implied by the high residual resistivity of the film. The grain size calculated from the broadened FWHM using the Scherrer equation, without considering the inner strain, is about 25nm.

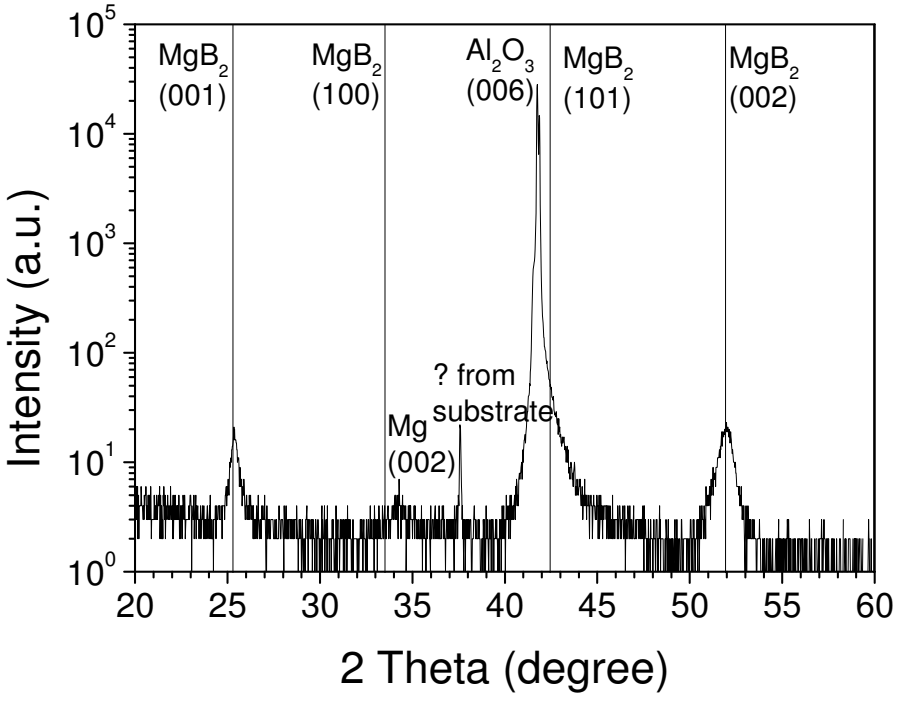

Fig.6-10. XRD θ-2θ pattern of the off-axis deposited film #300604V with a slow scanning rate of 0.2 degree/min. The vertical lines label the positions for all MgB_2 peaks in powder diffraction database. The unknown peak at 37.56º is also presents in the spectrum of a bare Al_2O_3-C substrate, so we assume it is not from the film.

6.4.3 Transmission Electron Microscopy and Selected Area Electron Diffraction results of the off-axis film

Figure 6-11 shows the TEM and the SAED pattern for the *in situ* MgB_2 film. The electron beam is perpendicular to the film plane. A small-grain feature is clearly revealed by both the bright field (BF) image and the SAED ring patterns. The grain size is about 20-30nm judging from the BF image. Strong diffraction rings from MgO also appear in the SAED image, indicating a significant amount of MgO phase exists in the film. Upon inspection of the SAED rings, we also found that all of the rings belong to (00*l*) are missing, once again suggesting a well c-axis orientation of thefilm. Also judging from the homogeneous SAED ring pattern, the off-axis film is not in-plane aligned.

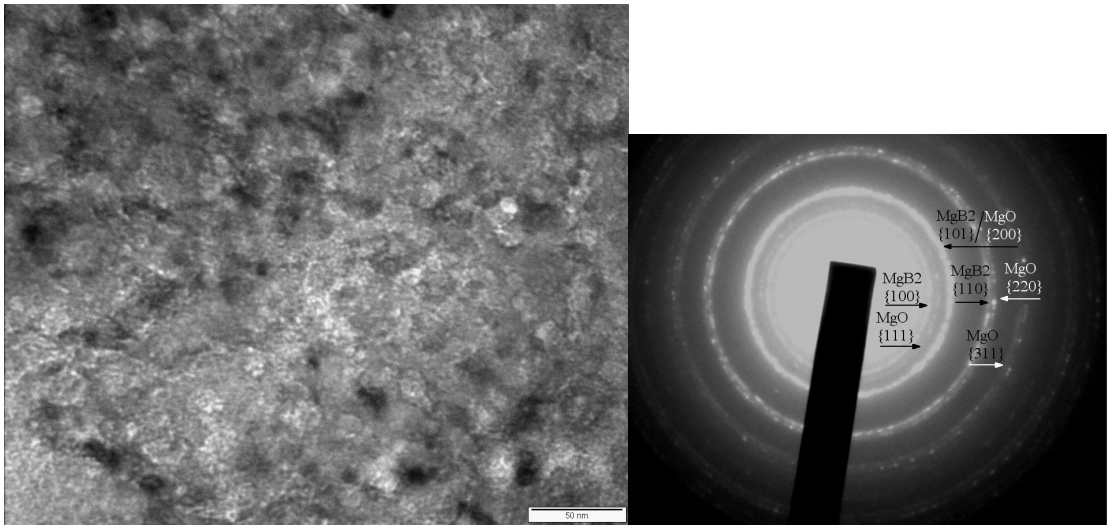

Fig.6-11. The left figure: Bright field TEM image of a planar specimen a typical off-axis MgB_2 film with a zero-resistivity T_c of 32K. The right figure is a SAD pattern from a Φ500 nm area of the film

6.5 Resistivity, upper critical field, activation energy and the critical current density of the off-axis MgB_2 films

Figure 6-12 shows the temperature dependence of the resistivity for our best off-axis film #300604V. The $T_{c\ onset}$ of the film is 33.1 K, and the zero resistivity T_c is 32.2 K, ~6 K below the values for bulk samples. This T_c is close to that of the high quality *in situ* MBE-produced MgB_2 films [5,23], and among the highest reported values for *in situ* PLD films [8-12]. The suppression of T_c for the films could be attributed to the lattice distortion resulted from the nano-grain structure or strong impurity scattering, especially inter-band scattering, which is pair-breaking in the two-gap superconductor. The resistivity difference $\Delta\rho_{300\text{-}40K}$ of the off-axis films is 8-9 μΩcm, comparatively low among MgB_2 films. Rowell *et al*. has argued that the resistivity difference between 300K and just above T_c is indicative of the effective current carrying area [24]. The low $\Delta\rho_{300\text{-}40K}$ value probably shows a high density and good connection between the MgB_2 grains in the off-axis film. The residual resistivity of ρ_{40K} = 30-60 μΩcm for the off-axis films is still quite high compared with the single crystalline MgB_2. The high resistivity is probably attributable to a high level of intra-grain disorders, which may also have considerably suppressed the T_c. On the other hand, the resistivity value of the off-axis films are generally lower than our on-axis *in situ* films (~120 μΩcm), indicating that the disorder level in the off-axis film is not as high as the on-axis films.

Fig.6-13 shows the field dependence of the ρ-*T* curves in perpendicular and parallel fields. We find that the superconducting transition width shows no significant broadening with increasing fields up to 8.7 T, which is quite different from what is observed in MgB_2 bulk samples [25], wires [26] and films [5]. Since the resistivity transition width represents the regime of flux-flow resistivity [27], this result may indicate that the flux pinning in our *in situ* MgB_2 films remains strong in both low and high fields.

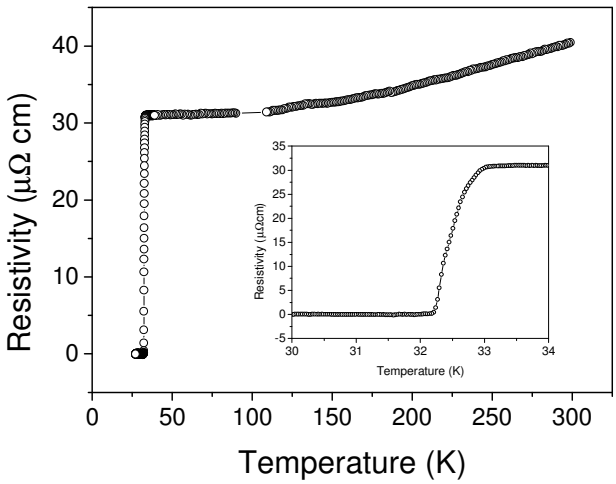

Fig.6-12 Resistivity versus temperature for an off-axis film #300604V. The inset is an enlargement of the transition part.

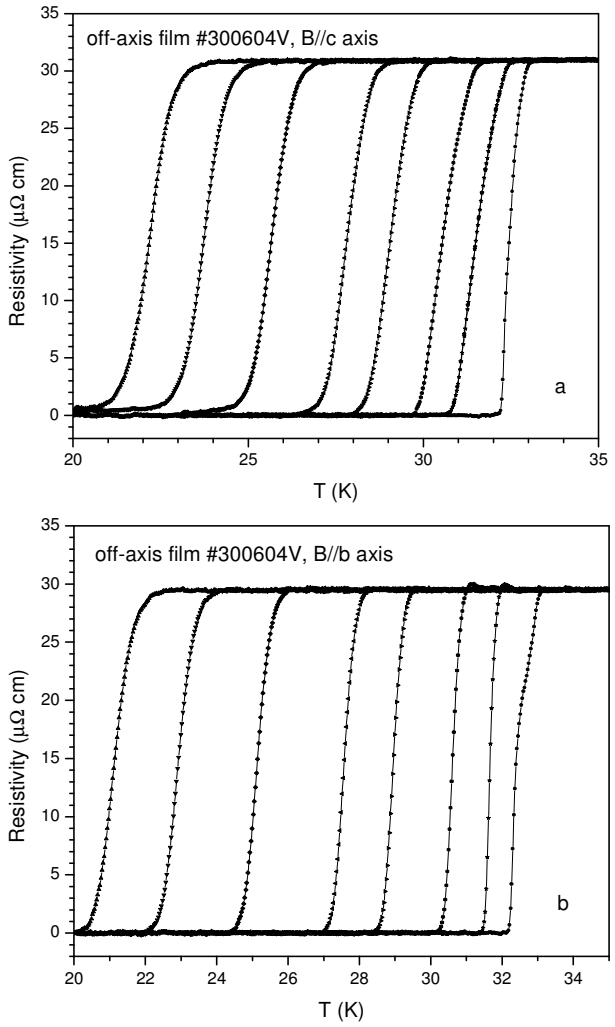

Fig.6-13 The field dependence of resistivity-temperature curves of the off-axis MgB2 film #300604V in a) perpendicular (H//c axis) fields and b) parallel fields (H//a-b plane).

The activation energy of thermally activated flux flow (TAFF) is deduced from the slope of Arrhenius plots of ρ(H, T) curves in the same way as described in Chapter 3 (Equation 3-6). Straight part can be clearly seen in ln(R)-T curves shown in Fig.6-14 in both perpendicular and parallel field circumstances. The U_0-B curve is shown in Fig.6-15. Although we should keep in mind that the activation energy U_0 is changing with temperature, the U_0 values obtained from the resistivity curves within a narrow temperature range usually have a field dependence of $U_0 \propto B^{-n}$ and can be used for comparison [28]. From Fig.6-15 we can see that the activation values for our off-axis MgB_2 film is approximately at the same level in both perpendicular and parallel fields. It appears that in perpendicular field, the U_0 drops quicker with the applied field than in a parallel field circumstance. This result indicates a slightly better pinning performance in high fields when the field is parallel to the film plane. The anisotropy in U_0 could be explained considering two facts: 1) The film is c-axis oriented which could display anisotropy pinning behavior due to the anisotropy of the two-gap MgB_2 superconductor; 2) the thin film with 300-500nm thickness is a nearly 2D structure, and the flux penetration behavior is different in different directions due to the quasi-2D geometry.

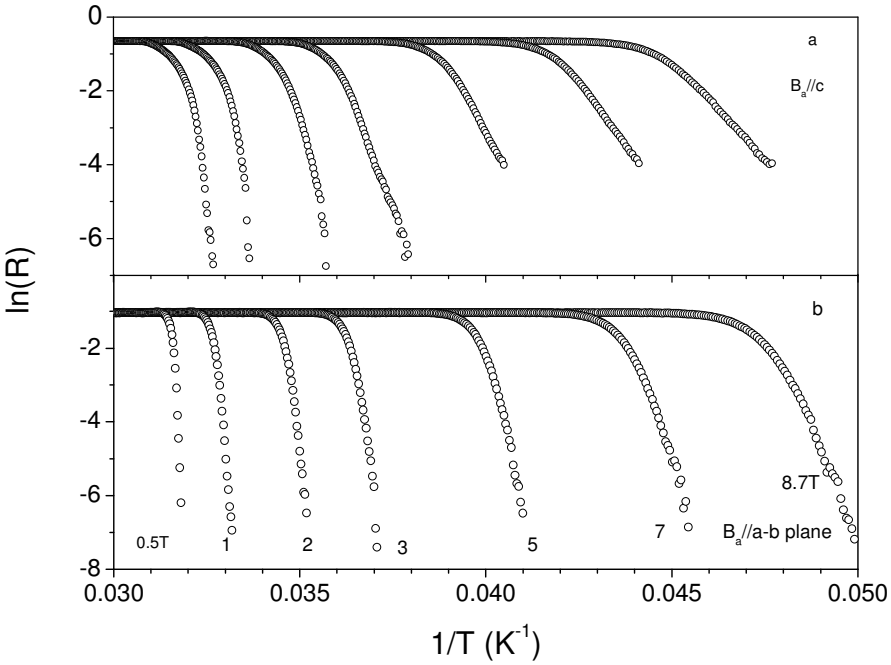

Fig.6-14 The Arrhenius plot of resistance R(T, H) for the off-axis MgB_2 film in a) perpendicular and b) parallel fields.

The H_{c2} curves, derived from transport curves using 90% ρ_{Tc} values, reveal a high H_{c2}-T slope, as shown in Fig.6-16. The value of dH_{c2}/dT near T_c is about 1.0 T/K, for both the H//*ab*-plane and H⊥*ab*-plane circumstances. The fact that the H_{c2} anisotropy of our *c*-oriented MgB_2 film is highly suppressed might be a result of a strong scattering, which may also dramatically increase the H_{c2} value in the films. For "dirty" MgB_2 samples, there is no significant H_{c2} saturation at low temperatures and the experimental H_{c2}-T curves are approximately linear [29,30]. Based on this, we roughly extrapolate that $H_{c2}(0) \approx 32$ T at 0 K, using a linear equation, $H_{c2}(0)=H'_{c2}T_c$, where $H'_{c2} = |dH_{c2}/dT|$ near T_c. An estimation of the electron mean-free path l using the equations for superconductors in GL theory, $H_{c2}(T) = \Phi_0/(2\pi\xi^2)$ and $\xi(T) = 0.855(\xi_0 l)^{1/2}/[1-T/T_c]^{1/2}$ (in the dirty limit), where Φ_0 is the flux quantum and ξ_0 taken as the single crystal coherence length of ~6.0 nm [31], gives $l \approx 2.3$ nm and $\xi \approx 3.1$ nm at zero temperature.

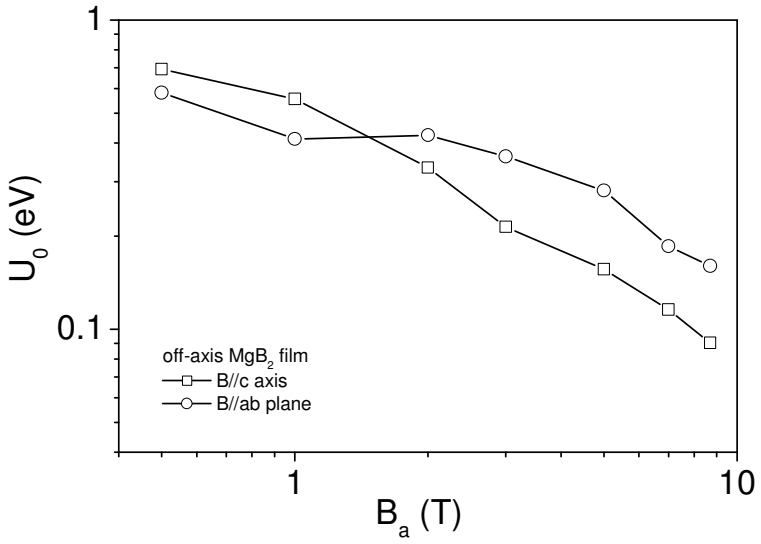

Fig.6-15 The activation energy U_0 of flux flow versus applied field, B_a for film #300604V.

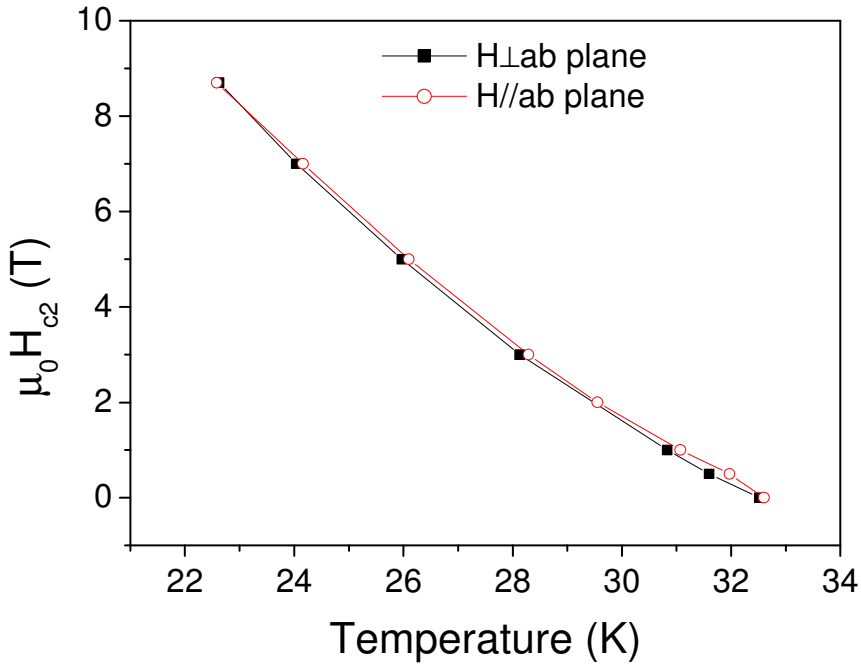

Fig.6-16. The H_{c2}-T curves for H // ab-plane and H ⊥ ab-plane. The H_{c2} values are derived from transport curves using 90% ρ_{Tc} values. In both H // ab-plane and H⊥ab-plane cases, the testing current was perpendicular to the applied field.

The hysteresis magnetization measurements of the off-axis films reveal quite high J_c values as well as weak field dependence in low temperatures. Fig.6-17 shows the calculated magnetic J_c values of an off-axis film using the Bean model in perpendicular fields up to 5 T at different temperatures. The J_c values in zero field are about 6×10^6 A/cm^2 at 10K, 3.5×10^6 A/cm^2 at 15K and 2×10^6 A/cm^2 at 20K. In a high field of 5 T, the J_c value remains ~5×10^5 A/cm^2 at 5 K and ~2.3×10^5 A/cm^2 at 10 K. The good J_c performance of the film is in agreement with the argument that the nano-grain structure may provide strong pinning. Also the above-mentioned possible high level of intra-grain disorders in the MgB_2 films may lead to a further pinning enhancement.

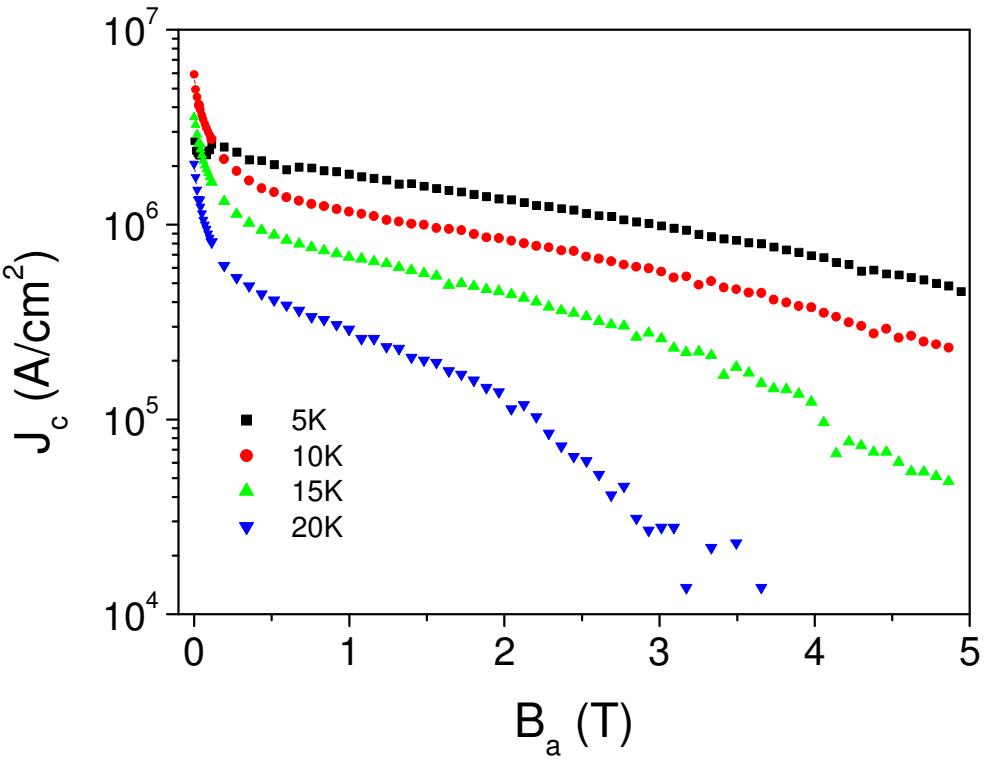

Fig.6-17 Magnetic J_c versus applied field for the off-axis film #300604V at different temperatures. The applied field is perpendicular to the film plane. It is difficult to estimate J_c at 5 T in low fields owing to the predominant magneto-thermal instability.

6.6 MOI results of the off-axis MgB_2 films in comparison with the on-axis films.

We found evidences of good thermo-magneto stablility in the off-axis films by MOI observation. This is in accordance with the smooth surface feature of the off-axis film, and may further indicate a good connectivity and thermal conductivity between the grains of the film.

Figure 6-18 shows the MOI images of an off-axis film taken at 4.6K, 5.9K, 7K, and 9K. At 4.6 K, the flux penetrates the off-axis film through abrupt avalanches and leaves dendritic paths, which is similar to the MOI images of our on-axis films (Fig.6-19). A similar dendritic path at low temperatures is also observed by other groups in MgB_2 films. It has been a consensus in literatures that this dendritic path is related to thermal-magneto instability in MgB_2 films at low temperatures. However, gradual flux

penetration can be seen at 4.6 K at the edge of our off-axis film. This is in contrast with that of the on-axis *in situ* films shown in Fig.6-19. For higher temperatures, the gradual penetration is becoming predominant for both kinds of films, but we can still see dendrite-like details in on-axis films, whereas in the off-axis films the flux penetrates very smoothly, without dendritic avalanches. No details can be recognized at our device resolution of about 5 μm. A comparison of the flux penetration in detail between the off-axis and on-axis film is shown in Fig.6-20.

By inspecting Fig.6-4 (a) and (d), the surface feature of the on-axis and off-axis MgB_2 films, we can clearly see the difference in profile of the two kinds of MgB_2 films. This could lead to very different local thermo-magnetic stability, which determines the scale and intensity of flux jump. Also the off-axis film is well c-axis oriented and shows slightly lower disorder level than the on-axis film, if we look at the H_{c2} (T) slope and the residual resistivity value. These facts may also increase the thermo-magnetic stability in the off-axis films. Ye et al. has demonstrated the total gradual flux penetration at temperatures as low as 1.8K in ultra-pure MgB_2 thin films prepared by HPCVD. They have suggested a correlation between the flux jump behavior and the residual resistivity in their MgB_2 films [32,33]. The lower residual resistivity determined in our off-axis MgB_2 film is in good agreement with Ye's argument.

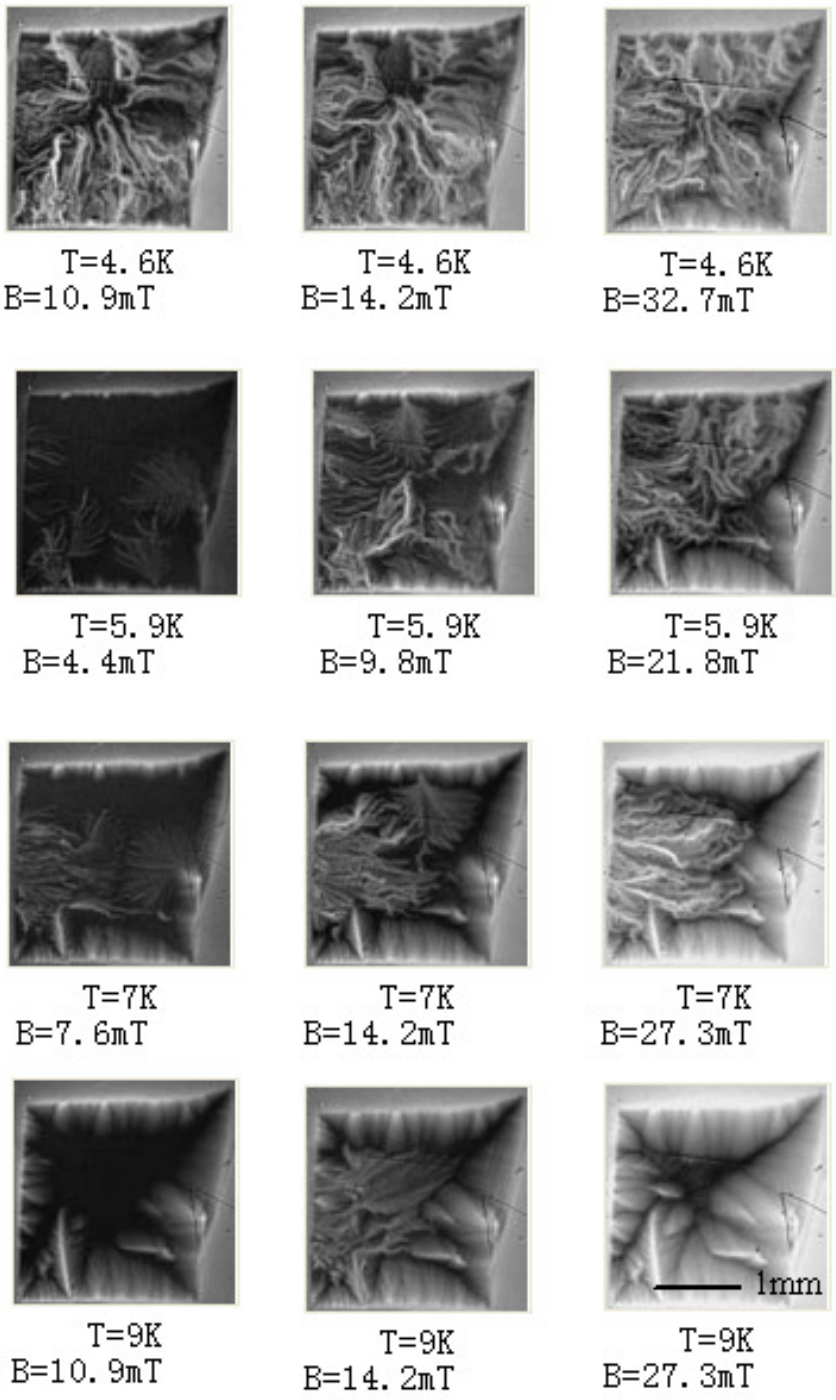

Fig.6-18 MOI of a typical off-axis MgB_2 film with a zero-resistivity T_c of 32K.

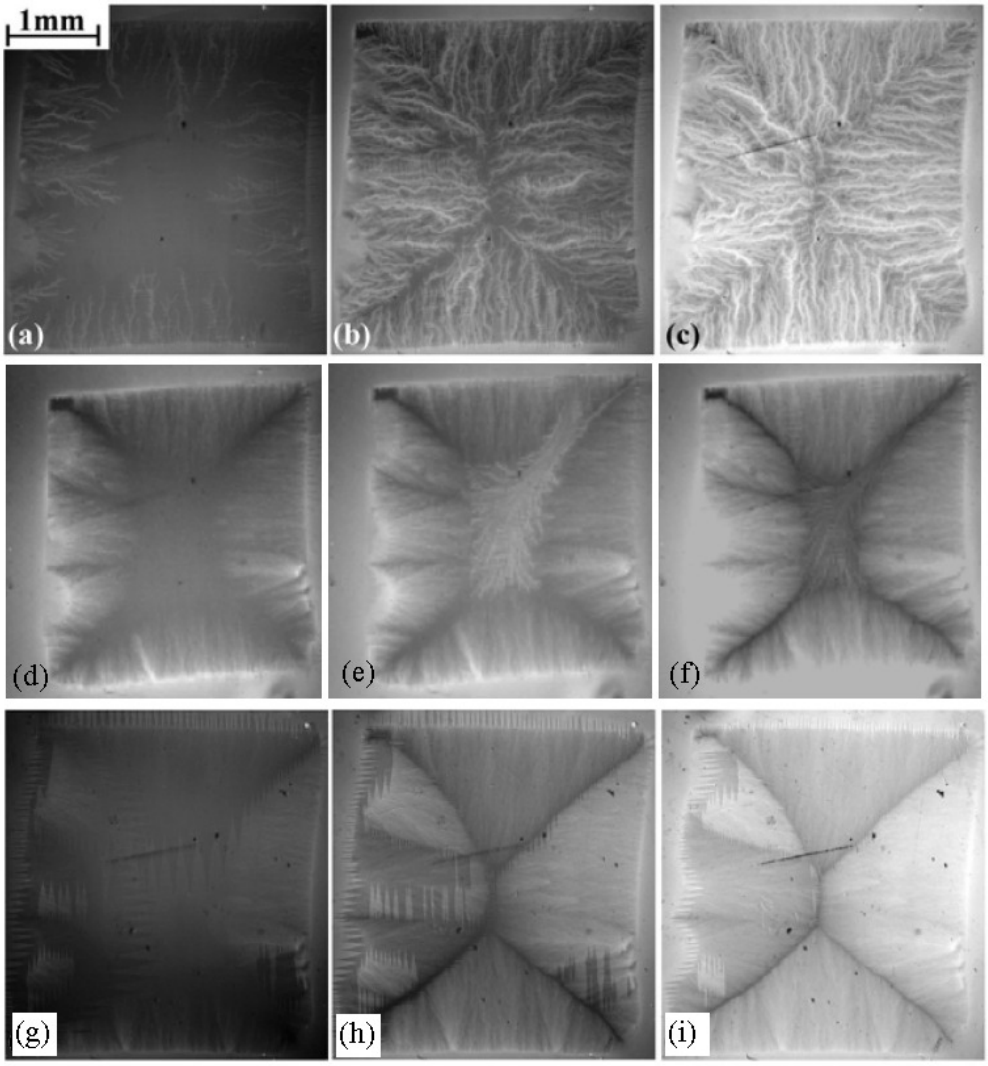

Fig.6-19 MOI of the on-axis MgB_2 film #030703 (a) 4K 3.4 mT (b) 4K 8.5 mT (c) 4K 25.5 mT; (d) 7.5K, 5.1mT (e) 7.5K, 10.2 mT (f)7.5K, 17 mT; (g)15K, 3.4 mT (h)15K, 10.2mT (i)15 K, 27.2 mT.

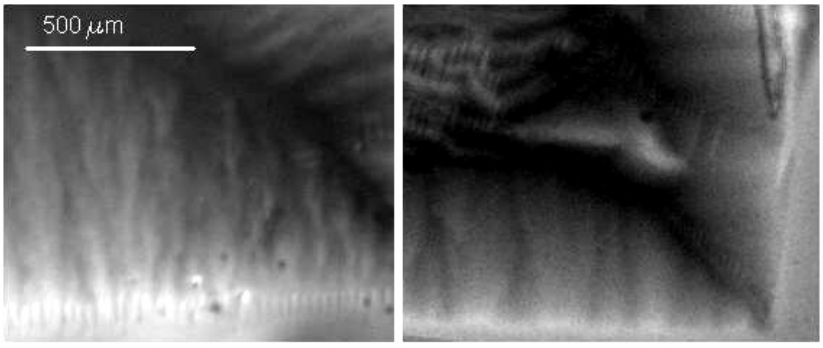

Fig.6-20 MOI image details of a) on-axis film 7.5K 10.5mT, and b) off-axis film at 7K 14.2 mT.

6.7 Summary

In this chapter we have illustrated that the off-axis deposition method is effective in improving the surface smoothness of PLD MgB_2 films. This is the first time that an off-axis deposition geometry has been applied for the MgB_2 thin film deposition among literature reports. Under the selected deposition and annealing parameters, we obtained *c*-oriented *in situ* MgB_2 films on Al_2O_3-C substrate with a root mean square roughness of 4 nm. The zero resistance T_c of the best off-axis MgB_2 film is 32 K with a narrow transition width of 0.9 K. The combined high qualities of our off-axis films, namely good T_c value, improved J_c performance in high fields, high H_{c2}-T slope of ~1 T/K and high surface quality, render it a good candidate for applications in middle-temperature superconducting electronics.

References:

[1] W. N. Kang, H.-J. Kim, E.-M. Choi, C. U. Jung, and S.-I. Lee, Epitaxial MgB_2 Superconducting Thin Films with a Transition Temperature of 39 Kelvin, Science **292,** 1521 (2001).

[2] C. B. Eom, M. K. Lee, J. H. Choi, L. J. Belenky, X. Song, L. D. Cooley, M. T. Naus, S. Patnaik, J. Jiang, M. Rikel, A. Polyanskii, A. Gurevich, X. Y. Cai, S. D. Bu, S. E. Babcock, E. E. Hellstrom, D. C. Larbalestier, N. Rogado, K. A. Regan, M. A. Hayward, T. He, J. S. Slusky, K. Inumaru, M. K. Hass, and R. J. Cava, High Critical current Density and Enhanced Irreversibility Field in Superconducting MgB_2 Thin Films, Nature **411,** 558-560 (2001).

[3] R. Vaglio, M. G. Maglione, and R. D. Capua, High-quality MgB_2 thin films *in situ* grown by dc magnetron sputtering, Supercond. Sci. Technol. **15,** 1236 (2002).

[4] S. D. Bu, D. M. Kim, J. H. Choi, J. Giencke, S. Patnaik, L. Cooley, E. E. Hellstrom, D. C. Larbalestier, and C. B. Eom, Synthesis and Properties of c-axis Oriented Epitaxial MgB_2 Thin Films, Appl. Phys. Lett. **81,** 1851 (2002).

[5] W. Jo, J.-U. Huh, T. Ohnishi, A. F. Marshall, M. R. Beasley, and R. H. Hammond, Appl. Phys. Lett. **80** (2002).

[6] X. H. Zeng, A. V. Pogrebnyakov, A. Kotcharov, J. E. Jones, X. X. Xi, E. M. Lysczek, J. M. Redwing, S. Y. Xu, Q. Li, J. Lettieri, D. G. schlom, W. Tian, X. Q. Pan, and Z. K. Liu, In-situ Epitaxial MgB_2 Thin Films for Superconducting Electronics, Nature Materials **1,** 35 (2002).

[7] A. B. Jadhav and S. H. Pawar, Electrochemical synthesis of superconducting magnesium diboride films: a novel potential technique, Supercond. Sci. Technol. **16,** 752 (2003).

[8] D. H. A. Blank, H. Hilgenkamp, A. Brinkman, D. Mijatovic, G. Rijinders, and H. Rogalla, Superconducting Mg-B Films by Pulsed-laser Depostion in an in situ Two-step Process Using Multicomponent Targets, Appl. Phys. Lett. **79,** 394-396 (2001).

[9] H. M. Christen, H. Y. Zhai, C. Cantoni, M. Paranthaman, B. C. Sales, C. Rouleau, D. P. Norton, D. K. Christen, and D. H. Lowndes, Superconducting Magnesium Diboride Films with T_c=24K Growth by Pulse Laser Deposition with in-situ Anneal, Physica C **353,** 157 (2001).

[10] H. Y. Zhai, H. M. Christen, L. Zhang, C. Cantoni, M. Parathaman, B. C. Sales, D. K. Christen, and D. H. Lowndes, Superconducting magnesium diboride films on Si with T_{c0}~24 K grown via vacuum annealing from stoichiometric precursors, Appl. Phys. Lett. **79,** 2603 (2001).

[11] A. Berenov, Z. Lockman, X. Qi, Y. Bugoslavsky, L. F. Cohen, M.-H. Jo, N. A. Stelmashenko, V. N. Tsaneva, M. Kambara, N. H. Babu, D. A. Cardwell, M. G. Blamire, and J. L. MacManus-Driscoll, Growth of strongly biaxially aligned MgB_2 thin films on sapphire by postannealing of amorphous precursors, Appl. Phys. Lett. **79,** 4001-3 (2001).

[12] Y. Zhao, M. Ionescu, J. Hovard, and S. X. Dou, Comparative study of in situ and ex situ MgB_2 films prepared by pulsed laser deposition, Supercond. Sci. Technol. **17,** S482-485 (2004).

[13] L. C. Chen, Chapter 6 of Pulsed Laser Deposition of Thin Films, edited by Chrisey D B and Hubler G K**,** (New York: Wiley) (1994).

[14] E. Agostinelli, A. Kaciulis, and M. Vittori-Amtisari, Great reduction of particulates in pilsed laser deposition of Ag-Co films by using ashaded off-axis geometry, Appl. Surf. Sci. **156,** 143 (2000).

[15] B. Holzafel, B. Roas, L. Schultz, P. Bauer, and G. Saemann-Ischenko, Appl. Phys. Lett. **61,** 3178 (1992).

[16] R. J. Kennedy, Thin Solid Films **214,** 223 (1992).

[17] V. F. Vratskikh, Y. N. Drozdov, and V. V. Talanov, Supercond. Sci. Technol. **10,** 766 (1997).

[18] K. Fujino, M. Konishi, and K. Sato, Large Area YBCO Film Fabricated by Pulsed Laser Deposition, Appl. Supercond. **5,** 41 (1997).

[19] J. T. Cheung and H. Sankur, CRC Crit. Rev. Solid State Mater. Sci. **15,** 63-109 (1988).

[20] K. Ueda and M. Nato, As-grown superconducting MgB_2 thin films prepared by molecular beam epitaxy, Appl. Phys. Lett. **79,** 2046 (2001).

[21] K. Ueda, H. Yamamoto, and M. Naito, Synthesis and photoemission study of as-grown superconducting MgB_2 thin films, Physica C: Superconductivity **378-381,** 225-228 (2002).

[22] Y. Bugoslavsky, L. Cowey, T. J. Tate, G. K. Perkins, J. Moore, Z. Lockman, A. Berenov, J. L. MacManus-Driscoll, A. D. Caplin, L. F. Cohen, H. Y. Zhai, H. M. Christen, M. P. Paranthaman, D. H. Lowndes, M. H. Jo, and M. G. Blamire, Effective vortex pinning in MgB_2 thin films, Supercond. Sci. Technol. **15,** 1392-1397 (2002).

[23] K. Ueda and S. Naito, Tunnel junctions on as-grown superconducting MgB_2 thin films, IEEE, Trans. Appl. Supercond. **13,** 3249 (2003).

[24] J. M. Rowell, S. Y. Xu, X. H. Zeng, A. V. Pogrebnyakov, Q. Li, X. X. Xi, J. M. Redwing, W. Tian, and X. Pan, Critical current density and resistivity of MgB_2 films, Appl. Phys. Lett. **83,** 102 (2003).

[25] P. C. Canfield, S. L. Budko, and D. K. Finnemore, An Overview of the Basic Physical Properties of MgB_2, Physica C (2002).

[26] D. K. Finnemore, J. E. Ostenson, S. L. Bud'ko, G. Lapertot, and P. C. Canfield, Thermodynamic and Transport Properties of Superconducting $Mg^{10}B_2$, Phys. Rev. Lett. 8**6,** 2420 (2001).

[27] Y. B. Kim and M. J. Stevens, S*uperconductivity* (Marcel Dekker, Inc., New York, 1969).

[28] T. T. M. Palstra, B. Batlogg, R. B. v. Dover, L. F. Schneemeyer, and J. V. Waszczak, Dissipative flux motion in high-temperature superconductors, Phys. Rev. B. 4**1,** 6621 (1990).

[29] S. L. Bud'ko, C. Petrovic, G. Lapertot, C. E. Cunningham, P. C. Canfield, M.-H. Jung, and A. H. Lacerda, Phys. Rev. B 6**3,** 220503(R) (2001).

[30] A. Gurevich, S. Patnaik, V. Braccini, K. H. Kim, C. Mielke, X. Song, L. D. Cooley, S. D. Bu, D. M. Kim, J. H. Choi, L. J. Belenky, J. Giencke, M. K. Lee, W. Tian, X. Q. Pan, A. Siri, E. E. Hellstrom, C. B. Eom, and D. C. Larbalestier, Very high upper critical fields in MgB_2 produced by selective tuning of impurity scattering, Supercond. Sci. Technol. 1**7,** 278 (2004).

[31] Y. Eltsev, S. Lee, K. Nakao, N. Chikumoto, S. Tajima, N. Koshizuka, and M. Murakami, Phys. Rev. B 6**5,** R140501 (2002).

[32] Z. X. Ye, Q. Li, Y. F. Hu, A. V. Pogrebnyakov, Y. Cui, X. X. Xi, J. M. Redwing, and Q. Li, Electron scattering dependence of dendritic magnetic instability in superconducting MgB_2 films, Appl. Phys. Lett. 8**5,** 5284-5286 (2004).

[33] Z. X. Ye, Q. Li, Y. F. Hu, A. V. Pogrebnyakov, Y. Cui, X. X. Xi, J. M. Redwing, and Q. Li, Magneto-Optical Imaging Studies of Flux ropagation in Ultra-Pure and

Carbon-Doped MgB_2 Thin Films, IEEE Transactions on Applied Superconcuctivity 1**5,** 3273 (2005).

Chapter 7. Multilayer MgB_2/Mg_2Si thin film

In chapter 6 we have illustrated the preparation of smooth MgB_2 films by a off-axis geometry. One of the advantages of the off-axis PLD deposition is that one can readily achieve a multilayer structure in the resultant film by switching the targets, due to the very smooth and continuous deposition feature of the off-axis PLD process. A multilayer structure, e.g. two layers of superconductors with a very thin insulate interlayer as a Josephson Junction, is generally required for superconducting electronic applications. With an artificially multilayered structure, a superconductor usually shows different behaviors from that of bulk, such as cross-over phenomenon[1], anomalous upper critical field behavior[2,3], scaling effect[4], and enhanced anisotropy in pinning energy[5]. There has been a number of experimental reports on multilayered low temperature superconductors (LTS)[3,6] and high temperature superconductors (HTS)[7-10]. The newly discovered moderate temperature superconductor MgB_2 has a layered structure and two separate superconducting gaps. The anisotropy factor of MgB_2 is close to 2, much smaller than HTSs[11]. The Ginzburg-Landau (GL) coherence length $\xi(0)$ is about 10 nm within a-b plane and 5 nm along c-axis[11]. The coupling between B layers in MgB_2 (c=0.352 nm) is strong, thus the superconductor does not display intrinsic two-dimensional pancake vortices that has been observed in HTS[12].

Si, since it is widely used in conventional electronics, is an attractive material for integrating the MgB_2 thin films into larger electronic devices. However, Mg_2Si is a very stable semiconductor and can be easily formed from Mg + Si at a temperature as low as 200ºC. By sequentially switching the MgB_2 and Si targets during an off-axis PLD deposition process, we have successfully obtained an MgB_2/Mg_2Si multilayer structure in the thin film without affecting too much the T_c.

In this chapter we report the work undertaken for the preparation of superconducting MgB_2/Mg_2Si multilayer film by PLD with the aid of an off-axis deposition method[13]. Structural characterization and transport measurements are carried out on the multilayer film. The results clearly show that this multilayer structure leads to a significant enhancement of pinning and the activation energy U_0 when the applied field is parallel to a-b plane of the film.

7.1 MgB_2/Mg_2Si multilayer preparation by using an off-axis target-switching PLD deposition method

The PLD process was conducted using an off-axis geometry described in Chapter 6. A stoichiometric MgB_2 target (84% density), a Si target and a magnesium target were set on a carousel in the chamber. Sapphire c-cut substrates with dimensions of about 6×2 mm^2 were used. With an off-axis geometry[13], the substrate is parallel to the normal axis of the target surface and aligned to the center of the laser spot. The substrate is mounted onto the edge of the heater with silver paste. The distance between the target and the substrate was about 25 mm for the off-axis deposition. A piece of metal screen was also attached to the heater just in front of the substrate to construct a shaded off-axis geometry.

The laser beam was generated by an excimer laser system (Lambda-Physik) operating on KrF gas (λ=248 nm, 25 ns). The chamber was first evacuated to a base vacuum of about 8×10^{-8} Torr and then filled with high purity argon to 120 mTorr as the background gas. Before the deposition, the heater was kept at 250℃. We consequently switch the targets of MgB_2 and Si 10 times during the deposition. At the end of the deposition, a Mg target (99.99% pure) was switched to the active depositing position, and used to deposit a Mg film to provide a protective Mg cap-layer. Then the

Ar pressure was increased to 760 Torr before the *in situ* annealing. The films were heated to 650℃ in 12 min and kept at that temperature for 1min. The resultant films have a thickness of 400-500nm, as detected by atomic force microscopy and transmission electron microscopy.

The transport measurements were carried out using a four-probe method with a dc current density of 10 A/cm^2. In both H//*ab*-plane and H⊥*ab*-plane cases, the testing current was perpendicular to the applied field.

7.2 Structural Characterization on the Multilayer film

Figure 7-1 is a cross-sectional SEM image of the Si-added MgB_2 film. It shows a multilayer structure within the film. A TEM bright field (BF) image is shown in the inset of Fig. 1 to illustrate the multilayer structure obtained as described above. Fig.7-2 shows a larger TEM bright field image of the cross-sectional view of the Si-added film. In both figures a layered structure is clearly revealed - where each MgB_2 layer is between 40-50 nm thick and the Si layers are about 4nm. Each MgB_2 layer consists of very fine-grains. Individual grains are less than 20 nm in size. A similar equiaxial fine-grain structure was also observed in our mono layer MgB_2 films. The inset of Fig.1 is a selected area electron diffraction (SAED) image of the film with the incident beam at a certain angle relative to the c-axis of the film. The divided MgB_2 rings indicate a textured grain structure with MgB_2 (0001) parallel to the film plane, the same orientation as that of our MgB_2 films. [13]. The 4 nm thick layers between the 10 MgB_2 layers are Mg_2Si, judging from the electron diffraction and X-ray energy dispersive spectroscopy (EDS) results. The existence of Mg_2Si is in accordance with the previous reports on Si addition in the Mg-B system[14,15].

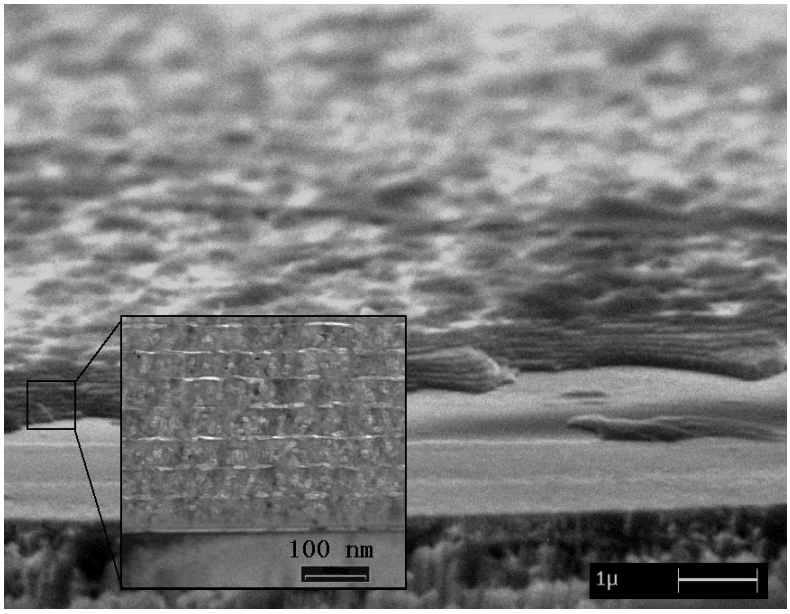

Fig.7-1: Cross-sectional SEM image of the multilayer film. The inset is a BF TEM image of the multilayer film.

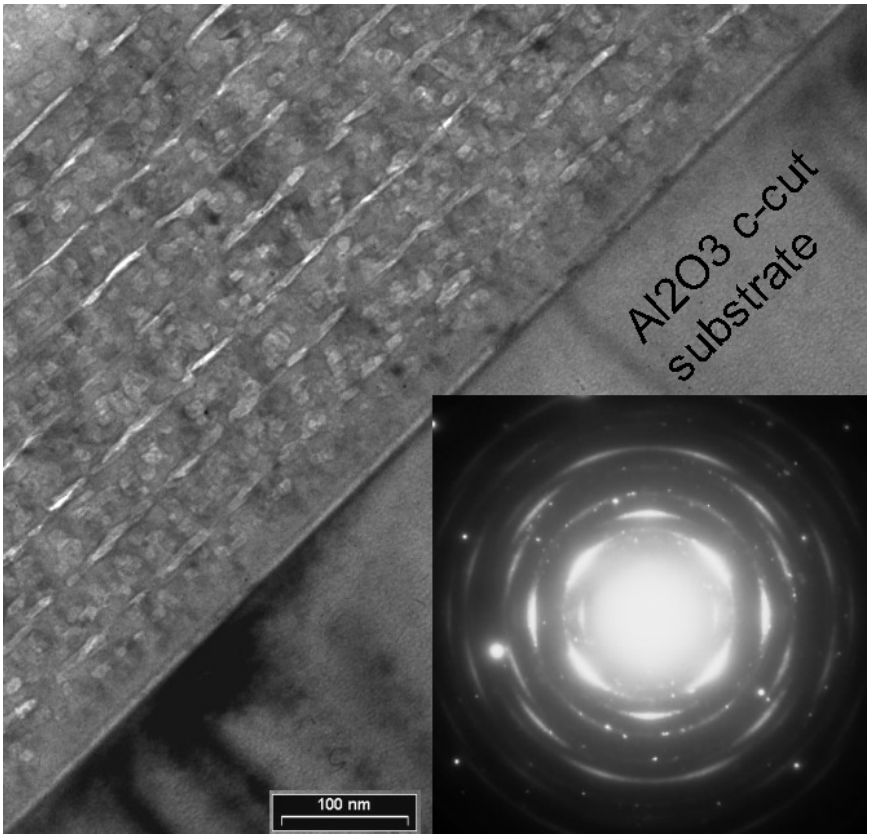

Fig.7-2: TEM BF image of the multilayer film. The scale bar is 100 nm. The inset is an SAED of the MgB_2 film, showing a clear textured grain orientation.

EDS detection of the whole cross-section area shows an average atomic ratio Si:Mg of 1:19. By assuming that only MgB_2 and Mg_2Si phases are present in the multilayered film, the Si addition level is estimated to be about 3.5wt%.

7.3 Transport properties of the Multilayer film

The T_c of the multilayer $MgB_2/Si/Al_2O_3$ film is slightly lower than pure MgB_2 film by ~1.5 K, as shown in Fig.7-3. The zero resistivity T_c of the multilayer film is 31 K. The transition widths from 10%ρ(40K) to 90% ρ(40 K) for both films are the same, about 0.5 K. The narrow transition width of the multilayered film indicates that the MgB_2 phase remain homogenous after the addition of Si. The residual resistivity at 40 K is 45 μΩcm in the Si-added film, slightly higher than the residual resistivity of the undoped film. The ρ-T curves of the two films are of the same shape. The residual resistivity value for the multilayer film is 1.5 times higher than the residual resistivity of the undoped film. As pointed out by Rowell et al.[16], the rise of the resistivity may indicate a reduction of the effective current carrying area or an increased defect level of the Si added film.

Figure 7-4 shows the field dependence of the resistivity-temperature curves of the multilayer film in parallel and perpendicular applied field circumstances. The T_c's are not shifted to lower temperatures as much in the parallel field than as in the perpendicular field situation. The T_c transition width is also narrower in parallel applied fields, indicating better pinning in this particular case.

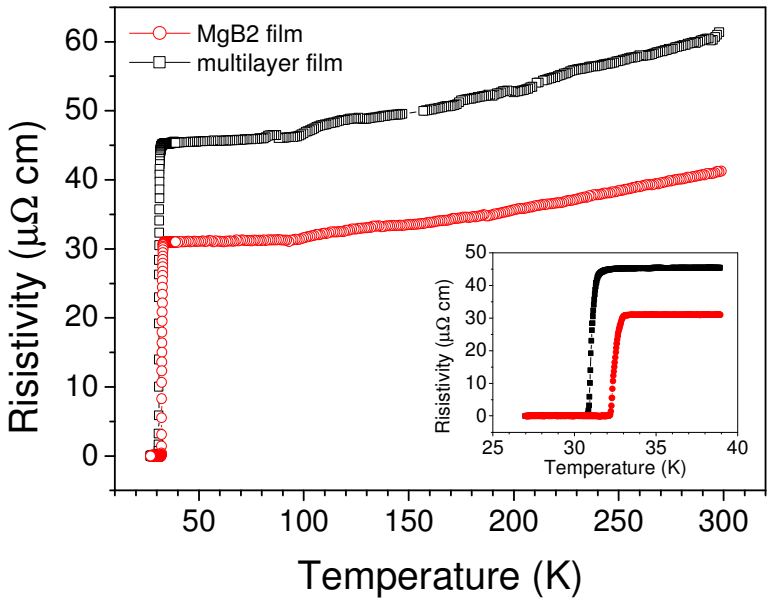

Fig.7-3: Resistivity versus temperature curves of multilayer film and MgB_2 film.

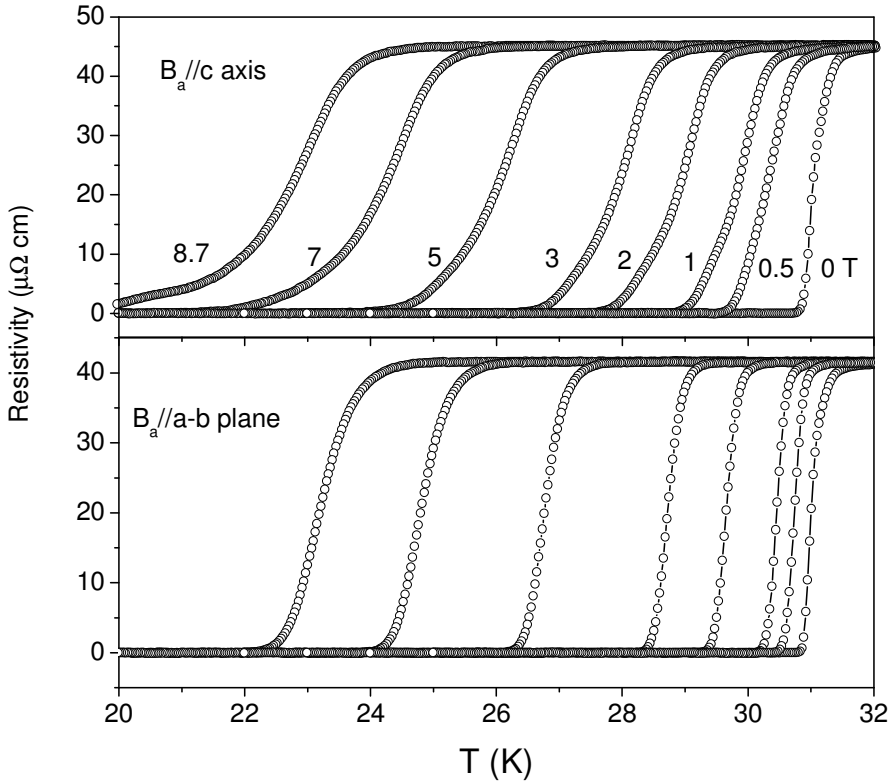

Fig.7-4: Resistivity versus temperature curves of a multilayer film in: a) perpendicular fields; b) in parallel fields.

Figure 7-5 shows the upper critical fields of the multilayer film and the MgB_2 film. The fact that the H_{c2} anisotropy of our *c*-oriented MgB_2 film is highly suppressed might be a result of the strong intra-grain scattering that is usually observed in the *in situ* PLD MgB_2 films. The upper critical fields in different temperatures are derived from the 90% ρ_{Tc} points in the ρ-T curves. The H_{C2}^{ab} and H_{C2}^{c} of the multilayer film are clearly increased, which may indicate that more intra-band scattering is introduced by Si addition. As predicted by Takahashi et al., the H_{C2}^{ab} of a layered superconductor will be much higher than the H_{C2}^{c} when the thickness of superconducting layers and normal layers is comparable to the coherence length ξ(0) of the superconductor [2]. A single MgB_2 layers is 40-50nm thick for our multilayer film, much larger than the ξ(0) of the MgB_2 layer. Therefore, the multilayer film did not show a pronounced two dimensional behavior of H_{c2}.

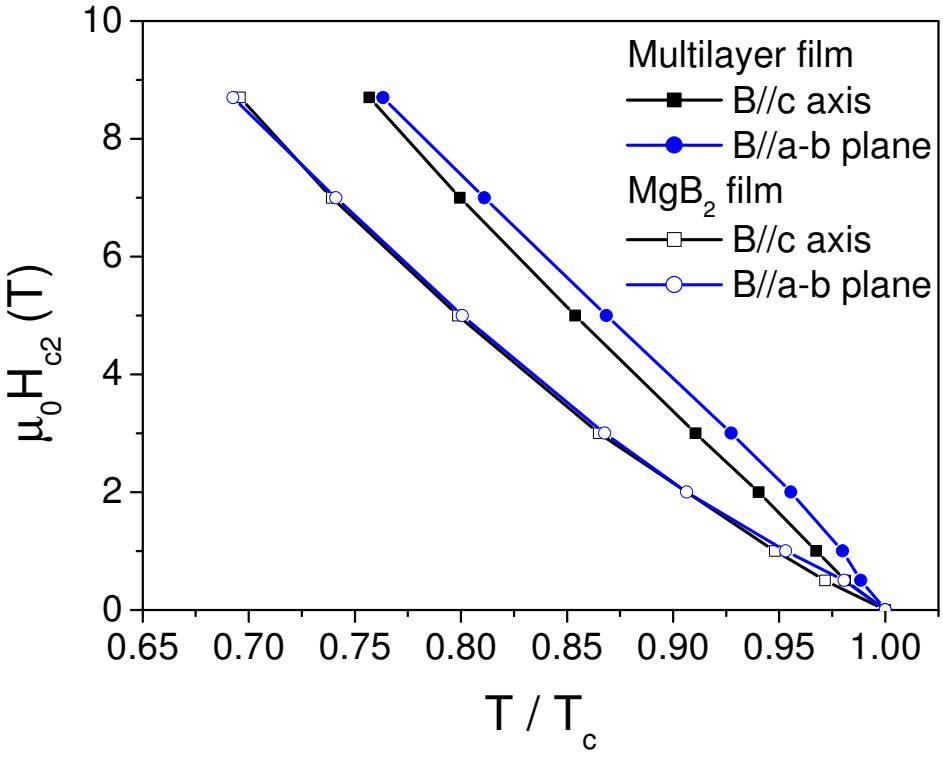

Fig.7-5: The H_{c2} versus T/T_c for the multilayered film and MgB_2 film.

The irreversibility fields of the multilayer film and the MgB_2 film was derived from transport curves using the 10% ρ_{Tc} values and shown in Fig.7-6. The irreversibility field H_{irr}^{c} for the multilayer film is almost identical to the H_{irr}^{ab} and H_{irr}^{c} of the MgB_2 film, showing the same level of flux pinning in these three circumstances. However, the H_{irr}^{ab} of the multilayer film is clearly increased, indicating a significant enhancement of pinning in parallel fields.

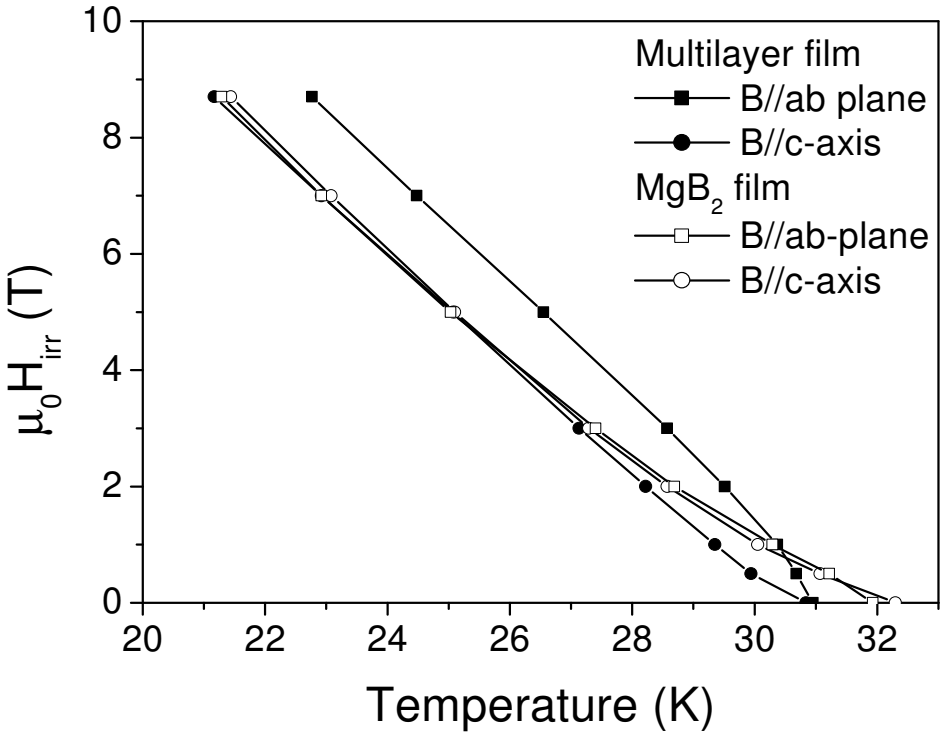

Fig.7-6: The irreversibility fields of the multilayer film and the MgB_2 film.

7.4 Arrhenius plot and the activation energy of flux flow for the multilayer film

The activation energy U_0 of our MgB_2 and multilayer films is estimated from Arrhenius law, using equation (3-6) [17-19]. The Arrhenius plots of resistance R(T, H) for the multilayer film in parallel fields are shown in Fig.7-7. The straight line part of the ln(R)-1/T curves represents the thermal activated flux flow (TAFF) regime. If we compare Fig.7-7 with the Arrhenius plots of an MgB_2 film in perpendicular and

parallel fields (Fig.6-13), we can see that the difference between the slopes of the TAFF part in perpendicular and parallel field is much smaller than that of the multilayer MgB_2 film.

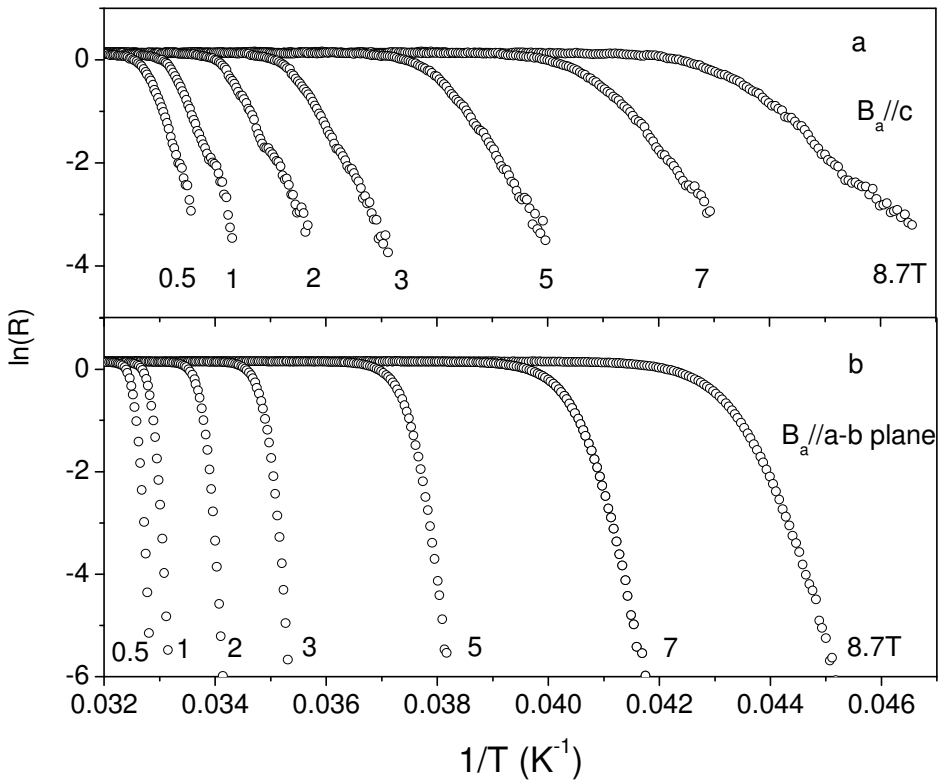

Fig.7-7: The Arrhenius plot of resistance R(T, H) for the multilayer film in: a) perpendicular and b) parallel fields.

Figure 7-8 shows the activation energy of flux flow versus applied field, B_a. An enhanced anisotropy of U_0 is clearly revealed. The activation energy of the MgB_2 film is 0.6-0.7 eV in the low field regime for both perpendicular and parallel fields. U_0 is significantly increased in the multilayer film (about 2 eV in the low field regime) when the applied field is parallel to the a-b plane of the film. The thickness of the non-superconducting Mg_2Si interlayer is typically 5 nm, of the same order as $\xi_{ab}(0)$ of MgB_2. The coupling of vortices across the Mg_2Si layer is relatively weak. When the

applied field is parallel to the a-b plane, the vortices are probably trapped in the non-superconducting Mg_2Si layers. Thus the two dimensional Mg_2Si defects provides both a strong flux pinning and an increases the thermal activation energy for flux flow in the parallel field. The activation energy for the multilayer film is decreased in perpendicular fields compared with the MgB_2 film, which may imply an easier TAFF due to the vortex decoupling across the non-superconductive inter-layers that has been observed and studied in HTS and other artificially multilayered superconducting films [5,7].

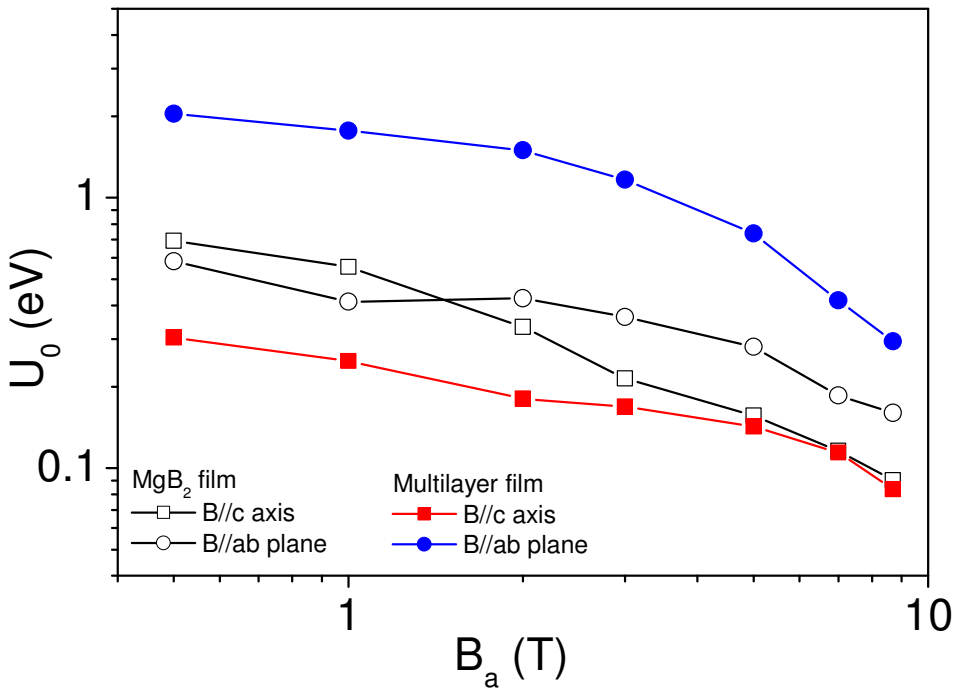

Fig.7-8: The activation energy, U_0 of flux flow versus applied field, B_a.

7.5 Summary

With the aid of the off-axis PLD method, we have fabricated MgB_2/Mg_2Si multilayer thin films with a clearly divided and homogeneous 10-layer structure. The 5 nm thick Mg_2Si inter-layers provide effective flux pinning for the MgB_2/Mg_2Si

multilayer film in parallel fields. An enhanced anisotropy of the flux activation energy U_0 is observed in the multilayer film. U_0 is significantly increased when the applied field is perpendicular to the c-axis and the testing current, which is in accordance with the enhancement of H_{irr}^{ab}. H_{c2} and the residual resistance are clearly increased, which may indicate that some defects and intra-band scattering is introduced by Si addition.

References:

[1] R. A. Klemm, A. Luther, and M. R. Beasley, Theory of Upper Critical-Field in Layered Superconductors, Phys. Rev. B **12,** 877-891 (1975).

[2] S. Takahashi and M. Tachiki, Phys. Rev. B **33,** 4620 (1986).

[3] M. G. Karkut, V. Matijasevic, L. Antognazza, J. M. Triscone, N. Missert, M. R. Beasley, and O. Fischer, Anomalous Upper Critical Fields of Superconducting Multilayers - Verification of the Takahashi-Tachiki Effect, Phys. Rev. Lett. **60,** 1751-1754 (1988).

[4] G. Jakob, M. Schmitt, T. Kluge, C. Tomerosa, P. Wagner, T. Hahn, and H. Adrian, Scaling of the Angular-Dependence of the Critical-Current Density in High-T_c Superconductors, Phys. Rev. B **47,** 12099-12103 (1993).

[5] J. R. Clem, Anisotropy and two-dimensional behaviour in the high-temperature superconductors, Supercond. Sci. Technol. **11,** 909-914 (1998).

[6] J. M. Murduck, D. W. Capone II, I. K. Schuller, S. Foner, and J. B. Ketterson, Critical current enhancement in NbN/AlN multilayers, Appl. Phys. Lett. **52,** 504 (1988).

[7] J. L. Martin, M. Velez, and J. L. Vicent, Multilayer pinning in a-axis-oriented $EuBa_2Cu_3O_7/PrBa_2Cu_3O_7$ superconducting superlattices, Phys. Rev. B **52,** R3872 (1995).

[8] K.-H. Kim, H.-J. Kim, S.-I. Lee, A. Iyo, Y. Tanaka, K. Tokiwa, and T. Watanabe, Enhanced two-dimentional properties of the four-layered cuprate high-T_c superconductor $TlBa_2Ca_3Cu_4O_y$, Phys. Rev. B **70,** 92501 (2004).

[9] P. N. Barnes, T. J. Haugan, C. V. Varanasi, and T. A. Campbell, Flux pinning behavior of incomplete multilayered lattice structure in $YBa_2Cu_3O_{7-d}$, Appl. Phys. Lett. **85,** 4088 (2004).

[10] J. Hanisch, C. Cai, R. Huhne, L. Schultz, and B. Holzapfel, Formation of nanosized BaIrO3 precipitates and their contribution to flux pinning in Ir-doped $YBa_2Cu_3O_{7-d}$ quasi-multilayers, Appl. Phys. Lett. **86,** 122508 (2005).

[11] A. D. Caplin, Y. Bugoslavsky, L. F. Cohen, L. Cowey, J. Driscoll, J. Moore, and G. K. Perkins, Critical fields and critical currents in MgB_2, Supercond. Sci. Technol. **16,** 176 (2003).

[12] J. R. Clem, Fundamentals of Vortices in the High-Temperature Superconductors, Supercond. Sci. Technol. **5,** S33-S40 (1992).

[13] Y. Zhao, M. Ionescu, J. Horvat, and S. X. Dou, Off-axis MgB_2 films using an in situ annealing pulsed laser deposition method, Supercond. Sci. Technol. **18,** 395-399 (2005).

[14] X. L. Wang, S. H. Zhou, M. J. Qin, P. R. Munroe, S. Soltanian, H. K. Liu, and S. X. Dou, Significant enhancement of flux pinning in MgB_2 superconductor through nano-Si addition, Physica C **385,** 461-465 (2003).

[15] L. D. Cooley, K. Kang, R. Klie, Q. Li, A. Moodenbaugh, and R. Sabatini, Formation of MgB_2 at low temprtatures by reaction of Mg with B6Si, Supercond. Sci. Technol. **17,** 942 (2004).

[16] J. M. Rowell, S. Y. Xu, X. H. Zeng, A. V. Pogrebnyakov, Q. Li, X. X. Xi, J. M. Redwing, W. Tian, and X. Pan, Critical current density and resistivity of MgB_2 films, Appl. Phys. Lett. **83,** 102 (2003).

[17] T. T. M. Palstra, B. Batlogg, R. B. v. Dover, L. F. Schneemeyer, and J. V. Waszczak, Critical currents and thermally activated flux motion in high-temperature superconductors, Appl. Phys. Lett. **54,** 763 (1989).

[18] T. T. M. Palstra, B. Batlogg, R. B. v. Dover, L. F. Schneemeyer, and J. V. Waszczak, Dissipative flux motion in high-temperature superconductors, Phys. Rev. B. **41,** 6621 (1990).

[19] A. Sidorenko, V. Zdravkov, V. Ryazanov, S. Horn, S. Klimm, R. Tidecks, A. Wixforth, Th. Koch, and T. Schimmel, Thermally Assisted Flux Flow in MgB_2 : Strong Magnetic Field Dependence of the Activation Energy, cond-mat/0406062 (2004).

Chapter 8. Summary and conclusions

We undertook our study as a preliminary step towards the highly expected applications of the new MgB_2 superconductor in superconducting electronic devices and coated conductors, and is part of the efforts from other research groups and companies worldwide using a number of different preparation methods. In addition, this study contributed to further understanding of the behavior and the underlying fundamental mechanisms of the MgB_2 thin films related to materials processing and the physics of superconductivity for this new material.

We first examined the process parameters of *in situ* annealed PLD MgB_2 thin film, which included depositing Mg+B precursor film at low substrate temperature and then heating the film to an elevated annealing temperature to form the MgB_2 phase. We found the T_c of the *in situ* PLD MgB_2 films is very dependent on the annealing parameters. With a stoichiometric MgB_2 target, the optimal *in situ* annealing temperature appears to be 670-690°C with a very short dwell time of 1min. A base vacuum of $9x10^{-8}$ Torr level is necessary for a good T_c. The target surface after laser ablation has a familiar cone structure, which is contributing to the droplets of material being formed and transported to the films surface, resulting in a very rough surface topography. The best zero resistivity T_c achieved under the optimized annealing condition is 32 K with a transition width of 2 K. Due to the short annealing time, the film has small grain size and high disorder level. This has been characterized by AFM and TEM, and indicated by the resistivity-temperature curves and the weak field dependence on the applied field. The J_c from magnetization hysteresis loops is of the order of $1x10^6$ A/cm^2 in fields as high as 5T, which reveals very good pinning.

Films with T_c of 38 K were prepared by an *ex situ* annealing procedure. In the *ex situ* annealing process, boron precursor film is wrapped in Ta foil and sealed together with Mg pellets and then annealed at 900ºC for 30 min. Owing to the high annealing temperature and long annealing time, the *ex situ* films are well crystallized. This result is similar to the results obtained by other research groups. AFM observation has revealed the surface topography with hexagonal crystalline features. Although the T_c is good in the *ex situ* MgB_2 films, the J_c decreases significantly with increasing fields at temperatures of 5K, 10K 15K and 20 K, rendering the film not suitable for coated conductor applications at this stage of development.

Significant difference in flux pinning as well as the slope of H_{c2}-T curve was detected between the *ex situ* and *in situ* annealed MgB_2 films. The small-grain and high-level-disorder features of the *in situ* annealed film, which is attributable to the low annealing temperature and short annealing time, may mainly contribute to the significant improvement of flux pinning in the *in situ* MgB_2 film. In contrast, our *ex situ* film is constructed of comparatively large and probably clean grains with weak links between the grains, as a result of the annealing process which was conducted in a temperature region favorable to the grain-growth. As a consequence, defect-controlled flux jump was observed by MO imaging in our *ex siu* annealed MgB_2 film. Therefore, a low temperature quick MgB_2 phase formation could be beneficial for maintaining disorder in the film, and thus of importance for high performance MgB_2 film preparation.

To examine the possibility of enhancing the Jc and H_{c2} performance of MgB_2 films, we added Si into the *in situ* annealed MgB_2 film by a target-switching method. The Si dopant is highly dispersed inside the resulting films. A clear improvement in J_c by low level Si doping in MgB_2 *in situ* films was achieved without significant decrease of the

T_c. The highest improvement in J_c was obtained by 3.5wt% Si addition using this method. The slope of the $H_{c2}(T)$ curve of the 3.5% Si added film is higher than that of the undoped film, indicating an increase in intra-grain scattering.

An off-axis deposition method has been applied and proved to be effective in improving the surface smoothness of PLD MgB_2 films. This is the first time that a off-axis deposition geometry has been applied for the MgB_2 thin film deposition among literature reports {Y. Zhao et al. SuST, **18**, 395}. Under the selected deposition and *in situ* annealing parameters, we obtained *c*-oriented *in situ* MgB_2 films on Al_2O_3-C substrate with a root mean square roughness of 4 nm. The zero resistance T_c of the best off-axis MgB_2 film was 33.1 K, with a narrow transition width of 0.9 K. Predominant c-axis orientation has been detected in the off-axis films by XRD θ-2θ scan and TEM SAED diffraction. The combined high qualities of our off-axis films, namely good T_c value, improved J_c performance in high fields, high H_{c2}-T slope of ~1 T/K and high degree of surface smoothness, represent a step forward in the process of incorporating the MgB_2 superconducting thin films into electronic devices.

With the aid of the off-axis PLD method established by this work, we have fabricated MgB_2/Mg_2Si multilayer thin films with a clearly divided and homogeneous 10-layer structure. The 5 nm thick Mg_2Si inter-layers provide effective flux pinning for the MgB_2/Mg_2Si multilayer film in parallel fields. An enhanced anisotropy of the activation energy U_0 was observed in this multilayer film. U_0 is significantly increased when the applied field is perpendicular to the c-axis and the testing current, which is in accordance with the enhancement of H_{irr}^{ab}. The H_{c2} and the residual resistance are clearly increased, which may indicate that some defects and intra-band scattering was introduced by Si addition.

List of Publications during PhD study period (from 2002 to 2005)

1. **Y. Zhao**, S. X. Dou M. Ionescu P. Munroe**, "**Significant improvement of activation energy in the MgB_2/Mg_2Si multilayer film", accepted by Appl. Phys. Lett., To be published in Feb. 2006
2. **Y. Zhao**, S. X. Dou M. Ionescu P. Munroe, "Transport properties of multilayered MgB_2/Mg_2Si superconducting thin film" accepted by J. Appl. Phys. To be published in Jun 2006
3. **Y. Zhao**, M. Ionescu, M. Roussel, a. V. Pan, J. Horvat, and S. X. Dou, "Superconducting and microstructural properties of two types of MgB_2 films prepared by pulsed laser deposition, IEEE Transactions on Applied Superconcuctivity" **15,** 3261 (2005).
4. **Y. Zhao**, M. Ionescu, J. Horvat and S. X. Dou, "Off-axis MgB_2 films using an *in situ* annealing pulsed laser deposition method", Supercond. Sci. & Technol. **18**, 395-399 (2005)
5. S. X. Dou, S Soltanian, **Y. Zhao**, E Getin, Z Chen, O. Shcherbakova and J. Horvat "The effect of nanoscale Fe doping on the superconducting properties of MgB_2" Supercond. Sci. Technol. **18**, 710 (2005)
6. M. Roussel, A. V. Pan, A. V. Bobyl, **Y. Zhao**, S. X. Dou, and T. H. Johansen, Magnetic flux penetration in MgB_2 thin films produced by pulsed laser deposition, Supercond. Sci. Technol. **18,** 1391 (2005).
7. **Y. Zhao**, M. Ionescu, J. Horvat and S.X. Dou "Comparative study of *in situ* and *ex situ* MgB_2 films prepared by pulsed laser deposition" Supercond. Science & Technology **17**, S482-S485 (2004)

8. **Y. Zhao**, M. Ionescu, J. Horvat, A.H. Li and S.X. Dou " Si addition in *in situ* annealed MgB_2 thin films by pulsed laser deposition" Superconductor Science & Technology **17** 1247-1252 (2004)

9. M. Ionescu, **Y. Zhao**, M. Roussel, S.X. dou, R. Ramer and M. Tomsic "Flux pinning in MgB_2 thin films grown by pulsed laser deposition" Journal of Optoelectronics and Advanced Materials, **6,** 169-176 (2004)

10. A.V. Pan, **Y. Zhao**, M. Ionescu, S.X. Dou, V.A. Komashko, V.S. Flis, and V.M. Pan, "Thermally activated depinning of individual vortices in $YBa_2Cu_3O_7$ superconducting films", *Physica C*, **407,** 10 (2004)

11. M. Ionescu, A. H. Li, **Y. Zhao**, H. K. Liu, A. Crisan, "Enhancement of critical current density in YBa2Cu3O7-d thin films grown by PLD on YSZ (001) surface modified with Ag nano-dots", J. Phys. D: Applied Physics, **37**, 1824 (2004)

12. **Y. Zhao**, M. Ionescu, A.V. Pan, S.X. Dou and E.W. Collings "*In situ* annealing of superconducting MgB_2 films prepared by pulsed laser deposition" Supercond. Sci. Technol. **16,** 1487-1492 (2003)